Bauhaus-Universität Weimar

Assessment of Numerical Prediction Models for Aeroelastic Instabilities of Bridges

DISSERTATION

zur Erlangung des akademischen Grades
Doktor-Ingenieur (Dr.-Ing.)

an der Fakultät Bauingenieurwesen
der Bauhaus-Universität Weimar

vorgelegt von
Tajammal Abbas
geboren am 20.12.1984
in Lahore, Pakistan

Gutachter: Prof. Dr. Guido Morgenthal
Prof. Dr. Yaojun Ge
Prof. Dr. rer. nat. Tom Lahmer

Tag der Disputation: 16.09.2016

Dedication

I dedicate this dissertation to my family for its love, endless support and encouragement. A special feeling of gratitude to my loving parents whose words of encouragement and push for persistence ring in my ears. My wife Sana who never left my side and my wonderful children Fatima and Ali who are very special for me.

Acknowledgements

Tajammal Abbas
Weimar, 2016

Abstract

The phenomenon of aerodynamic instability caused by the wind is usually a major design criterion for long-span cable-supported bridges. If the wind speed exceeds the critical flutter speed of the bridge, this constitutes an Ultimate Limit State. The prediction of the flutter boundary, therefore, requires accurate and robust models. The complexity and uncertainty of models for such engineering problems demand strategies for model assessment. This study is an attempt to use the concepts of sensitivity and uncertainty analyses to assess the aeroelastic instability prediction models for long-span bridges. The state-of-the-art theory concerning the determination of the flutter stability limit is presented. Since flutter is a coupling of aerodynamic forcing with a structural dynamics problem, different types and classes of structural and aerodynamic models can be combined to study the interaction. Here, both numerical approaches and analytical models are utilised and coupled in different ways to assess the prediction quality of the coupled model.

Bridge decks are often bluff and therefore the aeroelastic forces under wind action have to be experimentally evaluated in wind tunnels or numerically computed through Computational Fluid Dynamics (CFD) simulations. The detailed wind-tunnel investigations are expensive and time-consuming but are necessary during the design process of the long-span bridges. However, these tests have limitations in reproducing the full-scale problem and sometimes avoided or limited to the final design stage for less important structures. The CFD simulations are commonly used as alternative for such situations. This research aims at studying various combinations of analytical and numerical models to predict the flutter phenomenon. The self-excited forces are modelled using aerodynamic derivatives obtained through CFD forced vibration simulations on a section model. The structural representations were dimensionally reduced to two-degree-of-freedom section models calibrated from global models as well as multi-degree-of-freedom models.

A probabilistic flutter analysis approach utilising a meta-modelling technique is used to evaluate the effect of input parameter uncertainty. A bridge section is numerically modelled in the CFD simulations. Here flutter derivatives are considered as random variables. A novel approach for carrying out a sensitivity analysis of the flutter phenomenon is developed. The sensitivity with respect to the uncertainty of aerodynamic derivatives and structural parameters is considered by taking into account the probability distributions. A significant influence on the flutter limit is found by including uncertainties of the aerodynamic derivatives due to different interpretations of scatter in the CFD simulations. The results indicate that the proposed probabilistic flutter analysis provides extended information concerning the accuracy of the prediction of flutter limits. The ranking of flutter prediction models is done based on the concepts of total uncertainty. The final aim is to set-up a framework to estimate the flutter limit with probabilistic input parameters. The model choice for a given practical analysis scenario is also discussed in the context of the analysis findings. This study shows the difficulties in this regard which have to be overcome but also highlights some interesting and promising results.

Keywords: Flutter, bridges, sensitivity, uncertainty, meta-models, model assessment.

Contents

List of Figures

List of Tables

List of Symbols

Symbols not listed in the above table will be explained in the text.

List of Acronyms

Acronyms not listed in the following table will be explained in the text.

Chapter 1
Introduction

1.1   Motivation

Cable-supported bridges such as suspension and cable-stayed bridges are common to connect across great distances. These bridges are viewed as not only landmarks but lifeline structures. Bridges are an essential part of the fast economic growth as well as a link between people. The history of cable-supported bridges spans over two centuries. Before that time, the design of structures was based mostly on art and experience and not on engineering, since the structural knowledge was limited. As the material science and knowledge concerning the structural behaviour progressed, the design of structures became more science than art.

The first steel suspension bridge over the Jacob's Creek in the USA (with a span 21 m) was built in 1801 [1] whereas the first cable-supported bridge composed of drawn iron wires was built in Geneva (Switzerland) in 1823. The failure of the first Dryburgh Abbey Bridge in Scotland (1818) due to wind is the first significant example when several of the stay connections failed during a storm. The Brighton Chain Pier, England (1836), the Tay Bridge, Scotland (1879) and the original Tacoma Narrows Bridge, USA (1940) [2] are the most notable examples of long-span bridge failure where wind played a major role.

Figure 1.1: The original Tacoma Narrows Bridge collapse, USA [3].

Several bridges failed prior to the collapse of the original Tacoma Narrows Bridge due to wind actions; however, this was the failure that decreed bridge engineers to conduct scientific investigations of bridge aerodynamics. It was the third longest suspension bridge in the world with a main span of 853 m. The deck started to oscillate with very large amplitudes in the vertical vibration modes at a wind speed of about 68 km/h (19 m/s) and around 45 minutes later the motion changed into a torsional mode [4]. This eventually led to failure of some overstressed members and the main span collapsed as shown in Figure 1.1. The mechanics behind dynamic Wind-Structure Interaction (WSI) was not fully understood at that time. Traditional practices of design based on experience alone and the lack of understanding of the nature of wind mainly contributed to this [5]. Later, researchers [6] tried to explain the mechanisms of ultimate failure of the bridge and demonstrated, physically as well as mathematically, that the main cause was not the forced resonance but the self-excitation which is an aerodynamically-induced one. The new developments in the field of bridge aerodynamics started after the collapse of the original Tacoma Narrows Bridge and the investigations lead to the development of experimental and analytical tools for the prediction of long-span bridge response to the wind.

Today, the spans of the long-span suspension and cable-stayed bridges have been extended to new limits. The longest bridge in the world built at the end of the last century is the suspension bridge across the Akashi-Kaikyo Straits in Japan shown in Figure 1.2 with a main span of 1991 m and nearly 4 km of overall length. Aerodynamic characteristics governed the design of this bridge [2]. The Russky Bridge Russia (2012) is the world's longest cable-stayed bridge, with an 1104 m long central span. With the increase in bridge span length, the modern bridge structures are more flexible, lightweight and their structural characteristics require special treatment of aerodynamic analysis and design under wind action.

Figure 1.2: Akashi-Kaikyo Bridge, Japan [5].

1.2 Objective of the Study

The study of the WSI is essential for the analysis and design of long-span cable-supported bridges. The phenomenon of aerodynamic instability caused by the wind is usually a major design criterion for such structures. This interaction of the wind and structural response is potentially dangerous at high wind speeds and could lead to aeroelastic instabilities such as flutter. If the wind speed exceeds the critical flutter speed of the bridge, this constitutes an ultimate limit state. The prediction of the flutter

boundary, therefore, requires accurate and robust models. Bridge decks are often bluff, therefore, the aeroelastic forces under wind action have to be experimentally evaluated in wind tunnels or numerically computed through Computational Fluid Dynamics (CFD) simulations.

The assessment of models has gained much attention in recent years in the field of structural engineering. The complexity and uncertainty of models for engineering problems demand strategies for model assessment. There exist state-of-the-art prediction models which go through development and validation processes. A valid question concerns how the model itself can be utilised to quantify its quality by studying how well it predicts certain phenomena.

The main objective of this research is to develop a framework for assessing the quality of coupled models used in the analysis of aeroelastic instabilities of bridges by utilising uncertainty measures and the ability to predict the phenomena. A wide range of models has been used for this purpose. It is essential to assess the model for a certain range of parameters for which it is used. This makes it challenging to cover the whole range of parameters; however, it can be possible to cover some part of this range by selecting several parameter sets. A schematic for model assessment possibilities is shown in Figure 1.3. Bridges with streamlined as well as bluff cross sections subjected to aeroelastic instabilities are studied for this purpose. The ability to predict the flutter stability limit of the structure and the uncertainty related to this prediction is used as an indicator of the model quality.
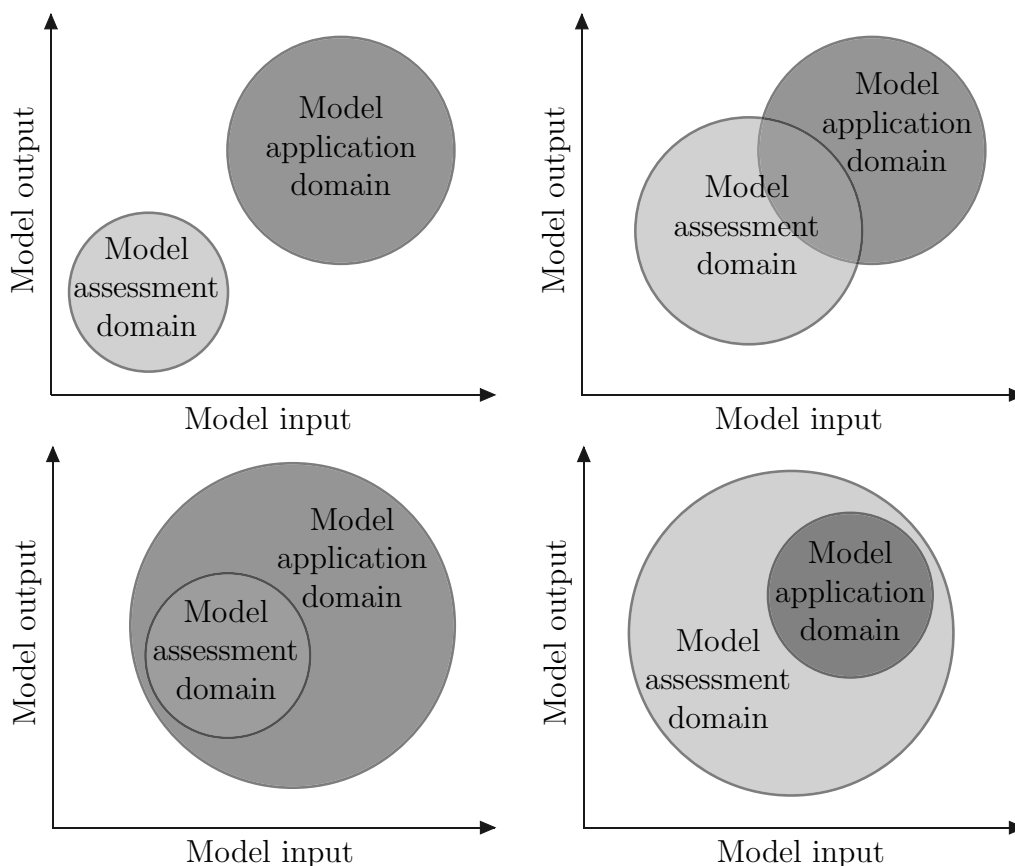
Figure 1.3: Model assessment domains vs. model application domains: (top-left) undesirable or unrealistic situation, (top-right) useful to show model robustness, (bottom-left) most common situation, (bottom-right) ideal situation.

1.3 Contribution of the Thesis

The framework developed for model assessment consists of three main steps as shown in Figure 1.4. In the first step, the models are selected for the quantity of interest i.e. flutter limit (Chapter 5 and Chapter 6). The next step is to identify the influential input parameters (Chapter 7). Then the parameter sensitivity and uncertainty are quantified (Chapter 8). Finally, the model ranking is done which is based on the overall uncertainty.

It is worth mentioning here that two assumptions are made throughout the thesis: the assessed models are ensured to converge and the numerical uncertainty is not considered. The models have been used without the optimum choice of numerical parameters. The aim of this research is not to improve the already existing models. Rather, the objective is to highlight their distinct features and to develop a framework to quantify uncertainties in the model predictions. The contribution of this research is summarized as follows:

- A thorough study is performed on the investigated problem to compute the flutter limit by using a wide range of available state-of-the-art models. It provides useful insight into understanding the physics underlying the complex aeroelastic phenomena of flutter.

- Individual models, as well as coupling strategies for structure and aerodynamic forcing, are reviewed and implemented to assess the prediction quality of the hybrid model. Additionally, an approach is presented to perform flutter analysis using a time integration scheme without performing an eigenvalue analysis.

- The concepts of sensitivity and uncertainty analysis are used to identify essential input parameters in flutter analysis. This was done by making use of deterministic as well as of probabilistic approaches. A framework is developed to examine sensitivities of flutter limit to structural parameters and aerodynamic behaviour of the bridge deck.

- An approach is presented to generate turbulent flow in a flow solver based on a uniform incident flow. The approach is computationally feasible and is very similar to the well-accepted approach used in the wind tunnel tests.

- A novel approach is presented to consider the uncertainty related to the prediction of the aerodynamic behaviour of a bridge cross section and it is shown how this uncertainty propagates to the model output.

- Meta-models are developed to make the numerical analysis more efficient by relating input parameters to the model output with simple mathematical functions. For this purpose, polynomial regression and moving least-squares were used to replace time intensive numerical simulations. Their ability and efficiency to perform and capture the output response for different ranges of input parameters is highlighted.

- Models are ranked by using the concept of total uncertainty which includes input parameter uncertainty and model uncertainty. This is done by making use of the adjustment factor approach to quantify model uncertainty which is estimated by the difference between the model average and the adjusted model.

- An approach is presented to make use of already available data for bridge cross

sections to utilise for flutter stability analysis of similar structures by using response surface techniques.

Model Combinations

Select Models

Quantity of interest
i.e. flutter limit

Deterministic Sensitivity Analysis

Sensitivities to flutter limit

Influential input
parameters

Probabilistic Assessment

Sensitivity analysis

Sensitivity
indices

Parameter uncertainty analysis

Mean, variance,
distribution

Model uncertainty

Overall uncertainty,
model ranking
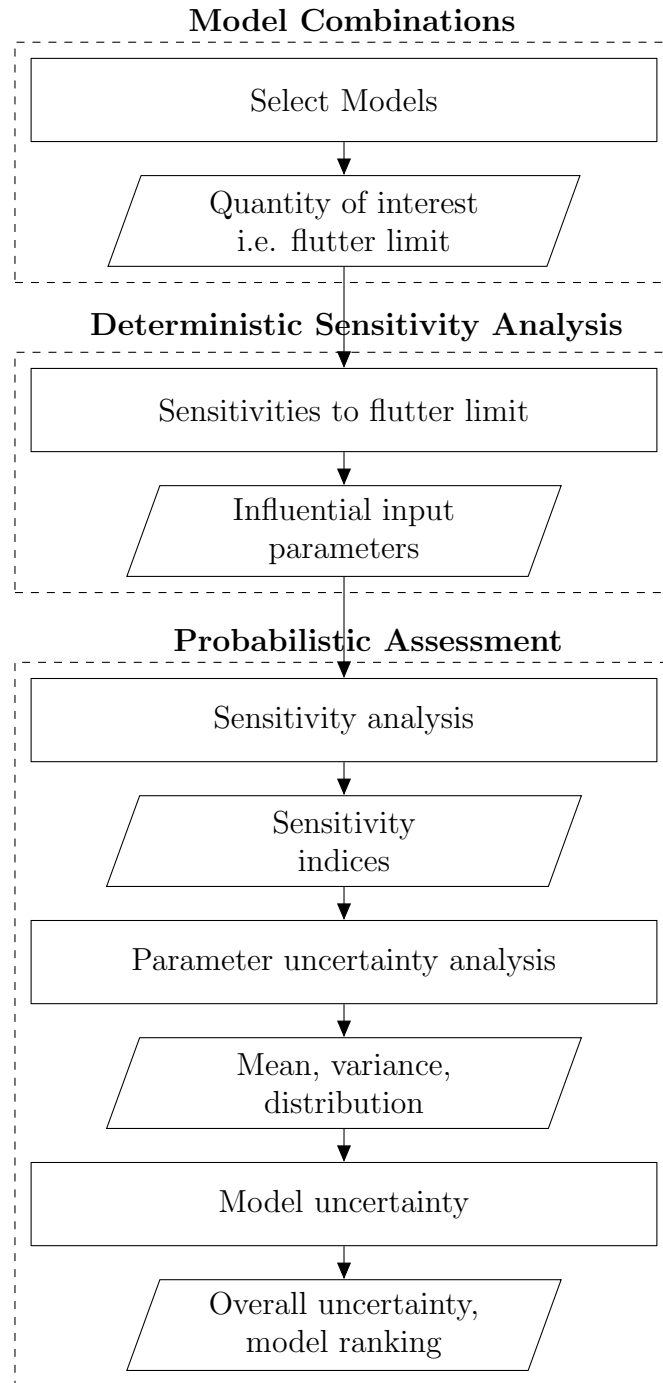
Figure 1.4: Developed framework for model assessment.

1.4 Outline of the Thesis

The layout of this dissertation is arranged as follows.

Chapter 2 provides fundamentals of probabilistic analyses and assessment procedures based on the sensitivity and uncertainty analyses. The algorithms and aspects related to their implementation are explained.

Chapter 3 introduces the subject of bridge aerodynamics and aeroelastic phenomena related to the design and analysis of long-span bridges. Important developments made in this field are reviewed and referenced.

The methods used in the aerodynamic analysis of structures are discussed in Chapter 4 focusing more on analytical and numerical approaches, whereas experimental methods are also briefly described. A comprehensive information on flutter analysis collected from the literature has been summarised in the appendices related to this chapter.

The analytical and numerical models for flutter analysis of bridges are explained in Chapter 5. A comprehensive review of different modelling techniques is provided. A wide range of models was utilised and coupled in different ways to perform flutter stability analysis. Furthermore, an approach to compute flutter limit is presented without the need of performing an eigenvalue analysis. The implementations of these models are described in detail.

In Chapter 6, the application of different flutter analysis approaches to the selected reference structures is shown. The merits and demerits of these approaches are discussed in detail. The flutter limits computed by means of these models are also compared.

Chapter 7 is devoted to the study of the sensitivity of the model output to the input parameters. It also provides studies concerning model robustness. The capabilities of models to consider different scenarios are shown including their limitations.

In Chapter 8, probabilistic sensitivity and uncertainty analyses have been used to identify the essential input parameters and their effects on the model response are quantified. A novel approach considering aerodynamic uncertainty for bridge deck sections is developed. The effectiveness of response surface methods is also highlighted. Input parameter uncertainties and model uncertainties are computed. Ranking of models is done based on their total uncertainty.

Finally, Chapter 9 provides conclusions derived from the obtained results and recommendations for applications and future research are offered.

Chapter 2

Fundamentals of Probabilistic Analysis

2.1 Introduction

The assessment of models require sensitivity and uncertainty analyses where model parameters are defined by their statistical properties and the subsequent model response is evaluated. This chapter explains the basis of stochastic input parameters and sampling strategies for sensitivity and uncertainty analyses. Deterministic as well as probabilistic methods are discussed. Moreover, response surface approaches are also described. Finally, the concepts of the Adjustment Factor Approach (AFA) have been utilised to quantify model framework uncertainty.

2.2 Random Variables and Random Vectors

Probability is commonly defined as the measure of the likelihood that an event will occur. The probability P of a single real random variable X to be smaller than a deterministic value x is defined by the Cumulative Distribution Function (CDF) $F(X)$ as:

$$F(X) = P[X < x].\tag{2.1}$$

The derivative of the CDF with respect to x is known as the Probability Distribution Function (PDF) $f(x)$:

$$f(x) = \frac{\delta F(X)}{\delta x}.\tag{2.2}$$

The mean value μ_X of the corresponding distribution type is

$$\mu_X = E[X] = \int_{-\infty}^{\infty} x f(x)\, dx.\tag{2.3}$$

The variance V_X is defined as

$$V_X = \int_{-\infty}^{\infty} (x - \mu_X)^2 f(x)\, dx.\tag{2.4}$$

The standard deviation σ_X is square root of variance

$$\sigma_X = \sqrt{V_X}.\tag{2.5}$$

Sometimes it is convenient to represent normalised standard deviation known as coefficient of variation CV_X

$$CV_X = \frac{\sigma_X}{\mu_X}.\tag{2.6}$$

Some typical distribution functions are shown in Table 2.1.

For multidimensional problems, the correlation between variable X_1 and X_2 is defined with the help of the covariance function $C_{XX}(X_1, X_2)$ as:

$$C_{XX}(X_1, X_2) = E[(X_1 - \bar{X}_1)(X_2 - \bar{X}_2)]. \tag{2.7}$$

The correlation coefficient $\rho(X_1, X_2)$ is used as a non-dimensional indicator of parameter dependence. A value of the correlation coefficient equal to 0 describes two variables as independent and 1 (or -1) implies full dependence. The coefficient of correlation is the standardised covariance between two random variables X_1 and X_2

$$\rho(X_1, X_2) = \frac{E[(X_1 - \bar{X}_1)(X_2 - \bar{X}_2)]}{\sqrt{V(X_1)V(X_2)}} = \frac{C_{XX}(X_1, X_2)}{\sigma_{X_1}\sigma_{X_2}}, \qquad -1 \leq \rho(X_1, X_2) \leq 1, \tag{2.8}$$

where X_1 and X_2 are the sample values, $\bar{X}_1$, $\bar{X}_2$ and σ_{X1}, σ_{X2} are the estimates of the mean values and the standard deviations, respectively. The significance of the correlation coefficient is further discussed for the variance based sensitivity and uncertainty analyses in Sections 2.5.1 and 2.5.2.

2.3   Sampling Techniques

Many statistical quantities can easily be estimated by sampling techniques. A large number of samples is required to represent multi-parameter problems with sufficient accuracy. The required number of samples increases exponentially with the increase in the number of input parameters. The design space of the input parameters is required to be scanned with discrete points. There are several techniques to generate samples from distributions such as simple Monte Carlo Sampling (MCS), Latin Hypercube Sampling (LHS) and Advanced Latin Hypercube Sampling (ALHS). Here each set of sampled parameter values belongs to the specified inputs.

After the identification of stochastic input parameters with their distributions, the design space is scanned by Design of Experiments (DoE) or sampling methods. These design schemes are mainly based on a regular arrangement of the samples. Hence stochastic sampling schemes can be used to reduce the number of samples. Further details about classical DoE schemes can be found in [10]. The DoE is the sampling plan in the input parameter space. In contrast to random sampling, the DoE provides a unique sample value in the input parameter space. The assessment of the quality of such designs is important, keeping in view the number of samples is limited to reduce computational costs. The accuracy of the sampled parameters is often tested by computing the mean and standard deviation of the generated samples.

2.3.1   Simple Random Sampling

The Simple Random Sampling (SRS), also called simple or crude MCS is the classical approach to study the propagation of input parameter uncertainties through model output. It assumes a uniform distribution with given lower and upper bounds. The input parameters are sampled independently with their respective PDF. Often clusters and gaps are observed when less number of samples are used. It produces undesired correlations between the input parameters which can influence the sensitivity measures. The intended correlations can be introduced in this approach; however, the sampling

Table 2.1: Typical probability distributions with their properties [7, 8, 9].

Limits	Distribution Functions	Distribution Plots
Uniform $a \leq x \leq b$	$f(x) = \frac{1}{b-a}$ $F(X) = \frac{x-a}{b-a}$ $\mu_X = \frac{a+b}{2}$ $\sigma_X = \frac{b-a}{\sqrt{12}}$	
Normal $-\infty \leq x \leq \infty$	$f(x) = \frac{1}{\sigma_X\sqrt{2\pi}} \exp\left(-\frac{(x-\mu_X)^2}{2\sigma_X^2}\right)$ $F(X) = \frac{1}{\sigma_X\sqrt{2\pi}} \int_{-\infty}^{x} \exp\left(-\frac{(t-\mu_X)^2}{2\sigma_X^2}\right) dt$	
Log-normal $q \leq x \leq \infty$	$f(x) = \frac{1}{\lambda\sqrt{2\pi}(x-q)} \exp\left(-\frac{\left[\ln\left(\frac{x-q}{m-q}\right)\right]^2}{2\lambda^2}\right)$ $F(X) = \frac{1}{x\sigma_X\sqrt{2\pi}} \int_{0}^{x} \exp\left(-\frac{\ln\left(\frac{x-q}{m-q}\right)^2}{2\lambda^2}\right) dt$ $\mu_X = \exp\left(q + \frac{\lambda^2}{2}\right)$ $\sigma_X^2 = \exp\left(2q + \lambda^2\right)\left(\exp\lambda^2 - 1\right)$ q: physical limit for x m: distribution median	
Triangular $a \leq x \leq b$	$f(x) = \frac{2(x-a)}{(b-a)(c-a)};\qquad a \leq x < c$ $f(x) = \frac{2(b-x)}{(b-a)(b-c)};\qquad c < x \leq b$ $F(x) = \frac{(x-a)^2}{(b-a)(c-a)};\qquad a \leq x < c$ $F(x) = 1 - \frac{(b-x)^2}{(b-a)(b-c)};\quad c < x \leq b$ $\mu_X = \frac{a+b+c}{2}$ $\sigma_X = \sqrt{\frac{a^2+b^2+c^2-ab-ac-bc}{18}}$	
Exponential $\epsilon \leq x \leq \infty$	$f(x) = \lambda\exp(-\lambda x)$ $F(x) = 1 - \exp(-\lambda x)$ $\mu_X = \lambda^{-1}$ $\sigma_X = \lambda^{-2}$	

where,

a, b: minimum and maximum distribution bounding limits, respectively

μ_X, σ_X: mean and standard deviation, respectively

λ: shape parameter

will not be random in actual the sense.   It provides straightforward and unbiased results. However, the number of samples required is large, making the simulations time consuming depending on the complexity of the model.

2.3.2   Latin Hypercube Sampling

The LHS allows to overcome such problems even for a smaller number of samples. The main idea is to divide the range of each input parameter into a certain number of intervals of equal marginal probability. Correlations can be introduced by the method of rank correlations by Iman and Conover [11]. It is an alternative approach which gives significantly better estimators of model response and covers the parameter space effectively. Figure 2.1 illustrates the advantage of the LHS sampling approach over the SRS. A smaller number of samples is required to obtain reasonable convergence. The limitation of this approach is that the sampling has to be done once in the beginning and more samples cannot be added later.
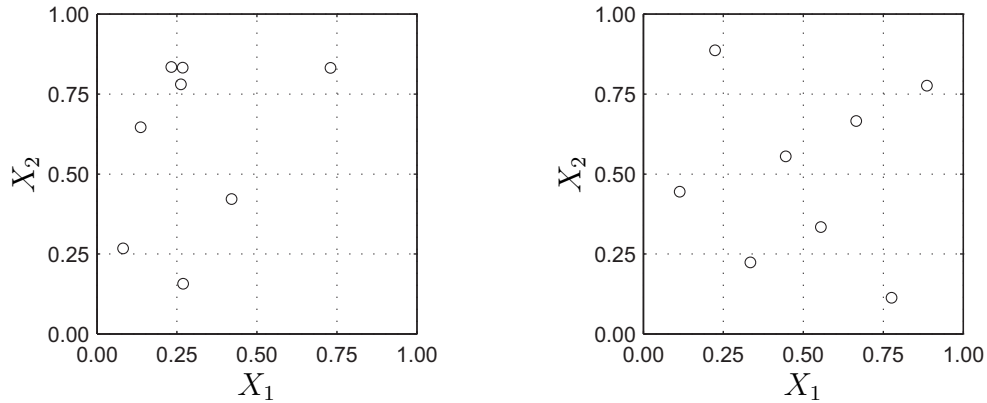
Figure 2.1: Comparison of sampling approaches:
(left) Simple Random Sampling,
(right) Latin Hypercube Sampling.

2.3.3   Introducing Correlations between Samples

The input parameters are assumed to be independent of each other when using the SRS, therefore the PDF should be uncorrelated. However, in actual situations these parameters can be correlated and therefore it may be necessary to introduce correlation between the parameter samples. If the input parameters are uncorrelated in reality but sampled as correlated then the model response can show false dependence. A common approach to generate correlated samples using a given correlation matrix is by generating a $\mathbf{U}$ matrix such that

$$\mathbf{U}^{\mathrm{T}}\mathbf{U} = \mathbf{C}, \tag{2.9}$$

where $\mathbf{C}$ is the given correlation matrix and $\mathbf{U}$ is the matrix which can be obtained by Cholesky decomposition. The correlated samples are generated from the uncorrelated samples by multiplying with the $\mathbf{U}$ matrix.

$$R_c = R\mathbf{U}, \tag{2.10}$$

where R are the uncorrelated samples and R_c are the correlated samples.

2.4 Response Surface Method

Variance based sensitivity and uncertainty analyses become expensive and inefficient for complex models. The response surface approach may be used in this case. Surrogate modelling can be viewed as a non-linear inverse problem for which the aim is to determine a continuous function of a set of parameters on the basis of limited data. The choice of surrogate model is important to obtain model parameters. A response surface with reasonable quality can be achieved if a sufficient number of numerical simulations are performed with suitable combinations of input parameters. This response surface can then be used for the sensitivity and uncertainty analyses.

2.4.1 Polynomial Regression

Polynomial regression is used to approximate the model response by polynomial basis function. This function could be linear, quadratic or higher order with or without coupling terms. This approach is simple and easy to implement. These parametric models relate the input parameters to the global model response. The model output Y_i for a given set X_i of the input parameters $\mathbf{X}$ can be formulated as the sum of the approximated value $\hat{Y}_i$ and an error term ϵ_i as:

$$Y(X_i) = \hat{Y}_i(X_i) + \epsilon_i = \mathbf{P}^{\mathrm{T}}(X_i)\boldsymbol{\beta} + \epsilon_i \tag{2.11}$$

where $\mathbf{P}^{\mathrm{T}}(X)$ is the polynomial basis,

$$\mathbf{P}^{\mathrm{T}}(X) = \begin{bmatrix} 1 & x_1 & x_2 & x_3 & \ldots & x_1^2 & x_2^2 & x_3^2 & \ldots & x_1 x_2 & x_1 x_3 & \ldots \end{bmatrix} \tag{2.12}$$

and $\boldsymbol{\beta}$ is a vector of unknown regression coefficients. These coefficients are determined from the support points by assuming independent errors with equal variance at each point. The regression coefficients $\hat{\boldsymbol{\beta}}$ can be estimated by least-squares by minimising the following:

$$L_{poly} = \sum_{i=1}^{N} \epsilon_i^2 = \boldsymbol{\epsilon}^{\mathrm{T}}\boldsymbol{\epsilon} = (\boldsymbol{Y} - \mathbf{X}\boldsymbol{\beta})^{\mathrm{T}} (\boldsymbol{Y} - \mathbf{X}\boldsymbol{\beta}). \tag{2.13}$$

The resulting least-squares solution in matrix form reads

$$\hat{\boldsymbol{\beta}} = (\mathbf{P}^{\mathrm{T}}\mathbf{P})^{-1}\mathbf{P}^{\mathrm{T}}\boldsymbol{Y} \tag{2.14}$$

where $\mathbf{P}$ is a matrix containing the basis polynomials of the support points and $\boldsymbol{Y}$ is the vector of sampled point values. The predicted response for any set of input parameters can be found as:

$$\hat{\boldsymbol{Y}} = \mathbf{X}\hat{\boldsymbol{\beta}}, \tag{2.15}$$

where $\hat{\boldsymbol{Y}}$ is the approximated response. This model can easily be used several times once it is developed.

2.4.2 Moving Lest-Squares

The Moving Least-Squares (MLS) approach has the ability to capture localised regions of the model response. This is achieved by introducing radial weighting functions which depend on the location of the data point being evaluated. This is a modified form of polynomial response surface approach where equal weights are considered. In the MLS, the data points close to the evaluated point influence more and points at a

larger distance have less effect. It provides superior behaviour but requires greater computational effort. Additionally, it requires being performed each time for a new data set. More detailed discussion on the MLS can be found in [12].

The weighted lest-squares solution is obtained by minimising the following:

$$L_{MLS} = \sum_{i=1}^{N} \epsilon_i^2 w_i = \boldsymbol{\epsilon}^{\mathrm{T}} \boldsymbol{W} \boldsymbol{\epsilon} = (\boldsymbol{Y} - \mathbf{X}\boldsymbol{\beta})^{\mathrm{T}} \boldsymbol{W} (\boldsymbol{Y} - \mathbf{X}\boldsymbol{\beta}). \tag{2.16}$$

Similarly the weighted regression coefficients $\hat{\boldsymbol{\beta}}$ can be estimated as:

$$\hat{\boldsymbol{\beta}} = (\mathbf{P}^{\mathrm{T}} \boldsymbol{W} \mathbf{P})^{-1} \mathbf{P}^{\mathrm{T}} \boldsymbol{W} \boldsymbol{Y}, \tag{2.17}$$

where $\boldsymbol{W}$ is the weighting function depending on the location of each support point. The approximated response from the set of input parameters can be found as:

$$\hat{\boldsymbol{Y}} = \mathbf{P}^{\mathrm{T}} (\mathbf{P}^{\mathrm{T}} \boldsymbol{W} \mathbf{P})^{-1} \mathbf{P}^{\mathrm{T}} \boldsymbol{W} \boldsymbol{Y}. \tag{2.18}$$

The Gaussian weighting function can be used such as:

$$w_G = e^{-\frac{s^2}{a^2}}, \tag{2.19}$$

where s is the normalised distance between the support point and approximated point and a is the shape factor, respectively. The normalised distance s can be computed as:

$$s = \frac{\| X - X_i \|}{\tilde{D}}, \tag{2.20}$$

where $\tilde{D}$ is the influence radius.

2.4.3 Coefficient of Determination

The Coefficient of Determination (CoD) R^2 shows the quality of approximation of a regression model.

$$R^2 = \frac{SS_R}{SS_T} = 1 - \frac{SS_E}{SS_T}, \qquad 0 \le R^2 \le 1 \tag{2.21}$$

where SS_T is equivalent to the total variation of the output $\boldsymbol{Y}$, SS_R represents the variation due to the regression, and SS_E is the unexplained variation:

$$SS_T = \sum_{i=1}^{N} (Y_i - \bar{Y})^2, \tag{2.22a}$$

$$SS_R = \sum_{i=1}^{N} (\hat{Y}_i - \bar{Y})^2, \tag{2.22b}$$

$$SS_E = \sum_{i=1}^{N} (Y_i - \hat{Y}_i)^2. \tag{2.22c}$$

If the CoD is close to 1, the approximation represents the support point values with small errors. However, the polynomial model would fit exactly through the support points, if their number is equivalent to the number of coefficients p. In this case, the CoD would be equal to 1, independent of the true approximation quality. In order to

penalise this over-fitting, the adjusted CoD was introduced [7]:

$$R_{adj}^2 = 1 - \frac{SS_E/(N-p)}{SS_T/(N-1)} = 1 - \frac{N-1}{N-p}(1 - R^2). \tag{2.23}$$

The Coefficient of Prognosis (CoP) [13] based on cross-validation error estimates can also be used as a model independent-measure to assess the model quality.

2.5   Probabilistic Model Assessment

Models in bridge aerodynamics are usually complex and use a large number of input parameters. These input parameters are often correlated and sometimes associated with high uncertainties. The uncertainties are propagated in the model solution and are depicted in the final output. The assessment of overall model quality requires to take into account these uncertainties in the analysis.

2.5.1   Sensitivity Analysis

Sensitivity analysis is the study of how the uncertainty in the output of a model can be associated, qualitatively or quantitatively, with different sources of variation in the model input [14]. A sensitivity analysis determines the change in model output values that results from the changes in model input values. Thus it measures the change in a localised region of the space of input parameters. The main objective of sensitivity analysis is to identify the input parameters which have a significant influence on the output and to quantify their relative importance. The parameters which have the least effect on the output can be ignored to simplify the problem for further analyses. Approach to sensitivity analysis can be divided into two main classes: deterministic and probabilistic, sometimes also known as local and global sensitivity analyses, respectively.

2.5.1.1   Local Sensitivity Analysis

A deterministic approach to sensitivity studies is more common for linear models. The model may be run for a few times with different parameter combinations varying one parameter each time to have an impact on the model output. Assuming a model with a scalar output Y as a function of a given set of n random input parameters X_i:

$$Y = f(\mathbf{X}) = f(X_1, X_2, \ldots, X_n), \tag{2.24}$$

$$S_i = \frac{(\triangle Y)_i}{\triangle X_i} = \frac{Y(X_i + \triangle X_i) - Y(X_i)}{\triangle X_i}, \qquad i = 1, \ldots, n \tag{2.25}$$

where S_i is the sensitivity coefficient reflecting the output according to a variation of the input parameter X_i, and $\triangle Y$ is the increment of estimated output. Applying a Taylor series expansion, the derivative of Eq. (2.24) can be given by [15],

$$\triangle Y = \sum_{i=1}^{n} S_i(X_i - \overline{X}_i) \tag{2.26}$$

where $\overline{X}_i$ is the mean value of the input parameter X_i. The variation of $\triangle Y$ and Y is the same because the probability distributions of the two variables coincide with each other with different locations of the mean value. Partial derivatives (cf. Eq. (2.25)) can

be seen as a mathematical definition of the sensitivity of the model output with respect to the model input.

This method is very efficient, easy to implement and requires only a few runs. However, it has limitations in that it does not consider the correlation between the input parameters and is not suitable for noisy data and non-linear response as the derivatives may lead to inaccurate results. Moreover, it gives only local information around a given parameter and does not give any information about the rest of the space whereas often input parameters of complex models have a wide range of variation.

2.5.1.2 Global Sensitivity Analysis

Variance based sensitivity analysis is a form of Global Sensitivity Analysis. This method is very suitable to quantify the contribution of noisy response. The proportion of the output variance caused by a random input variable is directly quantified by these methods. The parameter values are sampled with the PDF of the input parameters according to a predefined strategy. Simulations are then performed and results are post-processed. The important points to be addressed are:

- to find the influence of variation of each input parameter on the output,

- the contribution of the variance of each input parameter distribution to the variance of the output distribution,

- the order of the input parameters with respect to their importance on the model output

- identification of the parameter which has the highest influence,

- identification of the parameters which have insignificant influence,

- influence of parameter correlation on the model output,

- to measure the effect of interaction.

Variance based sensitivity analyses have been used to calculate first order and total effects sensitivity indices according to Saltelli et al. [14]. The direct measure of sensitivity is called first order sensitivity index S_i or the main effect which is defined as:

$$S_i = \frac{V_{X_i}(E_{\mathbf{X}\sim i}(Y|X_i))}{V(Y)} = 1 - \frac{E_{X_i}(V_{\mathbf{X}\sim i}(Y|X_i))}{V(Y)}, \qquad \sum_{i=1}^{n} S_i \leq 1 \qquad (2.27)$$

where $V(Y)$ is the unconditional variance of the model output and $V_{X_i}(E_{\mathbf{X}\sim i}(Y|X_i))$ is the variance of Y caused by a variation of X_i only or the variance of conditional expectation with $\mathbf{X}_{\sim i}$ denoting the matrix of all factors except X_i. Since first order sensitivity indices measure only the decoupled influence of each input variable, an extension for higher order coupling terms is necessary. Therefore, total effect sensitivity indices S_{T_i} are introduced as:

$$S_{T_i} = \frac{E(V(Y|\mathbf{X}_{\sim i}))}{V(Y)} = 1 - \frac{V_{\mathbf{X}\sim i}(E_{X_i}(Y|\mathbf{X}_{\sim i}))}{V(Y)}, \qquad \sum_{i=1}^{n} S_{T_i} \geq 1 \qquad (2.28)$$

where $V(Y|\mathbf{X}_{\sim i})$ is the variance of Y caused by all model inputs without X_i and measures the first order effects of $\mathbf{X}_i$ on the model output which does not contain any

effect corresponding to X_i. The sum of total sensitivity indices is 1 if the model is purely additive. This method is only suitable when the input parameters are uncorrelated.

Xu and Gertner [16] proposed a method by considering the contribution of model output uncertainty by an individual parameter to be divided into two parts: the correlated contribution and the uncorrelated contribution. This approach uses a regression-based method to quantitatively decompose the total uncertainty in the model output into partial variances contributed by correlated variations and partial variances contributed by uncorrelated variations. It can successfully measure the uncertainty contribution where the linear regression model describes well the actual model behaviour.

If the effect of each parameter X_i on model output Y is linear and only main effects are important then the model can be simplified by a linear regression model. The partial variance $\hat{V}_i$ can be estimated as follows:

$$\hat{V}_i = \frac{1}{N-1} \sum_{j=1}^{N} (\hat{Y}_j^{(i)} - \bar{Y})^2, \tag{2.29}$$

with

$$\hat{Y}_j^{(i)} = \hat{\theta}_0 + \hat{\theta}_i X_i, \tag{2.30}$$

where $\hat{\theta}_0$ and $\hat{\theta}_i$ are the estimates for linear regression. Finally, uncorrelated variance $\hat{V}_i^U$ can be derived as follows:

$$\hat{V}_i^U = \frac{1}{N-1} \sum_{j=1}^{N} (\hat{Y}_j^{(-i)} - \bar{Y})^2, \tag{2.31}$$

with

$$\hat{Y}_j^{(-i)} = \hat{r}_0 + \hat{r}_i X_i, \tag{2.32}$$

where $\hat{r}_0$ and $\hat{r}_i$ are the estimates for linear regression. The correlated variance $\hat{V}_i^C$ can be calculated by the following equation:

$$\hat{V}_i^C = \hat{V}_i - \hat{V}_i^U. \tag{2.33}$$

Using the ratio of the partial variance and the total variance, the first order sensitivity indices can be calculated for each parameter X_i:

$$S_i = \frac{\hat{V}_i}{\hat{V}}, \tag{2.34a}$$

$$S_i^U = \frac{\hat{V}_i^U}{\hat{V}}, \tag{2.34b}$$

$$S_i^C = \frac{\hat{V}_i^C}{\hat{V}}. \tag{2.34c}$$

2.5.2   Uncertainty Analysis

The main objective of uncertainty analysis is to quantify the uncertainty in the output as a result of uncertainty in the input parameters. This involves the identification of all sources of uncertainty in the input parameters and their effects on the model response. Uncertainty analysis helps to estimate the mean and standard deviation of the outputs. It also includes the identification of characteristics of various probability distributions of

the model output. The model output is described together with its associated probability of occurrence.

The first step is the identification of input parameters potentially contributing to uncertainty of the model predictions. The input parameter distributions are identified either through expert judgement or based on empirical evidence. The standard deviation of the probability density functions of each parameter expresses uncertainty on the respective input parameter. Samples of input parameter are generated from the corresponding PDF. Possible correlations between the varying parameters can also be considered. The model is run in a sequential way with a different set of sampled input parameters each time. The output is analysed using statistical methods. Extracting the central measures from the output such as the distribution of the predicted values, mean, standard deviation and the confidence intervals in order to quantify the uncertainty on the model prediction.

If the input parameters are independent to each other, then the combined standard uncertainty σ_X of the output can be expressed as:

$$\sigma_X = \sqrt{\sum_{i=1}^{n} S_i^2 \sigma_{X_i}^2} \tag{2.35}$$

where σ_{X_i} is standard uncertainty that is corresponding to standard deviation for expressing uncertainty of an input variable. In many cases, it is convenient to use relative uncertainty instead of standard uncertainty. The normalised uncertainty and corresponding normalised sensitivity coefficient can be obtained dividing them by their mean values. The normalised sensitivity coefficient $\widetilde{S}_i$, normalised uncertainty $\widetilde{\sigma}_X$ and output Y can be expressed as follows:

$$\widetilde{S}_i = \frac{(\triangle Y)_i/(\overline{Y})_i}{\triangle X_i/\overline{X}_i}, \tag{2.36}$$

$$\widetilde{\sigma}_X = \sqrt{\sum_{i=1}^{n} \widetilde{S}_i^2 \left(\frac{\sigma_{X_i}}{\overline{X}_i}\right)^2}, \tag{2.37}$$

$$Y = \overline{Y} + \overline{Y} \sum_{i=1}^{n} \widetilde{S}_i \left(\frac{\triangle X_i}{\overline{X}_i}\right) \tag{2.38}$$

where $\overline{Y}$ is the mean output.

Since the relation of output and input parameters is expressed in the above equation, the accuracy of the evaluated uncertainty is strongly depending on how the probability models used in uncertainty analysis properly fit the natural variability of the input parameters.

2.5.3 Model Framework Uncertainty

The uncertainties related to model output can be broadly classified into two categories. The first is known as the 'model parameter uncertainty' which occurs as a result of randomness in the input parameter which has been discussed in Section 2.5.2. The second is called 'model framework uncertainty' which is due to lack of knowledge, insufficient data and simplifications made in the modelling process. The approach

presented here quantifies the model framework uncertainty considering the relative use and accuracy of each model based on experts judgement. This is done by assigning model probabilities to each model based on expert opinion which represents that the selected model is the 'best model' among the set of models considered to be a good candidate for the given engineering problem. Mosleh and Apostolakis [17] used the Adjustment Factor Approach (AFA) to quantify model uncertainty with Bayes' theorem by utilising expert opinion in the absence of experimental data. This approach has been widely used in the engineering problems. Zio and Apostolakis [18] quantified the model uncertainty in the assessment of radioactive waste repository.

The model probabilities are decided from expert judgement based on the relative advantage of individual model. The laws of probability theory holds and for the N number of individual models from a set M of considered models,

$$M = \{M_1, M_2, \ldots, M_N\} \tag{2.39}$$

probability is bounded,

$$\sum_{i=1}^{N} P(M_i) = 1, \quad 0 \le P(M_i) \le 1 \tag{2.40}$$

where $P(M_i)$ is the probability of model i. In the absence of any information about the model accuracy, the model probabilities may be divided equally. In such situations any model can be considered as the 'best model' and the effect of other models can be seen on this selection.

2.5.3.1   Adjustment Factor Approach

The AFA [19] propagates the model uncertainty into the model prediction by considering an adjustment factor to be added to the best model to obtain the adjusted model. The adjusted system response from a set of models can be predicted as:

$$y_p = y^* + E_a^* \tag{2.41}$$

where y_p is the adjusted model, y^* is the prediction of best model and E_a^* is the adjustment factor. The best model is the one which has the highest model probability. The adjustment factor is used to account for the uncertainty in the selected best model. The factor E_a^* is assumed to be normally distributed which represents the uncertainty associated with the selection of most accurate model. The first and second moment of E_a^* [20] can be calculated with the known model prediction probabilities as:

$$E(E_a^*) = \sum_{i=1}^{N} P(M_i)(y_i - y^*), \tag{2.42}$$

$$V(E_a^*) = \sum_{i=1}^{N} P(M_i)(y_i - E(y_p))^2, \tag{2.43}$$

where $P(M_i)$ is the probability of model i, y_i is the prediction of model i without considering parameter uncertainty. The models considered here are assumed to be deterministic. The expected value of the adjusted model $E(y_p)$ can be calculated as follows:

$$E(y_p) = y^* + E(E_a^*). \tag{2.44}$$

Since the models are considered deterministic the variance of adjusted model $V(y_p)$ will be equal to the variance of the adjustment factor:

$$V(y_p) = V(E_a^*). \tag{2.45}$$

The Eqs. (2.44) and (2.45) represent a normally distributed adjusted model with some variance representing the model framework uncertainty in the output. The prediction is the weighted average of models with the help of model probabilities where the effect of reference model vanishes [21]. The limitation of this approach is that in this form it does not take into account the parameter uncertainty in each model since the models are assumed deterministic.

2.5.3.2 Probabilistic Adjustment Factor Approach

The Probabilistic Adjustment Factor Approach (PAFA) [20, 22, 23, 24] is an extension of the AFA to handle parameter uncertainty. The AFA in the current form is only capable of dealing with deterministic parameters. If the parameters are considered probabilistic, the approach needs to be derived again with this assumption. The approach does not quantify the parameter uncertainty but considers each model output to be represented with the PDF. It also assumes the distribution of the adjustment factor. Model probabilities are assumed in the same way as discussed before in the AFA. The adjusted model Y_p in this approach can be calculated as:

$$Y_p = E(y^*) + E_a^*. \tag{2.46}$$

Here, $E(y^*)$ has been used instead of y^* since the models are considered stochastic. The first and second moment of the adjustment factor are as follows:

$$E(E_a^*) = \sum_{i=1}^{N} P(M_i)(E(Y_i) - E(y^*)), \tag{2.47}$$

$$V(E_a^*) = \sum_{i=1}^{N} P(M_i)(E(Y_i) - E(Y_p))^2, \tag{2.48}$$

where Y_i is the prediction of each model considering parameter uncertainty. This leads to calculate the expected value $E(Y_p)$ and variance $V(Y_p)$ of the adjusted model as [20]:

$$E(Y_p) = E(y^*) + E(E_a^*), \tag{2.49}$$

$$V(Y_p) = V(E_a^*) + \sum_{i=1}^{N} P(M_i)(V(Y_i))^2. \tag{2.50}$$

Eq. (2.50) represents the combination of model and parametric uncertainty. The variance of the adjusted model is the sum of variance of the adjustment factor which is inter-model variance and the variance of each of the individual model which is intra-model variance. It can also be said that the first term represents the parameter uncertainty and the second term represents the model framework uncertainty in each model. The approach in this form considers the output of the model as normally distributed; however, it is also possible to consider models with other distributions. In that case, the approach needs to be derived considering that particular distribution [22].

Most [21] attempted to include the uncertainty inherent in the reference model selection to the total uncertainty. Since the sum of model probabilities is one, the following relations hold:

$$E\left(Y_p\right) = \sum_{i=1}^{N} P\left(M_i\right) E\left(Y_i\right), \tag{2.51}$$

$$V\left(Y_p\right) = \sum_{i=1}^{N} P\left(M_i\right) \left(E\left(Y_i\right) - E\left(Y_p\right)\right)^2. \tag{2.52}$$

The contribution of a single model in the total variance [25] is derived as:

$$\begin{aligned} V_i\left(Y_p\right) &= E\left[\left(Y_i - E\left(Y_p\right)\right)^2\right] \\ &= V\left(Y_i\right) + \left[E\left(Y_i\right) - E\left(Y_p\right)\right]^2 \end{aligned} \tag{2.53}$$

where $V\left(Y_i\right)$ is the variation of a single model as a result of parameter uncertainty. $\left[E\left(Y_i\right) - E\left(Y_p\right)\right]^2$ is the additive model framework uncertainty which is the difference between the average response of the single model and the average response of the adjusted model.

In complex engineering problems, $E\left(Y_p\right)$ may be unknown. Therefore, the best model Y^{ref} is assumed in place of Y_p to calculate total variance of the single model $V_i\left(Y_p\right)$ as follows:

$$V_i\left(Y_p\right) \approx V\left(Y_i\right) + V\left(\epsilon_i^\Delta\right) + V\left(\epsilon^{ref}\right), \tag{2.54}$$

$$V\left(\epsilon_i^\Delta\right) = \left[E\left(Y_i\right) - E\left(Y^{ref}\right)\right]^2, \tag{2.55}$$

where ϵ_i^Δ is the additional framework uncertainty with respect to the reference model and ϵ^{ref} is the uncertainty of the reference model. The modified response of a single model can be found by introducing a reference model in addition to additive model framework uncertainty as:

$$Y_i^M \approx Y_i + \epsilon_i^\Delta + \epsilon^{ref}. \tag{2.56}$$

The relative variation of each model is more important than the overall variation in the model. The value of ϵ^{ref} is not necessary since it is a constant additive term [21] or different values can be assumed to examine its effect on the total uncertainty of model prediction. The most suitable model will be one with the smallest value of $V_i\left(Y_p\right)$. The choice of $V\left(\epsilon^{ref}\right)$ affects the total model variance of the single model but does not affect the ranking of a single model [25]. The method is biased since the model probabilities are assumed in the beginning and the model adjustment factor is also assumed normally distributed.

2.6   Summary

The basis of stochastic input parameters and sampling techniques for sensitivity and uncertainty analyses have been discussed in this chapter. Deterministic as well as probabilistic methods are explained. Variance based sensitivity analyses have been described for uncorrelated as well as correlated input parameters. Response surface approaches are presented to be used for variance based sensitivity and uncertainty analyses to make the process more efficient. Finally, the procedure is described to estimate the total uncertainty of the model prediction and ranking the models based on their total variance.

Chapter 3

Aerodynamic Phenomena in Long-span Bridges

3.1 Introduction

The behaviour of long-span cable-supported bridges under wind action is essential to be studied as a part of the analysis and design. These structures can develop significant vibrations when exposed to atmospheric wind flow. The increased flexibility makes these bridges highly sensitive to the wind action, hence aerodynamic performance often becomes a decisive factor in the design process. The aerodynamic phenomena related to the design of these bridges are discussed in this chapter.

3.2 Long-span Bridges

The collapse of the Tacoma Narrows Bridge brought much attention to consider wind effects on long-span bridges. Scanlan [26] and Miyata [27] summarise a brief history of some developments in the field of bridge aerodynamics after the collapse and explain how the investigations have helped in the development of experimental and analytical methods for the prediction of long-span bridge response to wind action. Several examples of wind-induced bridge failure in the last two centuries are described by Gimsing and Georgakis [5], Xu [28] whereas Haifan [3], Gimsing and Georgakis [5], Myerscough [29] explain the history and development of long-span cable-supported bridges around the world.

With the increased bridge span length, the modern bridge structures are more flexible, lightweight and their structural characteristics require special treatment of aerodynamic analysis and design under wind action. Xu [28] lists the top 10 longest suspension bridges and the top 10 longest cable-stayed bridges in the world as of 2015. Weight [30] provides an informative and critical analysis of the Great Belt East Bridge in Denmark which is the third largest suspension bridge in the world. The proposed Messina Bridge takes the Wind Engineering to its new limits with a main span of 3300 m. There has been an extensive study made on the configuration of the bridge. An attempt has been made by Ge and Xiang [31] to introduce the limit of span length for suspension bridge equation and made an aerodynamic feasibility of a 5000 m span suspension bridge along with aerodynamic stabilisation. With the rapid growth of China's economy in the past couple of decades, more than 200 long-span bridges have been built. Ge and Xiang [32] provide history and new developments of building bridges in China with the important structural properties and configurations of some bridges. Some examples of the major long-span bridges are listed in Table 3.1.

Table 3.1: Some well known long-span cable-supported bridges in the world
[3, 33, 34, 35, 36, 37, 38, 39, 40].

Bridge name	Country	Year built	Main span [m]	Deck width [m]
Suspension				
Messina	Italy	Planned	3300	60.4
Akashi-Kaikyo	Japan	1998	1991	35.5
Zhejiang Xihoumen	China	2008	1650	36.3
Great Belt (Storebælt)	Denmark	1998	1624	31.0
Little Belt (Lillebælt)	Denmark	1970	600	33.0
Tacoma Narrows	USA	1940	854	12.0
Hålogaland	Norway	2017	1145	18.6
Bosporus	Turkey	1973	1074	28.0
Runyang	China	2005	1490	-
Tsing Ma	Hong Kong	1997	1377	-
Humen	China	1997	888	-
Cable-stayed				
Russky	Russia	2012	1104	-
Sutong	China	2008	1088	41.0
Stonecutters	Hong Kong	2009	1018	53.3
Indiano	Italy	1978	189	22.4
Guama	Brazil	-	320	14.2
Tsurumi	Japan	1994	510	38.0
Normandy	France	1995	856	23.8
Footbridge				
Siena	Italy	2006	59.4	3.3
Turin	Italy	2003	156	6.9
Kehl-Straßburg	Germany-France	-	183	6.6

3.3   Aerodynamic Phenomena

Cermak [41] describes Wind Engineering as the rational treatment of the interaction between the wind in the atmospheric boundary layer and man and his works on the surface of the earth. The fluctuating nature and the turbulence of the wind in the atmosphere produce very complex flow fields around structures. Due to flow separation and reattachment, highly fluctuating pressure fields are generated. Therefore, the aerodynamic loads are mainly dynamic. Such kind of an ambient load is known as 'aerodynamic load'. As a result, structure oscillations and instabilities may occur in the wind flow which depend not only on the geometry and mechanical properties of the structure but also on the wind flow characteristics and its mean speed.

The evaluation of wind loading and its effects depends on various interconnected considerations. Davenport [42, 43] divided the aerodynamic forces of the turbulent wind into static wind force and the buffeting forces by using statistical tools. The structural

responses can be divided similarly into a mean value and the oscillations around it. Figure 3.1 shows Davenport's wind loading chain which describes the approach to evaluate aerodynamic loads and wind-induced response of structures.
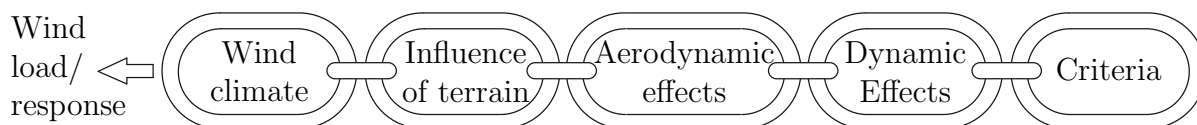
Figure 3.1: Devenport's Wind Loading Chain, after [44].

In the case of static phenomena, the divergence, lateral deflection and lateral buckling are considered. The static behaviour often does not lead to the most critical situation, whereas the dynamic behaviour is essential and much more critical in case of long-span cable-supported bridges. The bridge vibrates in its natural modes under the action of wind. The interaction of the aerodynamic forces and the structural motion is referred to as aeroelasticity. The motion of the oscillating body in the wind flow produces self-excited forces and this aeroelastic interaction of the bridge with the wind leads to instability when the energy input from the fluid exceeds the energy dissipated by structural damping. The main objective of studying aeroelastic instability is to determine the wind speed at which it is initiated. It is made sure that this wind speed is not exceeded during the design life of the bridge with a certain probability.

In general, with the increase in the mean wind speed, static as well as dynamic structural response will increase [45]. However, in the case of an aeroelastic instability, the response rapidly increases for even a small increase in the mean wind speed. The aerodynamic phenomena for long-span bridges, therefore, can be mainly classified into two groups based on the nature of amplitudes under wind action: limited-amplitude and divergent-amplitude wind-induced vibrations [41] as shown in Figure 3.2. The former consists of Buffeting, Vortex-induced Vibrations (VIV), Rain Wind-induced Vibrations and Wake-induced Vibrations which are related to the serviceable discomfort, increased internal stresses and may cause fatigue in the bridge structure. The latter comprises Galloping, Torsional Flutter and Coupled Flutter which can lead to structural instability. Instabilities resulted from the WSI are known as aerodynamic or aeroelastic instabilities. The term aeroelastic emphasises the behaviour of deformed bodies, and aerodynamic emphasises the rigid bodies [4]. Sometimes these two terms are used alternatively. The oscillation amplitude of the bridge deck can build up until it results in the failure of the bridge. The collapse of the original Tacoma Narrows Bridge was a result of such an aeroelastic instability.

3.3.1 Limited Amplitude Phenomena

Limited amplitude phenomena deal with the action of aerodynamic forces on the structure and the response of the structure as a result of this interaction. With the action of wind flow on the structure, the flow pattern changes around the structure which can create oscillations if the structure is flexible. If the oscillations gradually increase, it could damage the structure. The VIV, buffeting and rain wine-induced vibrations are examples of such phenomena which are considered in bridge aerodynamics.
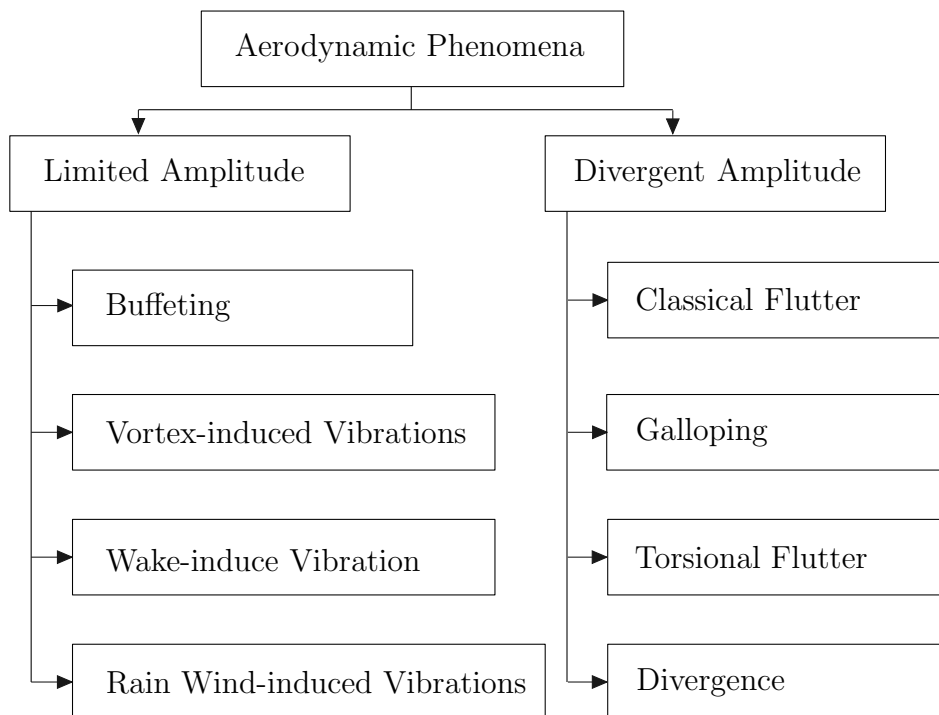
Figure 3.2: Aerodynamic phenomena for long-span bridges.

3.3.1.1 Vortex-induced Vibrations

The bluff body embedded in the fluid flow creates vortices behind the body originating from the separation of the boundary layer. The vortices, shed from the body, are carried to the downstream side. In the wake, the flow is turbulent but there can be some pattern in it. This shedding causes unsteadiness in the body perpendicular to the direction of the flow. The properties of vortex shedding, especially the frequency, depend on the velocity of flow, the geometry of the body and the fluid viscosity. If the body has some degree-of-freedom (DOF) with a certain stiffness and is not fixed, it oscillates in its DOF. When the shedding frequency is close to the natural frequency, the oscillations of the body take control of the vortex shedding and resonance may occur. These oscillations are very small if the Strouhal frequency of the alternating pressure is different to the natural frequency of the body. When these frequencies become the same, the response of the body starts to increase and the natural frequency of the body controls the vortex shedding phenomenon. This control of the situation by the mechanical forces is called Lock-in. The VIV may also be seen in flexible bridges. It can be avoided by increasing the stiffness or the damping of the structure.

3.3.1.2 Buffeting Response

The body immersed in a fluid flow with some turbulence is subjected to time-dependent surface pressure which can create oscillations. If these oscillations are due to flow fluctuations, then this phenomenon is known as 'buffeting'. The characteristics of natural wind flow are also not steady. Therefore, buffeting happens as a result of a fluctuating component of the oncoming wind. It is also possible to happen due to the wake of the structure on the upstream side and in this case, it is known as wake buffeting. The study of buffeting response is essential during the design process.

3.3.2 Divergent Amplitude Phenomena

Dynamically flexible, wind-sensitive structures or long-span bridges oscillate under the wind action. The motion of the structure generates aerodynamic forces which are known as motion-induced forces or self-excited forces. The amplitudes of the structure in wind flow decays if the energy input from the flow is smaller than the energy dissipated by the mechanical damping. The overall system damping, which is the combination of structural damping and the aerodynamic damping becomes, negative at very high wind speeds. If the structural damping is not sufficient to dissipate the energy input by the wind, the amplitudes of the oscillating body start to grow and diverge exponentially. The theoretical border between the decaying and diverging motions is known as the critical condition and the corresponding wind velocity is called the 'critical wind velocity'. Below the instability limit, the aerodynamic damping remains positive which helps in reducing vibrations. Exactly at the boundary, the sum of structural damping and aerodynamic damping is zero therefore, the structure vibrates in a harmonic motion with constant amplitudes. The motion-induced forces are insignificant for the short-span bridges; therefore, there is no concern about aerodynamic instability [46]. The typical response amplitude of the bridge elements along the increasing wind speed is shown in Figure 3.3. The turbulence in the flow is usually not considered in the study of some aeroelastic effects for reasons of simplicity.
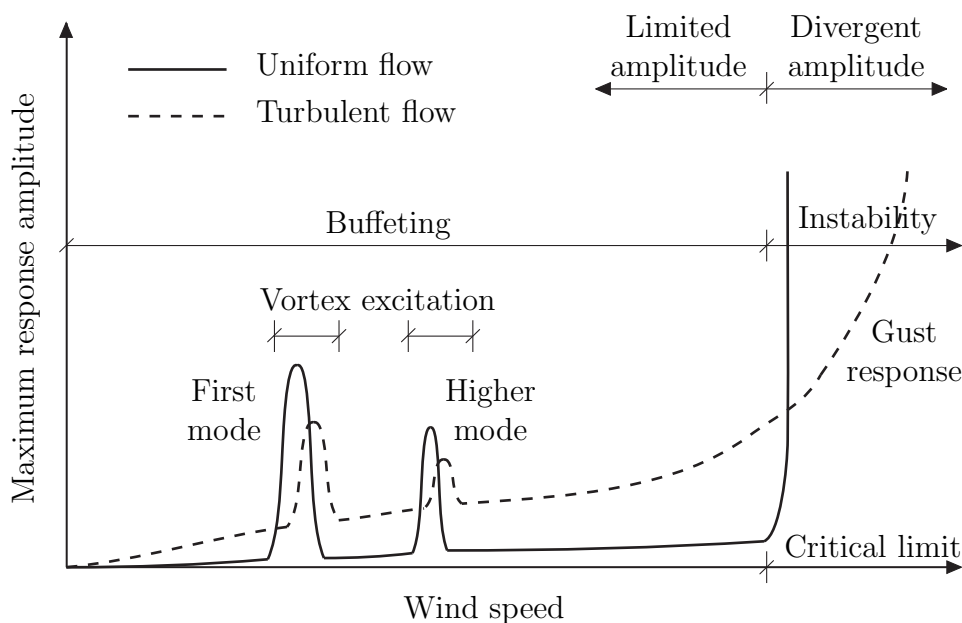
Figure 3.3: Schematic of structural response against wind speed.

3.3.2.1 Classical Flutter

Flutter is a self-feeding aeroelastic phenomenon which is potentially destructive to long-span cable-supported bridges. The aerodynamic forces generated on the bridge deck couple with its motion and if the energy input by the aerodynamic forces at high wind speeds in an oscillation cycle becomes larger than that dissipated by the mechanical damping of the bridge structural system, the amplitude of vibration will grow. This increasing vibration will then amplify the aerodynamic forces, resulting in continuously growing self-excited forces and self-exciting oscillations. If this situation continues for

some period of time, it can lead to the Ultimate Limit State of the bridge and ultimately to collapse.

The term classical flutter is originally applied to thin airfoils in the aircraft industry [28]. Classical flutter is an aeroelastic phenomenon in which two-degree-of-freedom (2DOF) of a structure, torsional motion and vertical bending, couple together in a flow-driven, unstable oscillation [41]. It is also known as '2DOF flutter', 'coupled flutter' or simply 'flutter'. The critical flutter condition occurs at the wind speed where energy input to the system is equal to the energy dissipated by the structural damping. The oscillatory motions of the contributing DOF in the structure couple to create a single frequency called the flutter frequency as shown in Figure 3.4.
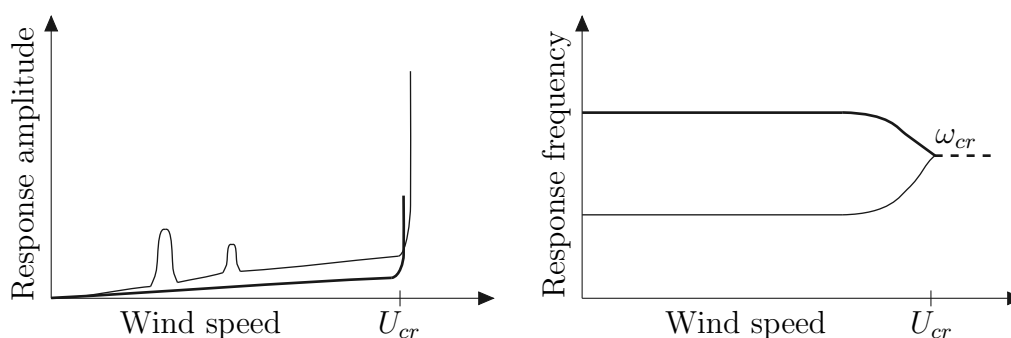
Figure 3.4: Schematic of structural behaviour along increasing wind speed:
(left) response,
(———) vertical displacement and
(━━) rotation,
(right) effective frequency,
(———) bending frequency and
(━━) torsional frequency,
(U_{cr}: flutter limit, ω_{cr}: flutter frequency).

Flutter can happen in both laminar as well as in turbulent flows. When flutter occurs, the displacements become infinite by the linear theory. Vertical and torsional motion occur with a phase difference which is essential for the energy transfer from wind to the structure. The mechanism of energy transfer in case of coupled flutter is described in Figure 3.5. The flutter phenomena will depend on phase lag or degree-of-coupling among the modes [46]. The smaller frequency separation between the coupled modes increases the risk of flutter to occur [48]. The self-excited motion can even cause flutter on several degrees-of-freedom where higher modes also participate in the phenomenon.

The damping characteristics categorise flutter behaviour of the system into 'soft flutter' or 'hard flutter'. Chen and Kareem [49] studied the rate of change in effective damping with increasing wind speed, which is related to soft or hard flutter. Hard-type flutter occurs by the rapid growth of negative aerodynamic damping with increasing wind speed beyond the flutter limit whereas soft-type flutter happens where the negative damping builds up slowly with increasing wind speed.

Flutter is destructive in nature with infinitely large amplitudes by the linear aerodynamic theory. In reality, the aerodynamic nonlinear effects take place which leads to the Limit Cycle Oscillation (LCO) where amplitudes are limited. This difference is visualised in Figure 3.6.
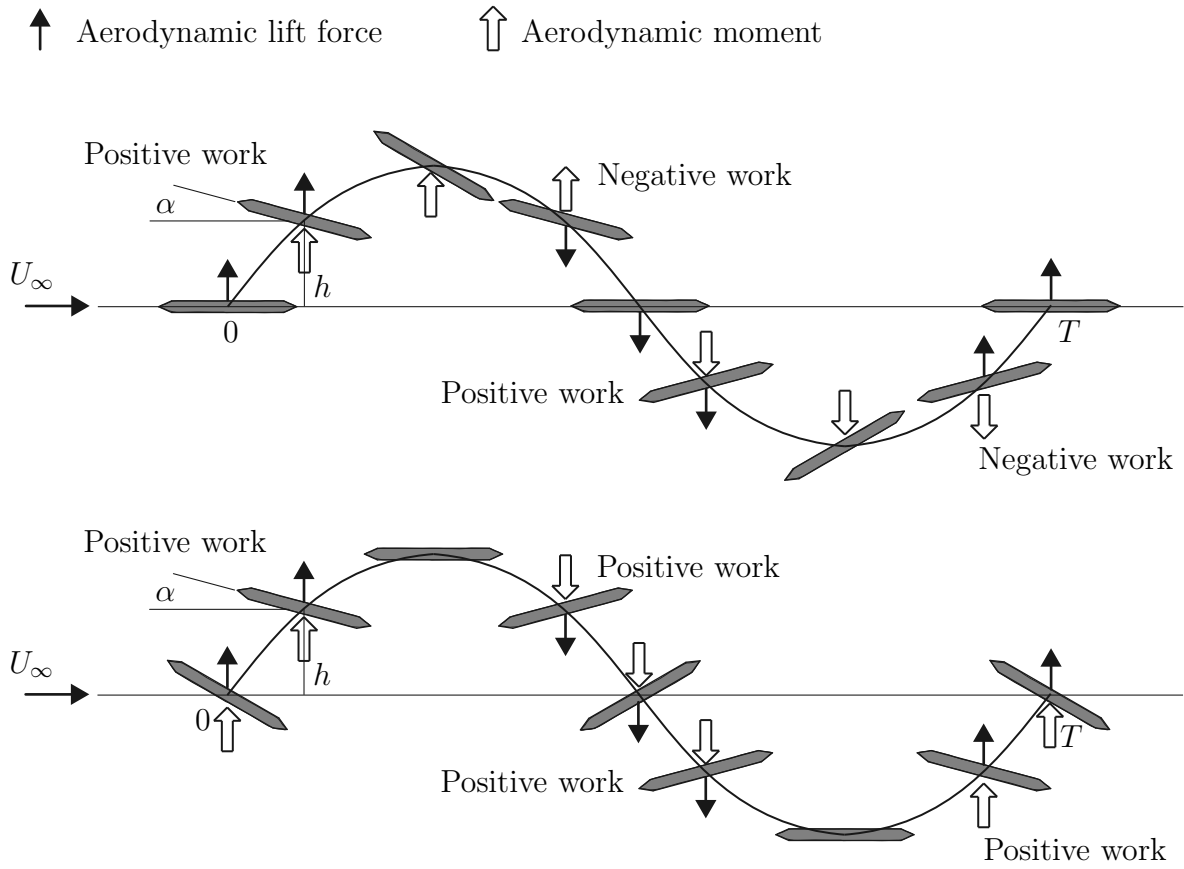
Figure 3.5: Excitation mechanism and energy effects of aerodynamic forces with:
(top) 0° phase difference,
(bottom) 90° phase difference, after [47].
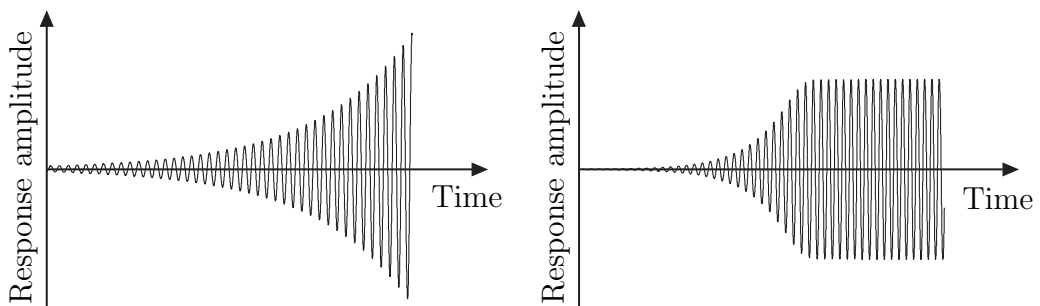
Figure 3.6: Schematic of
(left) flutter instability and
(right) limit cycle oscillation.

3.3.2.2   Galloping

Galloping is a single-degree-of-freedom (SDOF) large-amplitude aeroelastic oscillation in the transverse direction to wind. It occurs as a result of negative aerodynamic damping in the cross wind direction. The amplitudes of oscillation can reach up to many times the section depth. It is sometimes also called as 'translational galloping', 'cross-wind galloping' or 'bending flutter'. Galloping is usually experienced by D-shaped cross section, square section (at zero angle of attack) and circular sections with some accretion such as ice-coated transmission line or guyed cables. It can also happen for a bridge with bluff cross section and a lightweight superstructure even for a shorter span. The cross section with a smaller aspect ratio (width/depth) has a higher tendency to gallop which is known as 'soft galloping' whereas, the deeper sections require initial perturbation that leads to 'hard galloping'. The structural natural frequency is much lower than the vortex shedding frequency. Due to this reason, galloping can be seen as a low-frequency phenomenon.

Pedestrian bridges, pipe bridges and iced-up cables of power lines are the potential structures to gallop. Galloping can be classified into two main types: cross-wind galloping, which generates large amplitude oscillations in a direction normal to the wind flow, and wake galloping, which happens as a result of the wake shed from a structure on the upstream side.

Galloping occurs due to change in the effective angle of attack of the vertical or the torsional motion of the structure. It can be evaluated by checking signs of the time-averaged static wind coefficients for lift and moment at zero angle of attack. A negative slope of static lift (or moment) coefficient usually indicates a tendency for galloping. The negative lift coefficient implies that the section is pushed upward resulting in a divergent response or galloping [4].

Galloping depends mainly on the quasi-steady behaviour of the structure and therefore the mechanism of galloping can be explained by the quasi-steady aerodynamic theory. The analytical solution for Galloping can be obtained from [48]. The difference between the critical velocity predicted for galloping by the linear and non-linear aerodynamic theory is insignificant [46]; however, the nonlinear aerodynamic theory also provides amplitude and frequency. Some studies utilised wind tunnel experiments to explain different aspects related to understanding the mechanism of galloping of rectangular cylinders with different aspect ratios [50] and galloping behaviour of Yadagawa Bridge in Japan [51]. Galloping can be seen as a SDOF instability or a coupled phenomenon. Earlier, it was studied as a SDOF phenomenon and later, the studies were carried out on coupling in galloping for coupled torsional and vertical as well as for coupled translational galloping [41].

3.3.2.3   Torsional Flutter

Torsional flutter is a rotational SDOF aeroelastic instability. It is sometimes also known as 'rotational galloping', 'torsional galloping' or 'stall flutter' in aeronautical terminology. The mechanism of torsional flutter is related to aerodynamic damping of rotational motion. Torsional flutter occurs when the total damping (mechanical and aerodynamic) of the system in torsional motion becomes zero. The vertical mode of vibration of a structure has some contribution; however, the torsional action is more critical by far [46]. It occurs for long-span bridges with bluff deck sections such as H-shape, rectangular

section with a smaller aspect ratio (width/depth), or truss sections, whereas streamlined sections are more favourable for the classical flutter.

Blevins and Iwan [52] studied the mechanism of torsional flutter by the linear and nonlinear forms of quasi-steady theory. Nakamura and Mizota [53], Nakamura [54] explained the torsional flutter by the theoretical and experimental study as an unsteady phenomenon. Nakamura [54] also described torsional flutter by performing experimental forced vibration tests and gave the unsteady aerodynamic lifts and moments. Moreover, Washizu et al. [55] studied rectangular cylinders with the help of wind tunnel experiments and highlighted the effect of aspect ratio on the aeroelastic instability phenomena in the vicinity of the critical speed. The aerodynamic force with the same frequency as that of Strouhal number has a negative effect and can excite torsional motion in the deck [56]. Matsumoto et al. [57, 58], Matsumoto [59] described the torsional flutter mechanism of rectangular and H-shaped sections (Tacoma Narrows Bridge deck) and investigated the role of vortex excitation and Karman vortex excitation on the torsional flutter behaviour. Apart from that, the phenomenon of torsional flutter has been studied by several experimental [60] as well as numerical [40] approaches. The equations to solve torsional flutter problems can be found in [48]. Torsional flutter stability improves with the increase in the deck width or torsional frequency [61].

3.3.2.4 Aerostatic Divergence

Static divergence, sometimes also referred to as torsional divergence, is a phenomenon of loosing torsion stiffness at a relatively high wind speed. It represents a static type of instability phenomenon that occurs when the total torsional stiffness vanishes, which is the sum of aerodynamic and structural stiffness and the structure has no oscillations. The wind flow increases the angle of attack, due to which torsional moment increases by the increase in the wind velocity. If there is no sufficient torsional resistance available in the structure, the instability can occur. Divergence problem involves a combination of torsional divergence and lateral buckling. At a critical wind speed for torsional divergence, the bridge deck may experience out-of-plane buckling under the action of a drag force or torsionally diverge under a wind-induced moment that increases with the increase in geometric twist angle [4]. The torsional divergence wind velocity is usually higher than the design wind speed. Matsumoto et al. [62] additionally classified torsional divergence into a static SDOF torsional divergence and a dynamic 2DOF torsional divergence.

3.4 Counter Measures to Improve Aeroelastic Stability

The design of long-span bridges requires to eliminate the possibility of aeroelastic instability to occur entirely within the design life. The design should ensure that the critical flutter limit of the bridge under the worst condition is still higher than the reference wind speed. Long-span bridge girders can experience unstable flutter oscillations in very strong winds. The objective of flutter control is to enhance the critical flutter limit of the bridge by introducing some modification to the structural system. These modifications can be broadly classified into three main types based on their function as follows:

(i) Deck shape: changing or modifying deck cross section shape to change the aerodynamic behaviour which results in reducing aeroelastic forces and increasing flutter limit,

(ii) Tuned Mass Damper (TMD): introducing TMD increases the structural damping which reduces some critical structural mode response under wind action,

(iii) Control flaps: additional wing-like components attached to the section which sometimes requires external power and to change their relative position or orientation under structural vibration.

Fujino and Siringoringo [46, 63], Fujino et al. [64, 65] review long-span bridge vibrations under wind action and also describe some solutions as countermeasures for these vibrations. Figure 3.7 and Table 3.2 show some countermeasures to improve the behaviour of a section against flutter. Non-streamlined sections with smaller aspect ratio are susceptible to galloping. It can be improved by using aerodynamic countermeasures such as skirts and horizontal plate on the lower side of the cross section [46] which in turn reduces the wind velocity separated from the lower corner of leading edge of cross section thus, reducing the self-excitation forces.

Long and slender bridges with bluff sections of large aspect ratios are prone to torsional and coupled flutter. Low torsional rigidity and aerodynamically unstable girder cross section are the main factors responsible for torsional flutter which caused the dramatic collapse of the Tacoma Narrows Bridge. This can be avoided by streamlining the girder using a closed box section or by using the truss-stiffened girder with increased torsional rigidity.

Streamline sections with a larger aspect ratio (width/height) are generally prone to coupled flutter which occurs as a result of large pressure difference between upper and lower surfaces of the deck. This pressure difference can be reduced using open grating or central slot to improve behaviour against flutter instability. Several other attachments can be used to improve flutter stability such as fairings, grating, wind nose, slots, flaps and spoilers. The torsional flutter stability can be improved by attaching rails to the bottom of the fairing and vertical plates to the lower flange of the girder [66].

Ge and Xiang [67] studied aerodynamic stabilisation for bridges with a central stabiliser and adopting twin-box girder. It was found that the limit of span length for a traditional suspension bridge due to aerodynamic stability can be greatly increased from about 1,500 m up to 5,000 m by using a widely slotted deck or a narrowly slotted deck with vertical and horizontal stabilisers. Sato et al. [68] confirmed that slotted box girder was applicable for the super long-span bridge for the reason that it is excellent in economical efficiency and aerodynamic stability.

The use of a TMD on a long-span bridge has been shown to be promising for reduction of wind-induced vibration response. The effectiveness of these TMDs have been extended by changing the design from a single TMD [69] to Multi-Tuned Mass Damper (MTMD) [70] as well as nonlinear TMDs [71]. Körlin and Starossek [72], Körlin et al. [73] introduced the rotational mass damper, the movable eccentric mass damper and a mass damper system with two eccentric rotational actuators for active bridge deck flutter control. Using the concept of eccentric mass, Phongkumsing et al. [74] presented a method of suppression of flutter by placing the auxiliary mass on the windward side of a bridge deck to shift the centre of gravity, and thus, reducing the aerodynamic moment acting on the deck. Aslan and Starossek [75] presented a passive aeroelastic damper for long span bridges which consists of a TMD, control surfaces, and a transmission which couples the movement of the TMD with the control surfaces without the need for an external energy supply.

Table 3.2: Typical aerodynamic countermeasure used for bridge sections against aeroelastic instabilities, after [46] (cf. Figure 3.7).

Phenomenon	Girder type	Countermeasure
Galloping	deep box	low skirts, horizontal plates
Torsional flutter	H-section, rectangle with smaller aspect ratio (width/height)	fairings
Classical flutter	deep truss	open grating, vertical stabiliser
	streamlined	fairing, central slots, curved wind flaps, wind nose, wind spoilers
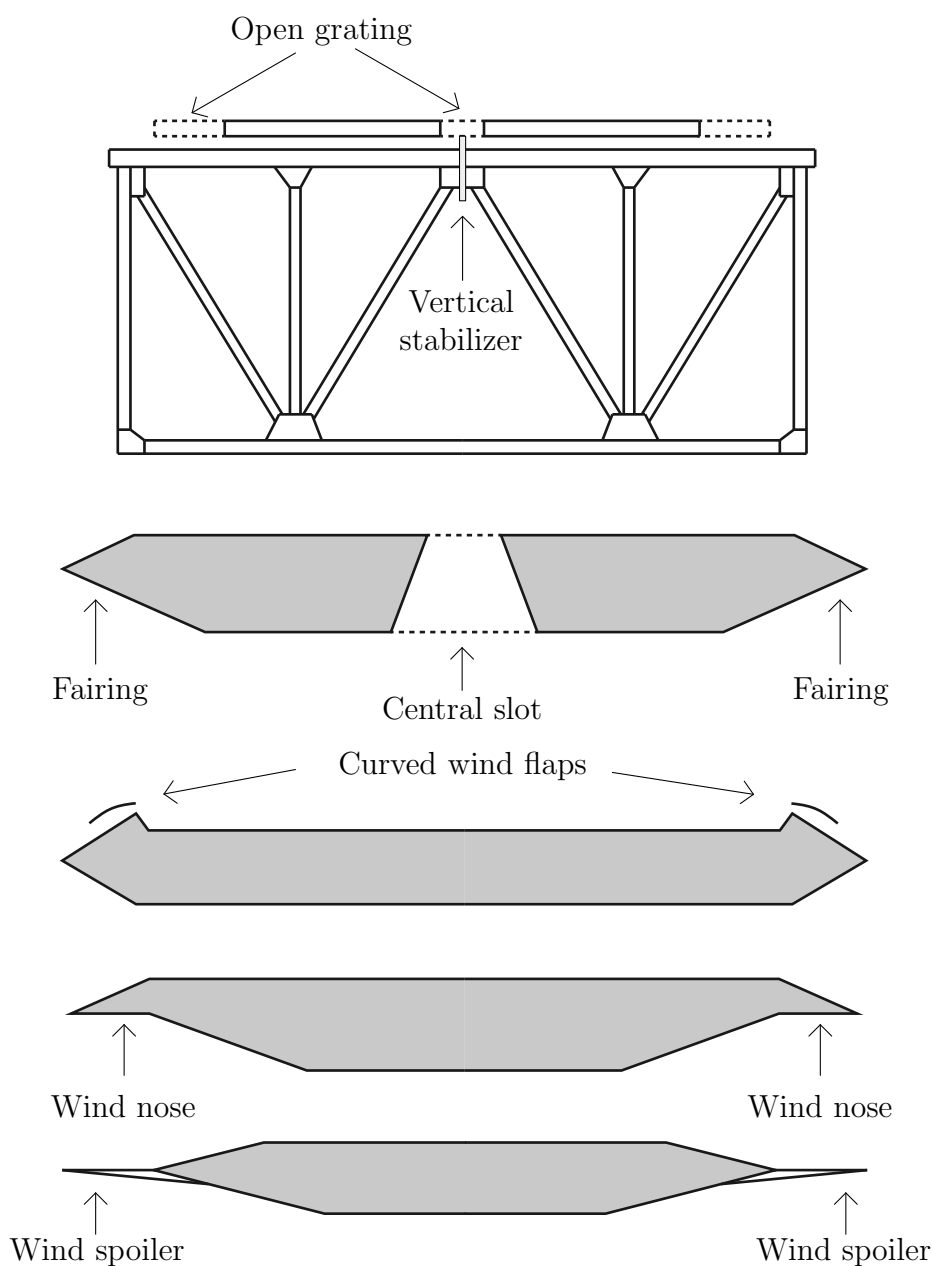
Figure 3.7: Examples of aerodynamic countermeasures for bridge deck against flutter, after [46, 63] (cf. Table 3.2).

The aerodynamic-based control method also has been proven to be effective towards the aerodynamic stability. This method uses control surfaces to generate forces counteracting the unstable oscillations. Graham et al. [76] used an integrated controllable trailing-edge flap and Huynh and Thoft-Christensen [77, 78] used separate control flaps to shown effective increase in the critical flutter limit of the suspension bridge. Phan and Nguyen [79] focused on a mechanically controlled system using the passive flap control driven by the motions of the bridge deck. Li et al. [80] presented an active aerodynamic control method of flutter oscillation comprising of a twin-winglet system which can improve aerodynamic stability to some extent.

3.5   Summary

The aerodynamic phenomena related to the design of long-span bridges have been discussed in this chapter. These phenomena are categorised based on the resulting amplitude of structure as limited or divergent. Special attention is given to aeroelastic instabilities which are addressed in the following chapters. Some countermeasures are also discussed to improve the aeroelastic behaviour of long-span bridges.

Chapter 4
Methods of Aerodynamic Analysis

4.1   Introduction

Arthur Roderick Collar defined aeroelasticity in 1947 as "the study of the mutual interaction that takes place within the triangle of the inertial, elastic, and aerodynamic forces acting on structural members exposed to an airstream, and the influence of this study on design" [81]. The interaction of forces is shown in Figure 4.1.
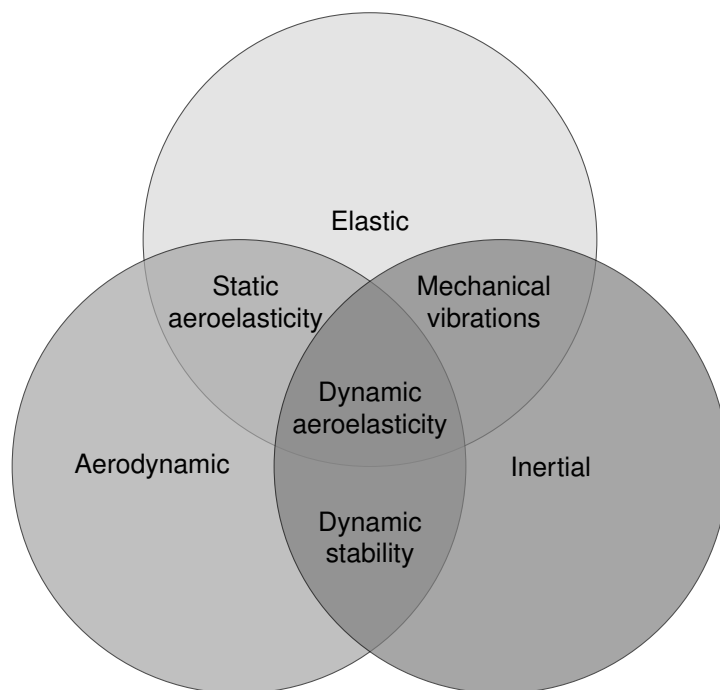
Figure 4.1: Aeroelastic triangle of forces, after [81].

There are three main approaches to deal with the aerodynamic problems:

  (i) Experimental methods,

 (ii) Analytical methods,

(iii) Numerical methods.

The experimental and analytical methods are used traditionally whereas, with the development in the field of computers, the numerical approach has become a focus of attention. This chapter provides a comprehensive review of the methods available for aerodynamic analysis with more focus on analytical and numerical methods for the solution of flutter stability problems. Flutter is a coupling of structural motion and aerodynamic motion-induced forcing and therefore, different structural and aerodynamic modelling techniques have been discussed here.

4.2   Structural Modelling

Modelling the behaviour of structures by a closed-form analytical solution of the differential equations is only possible in the simplest cases. Complex structures can be analysed numerically or by performing experiments on scaled models. Numerical models can be broadly characterised by their level of structural details, especially in terms of their ability to account for nonlinear structural effects as well as the applicability of dimensional reductions. For example in a detailed three-dimensional (3D) model, many modes of vibration can be considered but dimensional reduction from 3D to two-dimensional (2D) restricts to consider only two modes. In such a case, the choice of mode selection may compromise the quality of results. Some common structural idealisations are summarised here. For detailed description of the topic, the reader is referred to [45, 82, 83].

4.2.1   Full-DOF Structural Model

The finite element type of idealisation is applicable to both 2D and 3D structures and provides a convenient and reliable analysis of the system. This method divides the structure into a number of segments which are connected at the end-points or nodes. The Finite Element Method (FEM) allows the structures to be described in the matrix form with stiffness and mass distribution representing the DOF. The generalised equation of motion is given as

$$\mathbf{M}\ddot{\boldsymbol{Y}} + \mathbf{C}\dot{\boldsymbol{Y}} + \mathbf{K}\boldsymbol{Y} = \boldsymbol{F}, \tag{4.1}$$

where $\mathbf{M}$, $\mathbf{C}$, $\mathbf{K}$ are the mass, damping and stiffness matrices respectively. $\boldsymbol{Y}$ is the displacement vector and $\boldsymbol{F}$ is the external force vector. This finite element model can be used to calculate the response of the system under both static and dynamic loading. Material properties and details of structural geometry are the factors which affect the quality of the dynamic response prediction.

4.2.2   Mode-generalised Structural Model

A system with continuously distributed mass has an infinite number of DOF. However, the problem can be simplified by assuming that the masses are concentrated at discrete points as the inertial forces will develop only at those locations. The number of DOF will be then equal to the number of displacement components. This approach is effective for the systems where a major portion of the overall mass can be considered lumped at discrete points. The solution of a generalised SDOF system in such cases is very convenient and can be greatly simplified.

The approach describes the displacement amplitudes with the help of mode shapes. The use of mode shapes is efficient because, with only few mode shapes, necessary displacements can be described with sufficient accuracy. The accuracy can be increased by considering more DOF but the greater computational effort would be required. Mode shapes possess orthogonality properties which may be used to simplify the equations of motion of a multi-degree-of-freedom (MDOF) system. The MDOF system can be decomposed to obtain an independent SDOF equation for each mode of vibration. The equations of motion which are coupled by the off-diagonal terms in the mass and stiffness matrices can be transformed to independent normal coordinates. Then the dynamic

response can be obtained by separately solving each equation and then superimposing the response in the geometric coordinates.

The equation of motion related to time dependent lift forces is expressed in modal coordinates as follows:

$$\mathbf{M}\boldsymbol{\phi}_j \ddot{y}_j + \mathbf{C}\boldsymbol{\phi}_j \dot{y}_j + \mathbf{K}\boldsymbol{\phi}_j y_j = \boldsymbol{f}_L(t), \tag{4.2}$$

pre-multiplying with $\boldsymbol{\phi}_j^{\mathrm{T}}$ gives

$$\boldsymbol{\phi}_j^{\mathrm{T}}\mathbf{M}\boldsymbol{\phi}_j \ddot{y}_j + \boldsymbol{\phi}_j^{\mathrm{T}}\boldsymbol{C}\boldsymbol{\phi}_j \dot{y}_j + \boldsymbol{\phi}_j^{\mathrm{T}}\mathbf{K}\boldsymbol{\phi}_j y_j = \boldsymbol{\phi}_j^{\mathrm{T}}\boldsymbol{f}_L(t), \tag{4.3}$$

or

$$\boldsymbol{\phi}_j^{\mathrm{T}}\mathbf{M}\boldsymbol{\phi}_j \ddot{y}_j + 2\xi_j \omega_j \boldsymbol{\phi}_j^{\mathrm{T}}\mathbf{M}\boldsymbol{\phi}_j \dot{y}_j + \omega_j^2 \boldsymbol{\phi}_j^{\mathrm{T}}\mathbf{M}\boldsymbol{\phi}_j y_j = \boldsymbol{\phi}_j^{\mathrm{T}}\boldsymbol{f}_L(t), \tag{4.4}$$

where ω_j is the modal circular natural frequency, ξ_j is the modal damping ratio, $\boldsymbol{\phi}_j$ is the mode shape, the subscript j is the mode number and $\boldsymbol{f}_L$ is the lift force vector, respectively. Assuming a harmonic lift force excitation

$$\boldsymbol{f}_L(t) = \boldsymbol{f}_{L,0}\sin(\omega_s t), \tag{4.5}$$

where $\boldsymbol{f}_{L,0}$ is a constant representing amplitude of harmonic force and ω_s is the oscillation frequency. The equation of motion can be extended to the full length of the bridge L as

$$\int_L \boldsymbol{\phi}_j^{\mathrm{T}}\mathbf{M}\boldsymbol{\phi}_j dx \ddot{y}_j + \int_L 2\xi_j \omega_j \boldsymbol{\phi}_j^{\mathrm{T}}\mathbf{M}\boldsymbol{\phi}_j dx \dot{y}_j + \int_L \omega_j^2 \boldsymbol{\phi}_j^{\mathrm{T}}\mathbf{M}\boldsymbol{\phi}_j dx y_j = \int_L \boldsymbol{\phi}_j^{\mathrm{T}}\boldsymbol{f}_L(t)\, dx. \tag{4.6}$$

This expression in Eq. 4.6 is the basis for the pseudo-3D simulation. The necessary parameters can be defined by computing a 2D representation of the problem. Assuming that the lift force $\boldsymbol{f}_{L,0}(t)$ has same shape as that of mode of vibration along the entire bridge length, the previous expression can be divided by the integral $\int_L \boldsymbol{\phi}_j^2 dx$ as

$$\frac{\int_L \boldsymbol{\phi}_j^{\mathrm{T}}\mathbf{M}\boldsymbol{\phi}_j dx}{\int_L \boldsymbol{\phi}_j^2 dx}\ddot{y}_j + 2\xi_j \omega_j \frac{\int_L \boldsymbol{\phi}_j^{\mathrm{T}}\mathbf{M}\boldsymbol{\phi}_j dx}{\int_L \boldsymbol{\phi}_j^2 dx}\dot{y}_j + \omega_j^2 \frac{\int_L \boldsymbol{\phi}_j^{\mathrm{T}}\mathbf{M}\boldsymbol{\phi}_j dx}{\int_L \boldsymbol{\phi}_j^2 dx}y_j = \boldsymbol{f}_L(t), \tag{4.7}$$

where

$$\frac{\int_L \boldsymbol{\phi}_j^{\mathrm{T}}\mathbf{M}\boldsymbol{\phi}_j dx}{\int_L \boldsymbol{\phi}_j^2 dx} = M_{j,2D}, \tag{4.8}$$

is the 2D generalised mass associated to the jth mode shape. The simplified expression for the 2D case then becomes

$$M_{j,2D}\ddot{y}_j + 2\xi_j \omega_j M_{j,2D}\dot{y}_j + \omega_j^2 M_{j,2D}y_j = f_L(t). \tag{4.9}$$

This equation of motion represents a SDOF model defined by the vertical displacement h of the cross section, which is excited by the lift force.

4.2.3 SDOF Model

A SDOF system is the simplest form of structural representation. Under the action of time dependent force, a SDOF system can be described with the following equation,

$$m\ddot{y} + c\dot{y} + ky = F(t) \tag{4.10}$$

$$m\ddot{y} + 2\xi\omega m\dot{y} + \omega^2 my = F(t) \tag{4.11}$$

with

$$\omega = \sqrt{\frac{k}{m}} \qquad \text{and} \qquad \xi = \frac{c}{2m\omega} \tag{4.12}$$

where m, c and k are the mass, damping coefficient and stiffness coefficient, respectively. $F(t)$ is the time dependent force, ω is the natural circular frequency and ξ is the damping ratio.

4.2.4   Structural Damping

The damping of a MDOF system with N DOF is often expressed in terms of the modal damping ratios ξ_n with $(n = 1, \ldots, N)$. There are some limitations when this method of expressing damping ratio can not be used [82] such as:

- non-linear response where the mode shapes are changing with the change in the stiffness,

- linear system with non-proportional damping.

This requires to define an explicit damping matrix. Rayleigh damping is an alternative approach to the model damping. The system damping is assumed to be viscous. Further details about Rayleigh damping can be found in [82]. The damping matrix can be given by:

$$\mathbf{C} = a_0\mathbf{M} \qquad \text{and} \qquad \mathbf{C} = a_1\mathbf{K}, \tag{4.13}$$

where a_0 [s^{-1}] and a_1 [s] are the mass and stiffness proportional constants, respectively. Corresponding damping ratios are calculated as:

$$\xi_n = \frac{a_0}{2\omega_n} \qquad \text{and} \qquad \xi_n = \frac{a_1\omega_n}{2}, \tag{4.14}$$

where ξ_n is the damping ratio of the mode n. These expressions show that the damping ratio is inversely proportional to frequency for mass proportional damping and is directly proportional to frequency for stiffness proportional damping. The relation of mass and stiffness proportional damping ratios presented in Eq. (4.14) is shown in Figure 4.2. A better representation is achieved when the damping is assumed proportional to the combination of the mass and the stiffness terms as given by

$$\mathbf{C} = a_0\mathbf{M} + a_1\mathbf{K}. \tag{4.15}$$

This leads to the relation between damping ratio and frequencies as follows:

$$\xi_n = \frac{a_0}{2\omega_n} + \frac{a_1\omega_n}{2}. \tag{4.16}$$

The factors a_0 and a_1 can be evaluated by associating two specific frequencies ω_m and ω_n. Writing Eq. (4.16) for two modes m and n in the matrix form:

$$\left\{ \begin{array}{c} \xi_m \\ \xi_n \end{array} \right\} = \frac{1}{2} \left[\begin{array}{cc} 1/\omega_m & \omega_m \\ 1/\omega_n & \omega_n \end{array} \right] \left\{ \begin{array}{c} a_0 \\ a_1 \end{array} \right\}, \tag{4.17}$$

simultaneous solution results in

$$\left\{ \begin{array}{c} a_0 \\ a_1 \end{array} \right\} = 2\frac{\omega_m\omega_n}{\omega_n^2 - \omega_m^2} \left[\begin{array}{cc} \omega_n & -\omega_m \\ -1/\omega_n & 1/\omega_m \end{array} \right] \left\{ \begin{array}{c} \xi_m \\ \xi_n \end{array} \right\}. \tag{4.18}$$
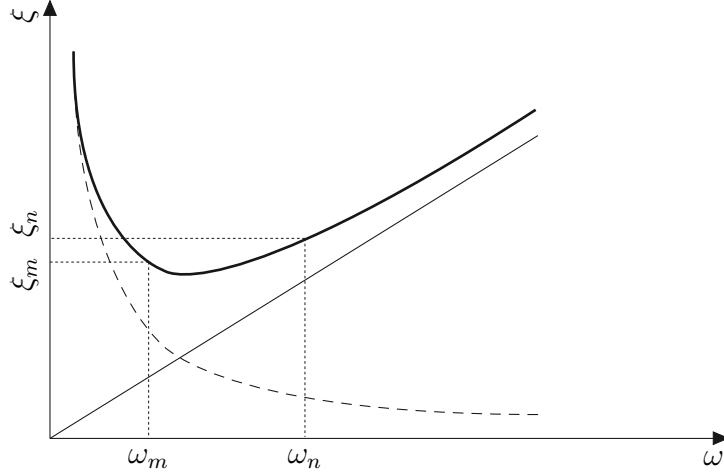
Figure 4.2: Relation between damping ratio and frequency:
(——) stiffness proportional part, $a_0 = 0$, $\xi = a_1\omega/2$,
(– –) mass proportional part, $a_1 = 0$, $\xi = a_0/2\omega$,
(——) combined.

Assuming same damping ratio for both frequencies i.e. $\xi = \xi_m = \xi_n$, the proportionality factors can be simplified as:

$$\left\{ \begin{array}{c} a_0 \\ a_1 \end{array} \right\} = \frac{2\xi}{\omega_m + \omega_n} \left\{ \begin{array}{c} \omega_m\omega_n \\ 1 \end{array} \right\}. \tag{4.19}$$

The two modes can be selected which are considered to be participating more in the response or have sufficient difference between the frequencies. The modes which have frequencies in-between these two modes will have relatively low damping and will participate more in the response; however, the modes out of this frequency range will have very high damping resulting in reduced effect in the overall response.

The limitation of this approach is that it can not be used for a MDOF system as the modes which are not tuned to correct damping may be distorted by the unsuitable damping ratios.

4.2.5   Solution Methods

Modal analysis is usually performed first to determine the natural frequencies and mode shapes necessary for the dynamic response analysis. The essential modes are often those with the lowest frequencies as they contribute most to the dynamic response. The structural representations can be dimensionally reduced to 2DOF section models calibrated from global models or directly MDOF models can be used. This dimensional reduction from 3D to 2D allows to consider only the important modes; however, selection of wrong modes may compromise the quality of the results. A numerical time integration scheme can be used to solve the system under external forces in the time domain. For this purpose, the Newmark-Beta method [82] may be used. The solution can be made manually if the number of DOF is small even in the FEM otherwise it is convenient to solve it by a numerical approach.

4.3   Aerodynamic Modelling

There are four important actions to induce aerodynamic forces on bluff bodies namely: static mean wind, vortex-induced excitation, the interaction between the wind and structural motion and in the case of turbulent inflow conditions additional aerodynamic force.   This will correspondingly result in static mean wind force, vortex-excited force, motion-induced force and buffeting force, respectively [84]. The motion-induced forces play the most important role in the bridge aeroelastic stability analysis. The motion-induced forces result from the interaction between wind forces and the motion of the oscillating structure. These forces are central to the flutter stability analysis which involves the coupling of aerodynamic and inertial forces with the elastic structure.

4.3.1   Analytical Models for Flat Plate

Analytical approach is essential in the Wind Engineering to study the complex phenomenon of Fluid-Structure Interaction (FSI). This method applies simplifications to a certain extent such as assuming two-dimensionality of the flow but in reality, the 3D effects are present. The closed-form solution is established by making a number of simplifications for the FSI. The study related to the flutter phenomenon is based on the classical theory of aeroelasticity within Aeronautical Engineering. This combines the theories of Fluid Dynamics and Deformable Solid Mechanics (DSM) by employing certain boundary condition for the FSI. Earliest studies about this phenomenon are made for aircraft wings in the begging of the 20th century.

The description of the self-excited forces based on a flat plate model of half-chord b with infinitesimal thickness is the basis of their formulation for bluff bodies. All of the analytical flat plate models have a set of common assumptions: the fluid is inviscid and incompressible; the velocity field is irrotational i.e. it is based on the potential flow and small angles of attack; the strip assumption applies regarding the finite-span effect. This means that the aerodynamic force at any chord-wise section is the same as if that section was situated in a two-dimensional flow. Dowell [85], Fung [86], Jurado and Hernández [87] give extended attention on the flat-plate problems.

A flat plate is considered subjected to a steady laminar flow with a direction rotated for angle α with respect to the chord of the flat-plate, a lift force and a moment are acting on the flat plate as shown in Figure 4.3.
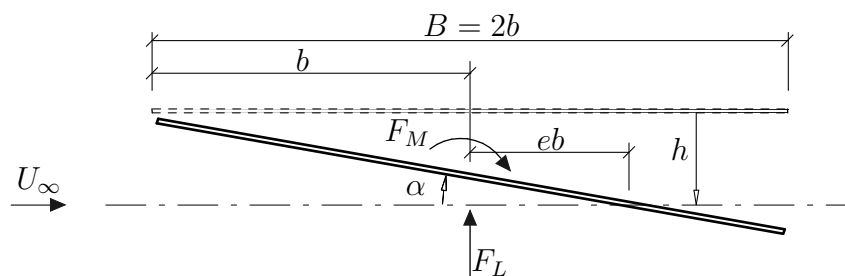
Figure 4.3: Definition of degrees of freedom (heave h and pitch α) and aerodynamic forces (lift F_L and moment F_M) for flutter analysis:
(– –) undeformed position,
(——) deformed position, ($e = 0.5$).

Considering a step rotation of the flat plate, a vortex is shed smoothly downstream from a single point of the trailing edge. The circulation due to this free vortex has its

counterpart on the flat plate of the same magnitude in order to satisfy zero circulation condition as assumed in the potential flow theory, which results in a force on the plate. The strength of the vorticity is time dependent which results in an asymptomatic rise in the lift force towards the steady state forces. This was initially studied by Wagner [88] who described the non-stationary lift force as a function of the reduced time by the so called Wagner indicial function $\phi(\tau)$ in order to describe the circulatory part of the unsteady lift and moment:

$$
\begin{aligned}
F_L ={}& -\rho b^2 \pi (\frac{U_\infty^2}{b}\alpha' + \frac{U_\infty^2}{b^2}h'') \\
& - 2\pi \rho b U_\infty^2 \left[\int_{-\infty}^{\tau} \phi(\tau - \tau_1)\frac{d}{d\tau_1}\left(\alpha(\tau_1) + \frac{h'(\tau_1) + 0.5b\alpha'(\tau_1)}{U_\infty}\frac{U_\infty}{b} \right) d\tau_1 \right], \quad (4.20a)
\end{aligned}
$$

$$
\begin{aligned}
F_M ={}& -\rho b^2 \pi (\frac{U_\infty^2}{2}\alpha' + \frac{U_\infty^2}{8}\alpha'') \\
& + \pi \rho b^2 U_\infty^2 \left[\int_{-\infty}^{\tau} \phi(\tau - \tau_1)\frac{d}{d\tau_1}\left(\alpha(\tau_1) + \frac{h'(\tau_1) + 0.5b\alpha'(\tau_1)}{U_\infty}\frac{U_\infty}{b} \right) d\tau_1 \right], \quad (4.20b)
\end{aligned}
$$

where ρ is the mass density of the air, b is the half chord ($b = B/2$), U_∞ is the oncoming wind velocity, $\tau = 2tU_\infty/B$ is the non-dimensional time and the prime is the differentiation with respect to the non-dimensional time. The inertial part is related to the additional forces from the apparent mass. The approximation of the Wagner function by Jones [89] is shown in Figure 4.4a.
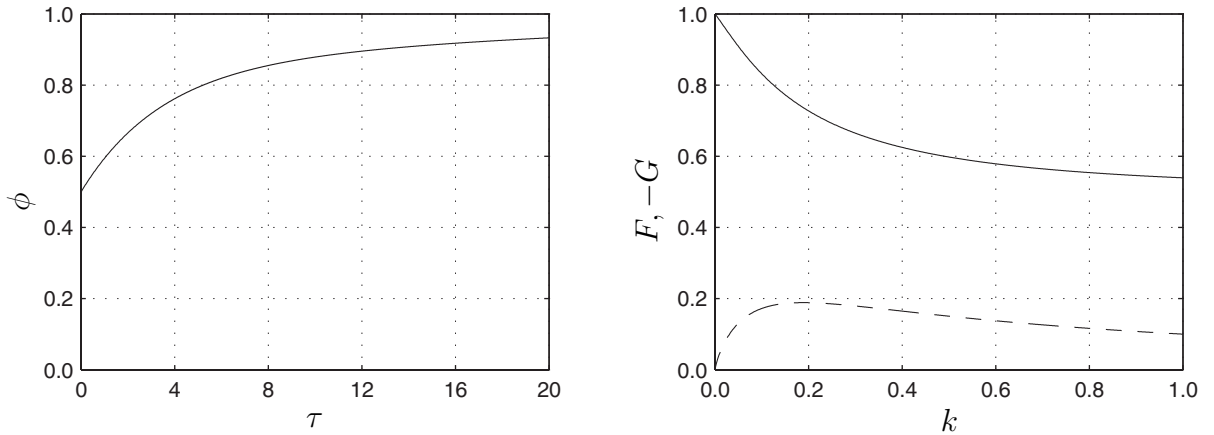
Figure 4.4: (left) Wagner function ϕ approximation along reduced time, $\tau = tU_\infty/b$, (right) real part (——) F and imaginary part (– –) G of Theodorsen circulation function along reduced frequency, $k = \omega U_\infty/b$.

4.3.1.1 Theodorsen Theory

Theodorsen investigated the flutter phenomenon for aircraft wings and gave a very popular approach for flutter analysis. This approach, on one hand, is independent of the shape of the body but on the other hand, neglects the effect originating from the simplification to the flat plate. For a flat plate oscillating harmonically with a certain frequency, each of the vortices in the wake will influence the forcing on the flat plate i.e. the forcing will be dependent on the history of the motion or the so-called fluid memory effect.

Considering a flat plate subjected to the action of a smooth oncoming flow. Theodorsen showed from the basic principle of potential flow theory that for thin airfoils in incompressible flow, the expressions for lift F_L and moment F_M are linear in displacement h and rotation α and their first and second derivatives [90]. The theoretical expressions on a flat plate or an airfoil for sinusoidal oscillating lift F_L and moment F_M are as follows:

$$F_L = -\rho b^2 \left[U_\infty \pi \dot{\alpha} + \pi \ddot{h} - \pi b a \ddot{\alpha} \right] - 2\pi \rho U_\infty b C \left[U_\infty \alpha + \dot{h} + b \left(\frac{1}{2} - a \right) \dot{\alpha} \right], \qquad (4.21a)$$

$$F_M = -\rho b^2 \left[\pi \left(\frac{1}{2} - a \right) U_\infty b \dot{\alpha} + \pi b^2 \left(\frac{1}{8} + a^2 \right) \ddot{\alpha} - a \pi b \ddot{h} \right] \qquad (4.21b)$$
$$+ 2\rho U_\infty b^2 \pi \left(a + \frac{1}{2} \right) C \left[U_\infty \alpha + \dot{h} + b \left(\frac{1}{2} - a \right) \dot{\alpha} \right],$$

where the complex function $C(k)$ is the Theodorsen circulation function which depends on the reduced frequency k, shown in Figure 4.4b, which describes the non-stationary contribution due to the FSI.

The Eqs. (4.21) are for the unsymmetrical flat plate where a is the distance between centre of mass and centre of rotation. In the case of symmetrical section, centre of mass lies in the vertical plane of the centreline. Therefore, $a = 0$ which gives the equation in the following form:

$$F_L = -\rho b^2 U_\infty \pi \dot{\alpha} - \rho b^2 \pi \ddot{h} - 2\pi \rho C U_\infty^2 b \alpha - 2\pi \rho C U_\infty b \dot{h} - 2\pi \rho C U_\infty b^2 \frac{1}{2} \dot{\alpha}, \qquad (4.22a)$$

$$F_M = -\rho b^2 \pi \frac{1}{2} U_\infty b \dot{\alpha} - \rho b^4 \pi \frac{1}{8} \ddot{\alpha} + 2\rho U_\infty b^2 \pi \frac{1}{2} C U_\infty \alpha + 2\rho U_\infty b^2 \pi C \dot{h} + 2\rho \frac{1}{2} U_\infty b^3 \pi C \dot{\alpha}, \qquad (4.22b)$$

with

$$C(k) = F(k) + \iota G(k), \qquad (4.23)$$

where $F(k)$ and $G(k)$ are the real and imaginary parts of Theodorsen circulation function. The relation between real and imaginary parts of Theodorsen circulation function is shown in Figure 4.5.
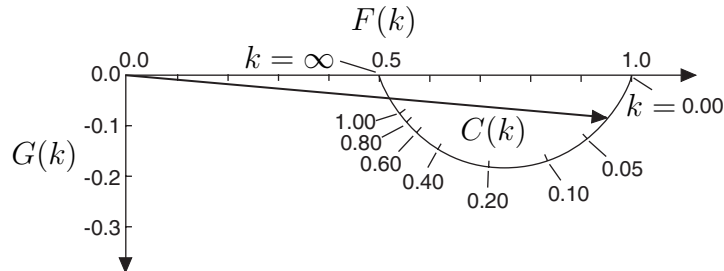
Figure 4.5: Vector diagram of Theodorsen circulation function, after [91].

There exist several representations of Theodorsen circulation function C and some are

given as follows:

$$C_1(k) = \frac{H_1^{(2)}(k)}{H_1^{(2)}(k) + \iota H_0^{(2)}(k)} = \frac{J_1 - J_{1y}\iota}{(J_1 + J_{oy}) - \iota(J_{1y} - J_o)}, \tag{4.24a}$$

$$C_2(k) = 1 - \frac{0.165k}{k - 0.0455\iota} - \frac{0.355k}{k - 0.3\iota}, \tag{4.24b}$$

$$C_3(k) = \frac{0.01365 + 0.2808\iota k - 0.5k^2}{0.01365 + 0.3455\iota k - k^2}, \tag{4.24c}$$

$$C_4(k) = \frac{(1 + 10.61\iota k)(1 + 1.774\iota k)}{(1 + 13.51\iota k)(1 + 2.745\iota k)}, \tag{4.24d}$$

$$C_5(k) = \frac{0.015 + 0.3\iota k - 0.5k^2}{0.015 + 0.35\iota k - k^2}, \tag{4.24e}$$

$$C_6(k) = \frac{0.500502k^3 + 0.512607k^2 + 0.210400k + 0.021573}{k^3 + 1.035378k^2 + 0.251239k + 0.021508}$$
$$- \iota\frac{0.000146k^3 + 0.122397k^2 + 0.327214k + 0.001995}{k^3 + 2.481481k^2 + 0.934530k + 0.089318}, \tag{4.24f}$$

$$C_7(k) = 0.99618 - \frac{0.16666\iota k}{\iota k + 0.05530} - \frac{0.31190\iota k}{\iota k + 0.28606}. \tag{4.24g}$$

with

$$k = \frac{b\omega}{U} = \frac{K}{2} \tag{4.25}$$

where H_i are the Hankel functions, J_i and J_{iy} are modified Basel functions of first and second kind, respectively. Eq. (4.24a) can be found in [90][76], Eq. (4.24b) in [92], Eq. (4.24c)(4.24d)(4.24e) in [22], Eq. (4.24f) in [61] and Eq. (4.24g) in [93]. These expressions (cf. Eq. (4.24)) are compared in Figure 4.6.

Theodorsen circulation function is unity for the quasi-steady case as the frequency is zero. There will be no coupling between the equations. The aerodynamic forces lift F_L and moment F_M in heave and pitch, greatly depend on the aerodynamic shape of the section. Therefore, this approach may only be used for approximate flutter analysis.

4.3.2 Semi-empirical Models for Bluff Bodies

The FSI for non-streamlined bluff bodies is a complex phenomenon and analytical models can not describe motion-induced forces for these sections. This is a consequence of the flow separation and reattachment which could occur at multiple points on the solid boundary, and it contradicts the assumption for the shedding of vortices from a single point. Therefore a significant amount of research has been associated with developing semi-empirical models dependent on the motion and its time derivatives and empirically based aerodynamic derivatives. For a 2DOF model the system could be described [91] generally by:

$$m\ddot{h} + 2m\xi_h\omega_h\dot{h} + m\omega_h^2 h = F_L(h, \dot{h}, \ddot{h}, \alpha, \dot{\alpha}, \ddot{\alpha}), \tag{4.26a}$$

$$I\ddot{\alpha} + 2I\xi_\alpha\omega_\alpha\dot{\alpha} + I\omega_\alpha^2\alpha = F_M(h, \dot{h}, \ddot{h}, \alpha, \dot{\alpha}, \ddot{\alpha}), \tag{4.26b}$$

where m and I are the mass and mass moment of inertia, ξ_h and ξ_α are the damping ratios, ω_h and ω_α are the natural circular frequencies for the heave and pitch direction, h and α are the vertical displacement and rotation, F_L and F_M are the lift force and
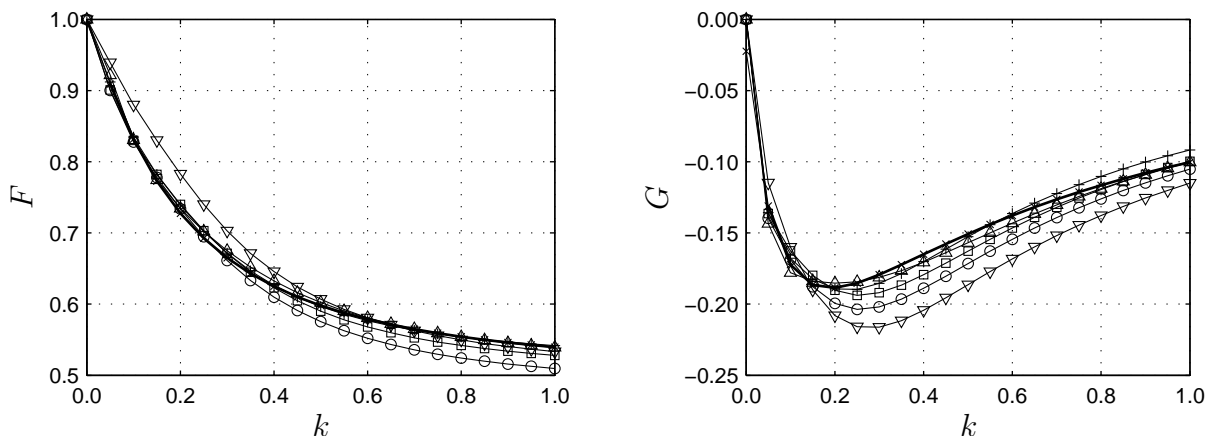
Figure 4.6: Comparison of different approximations for Theodorsen circulation functions:
(left) real part,
(right) imaginary part,
(—) C_1 Eq. (4.24a),
($\circ$) C_2 Eq. (4.24b),
($\square$) C_3 Eq. (4.24c),
($\triangle$) C_4 Eq. (4.24d),
($\triangledown$) C_5 Eq. (4.24e),
($\times$) C_6 Eq. (4.24f),
($+$) C_7 Eq. (4.24g).

moment, respectively. In the case of bridge decks, the apparent mass terms dependent on the acceleration are usually neglected [94]. Considering a whole structure, the equations of motion are:

$$\mathbf{M}\ddot{x}\left(t\right) + \mathbf{C}\dot{x}\left(t\right) + \mathbf{K}x\left(t\right) = \boldsymbol{F}_{ae}\left(t\right), \tag{4.27a}$$

$$\mathbf{M}\ddot{x}\left(t\right) + \mathbf{C}\dot{x}\left(t\right) + \mathbf{K}x\left(t\right) = \mathbf{C}_{ae}\dot{x}\left(t\right) + \mathbf{K}_{ae}\dot{x}\left(t\right). \tag{4.27b}$$

The left-hand side of Eq. (4.27) represents structural properties of the bridge deck with mass $\mathbf{M}$, damping $\mathbf{C}$ and stiffness $\mathbf{K}$ matrices, whereas the right-hand-side of equations describe the unsteady motion-induced aerodynamic force which can be divided into damping related and stiffness related terms. The term motion-induced indicates that the force acting on the deck not only depends on the instantaneous value but also on the history of the motion. Even if there is no coupling on the structural part, a coupling on the aerodynamic side could occur in the aerodynamic damping $\mathbf{C}_{ae}$ and aerodynamic stiffness $\mathbf{K}_{ae}$ matrices [4].

Duncan and Frazer [95] first offered 2D form for the flutter equations, followed by Bleich [96] with a series of publications for truss bridges; however, the major milestone in bridge flutter was set by Scanlan and Tomko [97] who formulated the problem by expressing the motion-induced forces based on Theodorsen theory and experimentally obtained aerodynamic derivatives, the so-called Scanlan derivatives, linearly dependent on the motion of the structure. Analytical evaluation of aerodynamic derivatives for bluff sections is not yet possible.

Considering only the first two terms in Taylor series expansion, and ignoring the static

component, the motion-induced aerodynamic forces as follows:

$$F_L = \frac{\partial F_L}{\partial \dot{h}}\dot{h} + \frac{\partial F_L}{\partial \dot{\alpha}}\dot{\alpha} + \frac{\partial F_L}{\partial \alpha}\alpha + \frac{\partial F_L}{\partial h}h, \tag{4.28a}$$

$$F_M = \frac{\partial F_M}{\partial \dot{h}}\dot{h} + \frac{\partial F_M}{\partial \dot{\alpha}}\dot{\alpha} + \frac{\partial F_M}{\partial \alpha}\alpha + \frac{\partial F_M}{\partial h}h. \tag{4.28b}$$

The aerodynamic forces are the nonlinear functions of vertical displacement and rotation, and their derivatives; however, assuming at flutter boundary small displacements Scanlan expressed the self-excited forces in the linearised form.

Scanlan introduced a mathematical framework for expressing the motion-induced aerodynamic forces on a cross section. As such it is a meta-model. It assumes that the self-excited lift F_L and moment F_M for a bluff body may be treated as linear in displacement h and rotation α and their first derivatives [97] in a linearised form:

$$F_L = \frac{1}{2}\rho U_\infty^2 B \left[K H_1^* \frac{\dot{h}}{U_\infty} + K H_2^* \frac{B\dot{\alpha}}{U_\infty} + K^2 H_3^* \alpha + K^2 H_4^* \frac{h}{B} \right], \tag{4.29a}$$

$$F_M = \frac{1}{2}\rho U_\infty^2 B^2 \left[K A_1^* \frac{\dot{h}}{U_\infty} + K A_2^* \frac{B\dot{\alpha}}{U_\infty} + K^2 A_3^* \alpha + K^2 A_4^* \frac{h}{B} \right], \tag{4.29b}$$

$$K = \frac{B\omega}{U_\infty}, \tag{4.30}$$

where ρ is the air density, B is the chord of the airfoil, H_i^* and A_i^* ($i = 1, \ldots, 4$) are non-dimensional function of K known as aerodynamic or flutter derivatives which are associated with self-excited lift and moment, respectively. K is the reduced frequency and ω is the frequency of bridge oscillation under aerodynamic forcing. As the aerodynamic derivatives are functions of this frequency, they can only be measured when the bridge is in an oscillatory state. These are often measured in special wind tunnel tests but can also be computed from the CFD simulations. Aerodynamic derivatives are more commonly represented in the normalised form as follows:

$$H_1^* = \frac{m}{\rho b^2 \omega}H_1, \qquad H_2^* = \frac{m}{\rho b^3 \omega}H_2, \qquad H_3^* = \frac{m}{\rho b^3 \omega}H_3, \tag{4.31a}$$

$$A_1^* = \frac{I}{\rho b^3 \omega}A_1, \qquad A_2^* = \frac{I}{\rho b^4 \omega}A_2, \qquad A_3^* = \frac{I}{\rho b^4 \omega}A_3, \tag{4.31b}$$

where H_i and A_i are dimensional aerodynamic derivatives. This ensures that they are non-dimensional and can be used for any other size of similar deck shape. Table 4.1 describes the relation of aerodynamic derivatives with the corresponding motion and forces. For example, H_4 represents the aerodynamic stiffness corresponding to vertical lift force induced by heaving motion displacement, whereas A_2 represents the aerodynamic damping corresponding to torsional moment induced by pitching motion velocity. Similarly these can be explained as follows:

$$\text{aerodynamic lift force } [F_L = \overbrace{...H_1^*\dot{h} + ...H_2^*\dot{\alpha}}^{\text{damping terms}} + \overbrace{...H_3^*\alpha + ...H_4^*h}^{\text{stiffness terms}}, \tag{4.32}$$

$$\text{aerodynamic moment } [F_M = \underbrace{...A_1^*\dot{h}}_{\text{heave}} + \underbrace{...A_2^*\dot{\alpha} + ...A_3^*\alpha}_{\text{pitch}} + \underbrace{...A_4^*h}_{\text{heave}}. \tag{4.33}$$

Table 4.1: Description of aerodynamic derivatives:
(▢) direct aerodynamic derivatives,
(▦) coupled aerodynamic derivatives.

Motion / Force	Heave		Pitch	
	$\dot{h}$	h	$\dot{\alpha}$	α
Lift	H_1^*	H_4^*	H_2^*	H_3^*
Moment	A_1^*	A_4^*	A_2^*	A_3^*

Theodorsen functions may also be expressed in terms of aerodynamic derivatives [41]. This gives the aerodynamic derivatives for flat plate based on analytical assumptions as follows:

$$H_1^* = -\frac{2\pi}{K}F, \qquad\qquad A_1^* = \frac{\pi}{K}F\left(\frac{1}{2}+a\right),$$

$$H_2^* = \frac{-\pi}{2K}\left[1+\frac{4G}{K}+2\left(\frac{1}{2}-a\right)F\right], \quad A_2^* = \frac{-\pi}{2K^2}\left[\frac{K\left(\frac{1}{2}-a\right)}{2}-2G\left(a+\frac{1}{2}\right)+KF\left(a^2-\frac{1}{4}\right)\right],$$

$$H_3^* = \frac{-\pi}{K^2}\left[2F-\left(\frac{1}{2}-a\right)GK\frac{aK^2}{4}\right], \quad A_3^* = \frac{\pi}{2K^2}\left[\frac{K^2}{4}\left(a^2+\frac{1}{8}\right)+2F\left(a+\frac{1}{2}\right)+KG\left(a^2-\frac{1}{4}\right)\right],$$

$$H_4^* = \frac{\pi}{2}\left[1+\frac{4G}{K}\right], \qquad\qquad A_4^* = \frac{-\pi}{2K^2}\left[\frac{aK^2}{4}+2KG\left(a+\frac{1}{2}\right)\right]. \qquad (4.34)$$

For a symmetrical deck section, $a=0$ which gives

$$H_1^* = -\frac{2\pi}{K}F, \qquad\qquad A_1^* = \frac{\pi}{2K}F,$$

$$H_2^* = \frac{-\pi}{2K}\left[1+\frac{4G}{K}+F\right], \qquad A_2^* = \frac{-\pi}{2K^2}\left[\frac{K}{4}-G-\frac{KF}{4}\right],$$

$$H_3^* = \frac{-\pi}{K^2}\left[2F-\frac{GK}{2}\right], \qquad A_3^* = \frac{\pi}{2K^2}\left[\frac{K^2}{32}+F-\frac{KG}{4}\right],$$

$$H_4^* = \frac{\pi}{2}\left[1+\frac{4G}{K}\right], \qquad\qquad A_4^* = \frac{-\pi}{2K}G. \qquad (4.35)$$

Scanlan and Tomko [97] introduced the self-excited forces by using aerodynamic derivatives obtained from experimental approach.

A 2DOF (heave and pitch) system may be considered to study classical flutter; however, the bridge deck in an actual case has lateral movement as shown in Figure 4.7. The equation of motions for the whole system can be written as

$$\mathbf{M}\ddot{x}\left(t\right)+\mathbf{C}\dot{x}\left(t\right)+\mathbf{K}x\left(t\right)=\boldsymbol{F}_{ae}\left(t\right)+\boldsymbol{F}_b\left(t\right), \qquad (4.36)$$

where $\boldsymbol{F}_b$ are the buffeting forces which can be defined as

$$F_D = \frac{1}{2}\rho U_\infty^2 B\left[2C_D\chi_{Du}\frac{u(t)}{U_\infty}+\left(C_D'-C_L\right)\chi_{Dw}\frac{w(t)}{U_\infty}\right], \qquad (4.37a)$$

$$F_L = \frac{1}{2}\rho U_\infty^2 B\left[2C_L\chi_{Lu}\frac{u(t)}{U_\infty}+\left(C_L'+C_D\right)\chi_{Lw}\frac{w(t)}{U_\infty}\right], \qquad (4.37b)$$

$$F_M = \frac{1}{2}\rho U_\infty^2 B^2\left[2C_M\chi_{Mu}\frac{u(t)}{U_\infty}+C_M'\chi_{Mw}\frac{w(t)}{U_\infty}\right], \qquad (4.37c)$$

where $u(t)$, $w(t)$ are the fluctuating components of wind speed in the along wind and across wind direction, respectively. χ_{Du}, χ_{Lu} and χ_{Mu} are the aerodynamic admittance coefficients in three directions. For laminar flow there will be no buffeting forces i.e. $\boldsymbol{F}_b = 0$ which leads to the following:

$$\mathbf{M}\ddot{x}\left(t\right) + \mathbf{C}\dot{x}\left(t\right) + \mathbf{K}x\left(t\right) = \boldsymbol{F}_{ae}\left(t\right), \tag{4.38a}$$

$$\mathbf{M}\ddot{x}\left(t\right) + \mathbf{C}\dot{x}\left(t\right) + \mathbf{K}x\left(t\right) = \mathbf{C}_{ae}\dot{x}\left(t\right) + \mathbf{K}_{ae}\dot{x}\left(t\right), \tag{4.38b}$$

where $\boldsymbol{F}_{ae} = [\begin{array}{ccc} F_D & F_L & F_M \end{array}]^{\mathrm{T}}$. $\mathbf{C}_{ae}$ is the aerodynamic damping matrix and $\mathbf{K}_{ae}$ is the aerodynamic stiffness matrix.

The full expression of Scanlan's model is expressed as linear function of the motion considered in Theodorsen theory in terms of aerodynamic derivatives as

$$F_L = \frac{1}{2}\rho U_\infty^2 B\left[KH_1^*\frac{\dot{h}}{U_\infty} + KH_2^*\frac{B\dot{\alpha}}{U_\infty} + K^2H_3^*\alpha + K^2H_4^*\frac{h}{B} + KH_5^*\frac{\dot{p}}{U_\infty} + K^2H_6^*\frac{p}{B}\right], \tag{4.39a}$$

$$F_M = \frac{1}{2}\rho U_\infty^2 B^2\left[KA_1^*\frac{\dot{h}}{U_\infty} + KA_2^*\frac{B\dot{\alpha}}{U_\infty} + K^2A_3^*\alpha + K^2A_4^*\frac{h}{B} + KA_5^*\frac{\dot{p}}{U_\infty} + KA_6^*\frac{p}{B}\right], \tag{4.39b}$$

$$F_D = \frac{1}{2}\rho U_\infty^2 B\left[KP_1^*\frac{\dot{p}}{U_\infty} + KP_2^*\frac{B\dot{\alpha}}{U_\infty} + K^2P_3^*\alpha + K^2P_4^*\frac{p}{B} + KP_5^*\frac{\dot{h}}{U_\infty} + K^2P_6^*\frac{h}{B}\right], \tag{4.39c}$$

where F_D is the aerodynamic drag force on the section, H_i^*, A_i^* and P_i^* (i=1...6) are the aerodynamic derivatives, $\dot{p}$ and p are the horizontal velocity and displacement, respectively. These aerodynamic derivatives for bluff sections cannot be computed analytically, however, it is possible to obtain them by experimental wind tunnel tests or through the CFD simulations which are discussed in Section 4.4.
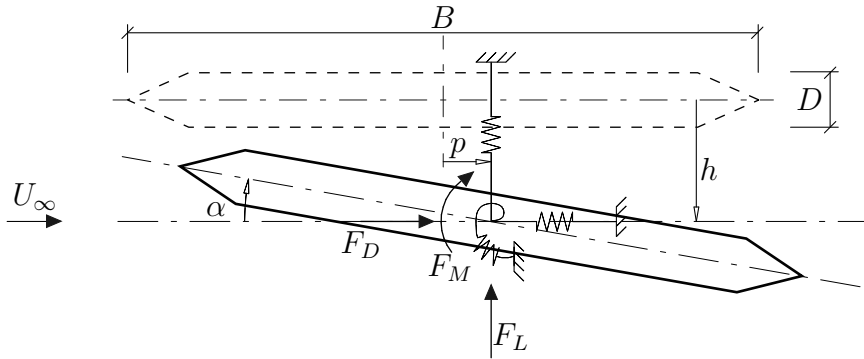
Figure 4.7: Definition of degrees-of-freedom and aerodynamic forces for flutter analysis of bluff sections.

Scanlan's model has been widely used for the solution of 2D and 3D aeroelastic instability problems in the field of bridge aerodynamics due to its applications to different types of bridge cross sections. The motion-induced aerodynamic forces are based on two assumptions [98]. Firstly, the displacement of structure follow harmonic vibration and is represented by 18 aerodynamic derivatives neglecting the apparent mass for the acceleration term. Secondly, if the motion-induced forces are considered to have a nonlinear relationship with structural motion, then these expressions would include the second-order or even high-order terms of the structural motion.

Scanlan and Tomko [97] initially studied free vibration method to identify aerodynamic derivatives (H_i^*, A_i^* with $i = 1, \ldots, 3$) by using experiments for 5 different deck shapes

and studied the effect of the change in depth of H-shape section. The reason for using 3 aerodynamic derivatives was the direct relationship with the flat-plate theory which is based only on vertical motion, angular rotation and angular velocity in the circulatory terms. Scanlan [99, 100] utilised (H_i^*, A_i^*, P_i^* with $i = 1, \ldots, 3$) aerodynamic derivatives for the linear dynamic analysis bridges having lateral vibration modes along with the energy considerations involved in the assessment of aerodynamic stability. Jain et al. [101, 102] made use of all 6 P_i^* (with $i = 1, \ldots, 6$) aerodynamic derivatives in the aerodynamic analysis.

4.3.2.1   Utilisation of Aerodynamic Derivatives

The aeroelastic instability of bridge depends greatly on the magnitudes and signs of some of the aerodynamic derivatives of the deck cross section. The aerodynamic derivatives can be used for preliminary examination of aeroelastic instability. The terms on the right-hand-side of the Eq. (4.29) can be separated into damping terms (associated with the velocity of motion) and stiffness terms (associated with the displacement of motion). The effect of the change in the damping related forces is considered to be more important and the effect of the change in the stiffness related forces is often insignificant for aeroelastic instability. The aerodynamic derivative related to velocity-proportional forces describes the aerodynamic damping of that DOF and the positive sign of this derivative indicates negative aerodynamic damping. The SDOF mechanism of aerodynamic instability is related to occurrence of negative aerodynamic damping. The aerodynamic derivative H_1^*, which is the aeroelastic lift force induced as a result of heave velocity, controls the vertical flutter and the aerodynamic derivative A_2^*, which is the aeroelastic moment induced as a result of pitch velocity, governs the torsional flutter instability. The flutter phenomenon is related to the negative aerodynamic damping whereas negative stiffness creates divergence.

In the case of a flat plate for SDOF instability, considering pure bending motion (cf. Eq. (4.29a)), the negative values of $H_1^* < 0$ and $H_4^* < 0$ will increase the overall system damping and stiffness, respectively. If the magnitude of the negative aerodynamic damping becomes greater than the structural damping, the amplitudes of oscillations will grow and aeroelastic instability will occur which happens usually for deep sections. Similarly, considering pure torsional motion (cf. Eq. (4.29b)), where $A_2^* < 0$ and $A_3^* > 0$ the overall system damping will increase and overall system stiffness will decrease. So it is unlikely for SDOF instability to occur and more likely to occur 2DOF flutter [103].

Table 4.2 presents some guidelines for the assessment of aeroelastic instability from aerodynamic derivatives of different sections. The derivatives H_4^* and A_3^* tend to increase vertical stiffness and reduce torsional stiffness. For streamlined sections, $-H_3^*$ and A_4^* feed energy into structural vibration whereas aerodynamic damping terms H_1^* and A_2^* extract energy. Phase difference for streamline sections is 180° and the system is less dependent on structural damping [48]. Coupled flutter can still occur even if A_2^* and H_1^* are positive. Trein and Shirato [104] reviewed the roles of aerodynamic derivatives in flutter stabilisation and pointed out some conditions that the unsteady pressure characteristics should present in flutter stabilisation.

If the instability limit exceeds the design wind speed of the site at the deck height (suitably factored for ultimate limit states), then modifications are required to be made to the deck cross-section in order to avoid the occurrence of aeroelastic instability. Section modifications can be made to avoid the positive (H_1^*, A_2^*) aerodynamic

Table 4.2: Types of aerodynamic instabilities, after [2, 5].

Phenomenon	Conditions	Type of motion	Type of section
Galloping	$H_1^*>0$	Translational	D-shape, square section, deep sections
Torsional flutter	$A_2^*>0$	Rotational	H-section, rectangle with smaller aspect ratio (width/depth)
Classical flutter	$H_2^*>0$, $A_1^*>0$	Coupled	flat plate, airfoils

derivatives [4]. Matsumoto [105] studied to stabilise flutter of long-span bridges by reduction of A_2^* through suitably combining deck section with $(A_1^* > 0,\ A_2^* < 0)$ and $(A_1^* < 0,\ A_2^* > 0)$.

4.3.2.2 Scanlan Equivalent Representations

In the field of bridge aerodynamics, the comparison of aerodynamic characteristics utilising the aerodynamic derivatives is a common and widely accepted approach. Various conventions have been developed and are used based on the same assumptions as Scanlan's. The earliest ones are developed by Miyata et al. [106]. Zasso [107] gave a representation of the motion-induced forces with the advantage of the better description in the low-frequency range where Scanlan's tend to become zero.

The aerodynamic derivatives $(H_i^*,\ A_i^*)$ are the real and the imaginary parts of the transfer functions between the non-dimensional forces and the non-dimensional displacements. Motion-induced aerodynamic forces are mathematically described in real number or complex number expressions and the flutter analysis performed using either of these lead to the same numerical results.

Based on the analytical theory of Theodorsen, Starossek [61] introduced a modified theory following the complex number approach. This also allows the use of aerodynamic derivatives computed by experimental or numerical methods. The advantage in the solution method is by solving a linear eigenvalue problem by which the complex flutter mode shape is obtained without additional effort. This approach is more popular among the researchers concerned with the aerofoils and aircraft flutter analysis. Some computational and programming benefits are highlighted in [108] by comparing real and complex number descriptions of the same mechanical phenomena. For more elaborate information on complex notation, the reader is referred to [61, 108, 109, 110, 111].

The aerodynamic forces can be expressed in the following linearised form:

$$F_L = \omega^2 \pi \rho b^2 \left(c_{hh} h + b c_{h\alpha} \alpha \right), \tag{4.40a}$$

$$F_M = \omega^2 \pi \rho b^2 \left(b c_{\alpha h} h + b^2 c_{\alpha\alpha} \alpha \right) \tag{4.40b}$$

where c_{mn} are the dimensionless complex force coefficients or derivatives which are the functions of reduced frequency k with

$$c_{mn} = c'_{mn} + \iota c''_{mn} \tag{4.41}$$

where c'_{mn} and c''_{mn} are the real and imaginary parts respectively. The real part is related to the component of the aerodynamic force that corresponds to the structural

displacement and the imaginary part is related to the velocity as shown in Figure 4.8. The first subscript m describes the direction of force and the second subscript n is related to the motion causing the force. These 4 coefficients describe the relationship between motion and the self-excited forces. The components c'_{hh}, c''_{hh}, $c'_{\alpha h}$ and $c''_{\alpha h}$ are computed from a forced heave simulation whereas $c'_{h\alpha}$, $c''_{h\alpha}$, $c'_{\alpha\alpha}$ and $c''_{\alpha\alpha}$ are computed from a forced pitch simulation.
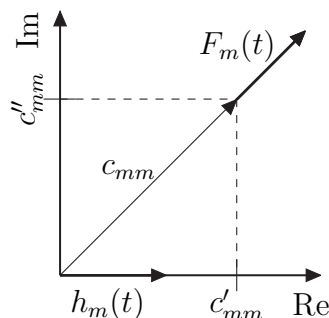
Figure 4.8: Motion and corresponding force representation in complex plane.

The relationship between real and complex notations can be established by comparing the corresponding aerodynamic force and moment expressions i.e. Eq. (4.29a) with Eq. (4.40a) and Eq. (4.29b) with Eq. (4.40b). Both the real and the complex notations have the same theoretical background. The relations are given in Table 4.3 and are as follows:

$$
\begin{aligned}
c_{hh} &\cong \tfrac{2}{\pi}\left(H_4^* + \iota H_1^*\right), \quad c_{h\alpha} \cong \tfrac{4}{\pi}\left(H_3^* + \iota H_2^*\right), \\
c_{\alpha h} &\cong \tfrac{4}{\pi}\left(A_4^* + \iota A_1^*\right), \quad c_{\alpha\alpha} \cong \tfrac{8}{\pi}\left(A_3^* + \iota A_2^*\right).
\end{aligned}
\tag{4.42}
$$

In the aerodynamic study for the Normandy Bridge in France, a so-called Küssner notation was used, with the aerodynamic derivatives known as Küssner coefficients (k_i^a, k_i^b, m_i^a, m_i^a with $i = 1, 2$) [112]. Zasso [107], Borri and Höffer [113] summarised some of these conventions and highlighted their merits and demerits. Jensen [114] compared Scanlan's derivatives with the ones developed for Marine Engineering usage based on the relative position of the bridge deck utilising the velocity and acceleration terms. Some of these conventions are summarised in Table 4.3.

Table 4.3: Conversion between the notations of the aerodynamic derivatives by Scanlan, Starossek, Küssner, Zasso and Jensen.

Scanlan	H_4^*	H_1^*	A_4^*	A_1^*	H_3^*	H_2^*	A_3^*	A_2^*
Starossek	$\frac{\pi}{2}c'_{hh}$	$\frac{\pi}{2}c''_{hh}$	$\frac{\pi}{4}c'_{\alpha h}$	$\frac{\pi}{4}c''_{\alpha h}$	$\frac{\pi}{4}c'_{h\alpha}$	$\frac{\pi}{4}c''_{h\alpha}$	$\frac{\pi}{8}c'_{\alpha\alpha}$	$\frac{\pi}{8}c''_{\alpha\alpha}$
Küssner	$\frac{-v_r^2}{2\pi}k_1^a$	$\frac{-v_r^2}{2\pi}k_2^a$	$\frac{-v_r^2}{4\pi}m_1^a$	$\frac{-v_r^2}{4\pi}m_2^a$	$\frac{-v_r^2}{4\pi}k_1^b$	$\frac{-v_r^2}{4\pi}k_2^b$	$\frac{-v_r^2}{8\pi}m_1^b$	$\frac{-v_r^2}{8\pi}m_2^b$
Zasso	$\frac{\pi}{2}h_4^*$	$\frac{-v_r}{2\pi}h_1^*$	$\frac{\pi}{2}a_4^*$	$\frac{-v_r}{2\pi}a_1^*$	$\frac{v_r^2}{4\pi^2}h_3^*$	$\frac{-v_r}{2\pi}h_2^*$	$\frac{v_r^2}{4\pi^2}a_3^*$	$\frac{-v_r}{2\pi}a_2^*$
Jensen	$-Y'_{\dot r}$	$Y'_v\frac{1}{K}$	$-N'_{\dot r}$	$N'_v\frac{1}{K}$	$-\left(Y'_r + Y'_{\dot v}\frac{1}{K^2}\right)$	$\left(Y'_r - Y'_{\dot v}\right)\frac{1}{K}$	$-\left(N'_{\dot r} + N'_v\frac{1}{K^2}\right)$	$\left(N'_r - N'_{\dot v}\right)\frac{1}{K}$

4.3.2.3 Quasi-steady Representations

The quasi-steady theory describes the aerodynamic forces without consideration of the fluid memory by mapping the instantaneous status of the system at the current time

into the corresponding status at the infinite time, such that the wake has convected far from the body for evaluating the flow-induced forces. In addition to these forces, there are apparent mass forces due to the inertial effect related to the portion of fluid surrounding the body that moves with it which are not associated with the creation of vorticity and are of minor importance in the coupled flutter and are usually neglected [86].

The quasi-steady theory for bluff bodies essentially does not differ from the one for flat-plate. The theoretical values for the slopes of the lift C'_L and moment C'_M coefficients are 2π and $\pi/2$, respectively. As discussed previously, this model does not consider the fluid memory effect; however, it offers a static nonlinear relationship between the instantaneous angle of attack and the flow-induced forces. Table 4.4 shows the relation between Scanlan's representation and quasi-steady theory for a selected reduced velocity.

Table 4.4: Conversion between the notations of the aerodynamic derivatives by Scanlan and corrected quasi-steady theory.

Scanlan	H_1^*	H_2^*	H_3^*	H_4^*	A_1^*	A_2^*	A_3^*	A_4^*
Quasi-steady	$-(C'_L+C_D)\frac{v_r}{2\pi}$	$-(C'_L+C_D)m_L\frac{v_r}{2\pi}$	$C'_L\frac{v_r^2}{(2\pi)^2}$	$-2C_L\frac{v_r}{2\pi}$	$-C'_M\frac{v_r}{2\pi}$	$C'Mm_M\frac{v_r}{2\pi}$	$C'_L\frac{v_r^2}{(2\pi)^2}$	$-2C_M\frac{v_r}{2\pi}$

4.3.3 Numerical Methods

The aerodynamic behaviour for the design of long-span bridges is traditionally studied through wind tunnel tests; however, these tests are cost-expensive and require time for planning, actual testing and may be restrictive at the design stage. Even a small modification sometimes requires to build a new model. The CFD has gained much attention and development in the last decades and is used as an alternative beside the analytical and experimental methods; however, it still has limitations with the complexity and nature of 3D bridge structures [115]. Blocken [116] provided a perspective on the past, present and future of Computational Wind Engineering (CWE).

The CFD is more accessible than Wind Tunnel Tests (WTT) for the aerodynamic analysis of bridge deck geometry and checking the performance of structure [32]. It allows simultaneous force coefficients, pressure distributions, structural response and flow visualisation which is very useful in understanding the FSI mechanism that is important for wind-induced vibrations [51]. The common methods used for flow discretisation include the Finite Volume Method (FVM), Finite Element Method (FEM) and Discrete Vortex Method (DVM) where the first two are Eulerian mesh-based and the third is Langrangian mesh-free. This further requires a turbulence model for the closure of the Navier-Stokes equations. In general, there are three primary numerical models to simulate flow turbulence: Reynolds-Averaged Navier-Stokes (RANS), Large Eddy Simulation (LES) and Detached Eddy Simulation (DES) [84]. Table A.1, A.2 and A.3 summarises different CFD approaches used to study aerodynamic behaviour of long-span bridges.

The accuracy of results from the CFD approach not only depends on the quality of the solver but also on the modelling itself. Therefore, the selection of the boundary conditions, grid refinement and time discretisation is also important. The numerical method must be reliable and robust to be used in place of WTT. The accuracy of the results depends on modelling errors, discretisation errors as well as iteration errors.

Such errors which are coming from inaccurate modelling assumptions and discretisation can only be detected by comparison with the experimental results.

4.3.3.1   Vortex Particle Method

The CFD simulations based on the vortex method has gained much attention in the 1990s to be used in the field of bridge aerodynamics. The success of the simulations is attributed to the bluff nature of the cross-sections and to the two-dimensional (2D) nature of flow around bridge decks [117]. Walther [118] developed a 2D-DVM to simulate flow past bluff bodies. It considers two-dimensional slightly viscous incompressible flow (constant density) which has the advantage in its 2D nature of flow around bluff bodies. This allows to compute static wind coefficients, Strouhal number, aerodynamic derivatives and critical flutter limits which are essential for aeroelastic analyses of a bridge [117, 119]. It has been used to study flow around flat plate as well as other bluff bridge deck cross sections to show the applicability and efficiency of the method and to help understanding mechanisms related to the phenomena of aeroelastic instability [120, 121, 122, 123, 124, 125, 126, 127].

The Vortex Particle Method (VPM) uses a grid-free Lagrangian formulation which has the advantage of high numerical efficiency and can be applied to complex structural geometries. This provides an alternative to classical Eulerian methods which are used in the finite volume approaches. For further information and comprehensive reviews on the VPM the reader is referred to the publications by [122, 123, 128].

Here, the Navier-Stokes equations are solved with the help of particles considering the equations of an incompressible and temperature-insensitive fluid without external volume forces. This allows a grid-less numerical scheme where the boundary of the modelled section is discretised into small panels and the vorticity is discretised on the boundary of the body using the boundary element method. The velocity field is required to be determined to evolve the flow. The pressure is computed on the body surface with the neighbouring velocity and the integration of pressure provides forces. The structure of the bridge is assumed to have a rigid cross-section and can be suspended on springs with its dynamic properties. The 'no-slip condition' is applied which means that the velocity at the surface of the panels is zero. Additionally, if the section is moving, the relative velocity of the section is also taken into account for flow velocity computation. The integrated pressures represent the global section forces in terms of lift, drag and moment.

4.3.4   Experimental Methods

Experimental methods are considered the most accurate as compared to the other methods. The approaches being used currently to study the aerodynamic behaviour of suspended span bridges include full-scale monitoring and wind tunnel testing [41].

4.3.4.1   Full-scale Monitoring

Wind tunnel tests are the basis for analysis and design of long-span bridges. However, small-scale experiments have limitations in predicting the full-scale behaviour due to scale effects such as Reynolds number and the structural damping. These modelling parameters can only be validated through full-scale measurements which is crucial

for bridge aerodynamics. Full-scale measurements are seldom performed for long-span bridges. Frandsen [129] utilised full-scale measurements on the Great Belt suspension bridge and provides several other references of full-scale measurements on different bridges around the world. Moreover, full-scale measurements have been used to validate the analytical response prediction [130] and to extract aerodynamic derivatives [131]. The full-scale aeroelastic behaviour of bridges is still not completely understood and is an active research topic.

4.3.4.2 Wind Tunnel Testing

The tests in the wind tunnel are commonly carried out either on section models, taut-strip models or full aeroelastic models. These methods are considered relatively accurate as compared to the other methods (analytical and numerical); however, such tests are expensive and cannot reproduce fully the physics of the full-scale problem. These tests require scaled models representing the structure by ensuring certain similarity laws. In these tests, the models are not only geometrically similar but reduced frequency, mass and stiffness distribution also satisfy the similarity requirements. The major drawback of boundary layer wind tunnel testing is that often sufficient structural details cannot be reproduced and fluid flow can have some scaling errors. Wind tunnel test for Akashi Kaikyo Bridge [132] and Great Belt East Bridge [133] are notable examples of 3D aeroelastic bridge models. Moreover, Sato et al. [68] and Yoshizumi and Inoue [134] describe 2D and 3D flutter analysis of full aeroelastic model test for long-span bridges.

Section models are more commonly used for defining static wind loads [135] and measuring aerodynamic derivatives of the section. These tests include the free or forced vibration tests of 2D sectional models. Often section models are made for economic reasons and only the first vertical and the first torsional modes are studied. The cross section of the bridge deck is modelled using springs at the ends tuned to natural frequencies of the selected modes. These tests are also useful to study the aeroelastic instability characteristics of the deck by making use of the results from wind tunnel experiments on dynamically mounted section models. Table A.4 provides some examples of wind tunnel tests performed on different structures.

Several parameters are determined from section models of decks through wind tunnel testing such as static wind coefficients, aerodynamic derivatives and Strouhal number etc. Static wind coefficients are defined as:

$$C_D = \frac{F_D}{\frac{1}{2}U_\infty^2 B} \tag{4.43}$$

$$C_L = \frac{F_L}{\frac{1}{2}U_\infty^2 B} \tag{4.44}$$

$$C_M = \frac{F_M}{\frac{1}{2}U_\infty^2 B^2} \tag{4.45}$$

where, C_D, C_L and C_M are the coefficients of drag, lift and moment, respectively. F_D, F_L and F_M are the time averaged drag force, lift and moment, respectively. If N_s is the primary frequency of vortex shedding generated by the static bluff body, then the Strouhal number is given by

$$St = \frac{N_s D}{U_\infty} \tag{4.46}$$

where, St is the Strouhal number depending on the geometry of the body, D is the across wind dimension of the body.

4.4   Extraction of Aerodynamic Derivatives

4.4.1   Free and Forced Vibration Techniques

The aerodynamic unsteady forces or motion-induced forces are assumed to be related to the aerodynamic derivatives and their linear combination of displacements and their first time derivatives. There are two main approaches [28, 91] to determine the aerodynamic derivatives for a section. First with direct measurements of aerodynamic force components by strain measurements on a sectional model when the section is given some forcing [57] and second to calculate the force indirectly by measuring unsteady surface pressure and phase difference from the flow-induced motion of the model [97]. The direct measurements require usually more complex experimental set-ups.

The motion of the structure in the flow induces aerodynamic forces which are characterised by aerodynamic derivatives. These aerodynamic derivatives describe the aerodynamic behaviour of the oscillating deck and are commonly measured from wind tunnel tests by using different methods such as free vibration, forced vibration and buffeting tests. In forced vibration tests the scaled deck section is forced to move with specific displacement and velocities (or angular rotations and angular velocities) and the aerodynamic forces are measured from which aerodynamic derivatives are extracted. Free vibration tests are more common where the decay in the system damping and the change in system stiffness is measured when a deck section model is given some initial displacement. The buffeting tests are simple but the measurements are needed to be treated to remove buffeting forces considering as noises which require more advanced system identification techniques. Some wind tunnel tests performed for different structures are summarised in Table A.4 using free, forced and buffeting approaches to compute aerodynamic derivatives.

The classical forced vibration tests are conducted on decoupled motions to compute aerodynamic derivatives; however, this decoupled motion generates the derivatives where the direct components of aeroelastic motions are dominant than the interactive components [136]. In addition to this, coupled forced vibration techniques are also used to determine aerodynamic derivatives [137, 138, 139, 140]. Table A.5 presents some examples of forced vibration analyses on different structures and corresponding displacement amplitude used.

The recommended values of amplitudes of motion are $h_o = 0.05B$ and $\alpha_o = 5°$. Walther [118] also suggested the amplitudes of the vertical and rotational motion for forced oscillation simulations as

$$h_o < \frac{1}{\omega}\sqrt{\frac{2\nu}{\triangle t}} = \frac{B}{2\pi}\left(\frac{v_r}{U_\infty}\right)\sqrt{\frac{2\nu}{\triangle t}}, \tag{4.47a}$$

$$\alpha_o < \frac{1}{\omega}\sqrt{\frac{8\nu}{\triangle t}} = \frac{B}{2\pi}\left(\frac{v_r}{U_\infty}\right)\sqrt{\frac{8\nu}{\triangle t}}, \tag{4.47b}$$

where ω is the oscillation frequency, ν is the kinematic viscosity and $\triangle t$ is the time step, respectively.

4.4.2 Meta Model Calibration

The determination of flutter limit for a structural system requires a set of aerodynamic derivatives. These aerodynamic derivatives can be obtained by performing forced vibration wind tunnel tests or CFD simulations. For this purpose, the section is forced to oscillate harmonically in its heave $[h = h_o \sin(\omega t)]$ or pitch $[\alpha = \alpha_o \sin(\omega t)]$ DOF with constant amplitude. Eqs. (4.29a) and (4.29b) (with $\alpha = 0$) thus constitutes a system of equations for heave motion as

$$F_L = \frac{1}{2}\rho U_\infty^2 B \left[KH_1^* \frac{\dot{h}}{U_\infty} + K^2 H_4^* \frac{h}{B} \right], \tag{4.48a}$$

$$F_M = \frac{1}{2}\rho U_\infty^2 B^2 \left[KA_1^* \frac{\dot{h}}{U_\infty} + K^2 A_4^* \frac{h}{B} \right]. \tag{4.48b}$$

Separately performing these tests give the time histories for lift $\bar{F}_L$ and moment $\bar{F}_M$ corresponding to known displacement traces h or α. Thus Eqs. (4.48a) and (4.48a) take the form

$$\bar{F}_L = \mathbf{C}_h^L \mathbf{H}_h^*, \tag{4.49a}$$

$$\bar{F}_M = \mathbf{C}_h^M \mathbf{A}_h^*, \tag{4.49b}$$

where

$$\mathbf{C}_h^L = \frac{1}{2}\rho U_\infty^2 BK \left[\begin{array}{cc} \frac{\dot{h}}{U_\infty} & K\frac{h}{B} \end{array} \right], \tag{4.50}$$

and

$$\mathbf{C}_h^M = B\mathbf{C}_h^L, \tag{4.51}$$

also

$$\mathbf{H}_h^* = \left\{ \begin{array}{c} H_1^* \\ H_4^* \end{array} \right\}, \quad \mathbf{A}_h^* = \left\{ \begin{array}{c} A_1^* \\ A_4^* \end{array} \right\}. \tag{4.52}$$

System (4.49a) and (4.49b) can be solved in the least-squares sense by left-multiplying with the $\mathbf{C}$ matrix:

$$\mathbf{C}_h^{L^\mathrm{T}} \bar{F}_L = \mathbf{C}_h^{L^\mathrm{T}} \mathbf{C}_h^L \mathbf{H}_h^*, \tag{4.53a}$$

$$\mathbf{C}_h^{M^\mathrm{T}} \bar{F}_M = \mathbf{C}_h^{M^\mathrm{T}} \mathbf{C}_h^M \mathbf{A}_h^*. \tag{4.53b}$$

Similarly, the procedure can be repeated for the pure pitch case $(h = 0)$, the equations will become

$$F_L = \frac{1}{2}\rho U_\infty^2 B \left[KH_2^* \frac{B\dot{\alpha}}{U_\infty} + K^2 H_3^* \alpha \right], \tag{4.54a}$$

$$F_M = \frac{1}{2}\rho U_\infty^2 B^2 \left[KA_2^* \frac{B\dot{\alpha}}{U_\infty} + K^2 A_3^* \alpha \right]. \tag{4.54b}$$

Heave and pitch motions are performed separately in forced vibration simulations to obtain aerodynamic derivatives as shown in Figure 4.9.

This gives two sets of aerodynamic derivatives in a least-squares sense. The same can be repeated for pitch case (with $h = 0$). The procedure to calculate these aerodynamic derivatives is summarised as follows:
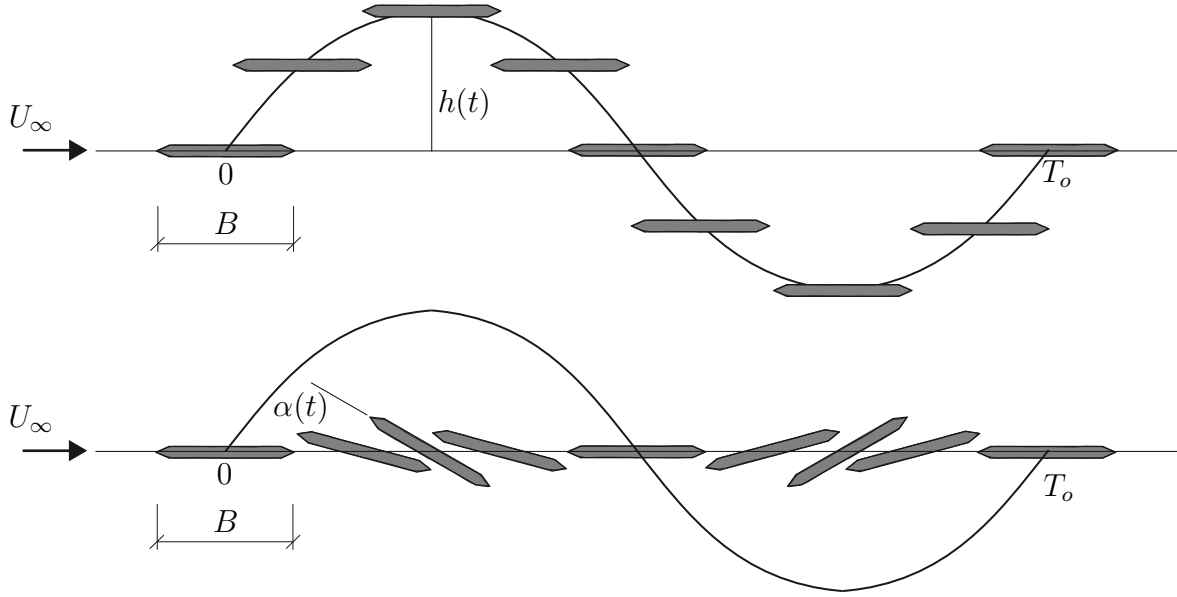
Figure 4.9: Schematic of forced vibration simulation:
(top) forced heave motion,
(bottom) forced pitch motion.

- impose forced vibration motion either in heave (h) or pitch (α) on the cross,

- extract the lift and moment time traces,

- calculate a best-fit harmonic of the same forcing frequency,

- obtain lift or moment coefficient and phase shift,

- calculate the required aerodynamic derivatives.

Figure 4.10 shows a schematic of forced vibration simulation for lift coefficient (C_L) and moment coefficient (C_M) time traces where least-square fit is performed to calculate aerodynamic derivatives. Two separate simulations in heave and pitch DOF are required to be performed to get one set of aerodynamic derivatives at a given reduced speed v_r which is defined as

$$v_r = \frac{2\pi U_\infty}{b\omega} = \frac{2\pi}{K}. \tag{4.55}$$

Alternatively, the procedure can be followed explained in [141]. The section is assumed to oscillate harmonically in heave $[h = h_o e^{(\iota\omega t)}]$ or pitch $[\alpha = \alpha_o e^{(\iota\omega t)}]$ DOF. The aerodynamic forces will have same harmonic frequency ω but with a phase shift φ. The Eqs. (4.29) can be written as:

$$C_L e^{\iota(\omega t - \varphi)} = 2K^2 \left[(\iota H_1^* + H_4^*) \frac{h}{B} + (\iota H_2^* + H_3^*) \alpha \right] e^{(\iota\omega t)}, \tag{4.56a}$$

$$C_M e^{\iota(\omega t - \varphi)} = 2K^2 \left[(\iota A_1^* + A_4^*) \frac{h}{B} + (\iota A_2^* + A_3^*) \alpha \right] e^{(\iota\omega t)}. \tag{4.56b}$$

Dividing the above equation with $e^{(\iota\omega t)}$ and replacing $e^{(\iota\varphi)}$ by $(\cos\varphi - \iota\sin\varphi)$
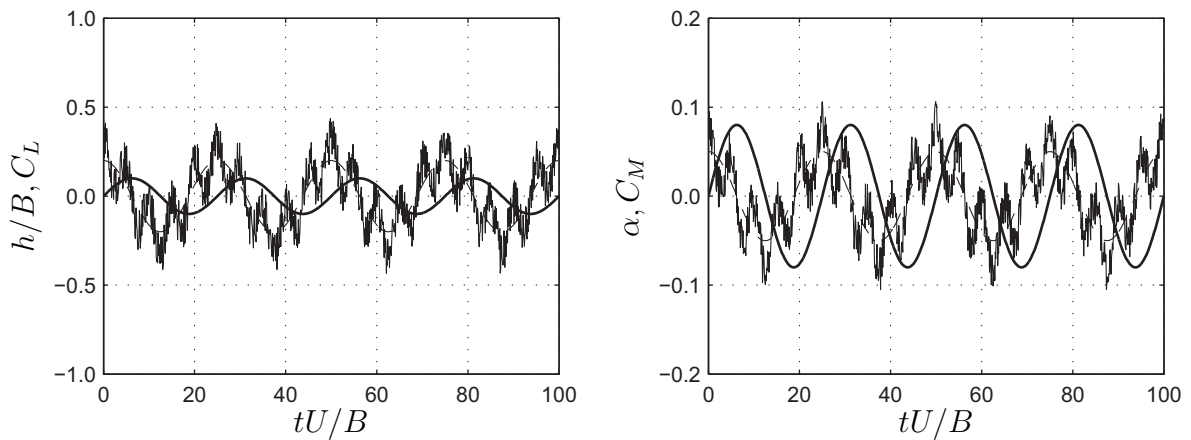
Figure 4.10: Forced oscillation simulations: lest-square fitting to calculate aerodynamic derivatives from
(left) lift coefficient C_L time traces,
(right) moment coefficient C_M time traces.
(——) forced displacement h/B and rotation α,
(—–) measured lift and moment,
(– –) least-squares fit on lift and moment.
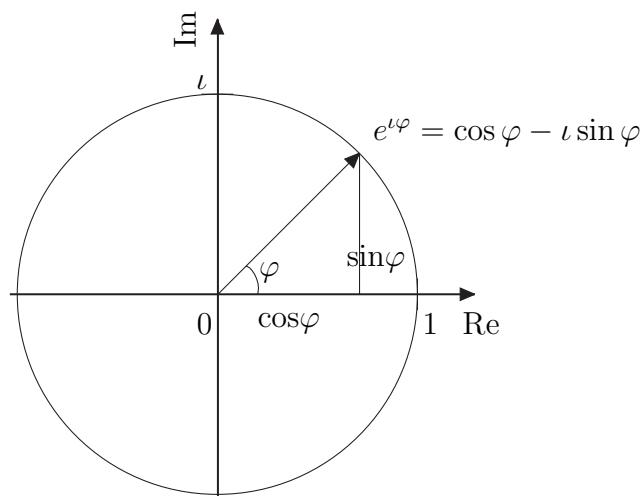
Figure 4.11: Schematic of harmonic oscillation.

(cf. Figure 4.11) will give the following set of equations:

$$
H_1^* = -\left(\frac{U_\infty}{Bf_o}\right)^2 \frac{C_L \sin \varphi_{L-h}}{(2\pi)^2 \, h_o/B}, \qquad\qquad H_2^* = -\left(\frac{U_\infty}{Bf_o}\right)^2 \frac{C_L \sin \varphi_{L-\alpha}}{(2\pi)^2 \, \alpha_o},
$$

$$
H_3^* = \left(\frac{U_\infty}{Bf_o}\right)^2 \frac{C_L \cos \varphi_{L-\alpha}}{(2\pi)^2 \, \alpha_o}, \qquad\qquad H_4^* = \left(\frac{U_\infty}{Bf_o}\right)^2 \frac{C_L \cos \varphi_{L-h}}{(2\pi)^2 \, h_o/B},
$$

$$
A_1^* = -\left(\frac{U_\infty}{Bf_o}\right)^2 \frac{C_M \sin \varphi_{M-h}}{(2\pi)^2 \, h_o/B}, \qquad\qquad A_2^* = -\left(\frac{U_\infty}{Bf_o}\right)^2 \frac{C_M \sin \varphi_{M-\alpha}}{(2\pi)^2 \, \alpha_o},
$$

$$
A_3^* = \left(\frac{U_\infty}{Bf_o}\right)^2 \frac{C_M \cos \varphi_{M-\alpha}}{(2\pi)^2 \, \alpha_o}, \qquad\qquad A_4^* = \left(\frac{U_\infty}{Bf_o}\right)^2 \frac{C_M \cos \varphi_{M-h}}{(2\pi)^2 \, h_o/B},
$$

$$(4.57)$$

where $f_o = 1/T_o$ is the frequency of harmonic oscillation.

4.5 Summary

This chapter provides a description of methods of aerodynamic analysis with a special focus on analytical and numerical methods. The approaches to model the motion-induced aerodynamic forces have been presented. For this purpose, Theodorsen expressions for motion-induced aerodynamic forces based on potential flow and Scanlan's aerodynamic derivatives as meta-model have been used. Finally, a procedure to calculate aerodynamic derivatives from forced vibration simulations is explained. This comprehensive review provides fundamentals for model combinations for flutter analysis which are further elaborated in Chapter 5.

Chapter 5

Models for Flutter Analysis

5.1 Introduction

The main objective of studying flutter phenomena is to find the instability limit which is also known as flutter limit or flutter wind speed. It is important to make sure in the design process that this wind speed is not exceeded during the design life of the bridge. Therefore, an accurate prediction of flutter boundary is essential. This chapter provides different model combinations to perform flutter analysis. For this purpose, analytical and numerical methods have been utilised. The aerodynamic and structural models are combined in different ways and the procedure to implement these models is described in detail. The assumptions made at each step are specified and their effects on the model predictions are highlighted. The advantages and limitations of each model combination are discussed within this chapter.

5.2 Coupled Models for Flutter Analysis

Flutter is a coupling of aerodynamic forcing with a structural dynamics problem. Therefore, different types and classes of models can be combined to study the interaction. In this study, both numerical approaches and analytical models are utilised and coupled in different ways to calculate the flutter limit from the hybrid model. This has allowed to investigate a very broad range of model combinations and to study their merits and drawbacks.

The flutter analysis is generally performed through complex eigenvalue solution. The analytical approach is being conducted predominantly in the frequency domain. This is mainly due to the computational efficiency offered by the frequency domain, especially when handling the aerodynamic forces that are functions of the oscillation frequency. Here, both the frequency and time domain approaches have been utilised to study the comparison.

Models for aerodynamic forces employed are the analytical Theodorsen expressions for the motion-induced aerodynamic forces of a flat plate and Scanlan derivatives as a Meta-model. Further, CFD simulations using the VPM are used to cover numerical models. The structural representations are dimensionally reduced to 2DOF section models calibrated from global models as well as multi-degree of freedom models. A 2DOF system is analysed analytically as well as numerically. The model combinations used in this study are summarised in Table 5.1.

Table 5.1: Model combinations for flutter analysis used in this study:
(○) regular model,
(●) meta-model.

Structural \ Aerodynamic	Analytical	Numerical
Analytical	○ Model#1	-
	○ Model#2	
	Model#3 ○ ●	
Numerical	Model#4 ○ ●	
	-	○ Model#5

Model#1 Fully Analytical: Theodorsen equations for motion-induced aerodynamic
forces with 2D structural model

Model#2 Empirical Approach: for 2D only

Model#3 Derivative-based Eigenvalue Analysis: Theodorsen flat plate aerodynamic
derivatives and Scanlan derivatives from the CFD forced vibration
simulations with 2D and 3D structural model

Model#4 Derivative-based FSI Simulations: Theodorsen flat plate aerodynamic
derivatives and Scanlan derivatives from the CFD forced vibration
simulations with 2D and 3D structural model

Model#5 Fully-coupled CFD Simulations: based on the VPM with 2D
and quasi-3D structural model

5.3   Wind Tunnel Aeroelastic Models

Wind tunnel tests are the basis for analysis and design of long-span bridges. These tests
are commonly used for important structures to study the aeroelastic instability behaviour
along with other aerodynamic phenomena.   The flutter limits of some well-known
bridges around the world have been shown in Table 5.2. The table also provides the
countermeasures used to improve the aeroelastic stability behaviour against flutter.

It is worth mentioning that the experimental models explained here are just for the sake
of completeness and not covered in this research. Generally, there are two types of tests
conducted in wind tunnels for the aeroelastic stability analysis against flutter [144].

- Section model tests with spring supports: the aerodynamic characteristics of some
  (2 or 3) selected modes can be studied.

- Full-3D aeroelastic model: the aerodynamic characteristics of more than three
  modes can be studied at the same time to examine coupling effect of different
  modes.

Section models represent the typical length of the structure. The section models are

Table 5.2: Long-span cable-supported bridges with their flutter limits and countermeasures [3, 28, 29, 32, 33, 39, 46, 142, 143].

Bridge name	Main span [m]	Girder type	Flutter limit [m/s]	Vibration countermeasures
Suspension				
Messina	3300	Triple box	75	Central slot
Akashi-Kaikyo	1991	Truss	84	Slotted deck, stabiliser, open grating
Zhejiang Xihoumen	1650	Twin box	78	Slotted deck, central slot
Great Belt (Storebælt)	1624	Single box	60	Guide vanes, spoiler
Little Belt (Lillebælt)	600	Single box	100	Guide vanes
Tacoma Narrows	854	H-shape	-	Fairings (planned)
Runyang	1490	Single box	75	Centre vertical stabiliser
Tsing Ma	1377	Single box	74	Central slot
Humen	888	Single box	88	-
Hålogaland	1145	Single box	71	-
Cable-stayed				
Russky	1104	Single box	-	-
Sutong	1088	Single box	88	Damper
Stonecutters	1018	Twin box	140	Damper
Normandy	856	Single box	78	-

supported in the wind tunnel with the help of springs with the required stiffness. These springs allow vertical and rotational motion and sometimes horizontal springs are used for lateral movement. These tests are very common for aeroelastic stability studies of long-span bridges.

A full aeroelastic model is constructed which is similar to prototype structure satisfying some similarity laws. It is ensured that the model has the same mass, stiffness and damping distributions of the prototype. It is much simpler to match the mass and stiffness similarities; however, some external devices may be required to match damping similarities. Although these tests are expensive to perform for long-span cable-supported bridges but are very helpful in reducing the uncertainties associated with the unexpected phenomena on the structure in its design life. These full aeroelastic models always include subsequent section model testing as well as analytical studies. Some details about the method have been discussed before in Section 4.3.4.

5.4 Fully-Analytical (Model#1)

The analytical formulation of aeroelastic instability problems started from aeronautical industry especially for the solution of flutter problem of aeroplane wings. Theodorsen [90] gave an analytical solution based on the potential flow theory for the motion-induced aerodynamic forces on a flat plate. Comparison of experimental data with the theoretical solution was made by Theodorsen and Garrick [145].

The phenomenon of flutter is characterised by coupling of oscillatory heave and pitch harmonic motion when the frequencies of these two modes coincide at a high wind speed. The analytical flutter analysis requires simultaneous solution of generalised equations of motion of a 2DOF system as a complex eigenvalue problem. The solution of eigenvalue problem using Theodorsen equation of motion for heave and pitch can be found in [126, 128, 146, 147, 148]. Often the first fundamental heave mode and the first fundamental torsional modes are considered and it is further simplified to a 2D system for which a simplified 2D flutter analysis can be performed. This simplification assumes that only these selected modes participate in the flutter analysis which may lead to the overestimation of the flutter limit.

Fully-analytical models are more direct models and allow a better insight into the force coupling. This approach is independent of the shape of the body but it neglects the effect originating from the simplification to the flat plate. Due to this simplification, this analysis is only valid for a flat plate or an airfoil.
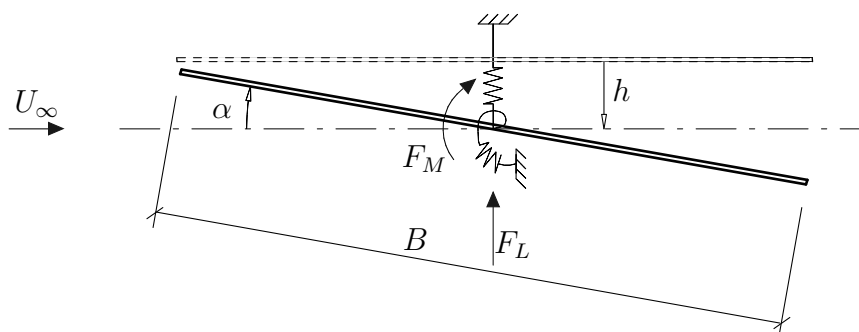
Figure 5.1: Definition of degrees-of-freedom (heave h and pitch α) and aerodynamic forces (lift F_L and moment F_M) for flutter analysis:
(– –) undeformed state,
(——) deformed state.

A simplified 2DOF representation of the bridge deck may be considered. The analysis of the fundamental equations of motion of the structure is accomplished through the structural parameters which include mass, mass moment of inertia, bending frequency, torsional frequency and damping ratios. Figure 5.1 shows an idealisation of a 2DOF system for a flat plate where U_∞ is the wind speed and B is the width of the section. The equations of motion can be written as:

$$m\ddot{h} + 2m\xi_h\omega_h\dot{h} + m\omega_h^2 h = F_L, \tag{5.1a}$$

$$I\ddot{\alpha} + 2I\xi_\alpha\omega_\alpha\dot{\alpha} + I\omega_\alpha^2\alpha = F_M, \tag{5.1b}$$

where m and I are the mass and mass moment of inertia, respectively. ξ_h and ξ_α are the damping ratios, ω_h and ω_α are the natural circular frequencies for the heave and pitch direction, h and α are the vertical displacement and rotation, F_L and F_M are the lift force and moment, respectively.

Comparing the corresponding lift F_L Eqs. (4.22a) and (5.1a) we get,

$$m\ddot{h} + 2m\xi_h\omega_h\dot{h} + m\omega_h^2 h = -\rho b^2 U_\infty \pi \dot{\alpha} - 2\pi\rho CU_\infty^2 b\alpha - 2\pi\rho CU_\infty b\dot{h} - 2\pi\rho CU_\infty b^2 \frac{1}{2}\dot{\alpha}, \quad (5.2)$$

$$m\ddot{h} + \rho b^2 \pi \ddot{h} = -m\omega_h^2 h - 2\pi\rho CU_\infty b\dot{h} - 2m\xi_h\omega_h\dot{h}$$
$$- 2\pi\rho CU_\infty^2 b\alpha - \rho b^2 U_\infty \pi \dot{\alpha} - 2\pi\rho CU_\infty b^2 \frac{1}{2}\dot{\alpha}, \quad (5.3)$$

$$\ddot{h} = \left(\frac{-m\omega_h^2}{m + \rho b^2 \pi}\right) h + \left(\frac{-2\pi\rho CU_\infty - 2m\xi_h\omega_h}{m + \rho b^2 \pi}\right) \dot{h}$$
$$+ \left(\frac{-2\pi\rho CU_\infty^2 b}{m + \rho b^2 \pi}\right) \alpha + \left(\frac{-\rho b^2 U_\infty \pi - 2\pi\rho CU_\infty b^2 \frac{1}{2}}{m + \rho b^2 \pi}\right) \dot{\alpha}. \quad (5.4)$$

Similarly for moment F_M Eqs. (4.22b) and (5.1b),

$$I\ddot{\alpha} + 2I\xi_\alpha\omega_\alpha\dot{\alpha} + I\omega_\alpha^2 \alpha = -\rho b^2 \pi \frac{1}{2}U_\infty b\dot{\alpha} - \rho b^4 \pi \frac{1}{8}\ddot{\alpha} + 2\rho U_\infty b^2 \pi \frac{1}{2}CU_\infty \alpha$$
$$+ 2\rho U_\infty b^2 \pi C\dot{h} + 2\rho \frac{1}{2}U_\infty b^3 \pi C\dot{\alpha}, \quad (5.5)$$

$$I\ddot{\alpha} + \rho b^4 \pi \frac{1}{8}\ddot{\alpha} = 2\rho U_\infty b^2 \frac{1}{2}\pi C\dot{h} + 2\rho U_\infty b^2 \pi \frac{1}{2}CU_\infty \alpha - I\omega_\alpha^2 \alpha$$
$$- \rho b^2 \pi \frac{1}{2}U_\infty b\dot{\alpha} + 2\rho \frac{1}{2}U_\infty b^3 \pi C\dot{\alpha} - 2I\xi_\alpha\omega_\alpha\dot{\alpha}, \quad (5.6)$$

$$\ddot{\alpha} = (0)\, h + \left(\frac{2\rho U_\infty b^2 \frac{1}{2}\pi C}{I + \rho b^4 \pi \frac{1}{8}}\right) \dot{h} + \left(\frac{2\rho U_\infty b^2 \pi \frac{1}{2}CU_\infty - I\omega_\alpha^2}{I + \rho b^4 \pi \frac{1}{8}}\right) \alpha$$
$$+ \left(\frac{-\rho b^2 \pi \frac{1}{2}U_\infty b + 2\rho \frac{1}{2}U_\infty b^3 \pi C - 2I\xi_\alpha\omega_\alpha}{I + \rho b^4 \pi \frac{1}{8}}\right) \dot{\alpha}. \quad (5.7)$$

For this, the resulting equations takes the form,

$$\ddot{h} = a_{21}h + a_{22}\dot{h} + a_{23}\alpha + a_{24}\dot{\alpha}, \quad (5.8a)$$
$$\ddot{\alpha} = a_{41}h + a_{42}\dot{h} + a_{43}\alpha + a_{44}\dot{\alpha}. \quad (5.8b)$$

Comparing the Eq. (5.4) with Eq. (5.8a) and Eq. (5.7) with Eq. (5.8b) we get,

$$a_{21} = \frac{-m\omega_h^2}{m + \rho b^2 \pi}, \qquad\qquad a_{41} = 0, \quad (5.9a)$$

$$a_{22} = \frac{-2\pi\rho CU_\infty - 2m\xi_h\omega_h}{m + \rho b^2 \pi}, \qquad a_{42} = \frac{2\rho U_\infty b^2 \frac{1}{2}\pi C}{I + \rho b^4 \pi \frac{1}{8}}, \quad (5.9b)$$

$$a_{23} = \frac{-2\pi\rho CU_\infty^2 b}{m + \rho b^2 \pi}, \qquad\qquad a_{43} = \frac{2\rho U_\infty b^2 \pi \frac{1}{2}CU_\infty - I\omega_\alpha^2}{I + \rho b^4 \pi \frac{1}{8}}, \quad (5.9c)$$

$$a_{24} = \frac{-\rho b^2 U_\infty \pi - 2\pi\rho CU_\infty b^2 \frac{1}{2}}{m + \rho b^2 \pi}, \quad a_{44} = \frac{-\rho b^2 \pi \frac{1}{2}U_\infty b + 2\rho \frac{1}{2}U_\infty b^3 \pi C - 2I\xi_\alpha\omega_\alpha}{I + \rho b^4 \pi \frac{1}{8}}. \quad (5.9d)$$

The system of differential equations can be written in the state space form as follows,

$$
\begin{bmatrix} \dot{h} \\ \ddot{h} \\ \dot{\alpha} \\ \ddot{\alpha} \end{bmatrix} = \begin{bmatrix} 0 & 1 & 0 & 0 \\ a_{21} & a_{22} & a_{23} & a_{24} \\ 0 & 0 & 0 & 1 \\ a_{41} & a_{42} & a_{43} & a_{44} \end{bmatrix} \begin{bmatrix} h \\ \dot{h} \\ \alpha \\ \dot{\alpha} \end{bmatrix}.
\tag{5.10}
$$

This is of the form

$$
\dot{X} = \mathbf{A}X,
\tag{5.11}
$$

and assuming the response X is of the form

$$
X = \boldsymbol{R}e^{\lambda t},
\tag{5.12}
$$

where $\boldsymbol{R}$ is real. This simplifies to eigenvalue problem as follows:

$$
[\mathbf{A} - \lambda \boldsymbol{I}]\,\boldsymbol{R}e^{\lambda t} = 0.
\tag{5.13}
$$

The solution for $h(t)$ and $\alpha(t)$ is of an exponential form. The four complex eigenvalues λ_n of matrix $\mathbf{A}$ are in the form of two complex conjugate pairs. The real a_n and imaginary b_n parts of the eigenvalues are associated to modal frequencies ω_n and modal damping ratios ξ_n as:

$$
\lambda_n = a_n \pm \iota b_n, \qquad n = 1, \dots, 4
\tag{5.14}
$$

$$
\omega_n = b_n,
\tag{5.15}
$$

$$
\xi_n = \frac{-a_n}{\sqrt{a_n^2 + b_n^2}}.
\tag{5.16}
$$

The nature of the eigenvalues of the matrix $\mathbf{A}$ characterise the response of the system as follows:

- positive real part: increasing response,

- negative real part: decaying response,

- imaginary part: oscillating response.

The main idea is to represent the aeroelastic instability as an eigenvalue problem. The response of the system at the flutter boundary is assumed sinusoidal with a constant amplitude. The system is solved successively for increasing wind speed U_∞ and will become unstable when at least one eigenvalue has a positive real part with a positive imaginary part. The corresponding wind speed will be the flutter limit U_{cr}. When the imaginary part goes towards zero, the oscillatory part vanishes and the phenomenon of static divergence is observed which is characterised by a pure real eigenvalue. In this situation, there will be pure heave or pitch motion which can be interpreted as the loss of stiffness. The procedure to compute flutter limit by performing eigenvalue analysis is explained in Figure 5.2.

5.5   Empirical Approach (Model#2)

The theory of thin airfoils helps to explain the aeroelastic phenomena of torsional divergence. The wind velocity U_d, called the divergence velocity, corresponds to the occurrence of a static stability problem, as even the smallest rotation of the airfoil
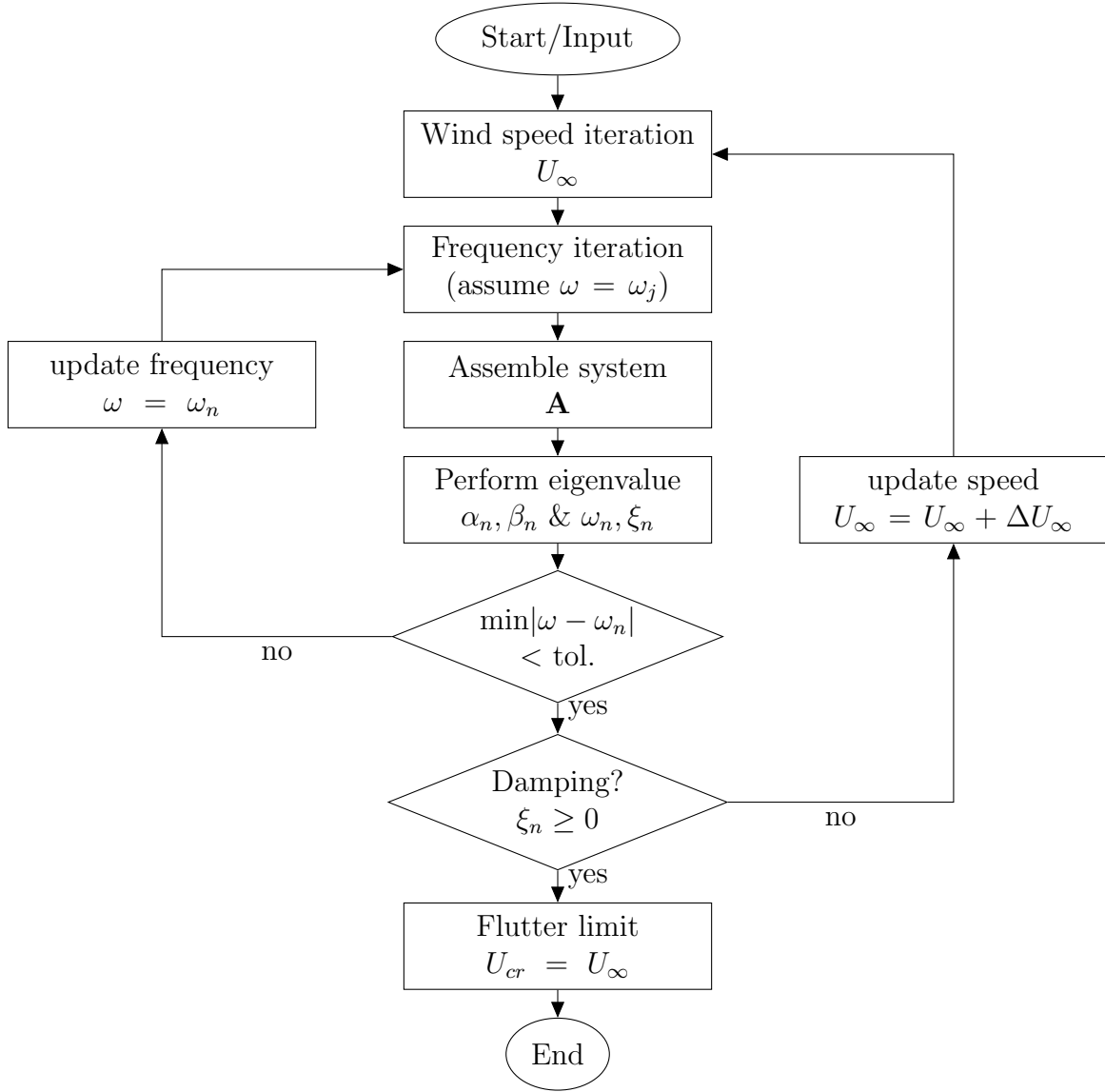
Figure 5.2: Flow chart to calculate flutter limit from fully-analytical eigenvalue analysis.

from the neutral position will imply displacements without limits. The divergence wind speed U_d can be calculated by using aerodynamic moment coefficient C_M of the deck for varying wind angles of attack θ as follows:

$$M_0 + \frac{1}{2}\rho U_\infty^2 B^2 C_M(\theta) - K_\alpha = 0, \tag{5.17}$$

where K_α is the torsional stiffness of the deck. It can be seen that stability is always met when the slope of moment coefficient at zero wind attack angle $C_M'(0) \leq 0$ [5]. However, if $C_M'(0) > 0$ then the stability limit with respect to static divergence is found as follows:

$$U_d = \sqrt{\frac{2K_\alpha}{\rho B^2 C_M'(0)}} = B\omega_\alpha \sqrt{\frac{2I}{\rho B^4 C_M'(0)}}. \tag{5.18}$$

The solution to obtain critical wind speed for static divergence in the modal coordinates

[45] is given by:

$$U_d = B\omega_\alpha \sqrt{\frac{2I}{\rho B^4 C_M'(0)} \frac{\int_L \phi_\alpha^2 dx}{\int_{L_{exp}} \phi_\alpha^2 dx}}, \tag{5.19}$$

where ϕ_α is the bending mode shape. It should be noted that the divergence velocity of above equation is only valid when the aerodynamic moment coefficient is linear for the angles of attack of interest.

It is often the case that the flutter limit U_{cr} is lower than the divergence wind speed U_d for cable-supported bridges which make static instability of less interest than flutter [5]. Generally, torsional frequency f_α is larger than vertical frequency f_h in case of cable-supported bridges with two cable planes; however, f_α may decrease with increasing wind speed due to the equivalent reduction of the torsional stiffness under the action of the aerostatic pressure. Frandsen [149] showed that this could lead to flutter limit for the airfoil as:

$$U_{cr} = U_d \sqrt{1 - \left(\frac{\omega_h}{\omega_\alpha}\right)^2}. \tag{5.20}$$

It is clear from the above equation that the flutter limit is smaller than the divergence velocity U_d. It also appears that flutter may occur at a lower wind velocity if the vertical and the torsional frequencies are close. Therefore, it is generally desired to keep frequency ratio f_α / f_h more than two in larger cable supported-bridges [5].

Bleich [96] introduced an empirical formula using Theodorsen's flutter theory for a flat plate to calculate critical flutter limit. Selberg [150] also developed a closed-form solution by introducing the shape ratio to apply for various types of bridge cross sections. Later Klöppel and Thiele [151] gave a formula which is suitable for hand calculations by making use of empirical diagrams [47]. The above expression (cf. Eq. (5.20)) agrees reasonably well with semi-empirical expression by Selberg [150] who gave the following expression which is based on theoretical thin airfoil for the flutter limit:

$$U_{cr} = 0.52 U_d \sqrt{\left[1 - \frac{1}{\gamma_\omega^2}\right] B \sqrt{\frac{m}{I}}}, \tag{5.21a}$$

$$U_{cr} = 3.7 B f_\alpha \sqrt{\frac{m\sqrt{I/m}}{\rho B^3} \left[1 - (\frac{\omega_h}{\omega_\alpha})^2\right]}, \tag{5.21b}$$

$$U_{cr} = 0.44 B \sqrt{[\omega_\alpha^2 - \omega_h^2] \frac{\sqrt{\tilde{\nu}}}{\tilde{\mu}}}, \tag{5.21c}$$

$$U_{cr} = 0.6 B\omega_\alpha \sqrt{\left[1 - \left(\frac{\omega_h}{\omega_\alpha}\right)^2\right] \frac{\sqrt{mI}}{\rho B^3}}, \tag{5.21d}$$

$$U_{cr} = 2.623 f_\alpha B \sqrt{\left[1 - \frac{1}{\gamma_\omega^2}\right] r_\alpha \mu_\alpha}, \tag{5.21e}$$

where

$$\tilde{\nu} = 8(r/B)^2, \qquad \tilde{\mu} = \pi \rho B^2 / 4m, \qquad r = \sqrt{I/m}, \tag{5.22a}$$

$$\mu_\alpha = \frac{2m}{\rho B^2}, \qquad r_\alpha = \sqrt{\frac{I}{mB^2}}, \qquad \gamma_\omega = \frac{\omega_\alpha}{\omega_h}. \tag{5.22b}$$

Selberg's expression is found in different forms such as Eq. (5.21a) in [5], Eq. (5.21b) in [91], Eq. (5.21c) in [2], Eq. (5.21d) in [45], and Eq. (5.21e) in [38]. Selberg's expression may be used to provide a first estimate of the flutter stability limit for a flat plate where frequency ratio $f_\alpha/f_h > 1.5$ [45].

Rocard reported very similar empirical formula [38, 149] as follows:

$$U_{cr} = 6.282 f_\alpha B \sqrt{\left[1 - \frac{1}{\gamma_\omega^2}\right] \frac{r_\alpha^2 \mu_\alpha}{1 + 8r_\alpha^2}}. \tag{5.23}$$

Matsumoto et al. [152] also gave a simplified formula to calculate flutter limit for a flat plate using relationships between mass m and mass moment of inertia I as $I = mb^2/3$ which is very similar to Selberg's form as follows:

$$U_{cr} = 3.81 B f_\alpha \sqrt{\frac{\sqrt{Im}}{\rho B^3} \left[1 - (\frac{\omega_h}{\omega_\alpha})^2\right]}. \tag{5.24}$$

Another simplified formula which was well known by its simplicity and convenience was given by Put [153] to calculate critical flutter limit as follows:

$$U_{cr} = \eta \left[1 + \left(\frac{\omega_\alpha}{\omega_h} - 0.5\right) \sqrt{\frac{r}{b} 0.72 \mu_\beta}\right] \omega_h b, \tag{5.25}$$

where $\mu_\beta = m/(\pi \rho (B/2)^2)$ and η is an empirical form factor giving the difference of the critical wind speed of a certain profile (1 for flat plate). The above equation was further simplified [154] as follows:

$$U_{cr} = \left[2.5 \sqrt{\frac{r}{b} \mu_\beta}\right] 2b f_\alpha. \tag{5.26}$$

A wide streamlined deck of a bridge shows usually critical velocity close to theoretical flat plate flutter limit whereas bluff girders, trusses and deep deck sections show a larger difference between the theoretical flutter limit and the measured in the wind tunnel. Usually, this difference is represented with the help of a ratio of measured flutter limit to flat plate prediction β_f which is about 90% for the streamlined box girders and can be up to 40% for the bluff box sections [5]. Semi-empirical approaches are suitable for hand calculations and are simple to use; however, they do not provide insight of the force coupling and can only be used for 2D cases and flat plates. It would appear to be unwise to rely on a prediction based on an empirical formula alone, therefore, more detailed analyses are required for important structures and at the final design stage.

5.6 Derivative-based Analysis (Semi-analytical Approach)

5.6.1 Solution in Frequency Domain

The flutter analysis is traditionally conducted in the frequency domain as the aerodynamic derivatives are functions of reduced speed which requires an iterative solution to determine flutter limit. There are two main analytical approaches for the solution of flutter problem: the Complex Eigenvalue Analysis (CEVA) [41] and the Step-by-step Analysis (SBSA) [155]. The CEVA has been used for a long time for flutter problems. In the CEVA main challenge is related to the investigation of the system frequency and damping ratio relationship with wind speed whereas the SBSA is

very useful for such limitations and also it describes the role of flutter derivatives on critical condition and on flutter stabilisation [156].

The motion-induced aerodynamic forces depend on the response frequency of the bridge, which is determined in the analysis of complex nonlinear eigenvalue problem and then the critical flutter limit is calculated [157, 158]. The iterative solution is necessary because the aerodynamic derivatives depend on the reduced speed v_r which is based on oscillation frequency ω which needs to be known [45]. The common approach of solving 2DOF coupled flutter equations is through CEVA where the flutter characteristics are solved based on an eigenvalue problem. Xu [28] applied this approach and computed flutter limit of Stonecutters bridge. Dyrbye and Hansen [48] provides modal form solution where real and imaginary parts are given with Mode Shape Similarity Factor (MSSF). Dung et al. [159] traces the system complex mode with the increasing wind speed which helps to describe the dynamic behaviour before flutter.

Matsumoto et al. [160] developed the SBSA and reported flutter characteristics including frequency, damping, amplitude ratio and phase difference characteristics and compared with the CEVA which showed reasonable agreement [155, 161]. Discrepancies were observed in the results obtained by the CEVA and the SBSA at higher reduced speeds than the flutter limit therefore both damping and flutter frequency must simultaneously converge in the iteration [62, 162]. Later modifications showed perfect agreement [62, 162]. In other studies [163, 164, 165, 166, 167, 168] the complex branch switch characteristics of coupled flutter instability were focused. This method was also applied to highlighting the characteristics of different bluff sections [169, 170]. Ge and Xiang [32], Yang et al. [171, 172, 173] also proposed, based on the concept of the SBSA analysis, a 2D coupled flutter analysis method for three-degree-of-freedom (3DOF) to investigate the mechanism of flutter with the focus on the aerodynamic damping, frequency and flutter modality. Chen [174] presents closed-form formulations for estimating the modal frequencies, damping ratios, and coupled motions of a 2D aeroelastic bridge with variation in the wind speed.

The two branches in coupled flutter are known as heaving branch (HB) and torsional branch (TB). In the SBSA, the flutter frequency in the HB and the TB are converged by iterative calculation. Matsumoto et al. [152, 162, 164, 167, 169, 170] investigated the behaviour of frequency and damping ratio of two coupled modes as well as several higher modes and showed the frequency-velocity, damping-velocity, amplitude ratio-velocity and phase difference-velocity characteristics. Based on several fundamental sections and flow-structure interaction, they also classified flutter generation mechanism into detailed branches [156]:

- Low-speed torsional flutter,

- High-speed torsional flutter,

- Heaving-branch coupled flutter,

- Torsional-branch coupled flutter and

- Heaving-torsional coupled flutter.

5.6.2 Solution in Time Domain

The frequency-domain approach for determining the flutter limit is limited to consider a linear system under the action of the stationary wind without taking into account aerodynamic or structural non-linearities. Therefore, a major part of recent research focuses on the time domain analysis, where it is possible to include these nonlinearities. One of the earliest implementation was by Beliveau et al. [175] utilising the indicial function for time and frequency domain. Initially the buffeting analysis was usually conducted in time domain using the quasi-steady approach [176, 177, 178, 179], with state-space model for impulse functions [180]. Boonyapinyo et al. [181], Chen et al. [182, 183, 184], Chen and Kareem [185], Thang et al. [186], Øiseth et al. [187, 188], Guo and Ge [189] present time-domain buffeting and flutter analysis based on the state-space using rational approximation of the impulse functions, for full and reduced model in modal coordinates.

5.6.3 Simplified Approach

Some attempts have been made to simplify flutter analysis by developing relationship and mutual dependence of aerodynamic derivatives [161] such as

$$
\begin{aligned}
H_1^* &= kH_3^*, & H_4^* &= -kH_2^*, \\
A_1^* &= kA_3^*, & A_4^* &= -kA_2^*.
\end{aligned}
\tag{5.27}
$$

Furthermore, there is another dependence between two pairs $(A_2^* - A_3^*)$ and $(H_1^* - H_4^*)$ because of the equivalent Wagner function. This concludes that there are only two independent aerodynamic derivatives among the eight. Scanlan et al. [190] analytically described the interrelations and the dependences among the aerodynamic derivatives of an airfoil and investigated experimentally obtained aerodynamic derivatives of three different bridge deck sections. It was found that this relation clearly does not hold for bluff sections. However, Xu [191, 192] investigated the relationship between aerodynamic derivatives of slender bridge and based on his previously proposed semi-analytical aerodynamic derivatives of flexible structure, showed that certain relations exist between these aerodynamic derivatives as follows:

$$
\begin{aligned}
H_1^* &= -4A_1^*, & H_2^* &= -4A_2^* - \frac{\pi}{k}, \\
H_3^* &= -4A_3^* + \frac{\pi}{16}, & H_4^* &= -4A_4^* + \frac{\pi}{2}, \\
H_1^* &= kH_3^* - \frac{\pi G}{2}, & H_2^* &= -\frac{H_4^*}{k} - \frac{\pi F}{2k}, \\
A_1^* &= kA_3^* - \frac{\pi k}{64} + \frac{\pi G}{8}, & A_4^* &= -kA_2^* - \frac{\pi}{8}\left(1 - F\right).
\end{aligned}
\tag{5.28}
$$

It also shows that semi-analytical aerodynamic derivatives are applicable to bridges with a streamlined cross-section. Additionally, Tubino [193] provides inter-relations among aerodynamic derivatives using generalised quasi-static theory. Al-Assaf [194] developed an alternative analytical approach to supplement the wind tunnel testing to estimate flutter limit of a bluff bridge section by synthesising the aerodynamic derivatives based on previous studies of a similar deck configuration to find critical flutter limit. Lute et al. [195] also used an aerodynamic derivative database to predict the flutter derivatives for any deck size for estimation of flutter limit. Mannini [196]

investigated flutter instability by analysing a large number of dynamic and aerodynamic data and proposed a simplified expressions which use only three or even two aerodynamic derivatives for the calculation of flutter limit [38, 197, 198]. Lee et al. [199] gave another simplified formula by applying the quasi-steady approach and using approximations in the aerodynamic derivatives, for calculating 2D flutter limit. Øiseth and Sigbjörnsson [200] also presented a simplified analytical formulation, including closed-form algebraic expressions, for the prediction of the critical flutter limit. Øiseth et al. [201] suggested a simplified approach to compute flutter limit by using a new set of modified quasi-steady coefficients. Banerjee [202] derived expressions for generalised mass, generalised stiffness and generalised aerodynamic force terms in compact explicit form. Vairo [203] proposed a simplified approach for the dynamic problem by considering a simple mechanical system with equivalent stiffness properties for capturing the main wind-bridge interaction mechanisms. All these simplifications generally provide a reasonable prediction for flat plate flutter but are not suitable for bluff bridge cross sections.

5.6.4   SDOF Instability

5.6.4.1   Pure Vertical Motion

The pure vertical bending of the bridge deck is described here by considering the aerodynamic lift of the bridge deck in the Scanlan form. The governing equation of motion for the SDOF can be derived by comparing the corresponding lift Eqs. (5.1a) and (4.29a) as:

$$m\ddot{h} + 2m\xi_h\omega_h\dot{h} + m\omega_h^2 h = \frac{1}{2}\rho U_\infty^2 B \left[KH_1\frac{\dot{h}}{U_\infty} + KH_2\frac{B\dot{\alpha}}{U_\infty} + K^2H_3\alpha + K^2H_4\frac{h}{B} \right]. \quad (5.29)$$

Since pure vertical motion ($\dot{\alpha} = \alpha = 0$) is considered, therefore

$$m\ddot{h} + 2m\xi_h\omega_h\dot{h} + m\omega_h^2 h = \frac{1}{2}\rho U_\infty^2 B \left[KH_1\frac{\dot{h}}{U_\infty} + K^2H_4\frac{h}{B} \right]. \quad (5.30)$$

Simplifying the above equation leads to the following form:

$$m\ddot{h} + 2m\xi_h\omega_h\dot{h} - \frac{1}{2}\rho U_\infty^2 BKH_1^*\frac{\dot{h}}{U_\infty} + m\omega_h^2 h - \frac{1}{2}\rho U_\infty^2 BK^2H_4^*\frac{h}{B} = 0. \quad (5.31)$$

As a result,

$$m\ddot{h} + \left(2m\xi_h\omega_h - \frac{1}{2}\rho U_\infty^2 BKH_1^*\frac{1}{U_\infty} \right)\dot{h} + \left(m\omega_h^2 - \frac{1}{2}\rho U_\infty^2 BK^2H_4^*\frac{1}{B} \right)h = 0. \quad (5.32)$$

Thus the total stiffness of the system is:

$$k_{sys} = m\omega_h^2 - \frac{1}{2}\rho U_\infty^2 BK^2H_4^*\frac{1}{B} = m\omega_h^2 - \frac{1}{2}\rho B^4\omega^2 H_4^*\frac{1}{B}. \quad (5.33)$$

From the above equation, the frequency of oscillation of the system can be written as:

$$\omega = \sqrt{\frac{k_{sys}}{m}} = \sqrt{\frac{m\omega_h^2}{m} - \frac{1}{2m}\rho B^3 \omega^2 H_4^*}, \tag{5.34}$$

$$\omega = \omega_h\sqrt{1 - \frac{1}{2m}\rho B^4 \left(\frac{\omega}{\omega_h}\right)^2 H_4^*} \approx \omega_h\sqrt{1 - \frac{1}{2m}\rho B^3 H_4^*}. \tag{5.35}$$

In the similar way the total damping of the system can be expressed as:

$$c_{sys} = 2m\xi_h\omega_h - \frac{1}{2}\rho U_\infty^2 BK H_1^* \frac{1}{U_\infty}. \tag{5.36}$$

This shows that if the derivative H_1^* is negative, the total damping will be positive and the system will remain stable. When H_1^* becomes positive, the total damping will become negative and this will cause the system to oscillate with divergent amplitudes leading to instability. Therefore at critical condition the above equation will take the form:

$$2m\xi_h\omega_h = \frac{1}{2}\rho U_\infty^2 BK H_1^* \frac{1}{U_\infty}. \tag{5.37}$$

Further simplifying, we can write:

$$H_1^* = \frac{4m\xi_h\omega_h}{\rho U_\infty BK}. \tag{5.38}$$

Since $K = B\omega/U_\infty$, therefore, the instability condition of the SDOF vertical bending can be expressed as:

$$H_1^* = \frac{4m\xi_h}{\rho B^2}\frac{\omega_h}{\omega} \approx \frac{4m\xi_h}{\rho B^2}. \tag{5.39}$$

5.6.4.2 Pure Torsional Motion

The streamline cross sections are prone to the classical flutter instability; however, there is a wide range of bridge deck sections which are not streamlined. It can be possible for bluff cross sections that the vertical and torsional motion remain uncoupled and only torsional flutter occurs. A bluff section shows significantly different behaviour to a streamline section. The response of such a section may be pure torsional motion which leads to SDOF torsional flutter. H-shape sections and rectangular sections with smaller aspect ratios (B/D) are usually more prone to the torsional flutter instability. The streamline cross sections have a negative trend of aerodynamic derivatives H_1^* and A_2^* whereas for bluff cross sections the aerodynamic derivative A_2^* may change sigh from negative to positive even at relatively low v_r range. This gives rise to SDOF torsional instability.

The pure torsional motion of the bridge deck is considered here for the SDOF torsional flutter analysis. Considering the aerodynamic moment of the bridge deck, the governing equation of motion for the SDOF can be derived by comparing the corresponding moment Eqs. (5.1b) and (4.29b) as:

$$I\ddot{\alpha} + 2I\xi_\alpha\omega_\alpha\dot{\alpha} + I\omega_\alpha^2\alpha = \frac{1}{2}\rho U_\infty^2 B^2 \left[KA_1^*\frac{\dot{h}}{U_\infty} + KA_2^*\frac{B\dot{\alpha}}{U_\infty} + K^2 A_3^*\alpha + K^2 A_4^*\frac{h}{B}\right]. \tag{5.40}$$

Since pure torsional motion ($\dot{h} = h = 0$) is considered, therefore

$$I\ddot{\alpha} + 2I\xi_\alpha\omega_\alpha\dot{\alpha} + I\omega_\alpha^2\alpha = \frac{1}{2}\rho U_\infty^2 B^2 \left[KA_2^* \frac{B\dot{\alpha}}{U_\infty} + K^2 A_3^* \alpha \right]. \tag{5.41}$$

Simplifying the above equation leads to the following form:

$$I\ddot{\alpha} + 2I\xi_\alpha\omega_\alpha\dot{\alpha} - \frac{1}{2}\rho U_\infty^2 B^2 KA_2^* \frac{B\dot{\alpha}}{U_\infty} + I\omega_\alpha^2\alpha - \frac{1}{2}\rho U_\infty^2 B^2 K^2 A_3^* \alpha = 0. \tag{5.42}$$

As a result,

$$I\ddot{\alpha} + \left(2I\xi_\alpha\omega_\alpha - \frac{1}{2}\rho U_\infty^2 B^2 KA_2^* \frac{B}{U_\infty} \right)\dot{\alpha} + \left(I\omega_\alpha^2 - \frac{1}{2}\rho U_\infty^2 B^2 K^2 A_3^* \right)\alpha = 0. \tag{5.43}$$

Thus the total stiffness of the system is:

$$k_{sys} = I\omega_\alpha^2 - \frac{1}{2}\rho U_\infty^2 B^2 K^2 A_3^* = I\omega_\alpha^2 - \frac{1}{2}\rho B^4 \omega^2 A_3^*. \tag{5.44}$$

From the above equation, the frequency of oscillation of the system can be written as:

$$\omega = \sqrt{\frac{k_{sys}}{I}} = \sqrt{\frac{I\omega_\alpha^2}{I} - \frac{1}{2I}\rho B^4 \omega^2 A_3^*}, \tag{5.45}$$

$$\omega = \omega_\alpha \sqrt{1 - \frac{1}{2I}\rho B^4 \left(\frac{\omega}{\omega_\alpha} \right)^2 A_3^*} \approx \omega_\alpha \sqrt{1 - \frac{1}{2I}\rho B^4 A_3^*}. \tag{5.46}$$

In the similar way the total damping of the system can be expressed as:

$$c_{sys} = 2I\xi_\alpha\omega_\alpha - \frac{1}{2}\rho U_\infty^2 B^2 KA_2^* \frac{B}{U_\infty}. \tag{5.47}$$

This shows that if the aerodynamic derivative A_2^* is negative, the total damping will be positive and the system will remain stable. When A_2^* becomes positive, the total damping will become negative and this will cause the system to oscillate with divergent amplitudes leading to instability. Therefore at critical condition the above equation will take the form:

$$2I\xi_\alpha\omega_\alpha = \frac{1}{2}\rho U_\infty^2 B^2 KA_2^* \frac{B}{U_\infty}. \tag{5.48}$$

Further simplifying, we can write:

$$A_2^* = \frac{4I\xi_\alpha\omega_\alpha}{\rho U_\infty B^3 K}. \tag{5.49}$$

Since $K = B\omega/U_\infty$, therefore, the instability condition of the SDOF torsional flutter can be expressed as:

$$A_2^* = \frac{4I\xi_\alpha}{\rho B^4} \frac{\omega_\alpha}{\omega} \approx \frac{4I\xi_\alpha}{\rho B^4}. \tag{5.50}$$

Chen and Kareem [204] observed that the critical wind speed is reduced by the coupling of heave and pitch motion even for torsional flutter. However, SDOF and 2DOF approaches show usually close results [196].

The influence of additional structural damping on the aeroelastic instability is low. Figure 5.3 shows the typical behaviour of aerodynamic derivative A_2^* for different cross sections. An increase in the structural damping (ΔD^*) does not improve significantly the behaviour against aeroelastic instability as compared to other phenomena such as VIV and buffeting response. However, the choice of the cross section is much more important than increasing only the structural damping.
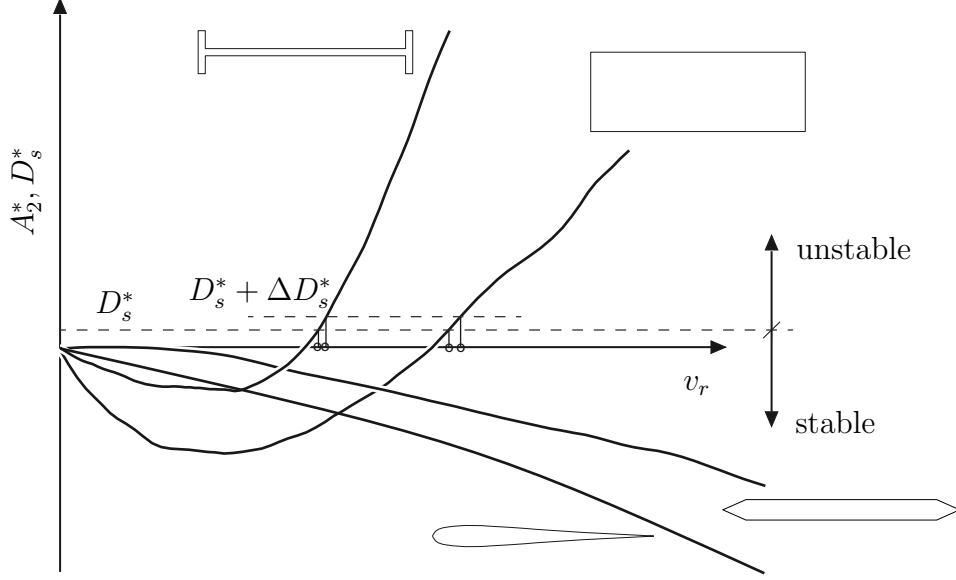
Figure 5.3: Schematic of aerodynamic derivative A_2^* related to torsional instability for different section configurations (D^*: structural damping).

In complex form, the aeroelastic instability in torsional motion is shown in Appendix B.1.

5.6.5 Derivative-based Eigenvalue Analysis (Model#3)

The formulation to the eigenvalue problem in case of Scanlan representation is similar as described in Section 5.4. Comparing the corresponding lift F_L Eqs. (5.1a) and (4.29a) we get,

$$m\ddot{h} + 2m\xi_h\omega_h\dot{h} + m\omega_h^2 h = \frac{1}{2}\rho U_\infty^2 B \left[KH_1\frac{\dot{h}}{U_\infty} + KH_2\frac{B\dot{\alpha}}{U_\infty} + K^2H_3\alpha + K^2H_4\frac{h}{B} \right], \qquad (5.51)$$

$$m\ddot{h} = \frac{1}{2}\rho U_\infty^2 BK^2H_4\frac{h}{B} - m\omega_h^2 h + \frac{1}{2}\rho U_\infty^2 BKH_1\frac{\dot{h}}{U_\infty}$$
$$- 2m\xi_h\omega_h\dot{h} + \frac{1}{2}\rho U_\infty^2 BK^2H_3\alpha + \frac{1}{2}\rho U_\infty^2 BKH_2\frac{B\dot{\alpha}}{U_\infty}, \qquad (5.52)$$

$$\ddot{h} = \left(\frac{1}{2m}\rho U_\infty^2 BK^2\frac{H_4}{B} - \frac{m}{m}\omega_h^2 \right) + \left(\frac{1}{2m}\rho U_\infty^2 BK\frac{H_1}{U_\infty} - \frac{2m\xi_h\omega_h\dot{h}}{m} \right)\dot{h}$$
$$+ \left(\frac{1}{2m}\rho U_\infty^2 BK^2H_3 \right)\alpha + \left(\frac{1}{2m}\rho U_\infty^2 BKH_2\frac{B}{U_\infty} \right)\dot{\alpha}. \qquad (5.53)$$

Similarly, for moment F_M by comparing Eqs. (5.1b) and (4.29b),

$$I\ddot{\alpha} + 2I\xi_\alpha\omega_\alpha\dot{\alpha} + I\omega_\alpha^2\alpha = \frac{1}{2}\rho U_\infty^2 B^2 \left[KA_1\frac{\dot{h}}{U_\infty} + KA_2\frac{B\dot{\alpha}}{U_\infty} + K^2A_3\alpha + K^2A_4\frac{h}{B} \right], \tag{5.54}$$

$$I\ddot{\alpha} = \frac{1}{2}\rho U_\infty^2 B^2 K^2 A_4 \frac{h}{B} + \frac{1}{2}\rho U_\infty^2 B^2 K A_1 \frac{\dot{h}}{U_\infty} + \frac{1}{2}\rho U_\infty^2 B^2 K^2 A_3\alpha$$
$$- I\omega_\alpha^2\alpha + \frac{1}{2}\rho U_\infty^2 B^2 K A_2 \frac{B\dot{\alpha}}{U_\infty} - 2I\xi_\alpha\omega_\alpha\dot{\alpha}, \tag{5.55}$$

$$\ddot{\alpha} = \left(\frac{1}{2I}\rho U_\infty^2 B^2 K^2 \frac{A_4}{B} \right) h + \left(\frac{1}{2}\rho U_\infty^2 B^2 K \frac{A_1}{U_\infty} \right) \dot{h}$$
$$+ \left(\frac{1}{2I}\rho U_\infty^2 B^2 K^2 A_3 - \omega_\alpha^2 \right) \alpha + \left(\frac{1}{2I}\rho U_\infty^2 B^2 K A_2 \frac{B}{U_\infty} - \frac{2I}{I}\xi_\alpha\omega_\alpha \right) \dot{\alpha}. \tag{5.56}$$

Comparing the Eq. (5.53) with Eq. (5.8a) and Eq. (5.56) with Eq. (5.8b) we get,

$$a_{21} = \frac{1}{2m}\rho U_\infty^2 B K^2 \frac{H_4}{B} - \frac{m}{m}\omega_h^2, \qquad a_{41} = \frac{1}{2I}\rho U_\infty^2 B^2 K^2 \frac{A_4}{B}, \tag{5.57a}$$

$$a_{22} = \frac{1}{2m}\rho U_\infty^2 B K \frac{H_1}{U_\infty} - \frac{2m\xi_h\omega_h\dot{h}}{m}, \qquad a_{42} = \frac{1}{2}\rho U_\infty^2 B^2 K \frac{A_1}{U_\infty}, \tag{5.57b}$$

$$a_{23} = \frac{1}{2m}\rho U_\infty^2 B K^2 H_3, \qquad a_{43} = \frac{1}{2I}\rho U_\infty^2 B^2 K^2 A_3 - \frac{I}{I}\omega_\alpha^2, \tag{5.57c}$$

$$a_{24} = \frac{1}{2m}\rho U_\infty^2 B K H_2 \frac{B}{U_\infty}, \qquad a_{44} = \frac{1}{2I}\rho U_\infty^2 B^2 K A_2 \frac{B}{U_\infty} - \frac{2I}{I}\xi_\alpha\omega_\alpha. \tag{5.57d}$$

The procedure to compute flutter limit by this approach is explained in Figure 5.4. Numerical forced vibration simulations or wind tunnel tests can be used to determine motion-induced aerodynamic forces. A flow solver based on the VPM has been used here to perform forced vibration simulations on the cross sections (cf. Section 4.3.3). The forced vibration simulations on a section are separately performed in the sinusoidal heave and pitch motion over a range of reduced speeds v_r. The reduced speed can be controlled by changing the period of heave and pitch forcing motion.

$$v_r = \frac{U_\infty}{Bf_o} = \frac{U_\infty}{B}T_o, \tag{5.58}$$

where f_o and T_o are the frequency and period of the forcing motion, respectively. The resulting lift force and moment time histories are then used to compute the aerodynamic derivatives. Aerodynamic derivatives can be computed following the procedure explained in Section 4.4. The response of oscillating section just at the flutter boundary is assumed sinusoidal with constant amplitude. Eigenvalue solution is then performed to compute the flutter limit.

5.6.5.1 Approach to Consider Mode Shapes

It is assumed until this point that the mode shapes for both heave and pitch motion are exactly the same; however, in actual situation they can be different. An approach to consider mode shape in flutter analysis is presented in this section. Assuming that the vertical displacement h and the rotation α of a bridge deck are represented by
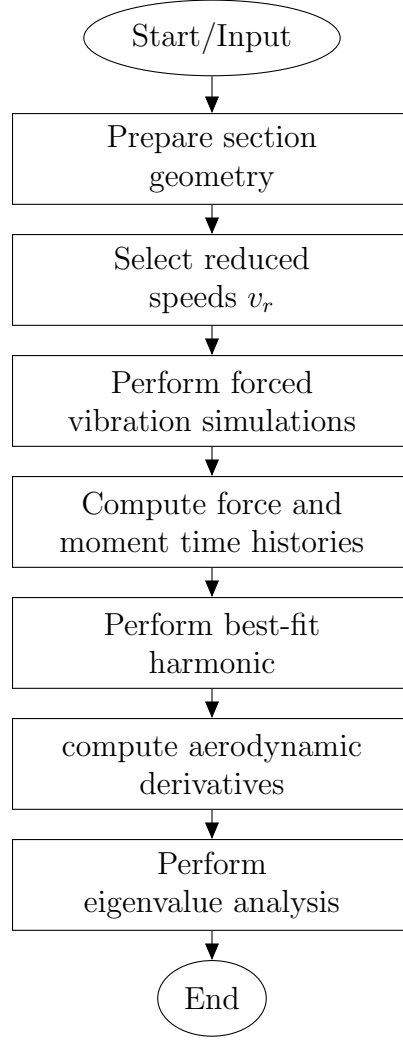
Figure 5.4: Flow chart to calculate flutter limit from derivative-based eigenvalue analysis.

generalised DOF as functions of $\phi(x)$ and $\eta(t)$ as follows:

$$h = \phi_h(x)\,\eta_h(t), \tag{5.59}$$

$$\alpha = \phi_\alpha(x)\,\eta_\alpha(t) \tag{5.60}$$

where $\phi_n(x)$ is the time invariant mode shapes and $\eta_n(t)$ is the modal coordinate. The solution of the equation of motion is assumed harmonic of the form:

$$\eta_n(t) = G_n(\omega)\,e^{(a+\iota b)t} \tag{5.61}$$

where G_n is the Fourier amplitudes of mode n. Inserting the harmonic functions h and α in Eqs. (5.1a), (4.29a), (5.1b) and (4.29b) and by comparing the corresponding equations for lift and moment gives the following two equations:

$$\left[m\left(-\omega + 2\xi_h\omega_h\iota\omega + \omega_h^2\right) - \frac{1}{2}\rho U_\infty^2 B\left(\frac{K}{U_\infty^2}H_1^*\iota\omega + \frac{K^2}{B}H_4^*\right)C_{hh}\right]G_h(\omega)$$

$$- \left[\frac{1}{2}\rho U_\infty^2 BC_{h\alpha}\left(\frac{KB}{U_\infty^2}H_2^*\iota\omega + K^2 H_3^*\right)\right]G_\alpha(\omega) = 0, \tag{5.62}$$

$$\left[I \left(-\omega + 2\xi_\alpha \omega_\alpha \iota\omega + \omega_\alpha^2 \right) - \frac{1}{2}\rho U_\infty^2 B^2 \left(\frac{KB}{U_\infty} A_2^* \iota\omega + K^2 A_3^* \right) C_{\alpha\alpha} \right] G_\alpha(\omega)$$

$$- \left[\frac{1}{2}\rho U_\infty^2 B^2 C_{\alpha h} \left(\frac{K}{U_\infty} A_1^* \iota\omega + \frac{K^2}{B} A_4^* \right) \right] G_h(\omega) = 0, \tag{5.63}$$

with

$$C_{ij} = \frac{\int_L \phi_i(x)\,\phi_j(x)\,dx}{\int_L \phi_i^2(x)\,dx}, \tag{5.64}$$

where C_{ij} is the dimensionless coefficient representing shape-wise similarity of the mode shapes i and j. The determinant of these equations can be set equal to zero and written as a function of $X_f = \omega/\omega_h$. Separating the equations in real and imaginary parts generate two characteristic equations as follows:

$$R_4 X_f^4 + R_3 X_f^3 + R_2 X_f^2 + R_1 X_f + R_0 = 0, \tag{5.65a}$$
$$I_3 X_f^3 + I_2 X_f^2 + I_1 X_f + I_0 = 0, \tag{5.65b}$$

where the coefficients R_i, I_j $(i = 0, \ldots, 4, j = 0, \ldots, 3)$ are as follows:

$$
\begin{aligned}
R_4 &= 1 + \frac{1}{2\chi_\alpha}A_3^* + \frac{1}{2\chi_h}H_4^* + \frac{1}{4\chi_\alpha\chi_h}\left(H_1^* A_2^* + H_4^* A_3^* - \psi_{h\alpha}H_3^* A_4^* + \psi_{h\alpha}H_2^* A_1^* \right), \\
R_3 &= \frac{1}{\chi_h}\xi_\alpha\gamma H_1^* + \frac{1}{\chi_\alpha}\xi_h A_2^*, \\
R_2 &= -\gamma^2 - 4\xi_\alpha\xi_h\gamma - 1 - \frac{1}{\chi_\alpha}A_3^* - \frac{1}{2\chi_h}\gamma^2 H_4^*, \\
R_1 &= 0, \\
R_0 &= \gamma^2,
\end{aligned}
\tag{5.66}
$$

$$
\begin{aligned}
I_3 &= \frac{1}{2\chi_\alpha}A_2^* + \frac{1}{2\chi_h}H_1^* + \frac{1}{4\chi_\alpha\chi_h}\left(H_4^* A_1^* + H_2^* A_4^* - \psi_{h\alpha}H_3^* A_1^* + \psi_{h\alpha}H_2^* A_4^* \right), \\
I_2 &= -\frac{1}{\chi_h}\gamma A_2^* - \frac{1}{\chi_\alpha}\xi_h A_3^* - 2\xi_h - 2\xi_\alpha\gamma, \\
I_1 &= -\frac{1}{2\chi_\alpha}A_2^* - \frac{1}{2\chi_h}\gamma^2 H_1^*, \\
I_0 &= 2\xi_\alpha\gamma + 2\xi_h\gamma^2
\end{aligned}
\tag{5.67}
$$

with

$$\gamma_\omega = \frac{\omega_\alpha}{\omega_h}, \tag{5.68}$$

$$\chi_h = \frac{m}{\rho B^2}, \qquad \chi_\alpha = \frac{\rho B^2}{I}, \tag{5.69}$$

$$\psi_{h\alpha} = C_{hh}C_{\alpha\alpha} = \frac{\int_L \phi_h(x)\,\phi_\alpha(x)\,dx}{\int_L \phi_h^2(x)\,dx}\frac{\int_L \phi_h(x)\,\phi_\alpha(x)\,dx}{\int_L \phi_\alpha^2(x)\,dx}. \tag{5.70}$$

where $\psi_{h\alpha}$ is known as Mode Shape Similarity Factor (MSSF). Modes are less likely to couple if the value of the MSSF is close to 0 and are more likely to couple if it is close to 1. This means that an asymmetric vertical bending mode is less likely to couple with a symmetric torsional mode and vice versa. The flutter limit is computed for critical X_f where both the roots of the real and imaginary equation are zero. Since the aerodynamic derivatives are functions of v_r, the solution is commonly found by plotting the roots of real and imaginary equations when with increasing v_r both parts become zero simultaneously.

5.6.5.2   Multimode Approach

The study of flutter phenomena is very much related to the understanding of nature of unsteady aerodynamic forces, mechanism of mode-coupling and methodology of

multi-mode analysis [205]. Scanlan [206], Scanlan and Jones [207] introduced single mode and 2D-flutter analysis methods using modal coordinates by considering the main contribution of selected fundamental torsional mode (for torsional flutter) and coupling between pitch and heave modes (for classical flutter). The 2D coupled flutter analysis is sometimes not sufficient when the contribution of higher modes is significant. Therefore mode-by-mode approach can be adopted [46]. A 2D analysis is applicable to a case where the deck is straight, with prismatic cross section and heave and pitch modes have the same form across the span of the bridge [91]. Additionally, it assumes constant wind velocity at whole deck level.

The horizontal movement of the deck along the direction of the wind for very flexible long-span bridges can play an important role. Sometimes it is necessary to consider the influence of the horizontal mode shape leading to 3D flutter analysis [208]. The lateral modes may have a significant influence on the accurate prediction of the flutter limit for long-span bridges [209, 210, 211]. Yamada et al. [205], Katsuchi et al. [212, 213] presented a classical example of Akashi-Kaikyo Suspension Bridge which is the world's longest with stiffened truss section. This method was used to highlight the effect of relative amplitude [214] and identification of critical structural modes [49]. It was observed from the multi-mode 3D flutter analysis that the significant participation of lateral modes in the flutter instability existed which has been never seen before [215]. It was shown that by including P_i^* aerodynamic derivatives flutter limit reduced considerably. Later, Matsumoto et al. [62] explained that it is due to the structural coupling of lateral mode with the torsional mode. Lateral aerodynamic derivatives P_i^* are usually not directly measured from wind tunnel tests, therefore, quasi-steady values may be used as shown in Table 5.3.

Table 5.3: Conversion between the notations of the aerodynamic derivatives by Scanlan and Quasi-steady theory, after [28].

Scanlan	P_1^*	P_2^*	P_3^*	P_5^*	H_5^*	A_5^*	$H_6^*,\ A_6^*$	$P_4^*,\ P_6^*$
Quasi-steady	$-\frac{1}{K}C_D$	$\frac{1}{2K}C_D'$	$\frac{1}{2K^2}C_D'$	$\frac{1}{2K}C_D'$	$\frac{1}{K}C_L$	$-\frac{1}{K}C_M$	0	0

The state-of-the-art flutter analysis is generally carried out in the frequency-domain by using generalised coordinate transformation in mode-space sometimes using the FEM [216, 217, 218, 219, 220, 221]. Only a few modes are involved in the flutter instability which are necessary to consider in the analysis for sufficient accuracy. In some cases, the significant effect of higher modes in the flutter limit prediction was observed instead of considering only fundamental bending and torsional mode [51, 101, 207, 212, 222]. The 3D flutter analysis uses superposition of modes in which dynamic coupling between the structural modes occurs through the self-excited aerodynamic forces [91]. Some selected modes of vibration are usually included in the flutter analysis which is an approximation; however, it can have a good precision if sufficient modes are chosen. The 3D effect of the structure and the wind characteristics, as well as the influence of coupled modes, is important for flutter stability analysis as the change in characteristics of dominant mode affects the critical flutter limit. It is possible to have multiple mode coupling at the same critical wind speed when more than one curves representing the real part of the eigenvalues (related to damping) simultaneously becomes positive [1, 223]. This is very similar to multiple buckling modes of a column under axial load.

Flutter analysis is often performed in mode-space for systems with multiple modes for which the development of analytical methods has been carried out by Agar [224, 225]. The approaches in modal space utilise generalised coordinate transform and modal superposition techniques [156, 215, 226]. Scanlan [99, 100], Jain et al. [101], Katsuchi et al. [212], Agar [224], Gu et al. [227], Ge et al. [228], Vu et al. [229] have utilised multi-mode approaches to study flutter response of long-span bridges. Hua and Chen [219], Ge and Tanaka [230], Ding et al. [231] examined full-order methods and compared the results with the two-mode and multi-mode procedures. In multi-mode approach, selected modes are included in the analysis whereas the full-order method considers all DOF which is more accurate flutter analysis from the viewpoint of methodology; however, requires often more computation time. Chen and Kareem [49, 204, 232, 233, 234, 235] provide valuable insight into multimode coupled flutter by introducing a closed-form expressions without using a CEVA for estimating modal characteristics of bridge systems. They presented 2D-flutter prediction as well as guidance on the selection of critical structural modes and understanding of the multimode coupled bridge flutter response.

Starossek [109, 236, 237] used the FEM to model bridge decks using beam elements to predict flutter limit for a MDOF system. The complex representation was utilised to predict 2D torsional flutter limit [110] and coupled flutter in the mode space [108] by comparing real-number and complex-number descriptions of the same mechanical phenomena. Starossek et al. [111], Thiesemann et al. [238], Thiesemann and Starossek [239] used complex representation to compare the aerodynamic derivatives from the CFD simulations based on the FVM and water tunnel tests.

The procedure to perform multimode flutter analysis in the mode space is explained herein. Considering a 3DOF system as shown in Figure 4.7, the equations of motion can be written as:

$$m_y\ddot{p} + 2m_y\xi_p\omega_p\dot{p} + m_y\omega_p^2 p = F_D, \tag{5.71a}$$

$$m_z\ddot{h} + 2m_z\xi_h\omega_h\dot{h} + m_z\omega_h^2 h = F_L, \tag{5.71b}$$

$$m_\theta\ddot{\alpha} + 2m_\theta\xi_\alpha\omega_\alpha\dot{\alpha} + m_\theta\omega_\alpha^2\alpha = F_M, \tag{5.71c}$$

where m_y, m_z and m_θ are the masses activated in translational y-axis, z-axis and and rotational about x-axis, respectively. p is the lateral displacement, ξ_p is the damping ratio, ω_p is the frequency of the lateral motion. F_D is the horizontal aerodynamic force, respectively. The Eq. (4.39) can be written in the matrix form as follows:

$$
\begin{pmatrix} F_D \\ F_L \\ F_M \end{pmatrix} = \frac{1}{2}\rho U_\infty BK \begin{pmatrix} P_1^* & P_5^* & BP_2^* \\ H_5^* & H_1^* & BH_2^* \\ BA_5^* & BA_1^* & B^2A_2^* \end{pmatrix} \begin{pmatrix} \dot{p} \\ \dot{h} \\ \dot{\alpha} \end{pmatrix}
$$
$$
+ \frac{1}{2}\rho U_\infty^2 K^2 \begin{pmatrix} P_4^* & P_6^* & BP_3^* \\ H_6^* & H_4^* & BH_3^* \\ BA_6^* & BA_4^* & B^2A_3^* \end{pmatrix} \begin{pmatrix} p \\ h \\ \alpha \end{pmatrix}, \tag{5.72}
$$

with

$$
\mathbf{C}_{ae} = \frac{1}{2}\rho U_\infty BK \begin{pmatrix} P_1^* & P_5^* & BP_2^* \\ H_5^* & H_1^* & BH_2^* \\ BA_5^* & BA_1^* & B^2A_2^* \end{pmatrix}, \tag{5.73}
$$

$$\mathbf{K}_{ae} = \frac{1}{2}\rho U_\infty^2 K^2 \begin{pmatrix} P_4^* & P_6^* & BP_3^* \\ H_6^* & H_4^* & BH_3^* \\ BA_6^* & BA_4^* & B^2A_3^* \end{pmatrix}. \tag{5.74}$$

The aerodynamic force acting on the elements of the structure can be written as:

$$\boldsymbol{Q}_{ae} = \frac{1}{2}\rho U_\infty^2 \left(\mathbf{A}_s \dot{\boldsymbol{u}} + \frac{B}{U_\infty}\mathbf{A}_d \boldsymbol{u} \right) = \mathbf{C}_{ae}\left(\omega\right)\dot{\boldsymbol{u}} + \mathbf{K}_{ae}\left(\omega\right)\boldsymbol{u}. \tag{5.75}$$

The vector $\boldsymbol{Q}_{ae}$ represents the aeroelastic force acting on the bridge deck which is the sum of aeroelastic stiffness $\mathbf{K}_{ae}$ multiplied by nodal displacements $\boldsymbol{u}$ and aeroelastic damping $\mathbf{C}_{ae}$ multiple by nodal velocities $\dot{\boldsymbol{u}}$. The dynamic equilibrium of the bridge deck under wind forces can be defined as:

$$\mathbf{M}\ddot{\boldsymbol{u}} + \mathbf{C}_0\dot{\boldsymbol{u}} + \mathbf{K}_0\boldsymbol{u} = \boldsymbol{Q}_{ae}, \tag{5.76}$$

$$\mathbf{M}\ddot{\boldsymbol{u}} + \mathbf{C}_0\dot{\boldsymbol{u}} + \mathbf{K}_0\boldsymbol{u} = \mathbf{C}_{ae}\dot{\boldsymbol{u}} + \mathbf{K}_{ae}\boldsymbol{u}, \tag{5.77}$$

$$\mathbf{M}\ddot{\boldsymbol{u}} + \left(\mathbf{C}_0 - \mathbf{C}_{ae}\right)\dot{\boldsymbol{u}} + \left(\mathbf{K}_0 - \mathbf{K}_{ae}\right)\boldsymbol{u} = \mathbf{0}. \tag{5.78}$$

Taking equivalent damping and stiffness as:

$$\mathbf{C}_R = \mathbf{C}_0 - \mathbf{C}_{ae}, \tag{5.79a}$$

$$\mathbf{K}_R = \mathbf{K}_0 - \mathbf{K}_{ae}. \tag{5.79b}$$

This leads to solution of the following equation:

$$\mathbf{M}\ddot{\boldsymbol{u}} + \mathbf{C}_R\dot{\boldsymbol{u}} + \mathbf{K}_R\boldsymbol{u} = \mathbf{0}. \tag{5.80}$$

A modal approach is used for the solution of multimode flutter problem. The structural displacement $\mathbf{r}\left(x\right)$ consists of mode shapes $\Phi\left(x\right)$ and the generalised DOF $\mathbf{q}\left(t\right)$ as follows:

$$\mathbf{r}\left(x\right) = \Phi\left(x\right)\mathbf{q}\left(t\right), \tag{5.81}$$

where

$$\Phi\left(x\right) = \begin{bmatrix} \phi_1\left(x\right) & \cdots & \phi_i\left(x\right) & \cdots & \phi_n\left(x\right) \end{bmatrix}, \tag{5.82}$$

$$\phi_i\left(x\right) = \begin{bmatrix} \phi_y\left(x\right) & \phi_z\left(x\right) & \phi_\theta\left(x\right) \end{bmatrix}_i^{\mathrm{T}}, \tag{5.83}$$

$$\mathbf{q}\left(t\right) = \begin{bmatrix} q_1\left(t\right) & \cdots & q_i\left(t\right) & \cdots & q_n\left(t\right) \end{bmatrix}^{\mathrm{T}}, \tag{5.84}$$

where $\phi_y\left(x\right)$, $\phi_z\left(x\right)$ and $\phi_\theta\left(x\right)$ are the mode shapes in lateral, vertical and torsional directions, respectively. Including all modes in the analysis corresponds to full-order analysis. This may require more time of computation. Some selected number of modes N can be chosen for practical purposes to reduce computation time while achieving sufficient accuracy. Dynamic equilibrium is defined in mode space as:

$$\tilde{\mathbf{M}}_0\ddot{\mathbf{q}}\left(t\right) + \tilde{\mathbf{C}}_0\dot{\mathbf{q}}\left(t\right) + \tilde{\mathbf{K}}_0\mathbf{q}\left(t\right) = \tilde{\boldsymbol{Q}}_{se}, \tag{5.85}$$

where $\tilde{\mathbf{M}}_0$, $\tilde{\mathbf{C}}_0$ and $\tilde{\mathbf{K}}_0$ are the modal mass, damping and stiffness matrices, respectively. $\tilde{\boldsymbol{Q}}_{se}$ is the modal aerodynamic force vector. Whereas subscript 0 indicates the structural properties without any wind action. The diagonal terms of the matrix $\tilde{\mathbf{M}}_0$ are given as:

$$\tilde{M}_{0,i} = \int_L \phi_i^{\mathrm{T}}\left(x\right)\mathbf{M}_0\phi_i\left(x\right)\mathrm{d}x, \tag{5.86}$$

with $\mathbf{M}_0$ given as:

$$\mathbf{M}_0 = \begin{bmatrix} m_y\left(x\right) & 0 & 0 \\ 0 & m_z\left(x\right) & 0 \\ 0 & 0 & m_\theta\left(x\right) \end{bmatrix}, \tag{5.87}$$

where $m_y\left(x\right)$, $m_y\left(x\right)$ and $m_y\left(x\right)$ are the distributed mass along the main span in the lateral, vertical and rotational directions, respectively. Each mode shape ϕ_i is associated with natural frequency $\omega_{0,i}$ and the modal damping $\zeta_{0,i}$ and hence the modal matrices can be obtained as:

$$\tilde{\mathbf{M}}_0 = \mathrm{diag}\left(\tilde{M}_{0,i}\right), \qquad i \in \{1, \ldots, N\}, \tag{5.88a}$$

$$\tilde{\mathbf{C}}_0 = \mathrm{diag}\left(2\zeta_{0,i}\omega_{0,i}\tilde{M}_{0,i}\right), \tag{5.88b}$$

$$\tilde{\mathbf{K}}_0 = \mathrm{diag}\left(\omega_{0,i}^2\tilde{M}_{0,i}\right). \tag{5.88c}$$

The motion-induced aerodynamic forces on the bridge deck can be written as:

$$\tilde{\boldsymbol{Q}}_{se} = \tilde{\mathbf{C}}_{ae}\left(\omega\right)\dot{\mathbf{q}} + \tilde{\mathbf{K}}_{ae}\left(\omega\right)\mathbf{q}, \tag{5.89}$$

$$\tilde{\mathbf{C}}_{ae} = \begin{bmatrix} \ddots & \vdots & \iddots \\ \cdots & \tilde{C}_{ae,ij} & \cdots \\ \iddots & \vdots & \ddots \end{bmatrix}, \qquad \tilde{\mathbf{K}}_{ae} = \begin{bmatrix} \ddots & \vdots & \iddots \\ \cdots & \tilde{K}_{ae,ij} & \cdots \\ \iddots & \vdots & \ddots \end{bmatrix}, \tag{5.90}$$

$$\tilde{C}_{ae,ij} = \int_{L_{exp}} \phi_i^{\mathrm{T}}\left(x\right)\mathbf{C}_{ae}\phi_j \mathrm{d}x, \tag{5.91a}$$

$$\tilde{K}_{ae,ij} = \int_{L_{exp}} \phi_i^{\mathrm{T}}\left(x\right)\mathbf{K}_{ae}\phi_j \mathrm{d}x, \tag{5.91b}$$

where L_{exp} is the part of the deck exposed to wind and often $L_{exp} \approx L$. The matrices $\mathbf{C}_{ae}$ and $\mathbf{K}_{ae}$ are already defined in Eq. (5.73) and (5.74). By combining Eqs. (5.85) and (5.89) as:

$$\mathbf{M}\ddot{\boldsymbol{u}} + \mathbf{C}_0\dot{\boldsymbol{u}} + \mathbf{K}_0\boldsymbol{u} = \mathbf{C}_{ae}\dot{\boldsymbol{u}} + \mathbf{K}_{ae}\boldsymbol{u}. \tag{5.92}$$

The characteristic solution of the homogeneous equation above is obtained as:

$$\boldsymbol{w} = \hat{\boldsymbol{w}}_\lambda e^{\lambda t}. \tag{5.93}$$

This provides quadratic complex eigenvalue problem:

$$\ddot{\eta} + \tilde{\mathbf{M}}_0^{-1}\left(\tilde{\mathbf{C}}_0 - \tilde{\mathbf{C}}_{ae}\right)\dot{\eta} + \tilde{\mathbf{M}}_0^{-1}\left(\tilde{\mathbf{K}}_0 - \tilde{\mathbf{K}}_{ae}\right)\eta = 0, \tag{5.94}$$

and by introducing the vectors $\psi = \begin{bmatrix} \dot{\eta} & \eta \end{bmatrix}$ and $\dot{\psi} = \begin{bmatrix} \ddot{\eta} & \dot{\eta} \end{bmatrix}$, gives the following equation:

$$\dot{\psi} = \left\{ \begin{array}{c} \ddot{\eta} \\ \dot{\eta} \end{array} \right\} = \begin{bmatrix} -\tilde{\mathbf{M}}_0^{-1}\left(\tilde{\mathbf{C}}_0 - \tilde{\mathbf{C}}_{ae}\right) & -\tilde{\mathbf{M}}_0^{-1}\left(\tilde{\mathbf{K}}_0 - \tilde{\mathbf{K}}_{ae}\right) \\ \mathbf{I} & \mathbf{0} \end{bmatrix} \left\{ \begin{array}{c} \dot{\eta} \\ \eta \end{array} \right\}, \tag{5.95}$$

which is of the form

$$\dot{\psi} = \mathbf{A}\psi, \tag{5.96}$$

where $\mathbf{I}$ is an identity matrix of size $N \times N$ and $\mathbf{0}$ is a matrix of size $N \times N$ with all zero elements. N is the number of modes included in the eigenvalue problem. Introducing the characteristic solution $\boldsymbol{w} = \hat{\boldsymbol{w}} e^{\lambda_n t}$ with its first derivative $\dot{\boldsymbol{w}} = \lambda_n \hat{\boldsymbol{w}} e^{\lambda_n t}$ and second derivatives $\ddot{\boldsymbol{w}} = \lambda_n^2 \hat{\boldsymbol{w}} e^{\lambda_n t}$, gives the following relations:

$$\psi = \left\{ \begin{array}{c} \lambda_n \hat{\boldsymbol{w}} \\ \hat{\boldsymbol{w}} \end{array} \right\} e^{\lambda_n t} = \hat{\psi} e^{\lambda_n t}, \tag{5.97a}$$

$$\dot{\psi} = \left\{ \begin{array}{c} \lambda_n^2 \hat{\boldsymbol{w}} \\ \lambda_n \hat{\boldsymbol{w}} \end{array} \right\} e^{\lambda_n t} = \lambda_n \hat{\psi} e^{\lambda_n t}. \tag{5.97b}$$

Introducing these relations into Eq. (5.95) leads to the following

$$\lambda_n \hat{\psi} e^{\lambda_n t} = \mathbf{A} \hat{\psi} e^{\lambda_n t}, \tag{5.98}$$

$$\mathbf{A} = \begin{pmatrix} -\tilde{\mathbf{M}}_0^{-1} \mathbf{C}_R & -\tilde{\mathbf{M}}_0^{-1} \mathbf{K}_R \\ \mathbf{I} & \mathbf{0} \end{pmatrix}, \tag{5.99}$$

$$\boldsymbol{w}_\lambda = \begin{pmatrix} \lambda \boldsymbol{w} \\ \boldsymbol{w} \end{pmatrix}, \tag{5.100}$$

$$(\mathbf{A} - \lambda \mathbf{I}) \, \boldsymbol{w}_\lambda e^{\lambda t} = \mathbf{0}. \tag{5.101}$$

The eigenvalue problem can be finally written as:

$$(\mathbf{A} - \lambda \mathbf{I}) \, \hat{\psi} e^{\lambda t} = \mathbf{0}, \tag{5.102}$$

$$\left(\lambda_n^2 \tilde{\mathbf{M}}_0 + \lambda_n \left(\tilde{\mathbf{C}}_0 - \tilde{\mathbf{C}}_{ae} \right) \dot{\eta} + \left(\tilde{\mathbf{K}}_0 - \tilde{\mathbf{K}}_{ae} \right) \right) \boldsymbol{w} = 0, \tag{5.103}$$

$$\left(\lambda_n^2 \mathbf{M} + \lambda_n \mathbf{C}_R + \mathbf{K}_R \right) \boldsymbol{w} = 0. \tag{5.104}$$

The above equation can be transformed into a complex nonlinear eigenvalue problem which can be solved iteratively. This results in $2N$ eigenvalues λ_n which are associated with eigenvector $\hat{\boldsymbol{w}}$. The solution is in terms of complex conjugate pairs such that $\lambda_n = a_n \pm \iota b_n$. The real a_n and imaginary b_n parts of eigenvalues are associated with the damping ratio and frequency as follows:

$$\lambda_n = a_n \pm \iota b_n, \qquad n = 1, \ldots, 2N \tag{5.105}$$

$$\omega_n = b_j, \tag{5.106}$$

$$\xi_n = \frac{-a_n}{\sqrt{a_n^2 + b_n^2}}. \tag{5.107}$$

The procedure of multimode flutter stability analysis is shown in Figure 5.5.

5.6.5.3 Sort and Arrange Eigenvalues

Flutter analysis in the frequency domain is performed by using eigenvalues and eigenvectors of a matrix in state-space form. Most of the roots of flutter equation at any iteration would be complex and unsorted with respect to the modes which requires sorting the roots in order to associate modal frequencies and modal damping ratios to the structural modes. Flutter occurs when at least one real part of the root becomes positive with the corresponding positive imaginary part. The process explained by Qiu
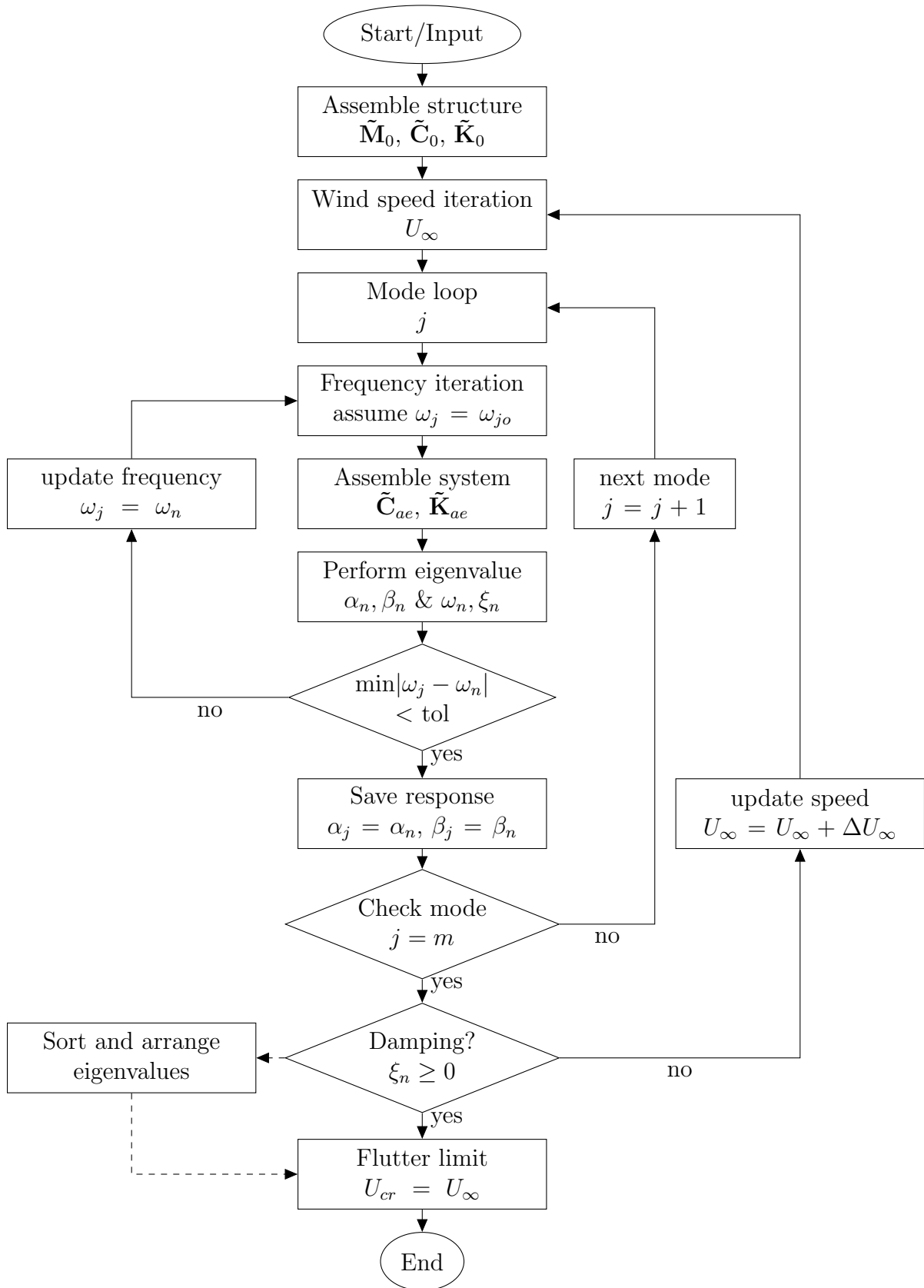
Figure 5.5: Flowchart for multimode flutter analysis in frequency domain.

and Sun [240] has been used here. At the start of the analysis, frequency ω_j of mode j is used in the reduced speed v_r to search for aerodynamic derivatives and to formulate the system matrices. Eigenvalues and eigenvectors are then computed which provide modal frequencies ω_n and modal damping ratios ξ_n. These are then compared to the corresponding natural modes in order to identify the order of modes. This new frequency ω_n is used for next iteration and the process is repeated until convergence is reached. The last converged frequency is used in the first calculation of the next velocity iteration ($U_\infty = U_\infty + \Delta U_\infty$). The eigenvectors of the converged modes are compared to the previous wind speed to identify the modes and to sort new eigenvectors. The process is repeated for next steps on the same lines.

5.6.6 Derivative-based FSI Simulations (Model#4)

The most general approach for the solution of the dynamic response of structural systems is the direct numerical integration of the dynamic equilibrium equations. This involves, after the solution is defined at time zero, the attempt to satisfy dynamic equilibrium at discrete points in time. A numerical method described here is for calculating the flutter limit without the need of an eigenvalue solution. The method makes use of the aerodynamic derivatives and modal data of the structure to compute the dynamic response of the system.

The developed approach is based on numerical integration and with small modifications, it can be adapted to other structures which exhibit similar aeroelastic phenomenon. Newmark-Beta method has been used for time integration with the average acceleration method which is identical to the trapezoidal rule and is used to numerically evaluate second order differential equations. The scheme shown in Figure 5.6 describes the procedure to compute flutter limit. Geometry, dynamic properties and the aerodynamic derivatives are required as input.

The approach was first formulated for a section model of the bridge with only 2DOF in heave and pitch direction. The dimensional reduction to a 2DOF system is a simplification but it neglects the effects coming from the higher modes. The scheme was then extended to be used for the bridge in the modal coordinates. The aerodynamic derivatives obtained through forced vibration analysis (cf. Section 4.4.2) are used to calculate the motion-induced aerodynamic forces for the section.

The scheme presented in the flow chart (see Figure 5.6) starts with input data and some initial value of wind speed U_∞. The trial frequency of oscillation ω at flutter could be somewhere between the heave frequency ω_h and the pitch frequency ω_α, therefore, trial frequency ω is varied from ω_h to ω_α. The aerodynamic derivatives are frequency dependent and are calculated on the basis of the oscillation frequency. The aerodynamic derivatives obtained by the forced vibration analysis based on the VPM (cf. Section 4.4.2) are then searched at this frequency. The motion-induced aerodynamic forces are then computed from these derivatives. The forced vibration simulations are performed at a certain amplitude of oscillation. Therefore, the calculated motion-induced forces will be accurate at only these amplitudes. This assumption is valid since the motion-induced forces are linearised with respect to the motion.
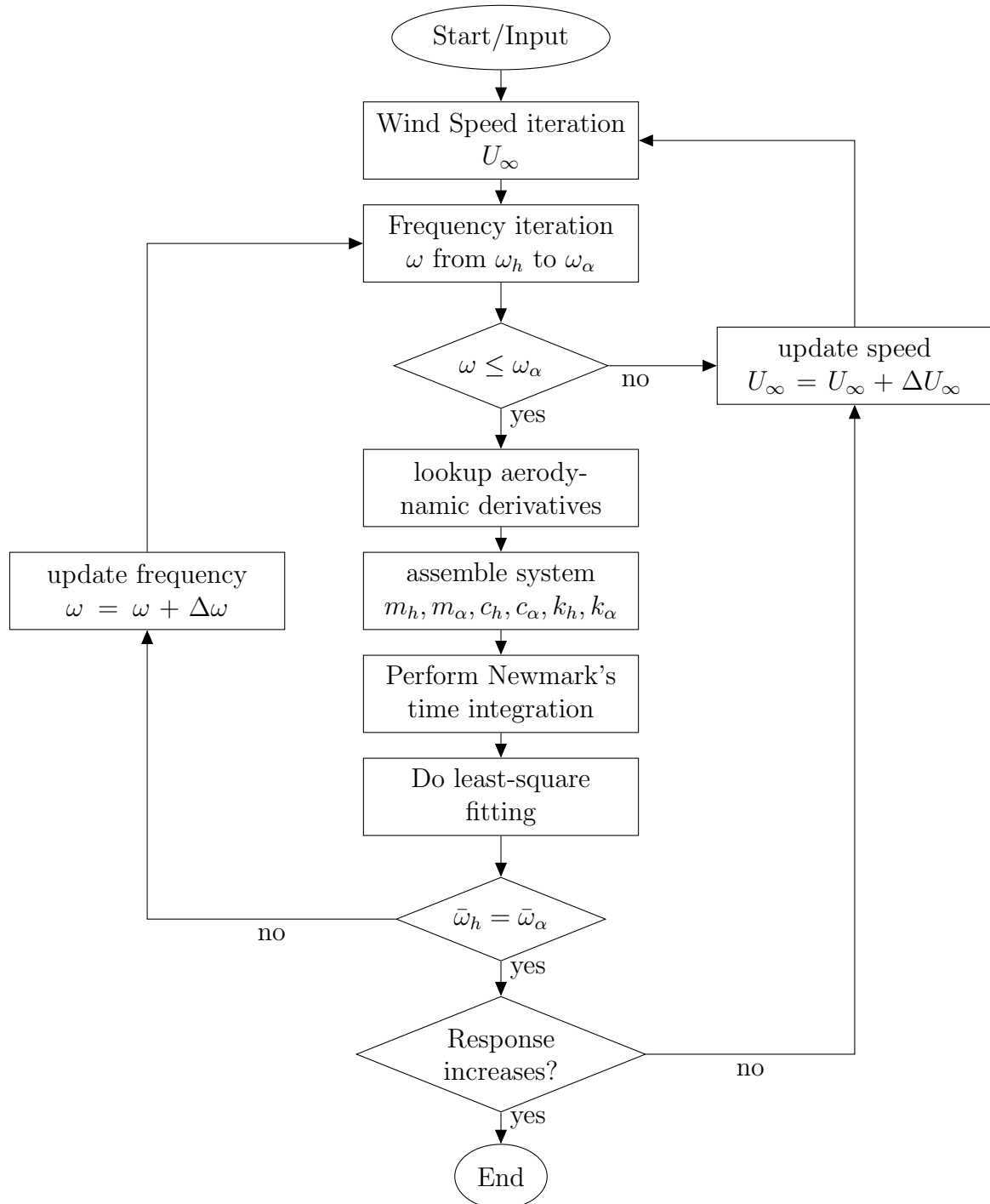
Figure 5.6: Flow chart to calculate flutter limit from derivative-based FSI simulations.

5.6.6.1 Time Integration

After obtaining aerodynamic forces, Eqs. (5.1a), (5.1b), (4.29a) and (4.29b) are then solved numerically by using Newmark algorithm [82]. Here, with discrete time steps Δt, the displacement vector h_{j+1} and the velocity vector $\dot{h}_{j+1}$ at the next time step $t = j+1$ are calculated. As for the initial conditions, the modal coordinates are given a small initial velocity and all other initial displacements and accelerations are set equal to zero. The governing equations for the heave and pitch DOF are outlined as follows:

$$\overline{k}_h = k_h + \frac{2c_h}{\Delta t} + \frac{2m_h}{\Delta t^2}, \qquad \overline{k}_\alpha = k_\alpha + \frac{2c_\alpha}{\Delta t} + \frac{2m_\alpha}{\Delta t^2}, \tag{5.108}$$

$$p_{h,j+1} = \frac{1}{2}\rho U_\infty^2 BL \left[\frac{KH_1^*}{U_\infty}\dot{h}_j + \frac{KH_2^*B}{U_\infty}\dot{\alpha}_j + K^2 H_3^* \alpha_j + \frac{K^2 H_4^*}{B}h_j \right], \tag{5.109}$$

$$p_{\alpha,j+1} = \frac{1}{2}\rho U_\infty^2 B^2 L \left[\frac{KA_1^*}{U_\infty}\dot{h}_j + \frac{KA_2^*B}{U_\infty}\dot{\alpha}_j + K^2 A_3^* \alpha_j + \frac{K^2 A_4^*}{B}h_j \right], \tag{5.110}$$

$$\overline{p}_{h,j+1} = p_{h,j+1} + c_h \left(\frac{2h_j}{\Delta t} + \dot{h}_j \right) + m_h \left(\frac{4h_j}{\Delta t^2} + \frac{4\dot{h}_j}{\Delta t} + \ddot{h}_j \right), \tag{5.111}$$

$$\overline{p}_{\alpha,j+1} = p_{\alpha,j+1} + c_\alpha \left(\frac{2\alpha_j}{\Delta t} + \dot{\alpha}_j \right) + m_\alpha \left(\frac{4\alpha_j}{\Delta t^2} + \frac{4\dot{\alpha}_j}{\Delta t} + \ddot{\alpha}_j \right), \tag{5.112}$$

which give response at next time step as follows:

$$h_{j+1} = \frac{\overline{p}_{h,j+1}}{\overline{k}_h}, \qquad \alpha_{j+1} = \frac{\overline{p}_{\alpha,j+1}}{\overline{k}_\alpha}, \tag{5.113}$$

$$\dot{h}_{j+1} = \frac{2}{\Delta t}(h_{j+1} - h_j) - \dot{h}_j, \qquad \dot{\alpha}_1 = \frac{2}{\Delta t}(\alpha_{j+1} - \alpha_j) - \dot{\alpha}_j, \tag{5.114}$$

$$\ddot{h}_{j+1} = \frac{4}{\Delta t^2}(h_{j+1} - h_j) - \frac{4}{\Delta t}\dot{h}_j - \ddot{h}_j, \quad \ddot{\alpha}_{j+1} = \frac{4}{\Delta t^2}(\alpha_{j+1} - \alpha_j) - \frac{4}{\Delta t}\dot{\alpha}_j - \ddot{\alpha}_j, \tag{5.115}$$

where $\overline{k}_h$, $\overline{k}_\alpha$ are the effective stiffness in heave and pitch, respectively. k_h, k_α are the stiffness c_h, c_α are the damping and m_h, m_α are the mass in heave and pitch, respectively. $p_{h,j+1}$, $p_{\alpha,j+1}$ are the self-excited force as given in Eq. (4.29a) and (4.29b). $\overline{p}_{h,j+1}$, $\overline{p}_{\alpha,j+1}$ are the effective force in heave and pitch, respectively. Δt is the time step. h, α are the displacement and rotation $\dot{h}$, $\dot{\alpha}$ are the velocity and $\ddot{h}$, $\ddot{\alpha}$ are the acceleration in heave and pitch, respectively. Subscripts j and $j+1$ correspond to current and next time steps, respectively. L is the element length.

5.6.6.2 Response Frequency Determination

After calculating the response for heave and pitch the next step is to identify the frequencies of the computed response. The usual way of calculating frequency is to apply Discrete Fast Fourier Transform (DFFT). However, for such small data set where only a few points have been calculated, this approximation would be insufficient. Therefore, another approach is used where the calculated response is assumed as a simple harmonic function and fitting is performed with another function of known parameters

thus calculating frequency indirectly. This method is found much more accurate than the DFFT. The equations of the assumed function are:

$$h_{fit} = \overline{h} \sin \left(\overline{\omega}_h t - \overline{\phi}_h \right), \qquad \alpha_{fit} = \overline{\alpha} \sin \left(\overline{\omega}_\alpha t - \overline{\phi}_\alpha \right), \qquad (5.116)$$

$$\dot{h}_{fit} = \overline{\omega}_h \overline{h} \cos \left(\overline{\omega}_h t - \overline{\phi}_h \right), \qquad \dot{\alpha}_{fit} = \overline{\omega}_\alpha \overline{\alpha} \cos \left(\overline{\omega}_\alpha t - \overline{\phi}_\alpha \right), \qquad (5.117)$$

$$\ddot{h}_{fit} = -\overline{\omega}_h^2 \overline{h} \sin \left(\overline{\omega}_h t - \overline{\phi}_h \right), \qquad \ddot{\alpha}_{fit} = -\overline{\omega}_\alpha^2 \overline{\alpha} \sin \left(\overline{\omega}_\alpha t - \overline{\phi}_\alpha \right), \qquad (5.118)$$

where h_{fit}, α_{fit} the displacement $\dot{h}_{fit}$, $\dot{\alpha}_{fit}$ are the velocity and $\ddot{h}_{fit}$, $\ddot{\alpha}_{fit}$ are the acceleration in heave and pitch of the assumed fitted function, respectively. $\overline{h}$, $\overline{\omega}_h$ and $\overline{\phi}_h$ are the unknown static displacement, circular frequency and the phase angle of the assumed fitted harmonic function, respectively.

Two schemes were used to apply the fitting. The first scheme applies fitting on the individual response of displacement, velocity and acceleration whereas the second scheme considers the fitting on displacement, velocity and acceleration simultaneously. The second scheme is found more efficient. The fitting function assumes velocity as a derivative of displacement and acceleration as a derivative of velocity. Therefore, following equation was used

$$\hat{f} \left(\overline{h}, \overline{\omega}_h, \overline{\phi}_h \right) = \sum_{k=1}^p \left(h_{cal} - h_{fit} \right)_{(k)}^2 + \sum_{k=1}^p \left(\dot{h}_{cal} - \dot{h}_{fit} \right)_{(k)}^2 + \sum_{k=1}^p \left(\ddot{h}_{cal} - \ddot{h}_{fit} \right)_{(k)}^2, \qquad (5.119)$$

$$\hat{f} \left(\overline{\alpha}, \overline{\omega}_\alpha, \overline{\phi}_\alpha \right) = \sum_{k=1}^p \left(\alpha_{cal} - \alpha_{fit} \right)_{(k)}^2 + \sum_{k=1}^p \left(\dot{\alpha}_{cal} - \dot{\alpha}_{fit} \right)_{(k)}^2 + \sum_{k=1}^p \left(\ddot{\alpha}_{cal} - \ddot{\alpha}_{fit} \right)_{(k)}^2 \qquad (5.120)$$

where h_{cal}, α_{cal} are the displacement and rotation, $\dot{h}_{cal}$, $\dot{\alpha}_{cal}$ are the velocity and $\ddot{h}_{cal}$, $\ddot{\alpha}_{cal}$ are the acceleration in heave and pitch calculated from Eqs. (5.113), (5.114) and (5.115). p is the number of selected points for fitting. $\hat{f}$ is the target function which needs to be minimised. Here, the aim is to minimise the square of the difference between the calculated response and fitted function. An optimisation solution is required to apply fitting of the assumed function to the calculated response. The fitting is applied separately to heave and pitch responses. The frequencies determined for both cases are then compared.

5.7 Fully-coupled CFD Simulations (Model#5)

The 2D flow simulations on bridge decks have found to provide a promising agreement for the prediction of coupled flutter limit with wind tunnel experiments [241]. These simulations could be used as a supplementary tool to wind tunnel testing for preliminary analysis. Often the simulations are performed by free or forced oscillation methods to compute aerodynamic derivatives and then calculating flutter limit by using semi-analytical methods in frequency or time domain. But these simulations do not represent the actual response of the system at or near the flutter limit because the aerodynamic derivatives are measured at some fixed amplitude and are sometimes extrapolated which may lead to erroneous results.

The FSI simulations are time-domain analyses performed using the interaction between flow and a rigid body as well as its motion is incorporated into the simulation. The incompressible Navier-Stokes equations are fully coupled to a rigid body which is elastically suspended on springs with lumped mass. The section of the bridge is

considered to move in its DOF heave, pitch and lateral motion. Often only the first bending mode and the first torsional mode are considered to contribute to the response.

The instantaneous application of the full wind speed to an initially stationary structure leads to large transient initial motions from which it is difficult to extract solid conclusions about the stability of small oscillations. This can be avoided by using large fictitious damping only for first few time steps and then replacing the actual damping values [241].

Several studies [128, 242, 243, 244, 245] have been performed to show the application and effectiveness of the approach on different test cases. It has the advantage of simultaneous force measurement and flow visualisation at each point of the domain. Some other examples of fully-coupled CFD simulations to compute flutter limits are given in Table A.1, A.2 and A.3.

The concept of dimensional reduction to 2D can be applied for line-like structures where the geometrical properties, as well as flow properties, remain unchanged along the entire length. The contribution of higher modes is generally low in the long-span bridge flutter. Therefore the 2D approach can provide a reasonable prediction of the flutter limit; however, this contribution can be sometimes significant and can not be ignored. The multi-slice approach can then be used to consider the additional modes where each slice acts as a separate 2D flow model and the structure is coupled with the help of structural modes. However, this approach has a limitation in contrast to the full aeroelastic model in wind tunnel that the aerodynamic force correlation is not established.

5.7.1 2D Simulations

The 2D numerical aerodynamic analysis using CFD based on the VPM has attracted much attention in the recent past. Typically 2D methods are used where the flow problem can be approximated for line-like structures which are analogous to section model testing in wind tunnels.

The procedure to compute flutter limit, in this case, is illustrated in Figure 5.7. The flow solver uses the coupled analysis of the vertical motion and rotation of a 2DOF spring supported section model. The coupling of fluid dynamics solution and the structural dynamics is done at every time step. The pressure on the surface of the body is integrated to get the resultant force in terms of lift and moment. These are associated with the 2DOF of the structural system. The equations of motion for the system are solved by time marching structural dynamics solution. A stiffness matrix is then created and the solution is performed. Rayleigh damping is used to model structural damping, for which the damping matrix is proportional to the combination of mass and stiffness matrices (see Section 4.2.4).

The simulations are run at different wind speeds and the response is recorded. The wind speed which shows divergent oscillatory response is the flutter limit. At this wind speed, the response to vertical displacement and rotation are coupled and the section oscillates with a different frequency than natural bending or torsion frequency which is the flutter frequency.
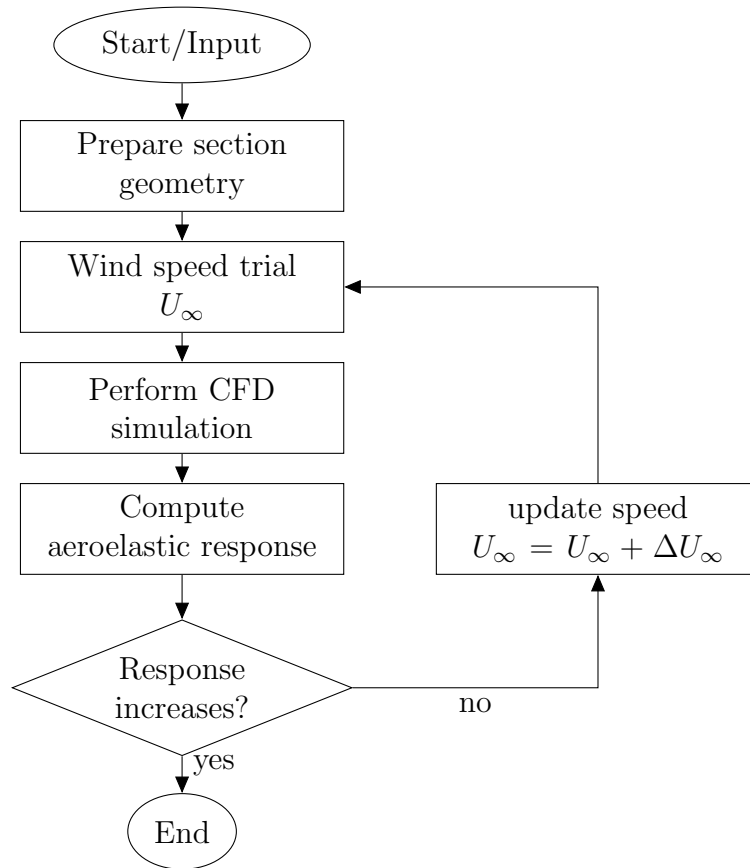
Figure 5.7: Flow chart to calculate flutter limit from fully-coupled CFD simulations.

5.7.2   Quasi-3D Simulations

The aerodynamic forces along the length of the structure are not fully correlated. In a 2D model, the effects coming from this aspect is not properly dealt with. The 2D CFD model can be extended to 3D where the whole length of the bridge is divided into discrete slices and each slice acts as a separate 2D wind model connected to each other with the modal properties. Figure 5.8 demonstrates this multi-slice arrangement along the structure. This quasi-3D approach is useful for the line-like structures such as bridge decks, towers and chimneys.
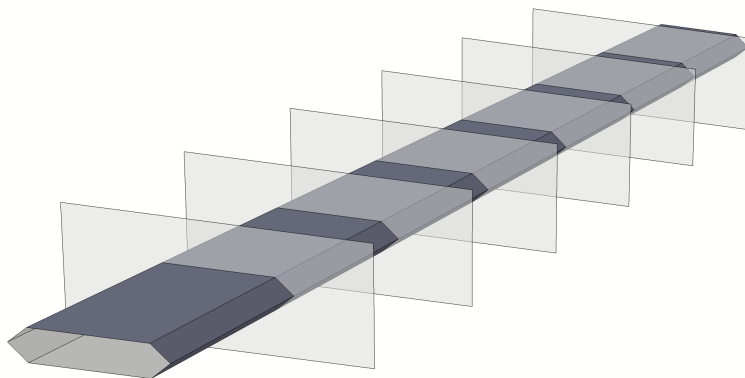
Figure 5.8: Fully-coupled CFD Simulations: schematic of the quasi-3D (multi-slice) arrangement along the bridge length.

The 3DOF are coupled at slice locations with the structural model. Selected modes

can be included in the analysis and total structural response $\boldsymbol{u}$ is computed by modal superposition as follows:

$$\boldsymbol{u} = \sum_{j=1}^{N} w_j \boldsymbol{\phi}_j, \tag{5.121}$$

where w_j is the modal displacement and $\boldsymbol{\phi}_j$ is the mode shape of mode j. N is the number of modes selected for the analysis. For further details about the method, the reader is referred to [128].

5.8 Summary

The model combinations to perform flutter stability analysis have been explained in this chapter. These models include fully-analytical, empirical, semi-analytical as well as fully-coupled CFD simulations. The analytical Theodorsen expressions of a flat plate and Scanlan aerodynamic derivatives are used to model the motion-induced aerodynamic forces. Theodorsen theory has been used for fully-analytical 2D analysis, whereas quasi-3D CFD simulations based on the VPM and the semi-analytical approaches have been used to cover 3D analysis. These models include one of the earliest presented for flutter analysis as well as state of the art models used in the design and analysis of bridges constructed in the recent years. This provides a wide range of model combinations to study the FSI.

Chapter 6

Flutter Analysis of Reference Objects

6.1 Introduction

Models presented in Chapter 5 are applied here on the reference objects. The selected reference objects for this purpose are also described. Two distinct reference bridges have been selected; however, the detailed finite element model was made only for one of the suspension bridges. Table 6.1 summarises some of the well-known examples of long-span cable-supported bridges built around the world. It can be seen that there is a wide range of structural parameter variation among the bridges depending upon the type and structural configuration of the bridge. In addition to that, the type of cross section introduces a large variation in the aerodynamic behaviour which sometimes becomes a challenging task to deal with. The choice of the first reference object was based on the availability of detailed information and structural properties. The second reference object is a classical example of bridge collapse as a result of aeroelastic instability. Although a detailed finite element model has not been made here for this bridge, extensive analyses have been presented on its cross section and discussed in detail. The aerodynamic characteristics for these sections are determined from the CFD simulations. The flutter limit predictions of these structures have been made by using models explained in Chapter 5 for 2D and 3D cases.

6.2 Reference Objects

The Lillebælt Suspension Bridge, Denmark, and the original Tacoma Narrows Suspension Bridge, USA, presented in Figure 6.2 have been used as reference objects within the study. The cross sections of selected bridges cover a wide range of structural and aerodynamic parameters. Their variation allows to study various effects on the aeroelastic stability behaviour. The elevations of these bridges are shown in Figure 6.1. Figure 6.3 shows the simplified cross sections considered in this study for the Lillebælt (Structure A) and the original Tacoma Narrows (Structure H) Suspension Bridges. Railings and other attachments on the sections are not considered for simplicity. These sections were modelled for the CFD forced vibration simulations to compute motion-induced aerodynamic forces and for fully-coupled CFD analyses to directly compute flutter boundary.

The structural parameters for these reference objects are given in Table 6.7. For convenience, non-dimensional parameters can be used for structural properties as given in Eq. (6.1).

Table 6.1: Structural properties of some well known long-span cable-supported bridges (cf. Table 3.1 and Eq. (6.1)) [3, 33, 34, 35, 36, 37, 38, 39, 40].

Bridge Name	B	m	I	f_h	f_α	μ	r_α	γ_ω
	[m]	[t/m]	[tm^2/m]	[Hz]	[Hz]	[-]	[-]	[-]
Suspension								
Messina	60.4	55.00	28000	0.061	0.080	24.1	0.374	1.31
Akashi-Kaikyo	35.5	43.79	9826	0.064	0.150	55.6	0.422	2.34
Zhejiang Xihoumen	36.3	-	-	0.100	0.232	-	-	2.32
Great Belt (Storebælt)	31.0	22.70	2470	0.099	0.272	37.8	0.336	2.75
Little Belt (Lillebælt)	33.0	11.66	1018	0.156	0.500	17.1	0.283	3.21
Tacoma Narrows	12.0	4.25	178	0.130	0.200	47.2	0.539	1.54
Hålogaland	18.6	11.94	355	0.143	0.441	55.2	0.293	3.08
Bosporus	28.0	13.55	1352	0.162	0.371	27.7	0.357	2.29
Runyang	-	-	-	0.124	0.225	-	-	1.81
Humen	-	-	-	0.112	0.426	-	-	3.80
Cable-stayed								
Sutong	41.0	-	-	0.171	0.521	-	-	3.05
Stonecutters	53.3	32.60	297	0.172	0.324	18.4	0.057	1.88
Indiano	22.4	17.40	545	0.573	1.179	55.5	0.250	2.06
Guama	14.2	22.51	567	0.331	0.649	178.6	0.353	1.96
Tsurumi	38.0	32.22	2880	0.204	0.486	35.7	0.249	2.38
Normandy	23.8	13.70	633	0.222	0.500	38.7	0.286	2.25
Footbridge								
Siena	3.3	1.42	0.810	1.735	4.839	208.6	0.229	2.79
Turin	6.9	3.35	13.502	0.510	0.590	112.6	0.291	1.16
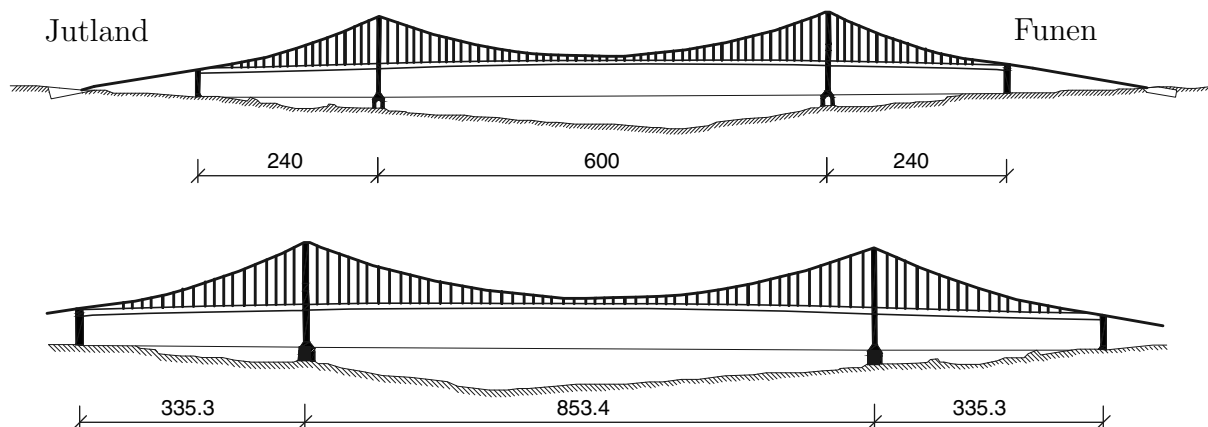
Figure 6.1: Reference objects:
(top) Lillebælt Suspension Bridge (Structure A),
(bottom) original Tacoma Narrows Suspension Bridge (Structure H) (units: [m]).

Figure 6.2: Reference objects:
(top) Lillebælt Suspension Bridge, Denmark,
(bottom) original Tacoma Narrows Suspension Bridge, USA
(pictures courtesy of wikimedia).
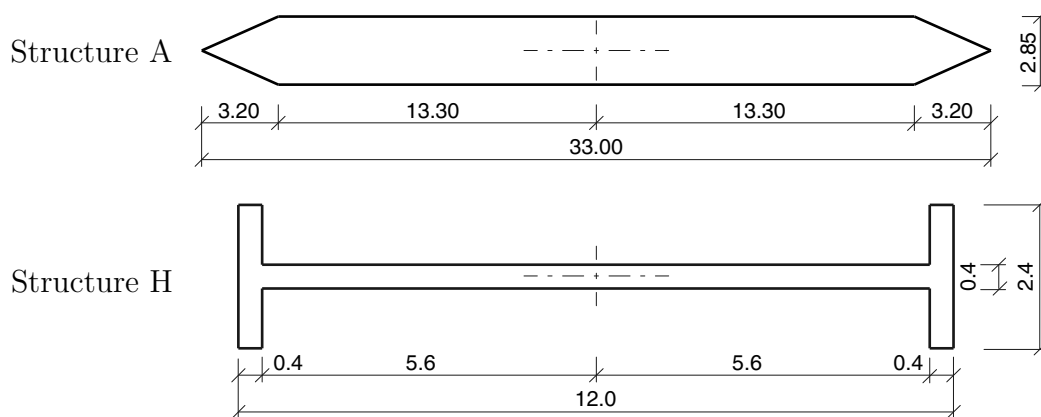
Figure 6.3: Reference objects: simplified cross sections of
(top) Lillebælt Suspension Bridge (Structure A),
(bottom) original Tacoma Narrows Suspension Bridge (Structure H) (units: [m]).

89

The non-dimensional parameters shown in Table 6.1 are as follows:

$$\mu = \frac{2m}{\rho B^2}, \tag{6.1a}$$

$$r_\alpha = \sqrt{\frac{I}{mB^2}}, \tag{6.1b}$$

$$\gamma_\omega = \frac{\omega_\alpha}{\omega_h}, \tag{6.1c}$$

$$\xi = \xi_h = \xi_\alpha, \tag{6.1d}$$

where μ is the ratio of the mass of the deck to the mass of the air moved by the deck, r_α is the non-dimensional radius of gyration of the deck, γ_ω is the still air frequency ratio between pitch and heave and ξ is the damping ratio mode of vibration.

The Lillebælt Suspension Bridge consists of a steel box girder deck with 1080 m suspended span. It is a bridge with a cable sag of 67 m and navigation height of 44 m. The measured frequencies from a 1:200 scaled bridge model, and other details about the bridge can be found in the design reports [33, 246].

6.3 Modal Analysis of Reference Object

The analysis of structures in the mode-space is a convenient approach to calculate the response of a complex structure. A limited number of modes are used in this approach. Therefore, it is important to know which modes contribute more to the overall response. The mode shapes only describe the behaviour of the structure when oscillating at a certain natural frequency but does not provide the information about the mode contribution. Effective modal mass is used for this purse which describes the participation of effective mass for a given mode in a respective direction. Larger values of effective mass imply larger contribution to the modal response. The normalisation of modal mass is often done with respect to the deck.

The mode shapes and frequencies of the bridge are required for the flutter analysis. This information provides structural behaviour without any influence of wind. A finite element model of the Lillbælt Suspension Bridge was prepared from the information of the bridge provided in [33]. A commercially available finite element software SOFiSTiK was used for this purpose. The model was calibrated using the information provided in [246]. Beam elements were used to model the deck and tower whereas cable elements were used for main cable and suspenders. The deck and tower were connected using springs. The stiffness of these springs was then varied in the calibration process. The calibrated model frequencies are compared with the required frequencies in Table 6.2. A perfect match between the first symmetrical bending and first symmetrical torsion frequencies was achieved; however, discrepancies are seen in the second unsymmetrical bending frequency. The objective here was to achieve relatively good agreement for the first symmetrical modes as often these modes are considered more important for flutter analysis. The frequency of unsymmetrical torsional mode was not provided in the reference literature.

This finite element model provides several modes which do not excite the deck and therefore are not important for flutter analysis. Figure 6.4 shows full 3D model of the bridge whereas Figure 6.5 shows first bending and first torsional modes. The bridge deck is not continuous along the whole suspended span length. There exists a special

Table 6.2: Natural frequencies from the calibrated finite element model of the Lillebælt Suspension Bridge (units: [Hz]) (cf. Figure 6.6).

Mode	Bending mode		Torsion mode	
	symmetrical	unsymmetrical	symmetrical	unsymmetrical
Measured [246]	0.156	0.153	0.500	-
Achieved	0.156	0.161	0.500	1.031

joint at the main tower which connects the main span with the side span. This joint is known as 'wind bearing' and is shown in Figure C.1. For this reason, some torsional modes show discontinuous behaviour at the location of main towers.
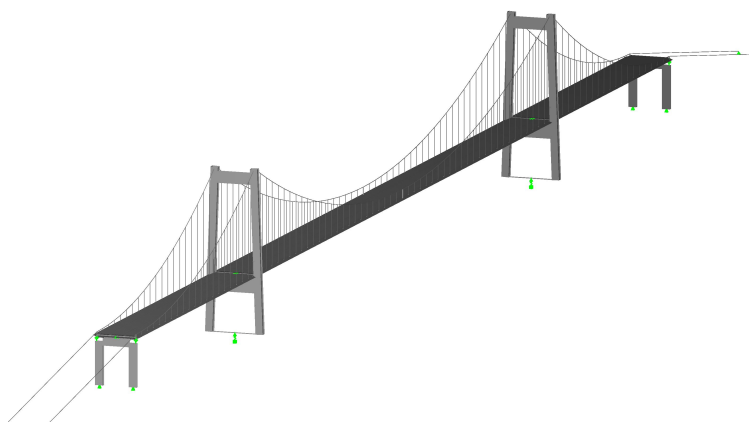
Figure 6.4: View of full 3D finite element model of the Lillebælt Suspension Bridge.
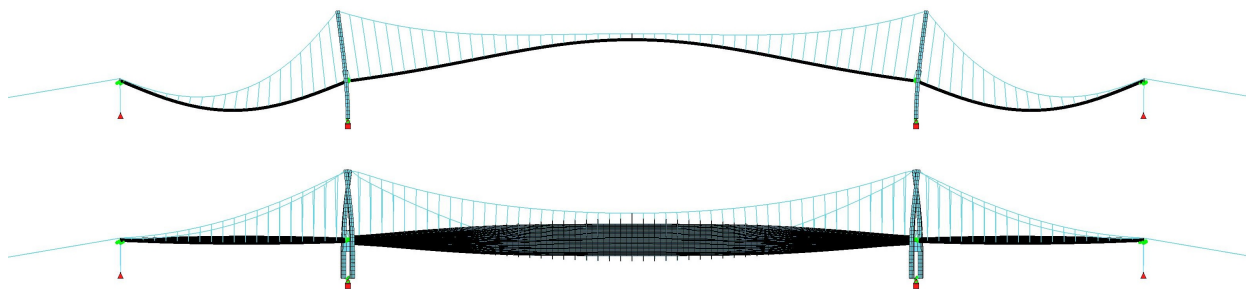
Figure 6.5: Mode shapes of the Lillebælt Suspension Bridge from finite element model:
(top) vertical bending mode,
(bottom) torsional mode.

Some more details of deck modes are provided in Figure 6.6 where first 8 bending modes, first 4 torsion and first 4 lateral modes are shown. In addition to that, the frequencies and modal masses of these modes along with their description are listed in Table 6.3. Furthermore, these selected modes are categorised into symmetrical and unsymmetrical modes which are later used in the multimode flutter analysis. The description of the first 50 modes is also provided in Table C.1 and C.2. The modes of the deck are only important here to be considered for flutter analysis; however, other modes are also shown for comparison which include tower mode and cable modes.
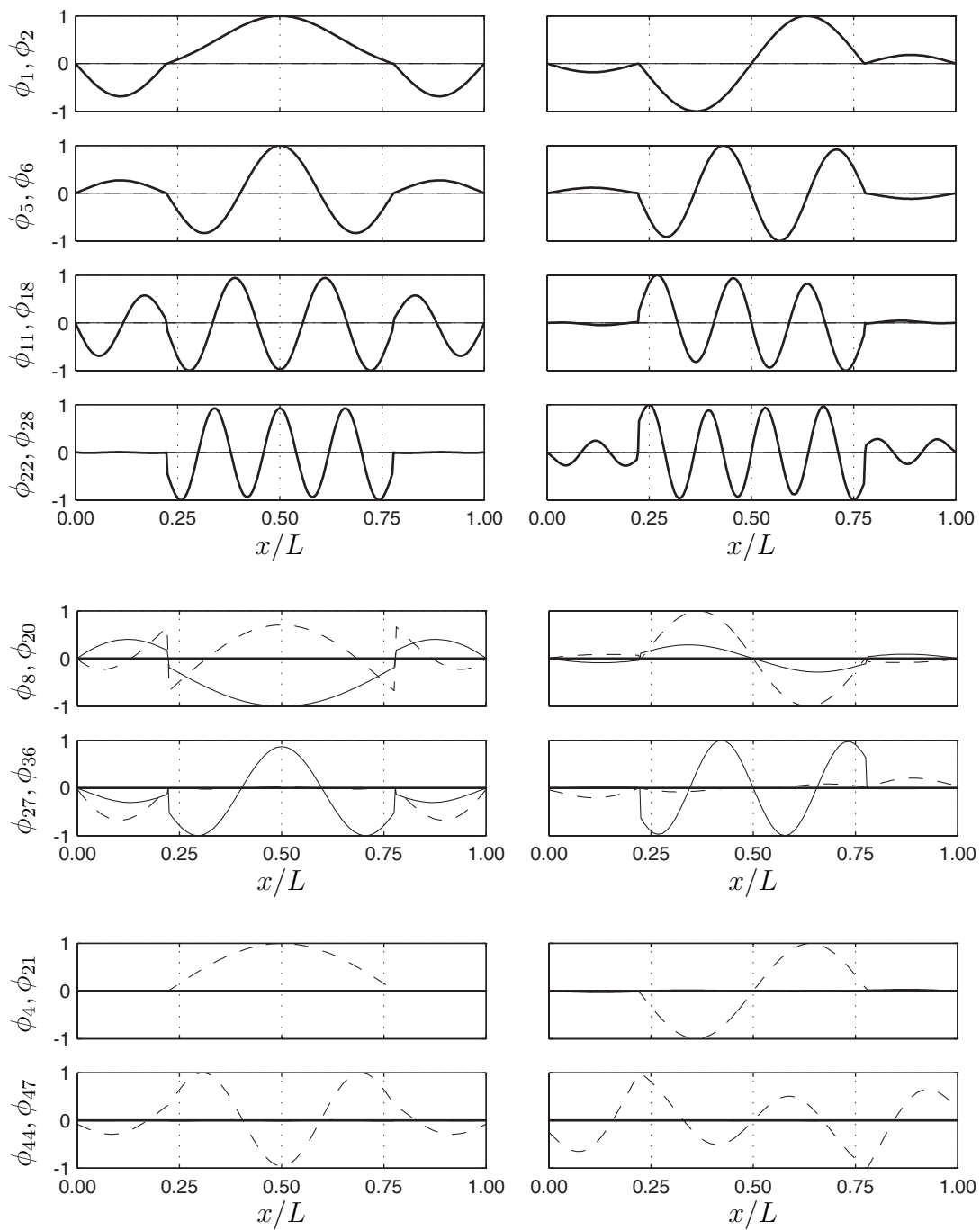
Figure 6.6: Mode shapes of the Lillebælt Suspension Bridge from finite element model:
(top) vertical bending modes,
(middle) torsional modes,
(bottom) lateral bending modes
(——) vertical displacement,
(——) rotation,
(– –) lateral displacement (cf. Table 6.3).

Table 6.3: Modal properties from the finite element model of the Lillebælt suspension bridge (cf. Figure 6.6) (cf. Table C.1 and C.2).

Mode number	Frequency [Hz]	Modal mass [kg] [kgm^2]	Mode type
Vertical bending modes			
1	0.156	4,224	1st symmetrical vertical
2	0.161	4,193	1st unsymmetrical vertical
5	0.294	3,000	2nd symmetrical vertical
6	0.460	3,378	2nd unsymmetrical vertical
11	0.674	4,542	3rd symmetrical vertical
18	0.903	3,258	3rd unsymmetrical vertical
22	1.187	3,289	4th symmetrical vertical
28	1.456	4,009	4th unsymmetrical vertical
Torsional modes			
8	0.500	3,89,789	1st symmetrical torsional
20	1.031	3,66,706	1st unsymmetrical torsional
27	1.391	3,36,512	2nd symmetrical torsional
36	1.843	3,22,336	2nd unsymmetrical torsional
Lateral bending modes			
4	0.287	3,501	1st symmetrical lateral
21	1.116	3,993	1st unsymmetrical lateral
44	2.295	3,949	2nd symmetrical lateral
47	2.644	3,055	2nd unsymmetrical lateral

The modal equivalent distributed mass and mass moment of inertia $\tilde{M}_i$ can be obtained:

$$\tilde{M}_i = \tilde{m}_y \int_L \phi_{yi}^2 \mathrm{d}x + \tilde{m}_z \int_L \phi_{zi}^2 \mathrm{d}x + \tilde{m}_\theta \int_L \phi_{\theta i}^2 \mathrm{d}x, \tag{6.2}$$

where $\tilde{m}_y$, $\tilde{m}_z$ and $\tilde{m}$ are the distributed masses for mode i in translational y-axis, translational z-axis and rotational about x-axis. In case of pure vertical bending mode, the modal contribution in lateral and rotational directions will be zero and only one term remain as

$$\tilde{m}_z = \frac{\tilde{M}_i}{\int_L \phi_{zi}^2 \mathrm{d}x}. \tag{6.3}$$

A similar procedure can be repeated for other uncoupled modes.

The focus of this study is related to aeroelastic instabilities; however, effective modal mass provides useful information about the structural characteristics. Figure 6.7 shows the effective modal mass of the deck from the Lillebælt finite element model with respect to the total effective mass of the first 50 modes. The figure shows an effective mass in three directions i.e. lateral (along y-axis), vertical (along z-axis) and rotational (about x-axis). The effective modal mass Γ_i can be computed as

$$L_i = \int_L \phi_i^{\mathrm{T}}(x) \mathbf{M}_0 \mathrm{d}x, \tag{6.4}$$

$$\Gamma_i = \frac{L_i}{M_i}. \tag{6.5}$$

where $\mathbf{M}_0$ is the mass matrix.

For any mode, if the peak modal values appear in a separate direction, this shows that the mode is uncoupled whereas for coupled modes, the peak appears in more than one directions. This also indicates that there is not a single mode in any direction which gives more than 20% contribution. This implies that there is a need to consider more modes in the response calculation for such type of bridges. However, for flutter analysis, other factors play an important role such as frequency separation of modes and mode shape similarity. Therefore only effective modal mass is not sufficient to select the modes for a simple two-mode analysis.
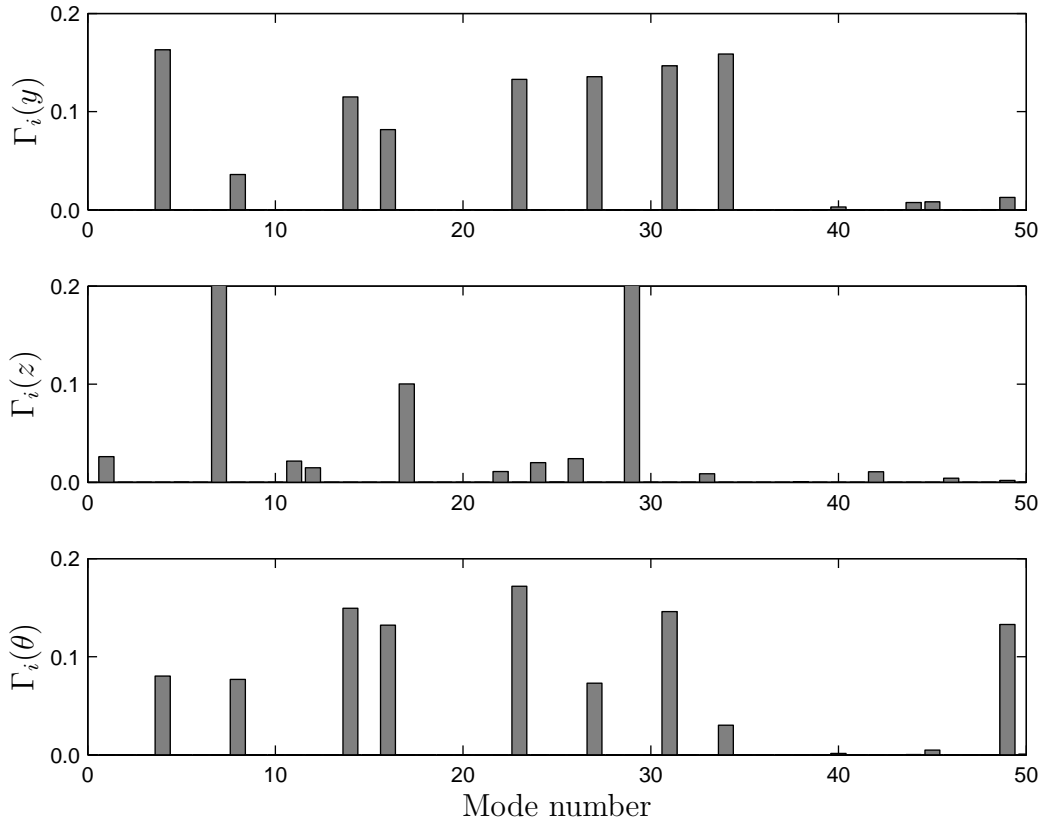
Figure 6.7: Modal contribution from the model of the Lillebælt Suspension Bridge,
(top) translational in y-axix,
(middle) translational in z-axis,
(bottom) rotational about x-axis.

Figure 6.8 shows the cumulative contribution of the effective modal mass in each direction. This sum is 1 or 100% for the first 50 modes. The jumps in the curves show the contribution of the mass in the mode in that direction.

6.4 Aerodynamic Properties from CFD Simulations

Motion-induced aerodynamic forces for real cross sections can be determined from numerical forced vibration simulations on the 2D section models. The resulting lift force and moment time histories are used to compute the aerodynamic derivatives as explained in Section 4.4.2.
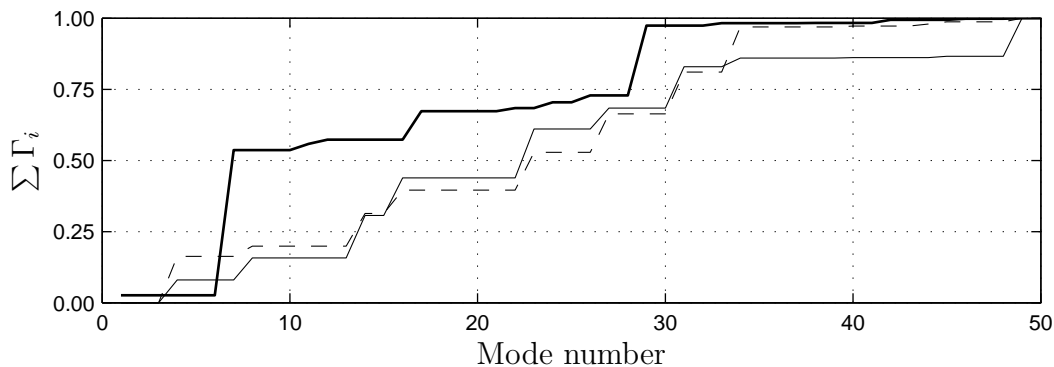
Figure 6.8: Cumulative modal mass contribution from the model of the Lillebælt Suspension Bridge:
(——) vertical bending,
(——) torsional,
(– –) lateral bending.

A flow solver VXflow developed by Morgenthal [128] based on the VPM has been used here. Static, as well as forced vibration simulations, have been performed on the bridge cross sections. Aerodynamic derivatives then can be computed in a least-squares sense from the resulting force and moment time histories of the sections. The CFD code has already been validated before in [120, 121, 122, 123] and shown to have acceptable results, therefore, this study does not focus on the validation of the code.

6.4.1 Simulations on a Flat plate

Forced vibration simulations are performed first on a thin flat plate and compared with the analytical values. A thin rectangular section of aspect ratio (B/D=100) has been used in the CFD simulations as shown in Figure 6.9. The simulations ensure no-slip boundary condition. Table 6.4 shows numerical parameters used in these simulation. The simulations are carried out to reach non-dimensional time step $t^*= tU_\infty/B$ around 45. Here t is the dimensional time. The section is given a predefined displacement or rotational oscillations with known period and amplitude as shown in Figure 6.10.

Figure 6.9: Forced vibration simulation on a flat plate (aspect ratio 100): instantaneous vortex pattern.

The aerodynamic derivatives for the flat plate section are then computed the measured lift $C_L(t)$ and moment $C_M(t)$ as described before in Section 4.4.2. The resulting aerodynamic derivatives are plotted in Figure 6.11 where analytical flat plate values are also shown for comparison.

Aerodynamic derivatives predicted from the CFD simulations are compared to the analytical values of a flat plate from Theodorsen theory. Figure 6.11 shows that all the aerodynamic derivatives match reasonably well except A_4^*. It can also be seen that the aerodynamic derivatives from forced heave simulation show fewer discrepancies as compared to the aerodynamic derivatives from forced pitch simulations where at higher
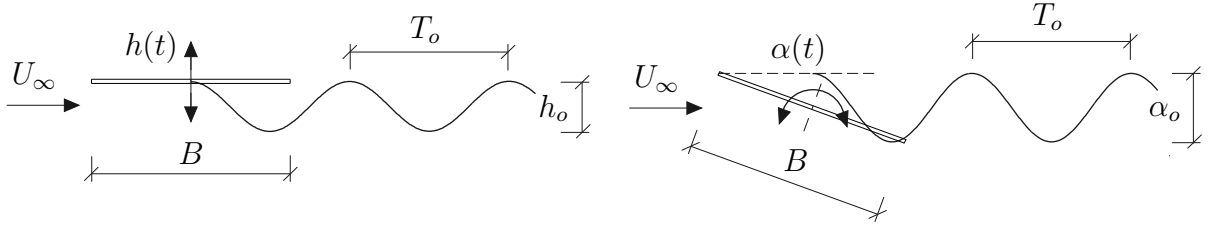
Figure 6.10: Schematic of forced vibration simulations:
(left) forced heave motion,
(right) forced pitch motion.

Table 6.4: Forced vibration simulations on a flat plate (aspect ratio 100): numerical parameters.

N_{step}	8000	v_r	2-16
N_{panel}	336	$t*$	48
L_{panel} [m]	0.2	T_o [s]	6.6-52.8
$\Delta t*$	1.0	U_∞ [m/s]	10
Δt [s]	0.0198	h_o [m]	0.5
ν [m^2/s]	0.000015	α_o [°]	5
$N_{particle}$	80,000	Re	22×10^6

reduced speeds v_r, the difference becomes greater. This comparison is not sufficient to see the prediction quality of these aerodynamic derivatives. The aerodynamic derivatives are used in computing flutter limit, therefore flutter limit could also be used as a quality measure. For this purpose flutter limit was determined using aerodynamic derivatives and structural properties of Structure A (cf. Table 6.7). Figure 6.12 shows the effect each of aerodynamic derivative of thin rectangular plate computed from the forced vibration simulations on the flutter limit by replacing each analytical flat plate derivatives with the one computed from the CFD. This means that for the case of H_1^* all of the analytical flat plate aerodynamic derivatives were used from Eq. (4.35) except H_1^* which was taken from the CFD simulations as shown in Figure 6.11 with dot symbols. It can be seen in Figure 6.12 that A_1^*, A_3^* and A_4^* show the most significant effect in the flutter limit prediction for this case. However, often aerodynamic derivatives H_4^* and A_4^* are of little significance [247] and are ignored in the analysis. The representations of motion-induced forces initially introduced by Scanlan and Tomko [97] also did not include aerodynamic derivatives H_4^* and A_4^*. It is important to mention here that it is not expected to get exactly the same aerodynamic derivatives as the assumptions made in the analytical approach are different than in the CFD simulations. The main idea of generating these plots is to provide a quantitative comparison of the computed aerodynamic derivatives from numerical simulations and analytical values.

6.4.2 Simulations on Reference Sections

The forced vibration simulations have been performed separately in the sinusoidal heave and pitch motions. These simulations provide aerodynamic derivatives H_i^* and A_i^* (with i=1,...,4). The lateral aerodynamic derivatives could not be computed from the CFD simulations as the lateral forced vibration scheme is not yet implemented in this CFD code. These tests are often not performed. Therefore quasi-steady values were
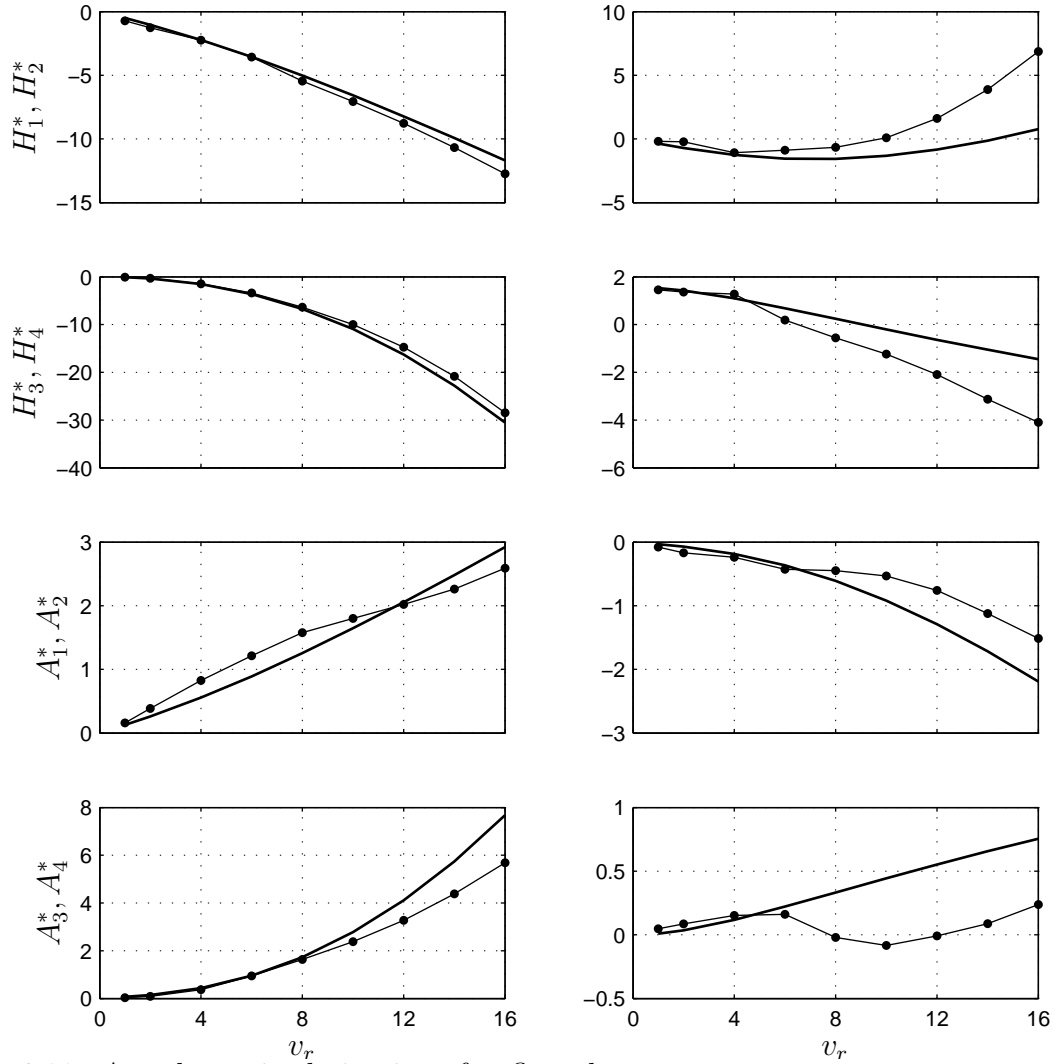
Figure 6.11: Aerodynamic derivatives for flat plate:
(——) Theodorsen theory,
(—•—) forced vibration analysis on a flat plate (aspect ratio 1:100).
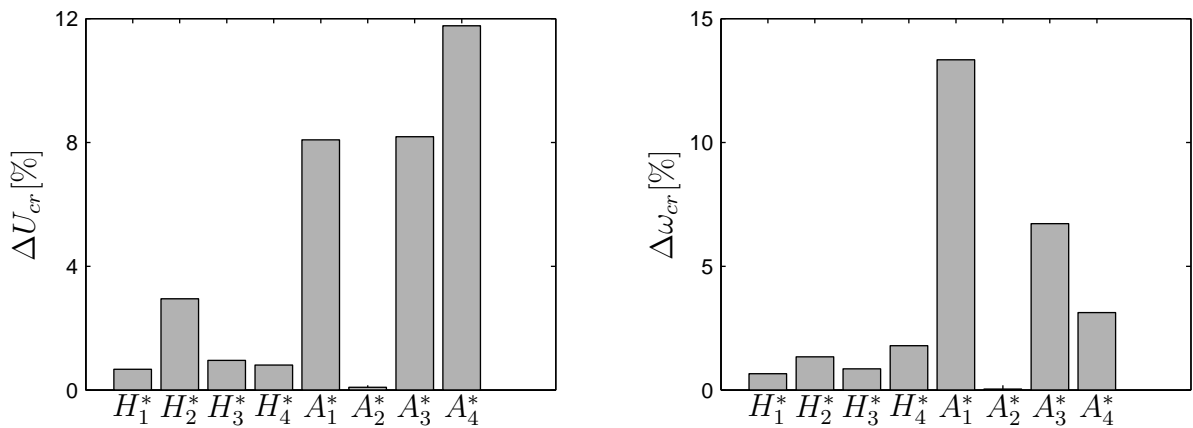
Figure 6.12: Variation in flutter prediction by replacing each time a single aerodynamic derivative obtained from the CFD simulations in analytical flat plate aerodynamic derivatives (using dynamic properties of Structure A):
(left) change in critical flutter limit,
(right) change in critical flutter frequency.

selected to be used for the lateral aerodynamic derivatives as provided in Table 5.3. The quasi-steady aerodynamic derivatives are the functions of time averaged static wind coefficients (C_D, C_L and C_M) and their slopes (C'_D, C'_L and C'_M) at zero angle of attack ($\theta = 0$) of the section. Therefore static simulations were performed first on Structure A. The flow past the bridge section was simulated to compute time averaged (or static) wind coefficients of drag C_D, lift C_L and moment C_M for a various angle of attacks θ. The slopes of coefficients were also calculated by fitting a linear function. The results of the simulations are presented in Figure 6.13.
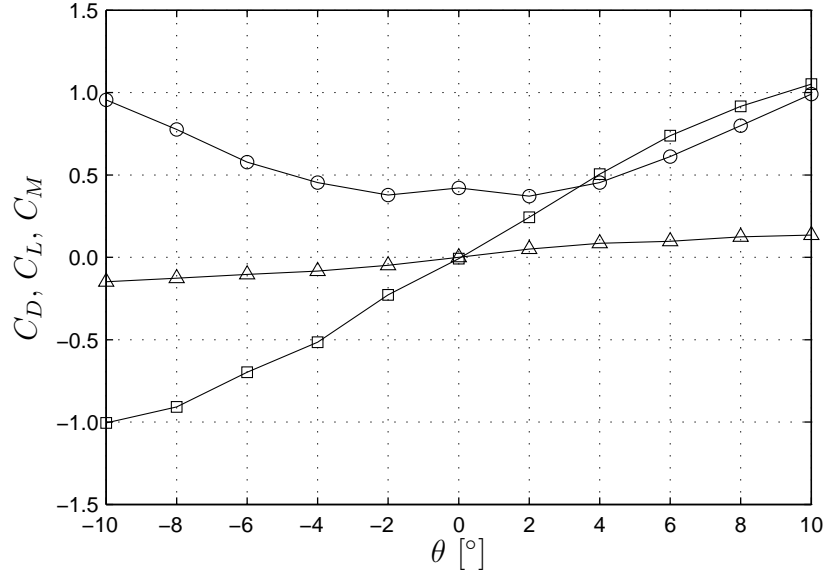
Figure 6.13: Static simulations on Structure A: static wind coefficients, (○) C_D, (□) C_L, (△) C_M
(at $\theta=0$, $C_D=0.422$, $C'_D=0.002$, C_L=-0.008, C'_L=0.111, C_M=0.0, C'_M=0.002).

The forced vibration simulations were then performed for Structure A and Structure H over a range of reduced speeds for the reference sections (cf. Figure 6.1). The aerodynamic derivatives were then computed from the resulting force and moment time histories. The aerodynamic derivatives are shown in Figure 6.16. Analytical values for a flat plate are also plotted for comparison. The quality of the results varies along the v_r range depending on different factors such as time step, the length of simulated time history and the quality of the least-squares fit. In Wind Engineering, aerodynamic derivatives H_4^* and A_4^* are often neglected and are considered insignificant in the prediction of flutter limit [247]. Table 6.5 and 6.6 provide numerical parameters for the forced vibration simulations performed on Structure A and Structure H.

Figure 6.14 shows instantaneous frames from the simulations performed on Structure A. It can be seen that the vortices generated from the section create a wake on the downstream side. As the section is streamlined, the wake is not wide which implies that the lift forces created by the vortex shedding are smaller but have higher vortex shedding frequency. It is important to note that the effect of vortex shedding is removed in the measured lift and moment time histories by least-squares fit to compute aerodynamic derivatives; however, the forces generated by the vortex shedding may influence the quality of the fit. It can be visualised in Figure 6.15 that for Structure H, larger vortices are formed which creates a wider wake on the downstream side. The vortices created in the concave region are trapped for some instances inducing larger pressure on that face which results in increasing the torsional moment on the section.
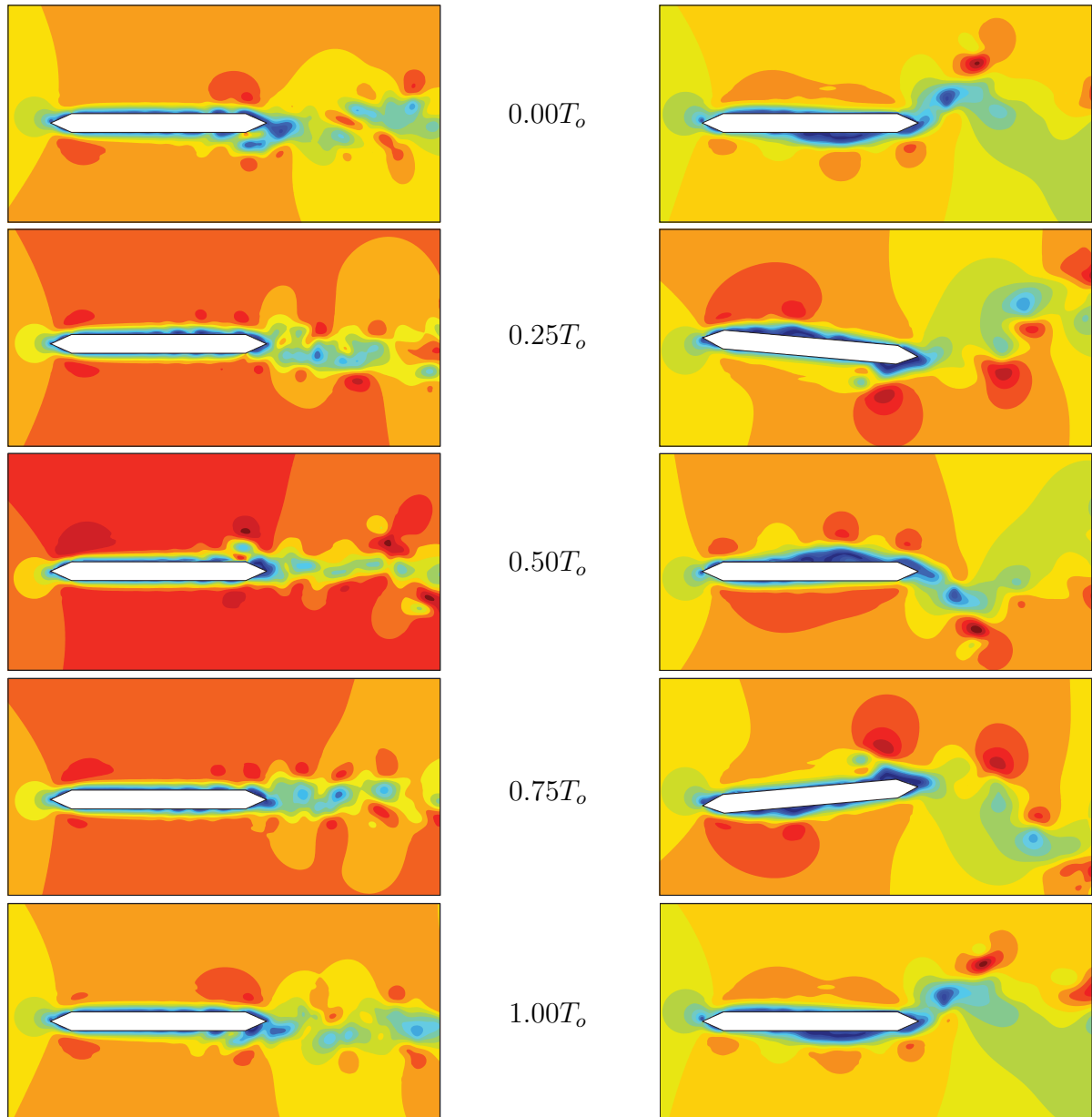
Figure 6.14: Forced vibration simulation on Structure A: instantaneous velocity fields from
(left) forced heave simulations with $h_o = 0.015B$
(right) forced pitch simulations with $\alpha_o = 5°$ (cf. Table 6.5).

Table 6.5: Forced vibration simulation on Structure A: numerical parameters (cf. Figure 6.14).

N_{step}	8,000	v_r	2-16
N_{panel}	340	$t*$	48
$N_{particle}$	80,000	T_o [s]	6.6-52.8
$\Delta t*$	1.0	h_o [m]	0.5
Re	22×10^6	α_o [°]	5
L_{panel} [m]	0.2	Δt [s]	0.02
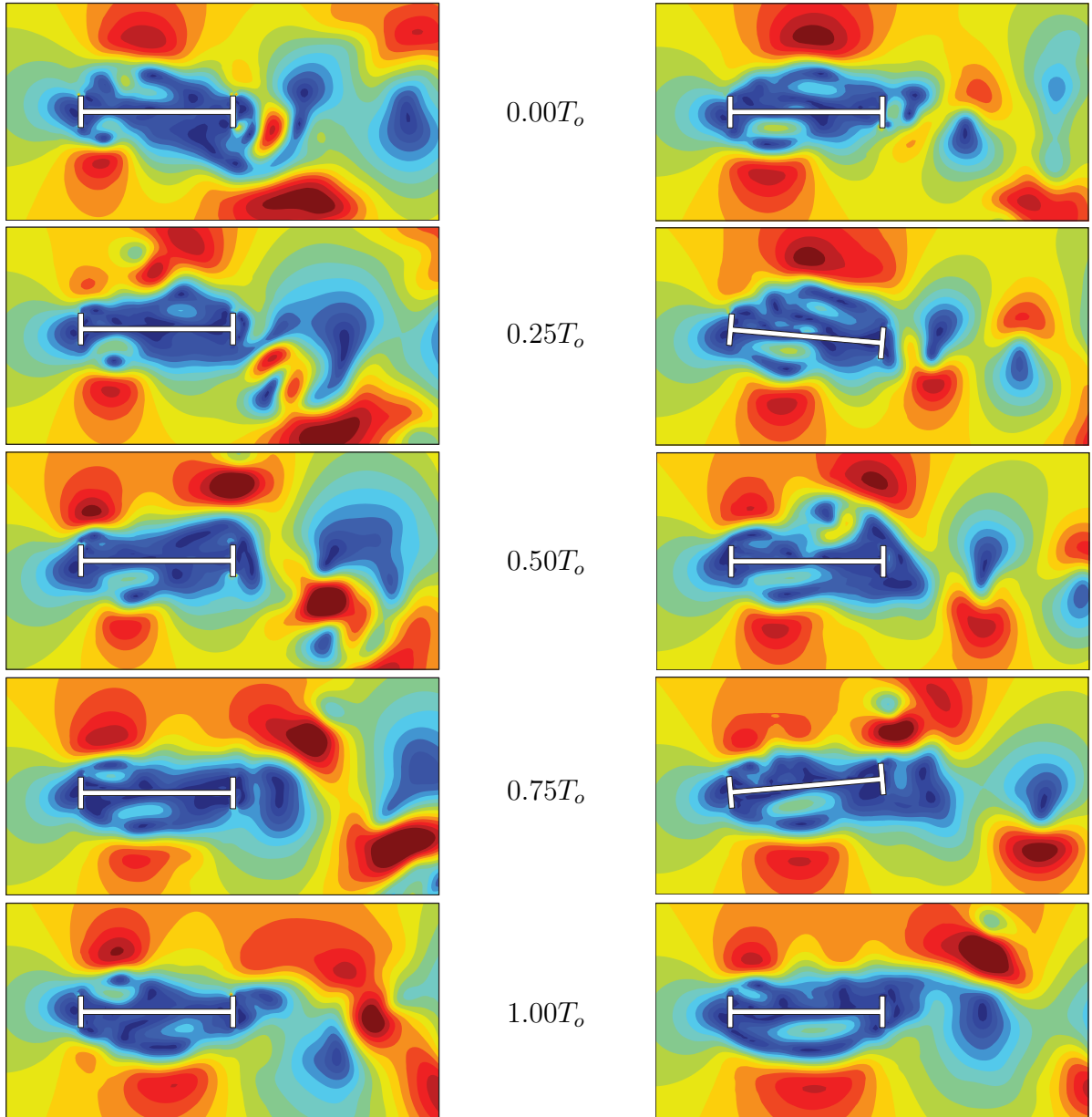
Figure 6.15: Forced vibration simulation on Structure H: instantaneous velocity fields from
(left) forced heave simulations with $h_o = 0.042B$
(right) forced pitch simulations with $\alpha_o = 5°$ (cf. Table 6.6).

Table 6.6: Forced vibration simulation for Structure H: numerical parameters (cf. Figure 6.15).

N_{step}	10,000	v_r	1-8
N_{panel}	328	$t*$	85
$N_{particle}$	70,000	T_o [s]	1.2-9.6
$\Delta t*$	1.0	h_o [m]	0.5
Re	8×10^6	α_o [°]	5
L_{panel} [m]	0.1	Δt [s]	0.01

In the high Reynolds number range, the effect of Reynolds number is low and the wind force only depends on section geometry. Starossek et al. [111] performed several tests in water tunnel to determined the aerodynamic derivatives for different cross sections and studied the effect of amplitudes and Reynolds number. It was found that Reynolds number has an insignificant effect on the prediction of aerodynamic derivatives.

Some important factors which must be considered in performing the forced vibration simulations are as follows:

- Relative amplitude of vortex shedding forces and motion-induced forces: if the peaks from vortex shedding forces are larger in the force time histories as compared to motion-induced forces then the fitting quality may decrease. This can be improved by using the larger amplitude of oscillation for forced vibration simulations.

- Length of force time-history: there should be a sufficient number of cycles completed to achieve a better quality fit. At least 5 to 6 cycles of oscillations are necessary.

- Period of oscillation: this is also related to the length of time series. The period of oscillation is decided by the required reduced speed. If the period is large, then computational cost increases.

- Size of the time step: this should be decided based on capturing the motion of the section as well as resolving vortex shedding and flow around the body. The vortex shedding frequency is often significantly higher than the frequency of forced oscillation in these simulations.

- Number of panels: this should be adequate so that enough particles are generated for the solution but should not be very large to avoid excessive runtime.

The aerodynamic derivatives for Structure A show similar values as that of analytical values. This cross section is very similar to a flat plate and due to this reason it also follows the similar trend. The aerodynamic derivative H_1^* is negative for the whole range of reduced speed v_r for which it is computed. This shows a stable SDOF behaviour of this section against vertical instability. The aerodynamic derivative A_2^* is related to the SDOF torsional stability. Negative values of this derivative imply that this section is also not prone to torsional flutter.

The aerodynamic derivative H_1^* for Structure H also show similar behaviour to that of Structure A; however, the aerodynamic derivative A_2^* becomes positive after a certain reduced speed v_r which mean that this section is susceptible to the SDOF torsional flutter. In such cases, the SDOF critical limit can be determined without the need of performing an eigenvalue analysis as explained in Section 5.6.4. Such cross sections with unstable behaviour can be avoided by selecting other types of cross sections which are more streamlined or the behaviour of this cross section can be improved by using fairings on the sides to make the cross section streamlined.

6.5   Flutter Limits of Reference Objects

In this section the models explained in Chapter 5 are applied on the reference objects (cf. Section 6.2) to compute the flutter limits. The advantages and limitations of the
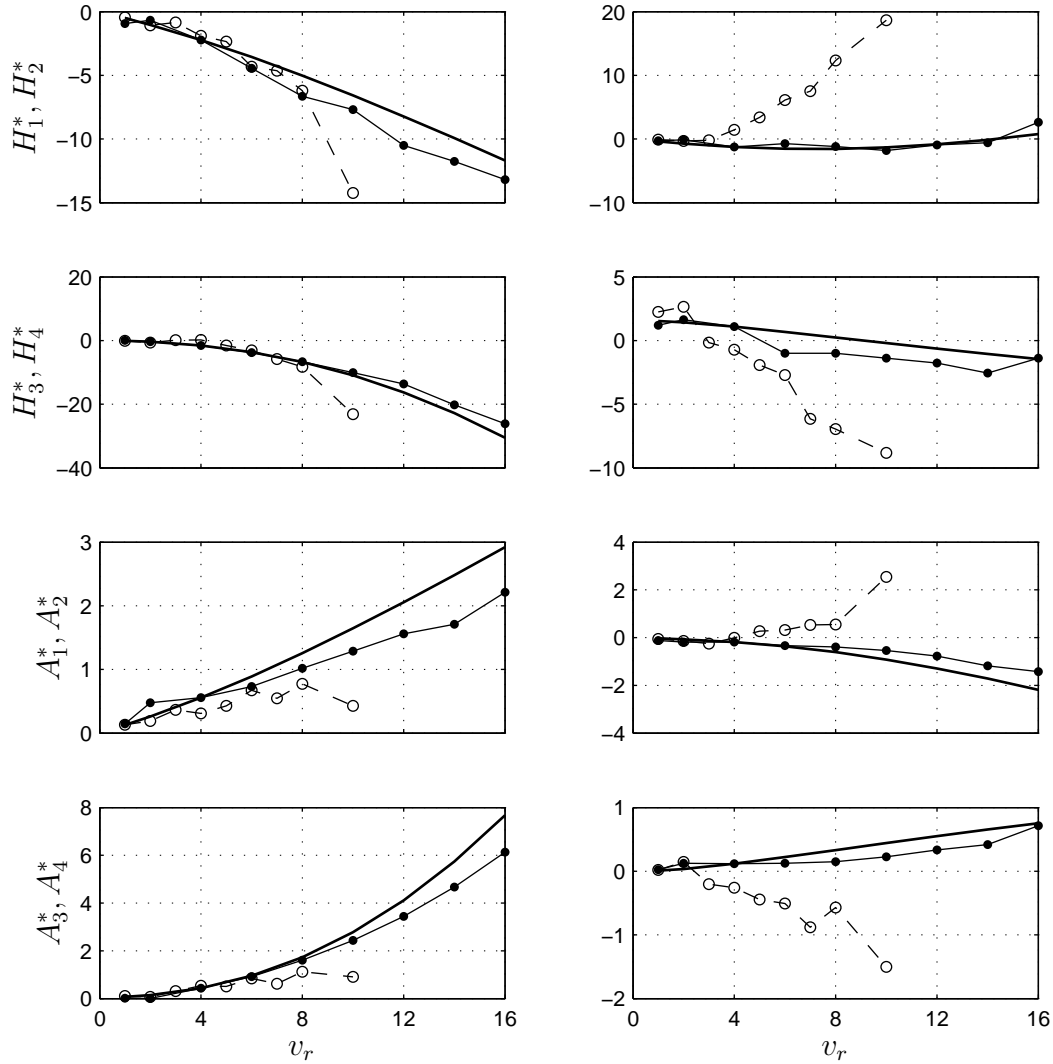
Figure 6.16: Aerodynamic derivatives (H_i^* and A_i^* where $i = 1, \ldots, 4$):
(——) flat plate by Theodorsen theory,
forced vibration analysis on
(——•——) Structure A and
(– –∘– –) Structure H.

models are explained. The assumptions made during this process are also discussed at each step and finally the flutter limits are predicted.

The structural properties of the selected reference structures are summarised in Table 6.7. These parameters have been used in the 2D flutter analyses. For 3D analysis, structural properties presented in Section 6.3 have been utilised. The non-dimensional parameters are also presented in the last three columns of the table by using Eq. (6.1). Comparing these non-dimensional parameters to the list of long-span bridges provided in Table 6.1 implies that the selected structures well represent the range of structural properties. More discussion related to these non-dimensional parameters follows in Chapter 7.

Table 6.7: Basic data and structural properties of the reference bridge sections [33][38].

Structure	Span	B	m	I	f_h	f_α	ξ_h, ξ_α	μ	r_α	γ_ω
	[m]	[m]	[kg/m]	[kgm^2/m]	[Hz]	[Hz]	[-]	[-]	[-]	[-]
A	600	33	11,667	10,17,778	0.156	0.500	0.01	17.1	0.283	3.21
H	854	12	4,250	1,77,730	0.130	0.200	0.01	47.2	0.539	1.54

6.5.1   Fully-Analytical (Model#1)

Using the structural parameters for Structure A (cf. Table 6.7), and performing eigenvalue analysis presented in Section 5.4, the flutter limit was found 94 m/s. The flutter limit is determined when the real part of at least one eigenvalue becomes positive with the corresponding positive imaginary part. Figure 6.17 shows the eigenvalue paths from the flutter analysis of a 2DOF system using Theodorsen analytical flat plate values. The imaginary parts of the eigenvalues are related to the oscillations whereas the real parts describe the stability. When the real part of eigenvalues with increasing wind speed becomes positive, the system becomes unstable and the flutter limit is reached. If the imaginary part becomes zero, this means that there is no oscillation in the response and when this eigenvalue becomes positive real that means the system has divergence instability.
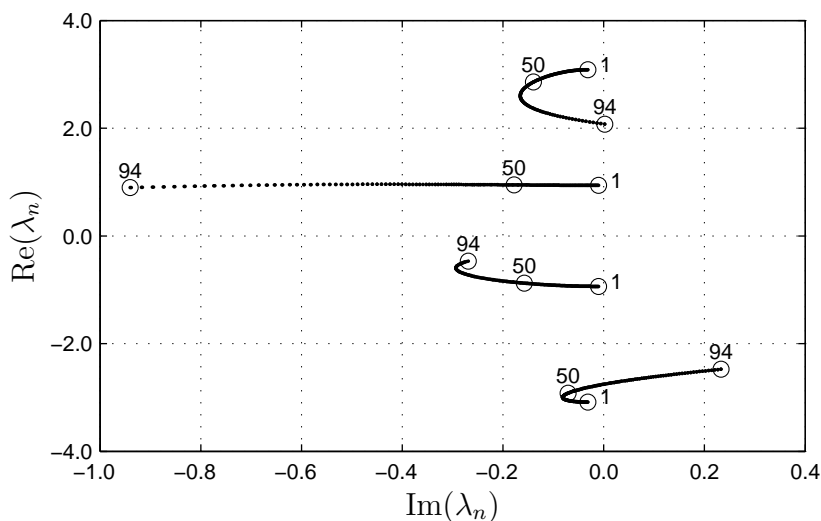
Figure 6.17: Fully-analytical model: sample 4 eigenvalue paths λ_n as wind speed U_∞ increases from 1 m/s to the instability limit of 94 m/s using Eq. (4.24a) (start U_∞=1 m/s, ΔU_∞=0.5 m/s).

The analysis was also performed on the reference structures by considering different representations of Theodorsen circulation function (cf. Section 4.3.1). The resulting flutter limits are compared in Table 6.8. Eq. (4.24a) uses Hankel and modified Bassel functions. The results show that the prediction by Eq. (4.24f) is closest to Eq. (4.24a), whereas maximum difference from Eq. (4.24a) is shown by Eq. (4.24e) which is upto 3%.

A major limitation of this approach is that it does not consider the shape of the structure which plays a decisive role in the flutter analysis. It considers a 2D flow and assumes for a 2DOF system that the selected heave and pitch modes have exactly the same mode shapes and are more likely to couple. However, the mode coupling greatly depends on the actual mode shapes and the frequency separation between the

Table 6.8: Fully-analytical model: flutter limits computed using different Theodorsen circulation function approximations (cf. Table 6.7).

Eq.	(4.24a)	(4.24b)	(4.24c)	(4.24d)	(4.24e)	(4.24f)	(4.24g)
Structure A							
U_{cr} [m/s]	93.85	95.14	93.98	93.05	91.80	93.85	93.65
U_{cr}/Bf_h [-]	18.23	18.48	18.26	18.07	17.83	18.23	18.19
ω_{cr} [rad/s]	2.075	2.009	2.051	2.074	2.039	2.076	2.064
v_{cr} [-]	8.62	9.05	8.72	8.58	8.59	8.62	8.67
Structure H							
U_{cr} [m/s]	26.15	26.35	25.98	25.84	25.26	26.15	25.94
U_{cr}/Bf_h [-]	16.76	16.89	16.65	16.57	16.19	16.76	16.63
ω_{cr} [rad/s]	1.100	1.096	1.102	1.104	1.100	1.100	1.103
v_{cr} [-]	12.62	12.66	12.35	12.33	12.14	12.62	12.34

modes. Therefore, it is often important to consider the shape-wise similarity of the relevant mode pairs.

6.5.2 Empirical Approach (Model#2)

During the early design stage of the long-span bridges, empirical formulas may be used to estimate the flutter limit. These expressions are easy to use and do not require detailed calculations. Basic structural parameters are required as input and flutter limit can be calculated without performing an eigenvalue analysis. These are usually based on flat plate assumptions; however, the effect of cross section geometry is introduced as a multiplying factor obtained from already existing curves for the similar sections.

Table 6.9 shows the results of flutter limit predictions by the equations explained in Section 5.5. Most of the values by these equations are close to the fully-analytical prediction made in Section 6.5.1 for Structure A. The values obtained through Eqs. (5.25) and (5.26) over estimate the flutter limits. For Structure H, the flutter limit obtained by Eq. (5.20) is also higher than that from fully-analytical prediction shown in Table 6.8.

Table 6.9: Empirical approach: flutter limits computed with different empirical models (cf. Table 6.7).

Eq.	(5.20)	(5.21a)	(5.21b)	(5.21c)	(5.21d)	(5.21e)	(5.23)	(5.24)	(5.25)	(5.26)
Structure A										
U_{cr} [m/s]	92.1	90.0	90.3	90.6	92.0	90.6	90.6	93.0	108.4	102.5
U_{cr}/Bf_h [-]	17.9	17.5	17.5	17.6	17.9	17.6	17.6	18.1	21.1	19.9
Structure H										
U_{cr} [m/s]	33.9	24.0	24.1	24.1	24.5	24.1	24.1	24.8	29.5	34.2
U_{cr}/Bf_h [-]	21.7	15.4	15.4	15.5	15.7	15.5	15.5	15.9	18.9	21.9

The difference in Selberg's predictions is due to representations and assumptions in the constant parameters. This approach is valid only for 2D cases and the mode shapes are assumed to be perfectly similar. Although structural damping is less significant for

flutter limit prediction as compared to the other parameters but these equations do not take into account its effect. The common problem in 2D analyses is that the vertical bending and torsional modes need to be selected in advance by assuming that these modes will provide the most critical outcome and if the wrong modes are selected, the result will be inaccurate.

The divergence limit can also be calculated from Eq. (5.19).   Using properties of Structure A and Structure H, the divergence critical limits were calculated as 96.9 m/s and 33.9 m/s respectively.

6.5.3   Derivative-based Eigenvalue Analysis (Model#3)

The model combinations explained in Section 5.6.5 were used here to compute flutter limits for the reference sections (cf. Section 6.3). The aerodynamic derivatives determined from the CFD forced vibration simulations presented in Section 6.4 have been used here.   Structural parameters given in Table 6.7 were utilised to compute the flutter limit by performing eigenvalue analysis. The flutter limit for Structure A was calculated at 94 m/s.   For comparison, flutter limit predicted by using aerodynamic derivatives presented in Section 6.4.1 for flat plate (aspect ratio 100) is 89 m/s.

Figure 6.18 shows the results of eigenvalue solution.   The four eigenvalues start with increasing wind speed and when at least one eigenvalue enters the positive real quadrant, and the corresponding effective damping becomes zero which shows an unstable response.

Any point on one of these four eigenvalue paths has coordinates represented by its real and imaginary parts. When the eigenvalue paths move towards negative and eventually touch zero imaginary axis, the oscillating response vanishes.   Since the real part is negative, the response would decay and the structure will be stable. If the wind speed is further increased, the imaginary part remains zero, whereas the real part becomes positive which indicates the divergence limit.   This is a hypothetical situation when the flutter boundary is already reached, the system is unstable; however, in the case when onset of flutter is higher, static divergence may reach earlier. Often the torsional frequency of the bridge is larger than the bending frequency and at very high wind speeds, the torsional frequency decreases as a result of the decrease in the effective torsional stiffness and the bridge starts to oscillate with a coupled frequency.

The results of the analysis are presented in Table 6.10. For comparison, results from by using analytical flat plate derivatives for Structure A and Structure H are also displayed which are same as that from Model#1. It is clear from the results that the analytical flat plate prediction diverges significantly from the results obtained by using numerically computed aerodynamic derivatives for the bluff cross sections; however, for a streamlined section, the flutter limit predictions are rather similar.

The surface plots presented in Figure 6.19 help to understand how the effective damping ratios and the effective frequencies change in the increasing reduced speed v_r and oscillation frequency ω space.
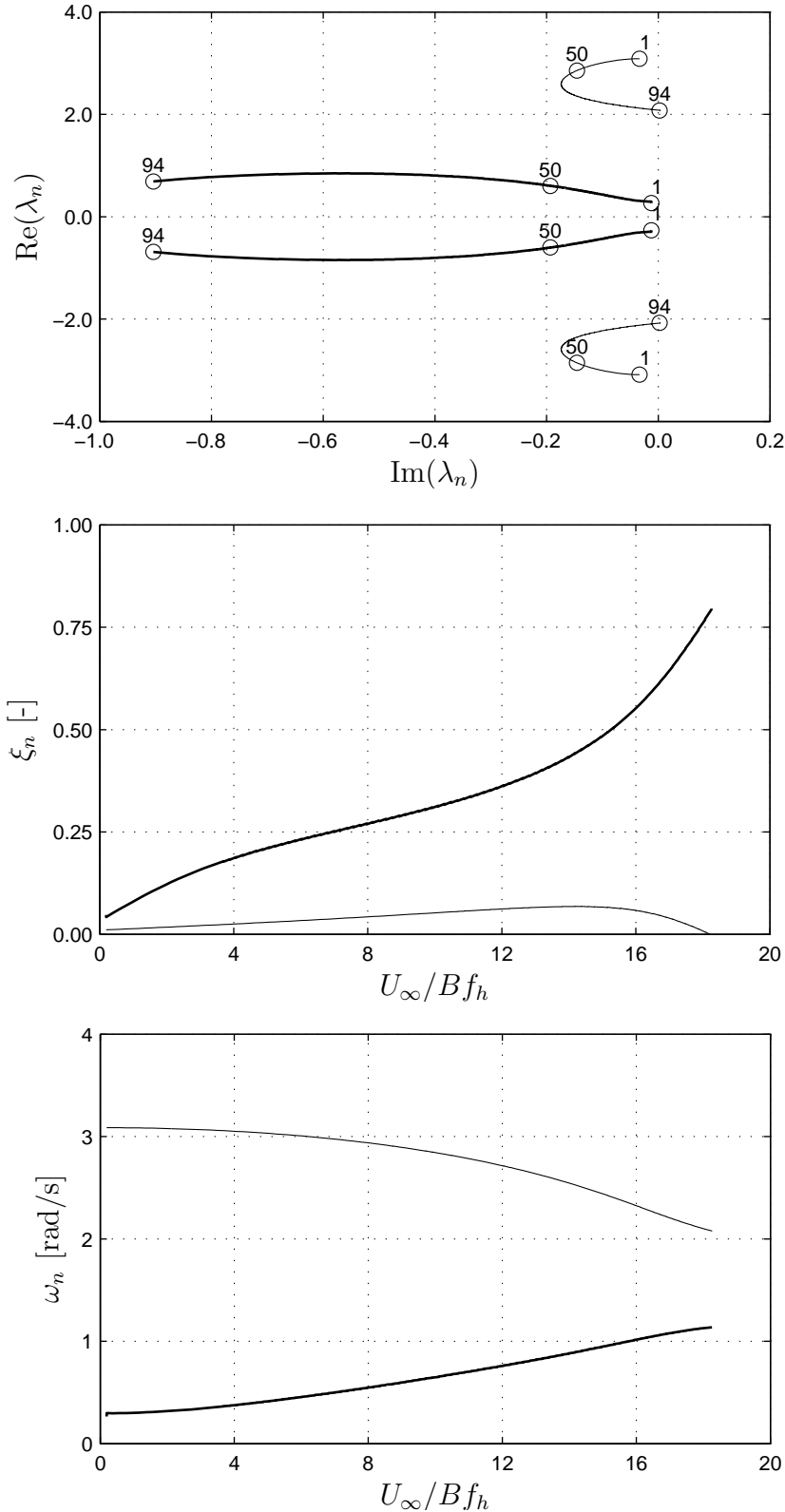
Figure 6.18: Derivative-based eigenvalue analysis: flutter stability analysis for 2DOF system using properties of Structure A and analytical aerodynamic derivatives as wind speed U_∞ increases from 1 m/s to the instability limit of 94 m/s
(top) sample 4 eigenvalue paths λ_n,
(middle) effective damping ratios ξ_n,
(bottom) effective frequencies ω_n.
(——) heave mode,
(——) pitch mode
(start U_∞=1 m/s, ΔU_∞=0.5 m/s, ω_{cr}=2.08 rad/s, U_{cr}/Bf_h=18.2).

Table 6.10: Derivative-based eigenvalue analysis: flutter stability analysis for the 2DOF system.

Structure	Aerodynamic derivatives	U_{cr} [m/s]	U_{cr}/Bf_h [-]	ω_{cr} [rad/s]	v_{cr} [-]
A	Analytical	93.8	18.2	2.08	8.6
H	Analytical	26.2	16.8	1.10	12.6
A	CFD	94.1	18.3	2.21	8.2
H	CFD	11.1	7.1	1.23	4.9
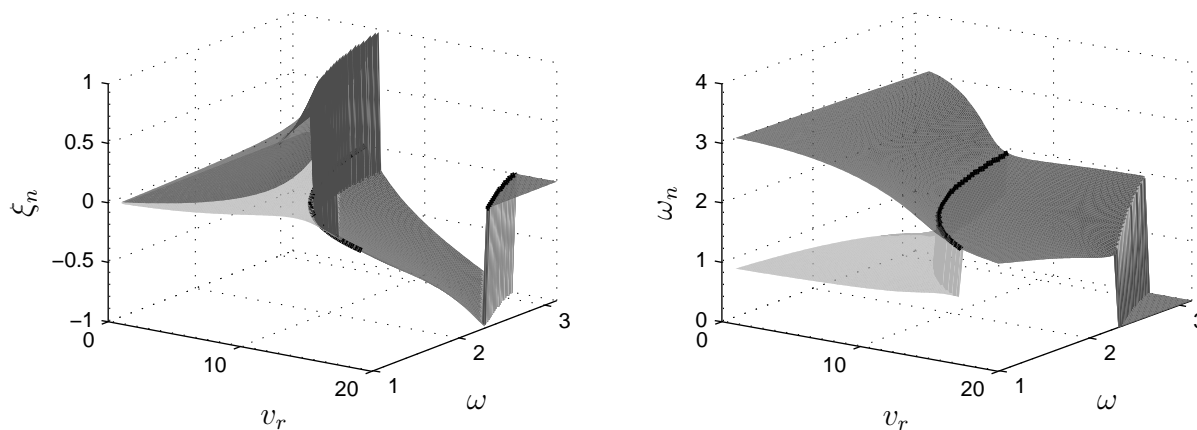
Figure 6.19: Derivative-based eigenvalue analysis: flutter stability analysis for 2DOF system using properties of Structure A and analytical aerodynamic derivatives,
(left) effective damping ratios ξ_n and
(right) effective frequencies ω_n in reduced speed v_r and oscillation frequency ω space.
(▢) heave mode,
(▪) pitch mode,
(——) positions where effective damping is zero and positions where effective heave and pitch frequencies coincide.

6.5.3.1 Divergence Limit

The divergence wind speed predicted by an empirical formula in Section 6.5.2 for Structure A is 96.9 m/s; however, using fully-analytical model it is calculated as 144.0 m/s. In eigenvalue analysis, the divergence limit is reached when the imaginary part of eigenvalues vanishes and this eigenvalue moves towards the right when the real part becomes positive as shown in Figure 6.20. Similarly, analysis was also performed for Structure H and divergence limit was found to be 52.5 m/s, whereas it was predicted to be 33.9 m/s by empirical formula.
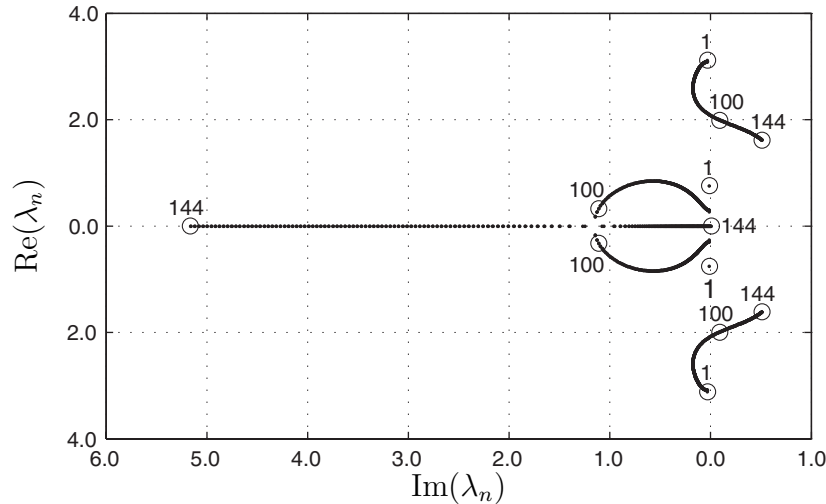
Figure 6.20: Derivative-based eigenvalue analysis: divergence limit for 2DOF system using properties of Structure A and analytical aerodynamic derivatives (start U_∞=1 m/s, ΔU_∞=0.5 m/s).

6.5.3.2 Alternative Approach

Flutter limit can also be computed by treating flutter equations as real and imaginary parts as described in Section 5.6.5.1. Here, the real and imaginary equations are solved for increasing wind speed to make them zero at the same time. This also requires a two-level iterative procedure where at first the wind speed is assumed and at the second level the oscillation frequency is assumed. At each selected wind speed, the assumed oscillation frequency is tested if it nullifies both real and imaginary Eqs. (5.65). Figure 6.21 shows a final curve which satisfies this condition where real and imaginary parts touch the zero axis.

It becomes clear if the values for Eqs. (5.65) are calculated for a series of oscillation frequency ω and the wind speed U_∞ (or reduced wind speed v_r). This approach is presented in Figure 6.22 where two surfaces are shown representing real and imaginary equations. First, the line is determined where these surfaces coincide each other. This line then is traced where it touches zero vertical axis. That combination of ω and v_r will correspond to the critical limit.
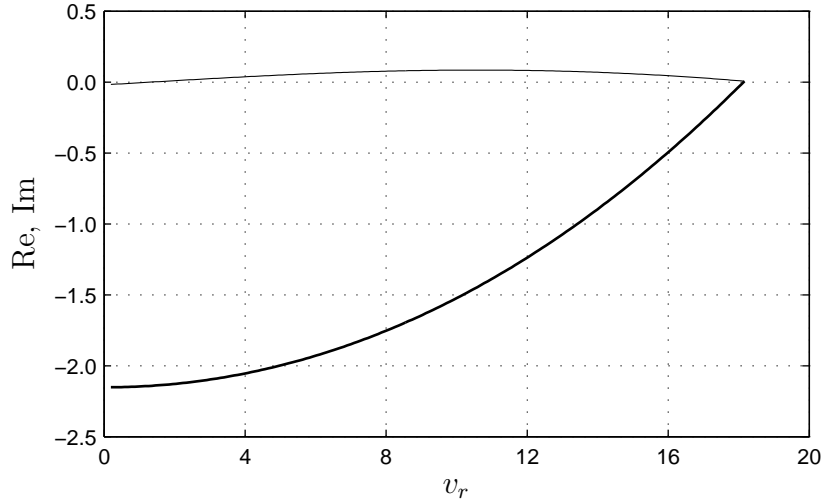
Figure 6.21: Derivative-based eigenvalue analysis: flutter stability analysis for 2DOF system using properties of Structure A and analytical aerodynamic derivatives from alternative approach,
(——) real Eq. (5.65a),
(——) imaginary Eq. (5.65b).
(cf. Section 5.6.5.1) (U_{cr}=93.5 m/s, ω_{cr}=2.10 rad/s, $v_{r_{cr}}$=8.5.)
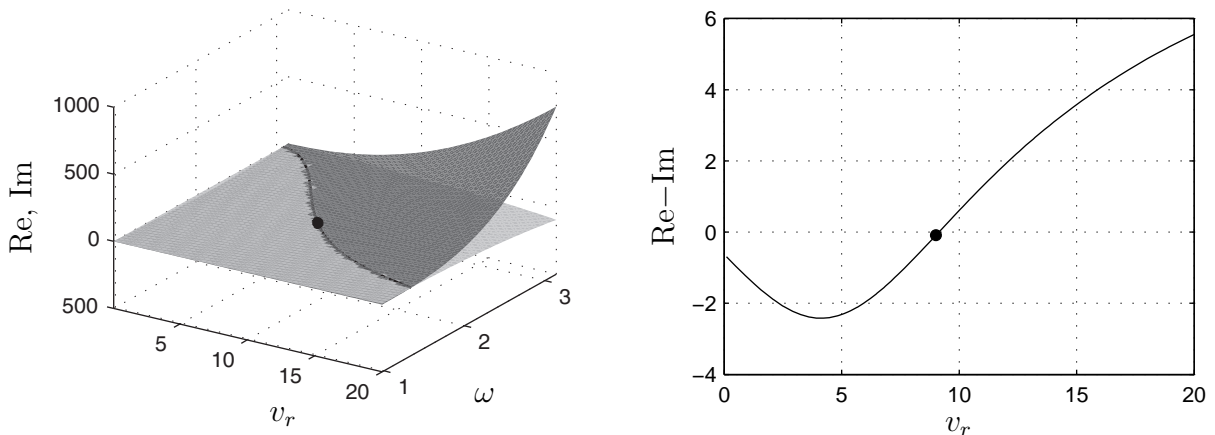
Figure 6.22: Derivative-based eigenvalue analysis: flutter stability analysis for 2DOF system using properties of Structure A and analytical aerodynamic derivatives from alternative approach,
(left) real and imaginary equation
(■) real Eq. (5.65a),
(■) imaginary Eq. (5.65b),
(right) difference of real and imaginary equation.

6.5.3.3   Effect of Mode Shape

The 2D flutter analysis assumes that the selected bending and torsional modes have exactly the same shapes. That means the value of Mode Shape Similarity Factor (MSSF) shown in Eq. (5.70) is 1.0; however, in actual case the mode shapes may be different and the value of the MSSF could be much smaller. Considering the mode shapes in this manner is more realistic but leads to higher flutter limit prediction.

The study of the effect of mode shape is kept limited only to the Lillebælt Suspension

Bridge model. The mode shapes shown in Figure 6.6 are used here to calculate mode shape similarity between bending and torsional modes. The resulting mode shape similarity matrix is shown in Table 6.11. Looking at the mode shapes, a rough estimate of the possible value of the MSSF can be made such as it appears for the first bending and the first torsional mode the value of the MSSF would be larger than the one from the second bending and the second torsional mode. Similarly, there would be lower value of the MSSF if the first symmetrical bending mode is considered with the first unsymmetrical torsional mode. In some cases, it can also be possible to have a smaller value of MSSF for the fist symmetric bending and first symmetric torsion mode. The reason could be the bending restraint provided by the main cables in the first bending mode as this mode requires elongation of the main cables.

The results shown in Table 6.11 also reflect similar outcome. The largest value of the MSSF is obtained for modes $\phi_1 - \phi_8$. Other mode combinations show lower values and the mode shapes which are dissimilar to each other show almost zero values. The largest four values of the MSSF are highlighted as bold in the table which were selected to be used in the flutter analysis to show their contributions. This table can also provide information about which modes might couple in the multimode analysis.

Table 6.11: Mode shape similarity $\psi_{h\alpha}$ [-] matrix by combining bending and torsional modes for the Lillebælt Suspension Bridge model (cf. Figure 6.6).

Bending modes	Torsional modes			
	ϕ_8	ϕ_{20}	ϕ_{27}	ϕ_{36}
ϕ_1	**0.903**	0	0.054	0
ϕ_2	0	**0.771**	0	0.041
ϕ_5	0.003	0	**0.669**	0
ϕ_6	0	0.016	0	**0.876**
ϕ_{11}	0.003	0	0.027	0
ϕ_{18}	0	0.034	0	0.063
ϕ_{22}	0.002	0	0.018	0
ϕ_{28}	0	0.003	0	0.020

The flutter analysis is performed using two modes at a time considering the effect of mode shapes by introducing the MSSF which is shown in Table 6.11. Analytical flat plate aerodynamic derivatives have been used here to show only the effect of MSSF. It is clear from the values obtained that the mode combination $\phi_1 \sim \phi_8$ comprising of the first bending and the first torsional mode would provides the lowest flutter limit. The participation of the MSSF increased the flutter limit from 93.8 m/s to 96.0 m/s. Other mode combinations show much higher critical limits and the MSSF further increases these values as presented in Table 6.12.

Figure 6.23 illustrates the effect of the change in the MSSF on the flutter limits for different mode combinations. It can be visualised that with the MSSF $\psi_{h\alpha}$ value of 1.0, the flutter limits corresponds to the bending and the torsional mode shapes which are exactly the same. It can also be seen that the increase in the flutter limit with the MSSF is nonlinear. The reason is that the MSSF is incorporated only in the coupled aerodynamic derivatives and not in the direct aerodynamic derivatives in the motion-induced aerodynamic forces.

Table 6.12: Derivative-based eigenvalue analysis: flutter stability analysis for 2DOF system using properties of Structure A and analytical aerodynamic derivatives considering the effect of MSSF $\psi_{h\alpha}$ in the flutter analysis (cf. 6.11).

Mode coupling Bending∼Torsional	f_h [Hz]	f_α [Hz]	$\psi_{h\alpha}$ [-]	U_{cr} with $\psi_{h\alpha}$ [m/s]	U_{cr} without $\psi_{h\alpha}$ [m/s]
ϕ_1-ϕ_8	0.156	0.500	**0.903**	96.0	93.8
ϕ_2-ϕ_{20}	0.161	1.031	**0.771**	208.4	198.2
ϕ_5-ϕ_{27}	0.294	1.391	**0.669**	287.4	265.6
ϕ_6-ϕ_{36}	0.460	1.843	**0.876**	360.0	349.9
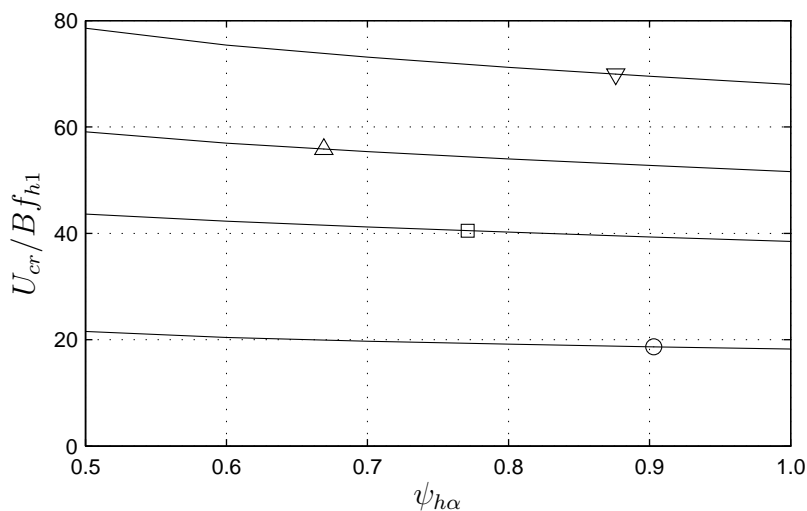
Figure 6.23: Derivative-based eigenvalue analysis: flutter stability analysis for 2DOF system using properties of Structure A and analytical aerodynamic derivatives considering the effect of MSSF $\psi_{h\alpha}$ in the flutter analysis,
($\circ$) ϕ_1-ϕ_8,
($\square$) ϕ_2-ϕ_{20},
($\triangle$) ϕ_5-ϕ_{27},
($\triangledown$) ϕ_6-ϕ_{36},
(f_{h1}=0.156 Hz, first heave frequency)(cf. Table 6.12).

6.5.3.4 Multimode Flutter Analysis

A multimode flutter analysis was performed on the Lillebælt Suspension Bridge model using the approach explained in Section 5.6.5.2. Full-order analysis can also be made using all modes of the bridge; however, to better understand the underlying physics behind the phenomenon, different combinations of selected modes have been used here. Only the deck modes are utilised in the analysis and the modes related to tower and cables were not considered. In some cases, the significant effect of higher modes in the flutter limit prediction was observed instead of considering only the fundamental bending and torsional mode [101, 207, 212, 222, 230]. In this study, the analysis is restricted only to consider deck modes.

A code was written in MATLAB for multimode flutter analysis. This requires basic information about the structure under study such as nodal coordinates, nodal mass, element information, modal properties and aerodynamic derivatives. This information is used to assemble the structure to perform multimode flutter analysis. Figure 6.24 shows the model from the flutter analysis code with coordinate axes considered.
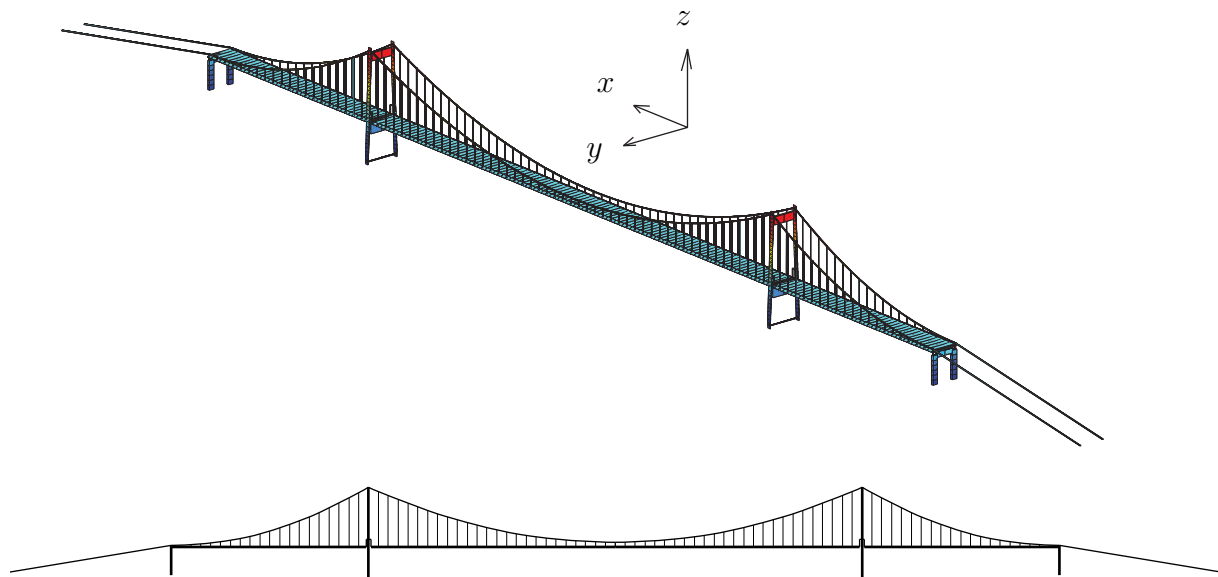
Figure 6.24: Model of the Lillebælt suspension bridge from multimode flutter analysis code:
(top) 3D view,
(bottom) elevation.

A modal damping ratio of 1% has been used to model the structural damping. Some basic deck modes are identified and shown in Table 6.3; however, the first 50 mode shapes are listed in Table C.1 and C.2. The selected mode shapes are also shown in Figure 6.6 where dominant vertical bending modes, lateral modes and torsional deck modes are separately shown. It can also be visualised in this figure that the first symmetrical torsional mode and the first unsymmetrical torsional modes show strong coupling with the lateral bending. This implies that there exist structural coupling of modes which is important to be noted before using these modes in the flutter solution. After retrieving mode shapes from the modal analysis, the modal mass for each mode shape is calculated. This is also provided in Table 6.3 and in Table C.1 and C.2 for the first 50 modes.

The analysis was performed on the Lillebælt Suspension Bridge by using analytical

aerodynamic derivatives as well as derivatives computed from the CFD simulations on Structure A to compare with the flutter limit predicted from the 2D flutter analyses. The results of this analysis are shown in Table 6.13 and Figure 6.25. The iterative analysis is performed for the increment of wind speed U_∞. The wind speed step ΔU_∞ is adjusted in the code automatically such that near to flutter limit the step is reduced to half for each iteration.

Table 6.13: Derivative-based eigenvalue analysis: multimode flutter analysis for the Lillebælt Suspension Bridge (cf. Table 6.3 and Figure 6.6).

Mode combination		U_{cr}	U_{cr}/Bf_h	ω_{cr}	v_{cr}	$U_{cr}/U_{cr,I}$	Time
		[m/s]	[-]	[rad/s]	[-]	[-]	[s]
Analytical aerodynamic derivatives for flat plate							
I	1+8	98.1	19.05	1.984	9.4	1.00	<1
II	1+4+8	98.1	19.06	1.985	9.4	1.00	<1
III	2+20	220.4	42.81	3.633	11.6	2.25	<1
IV	2+20+21	217.7	42.30	3.471	11.9	2.22	1
V	1+4+5+8+27+44	98.0	19.04	1.991	9.4	0.99	2
VI	2+6+20+21+28+36+47	216.1	41.98	3.556	11.6	2.20	5
VII	1+4+5+8+11+22+27+44	98.1	19.05	1.990	9.4	0.99	4
VIII	2+6+18+20+21+28+36+47	217.2	42.20	3.522	11.7	2.22	7
IX	all above	98.1	19.05	1.990	9.4	0.99	33
CFD aerodynamic derivative for Structure A							
I	1+8	98.3	19.10	2.154	8.6	1.00	8
II	1+4+8	98.3	19.11	2.155	8.6	1.00	9
III	2+20	241.0	46.83	3.758	12.2	2.45	14
IV	2+20+21	246.8	47.95	3.415	13.7	2.50	18
V	1+4+5+8+27+44	101.0	19.62	2.123	9.0	1.02	35
VI	2+6+20+21+28+36+47	237.0	46.05	3.663	12.3	2.40	36
VII	1+4+5+8+11+22+27+44	98.3	19.10	2.158	8.6	0.99	56
VIII	2+6+18+20+21+28+36+47	244.4	47.48	3.506	13.2	2.48	44
IX	all above	102.3	19.87	2.107	9.2	1.03	224

Considering only the first bending mode and the first torsional mode in multimode flutter analysis provides flutter limit as 98.1 m/s. This is slightly higher as compared to a 2D flutter analysis made by taking into account mode shapes in Section 6.5.3.3 which is 96.0 m/s. The reason for this could be the mass per unit length considered in the 2D flutter analysis which was 11,677 kg/m (cf. Table 6.7); however, if the total deck translational mass in z-axis (i.e. 12.5 t) is taken from the model and divided over the deck length (i.e. 1080 m) the distributed mass results in 11,563 kg/m. The same is the case with the torsional mass about x-axis which is 1089.5 tm^2 for full deck length and 10,08,700 kgm^2/m for unit length that is lesser as compared to 10,17,778 kgm^2/m which was considered for 2D analysis (cf. Table 6.7). As it has been explained earlier that the deck of the Lillebælt Suspension Bridge has special joints at the towers. The reason for this reduction in mass is the discontinuation of the deck at these locations. The actual distributed masses in translation and rotation directions can also be used in
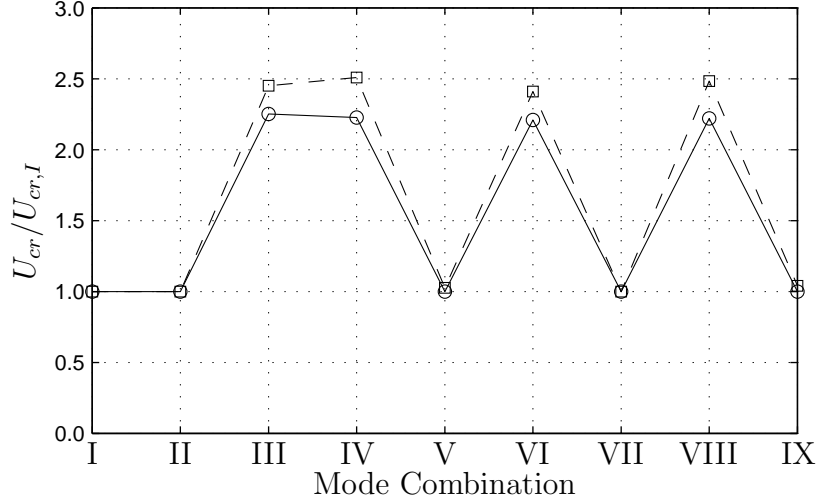
Figure 6.25: Derivative-based eigenvalue analysis: multimode flutter analysis using
($\circ$) analytical aerodynamic derivatives,
($\square$) CFD aerodynamic derivative for Structure A
($U_{cr,I}$: flutter limit for mode combination I)(cf. Table 6.13).

the 2D flutter analysis and the flutter limit may be computed to show the difference. However, in the full-mode analysis, it is also important to note that the modal mass is calculated by the nodal mass and the corresponding modal displacements.

The results show that the symmetrical modes provide lowest flutter limit whereas unsymmetrical modes provide much higher flutter limit indicating that the symmetrical modes couple before. It is also observed that adding more modes does not decrease flutter limit as expected. The eigenvalue paths are shown in Figure 6.26 for one of the mode combinations. The corresponding effective frequencies and effective damping ratios are also presented. These effective values are obtained after sorting and rearranging the eigenvalues as explained in Section 5.6.5.2. Untreated values are shown in Figure C.2 for reference. The instability limit is achieved when at least one of the eigenvalues become positive real or the effective damping becomes zero. The corresponding effective frequency shows that how it has changed with increasing wind speed. The results of multimode analysis by using CFD aerodynamic derivatives for Structure A are also shown in Figure C.4 for selected mode combination (V). Untreated values are also shown in Figure C.3 for reference.

The computational time is also important especially when such analysis are used for the variance based sensitivity and uncertainty analyses. Figure 6.27 shows the relative computation time with respect to the number of modes considered in the analysis. The computation time increases exponentially by adding more modes. This also depends on the type and complexity of the structure. A large number of nodes and a higher onset of flutter requires more time of analysis.
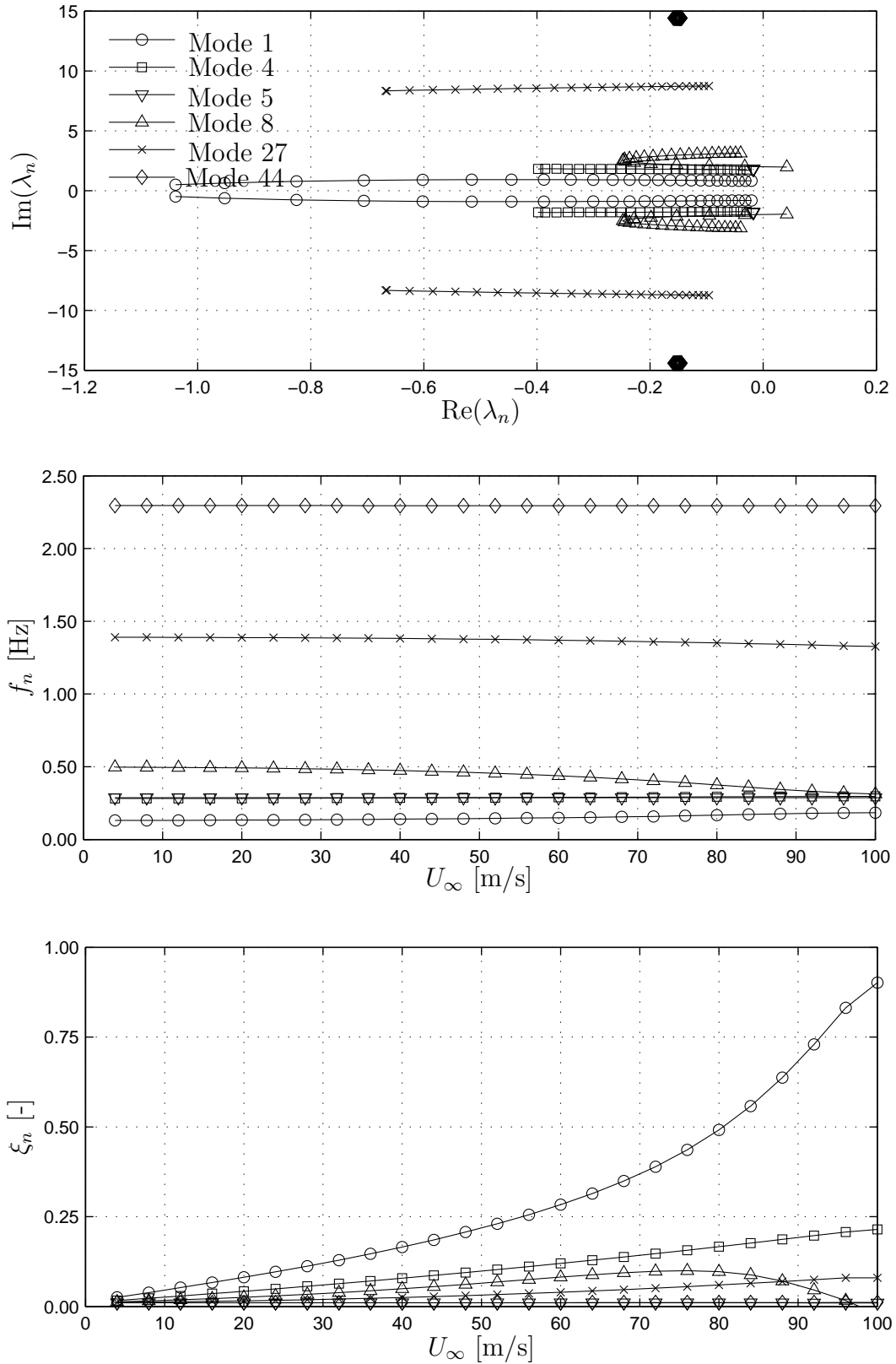
Figure 6.26: Derivative-based eigenvalue analysis: multimode flutter analysis for the Lillebælt Suspension Bridge using analytical aerodynamic derivatives:
(top) eigenvalue paths λ_n as wind speed U_∞ increases to the instability limit,
(middle) effective frequencies f_n,
(bottom) effective damping ratios ξ_n,
(mode combination V, start U_∞=1 m/s, ΔU_∞=0.5 m/s, U_{cr}=98.0 m/s).

115
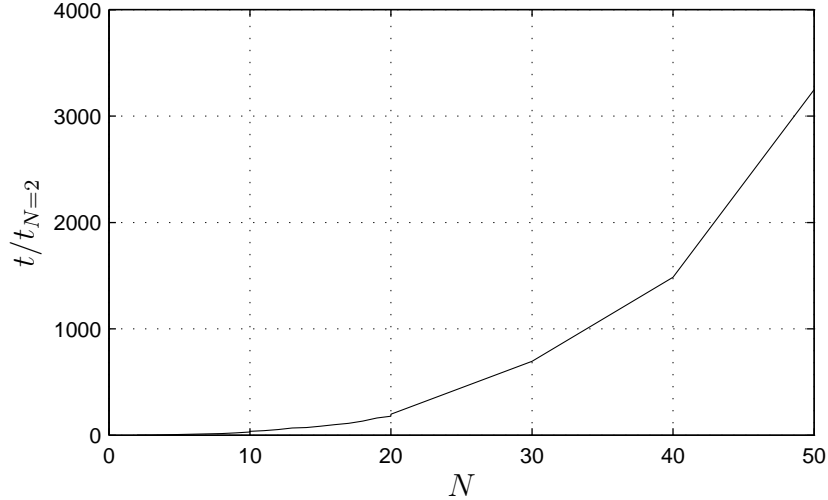
Figure 6.27: Derivative-based eigenvalue analysis: computation time for multimode flutter analysis (N: number of modes, $t_{N=2}$: time for 2 modes only).

6.5.4 Derivative-based FSI Simulations (Model#4)

The approach presented in Section 5.6.6 has been applied and flutter limit for the reference bridge was computed. The parameters presented in Table 6.14 have been used in the analysis. The simulation is set to performed time integration for a total of 150 discrete points in time. As a result response for displacement, velocity and acceleration are recorded for both heave and pitch cases where one cycle of oscillation has around 100 points. The effect of number of points per cycle on the results is shown in Figure 6.29a. The least-squares fit is then performed by selecting 10 points on the response curve for the fitting at a time and then with the increment of 1 again 10 points are selected. This process is repeated 50 times. First few points in the calculated response are ignored to have only steady response.

Table 6.14: Derivative-based FSI Simulations: numerical parameters.

Initial velocity	Initial displacement	Time step	Start velocity	Velocity step	Convergence limit
$\dot{h}_0$ [m/s]	h_0 [m]	Δt [s]	U_{start} [m/s]	U_{step} [m/s]	tol [-]
0.015	0.0	0.01	1	0.5	0.001

Figure 6.28 demonstrates the fitting on the displacement, velocity and acceleration response using 10 selected points on the same time axis. This is done to make sure that the most part of the cycle is covered instead of relying only on one value on the curve which could lead to inaccurate results. These 50 frequency values are then averaged. The same process is repeated for the pitch case and comparison of resulting frequencies ($\overline{\omega}_h$ and $\overline{\omega}_\alpha$) is made. If frequencies differ then a new value of ω is considered otherwise the response is checked if it is increasing or decreasing. The total work turns to a negative which means a shift of negative aerodynamic damping to positive damping, and the aerodynamic stability of the structure is thus altered. The wind speed is considered as flutter limit if the response increases otherwise cycle is repeated with another value of U_∞.

The scheme was used to calculate the flutter limit for a 2DOF section model using aerodynamic derivatives from forced vibration analysis of the Structure A (cf. Table 6.7)

116
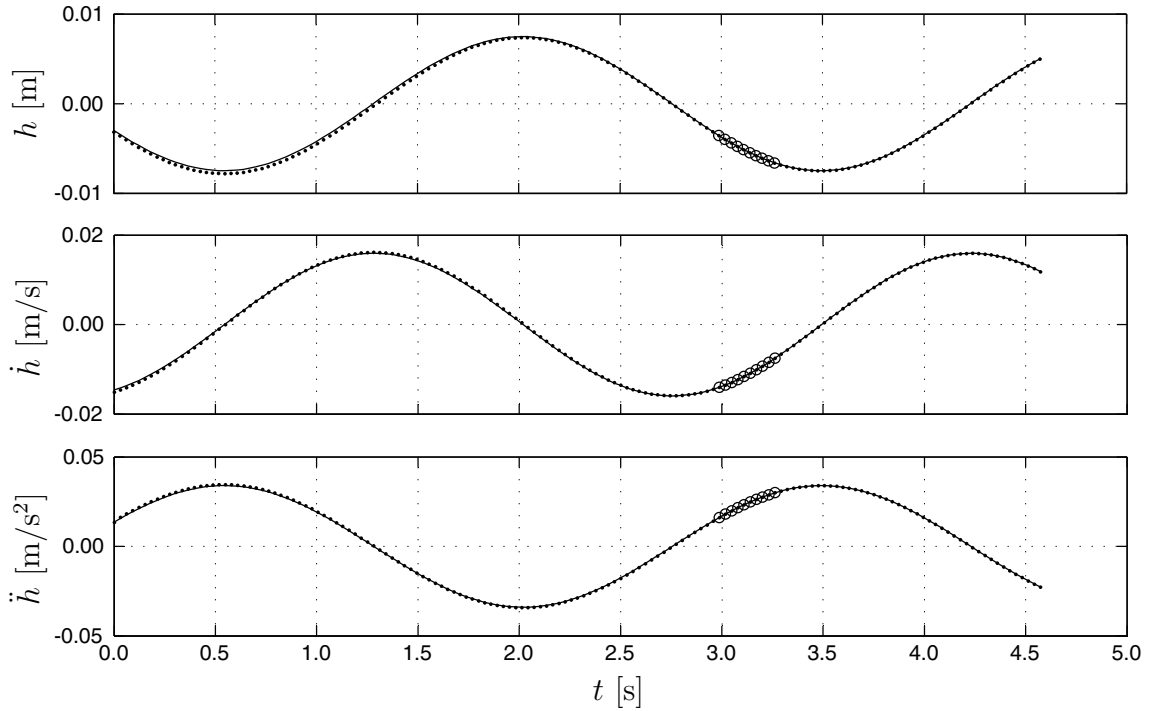
Figure 6.28: Derivative-based FSI Simulations: response fitting for frequency calculation,
($\bullet$) calculated response,
($-$) fitted response,
($\circ$) selected points for fitting.
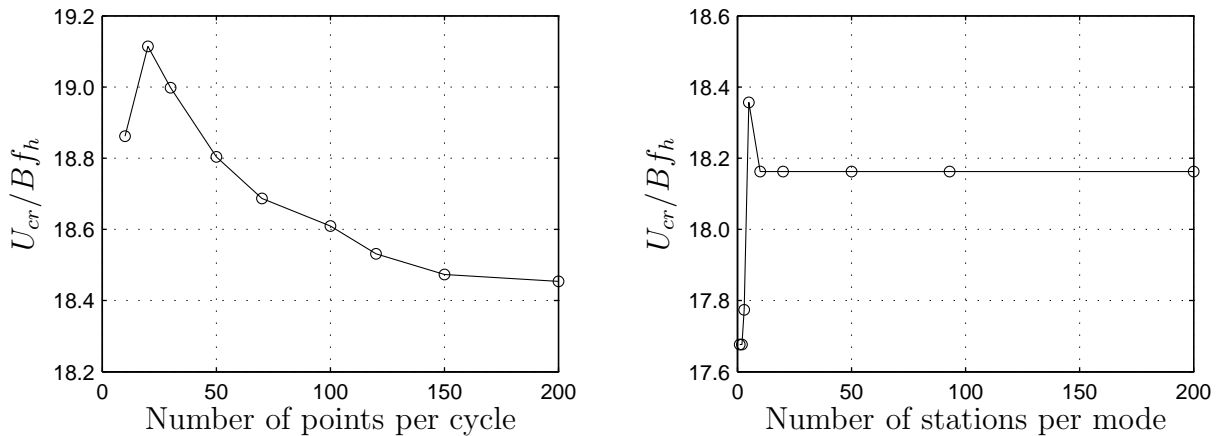
Figure 6.29: Derivative-based FSI Simulations:
(right) relative error in the flutter limit computation with increasing numbers of points
defining one cycle of oscillation,
(left) accuracy of the computation with increasing number of points defining each mode.

and the flat plate ($B/D = 100$). The flutter limit was found to be 99 m/s for
Structure A and 92 m/s for the flat plate for the 2D case. The analytical flat plate
values of the aerodynamic derivatives were also used to calculate the flutter limit which
was found to be 96 m/s.

The approach from the 2DOF model was extended to the 3D model of the bridge
(cf. Section 6.3) in mode space and the flutter limits were computed. For this purpose,
the first bending and the first torsional modes were used. Mode shapes are defined using

117

some number of stations. A larger number of stations describe better the modes shape and therefore the effect of number of stations was also studied on the results computed which is shown in Figure 6.29b. The flutter limit calculated for the quasi-3D model was 101 m/s for Structure A and 94 m/s for the flat plate.

The scheme was also used for a multimode analysis where the first three bending and the first two torsional modes were considered. Table 6.3 and Figure 6.6 show the modal data considered in the multimode analysis. The flutter limit found in this case was 95 m/s for both Structure A and the flat plate. Some effects of the higher modes were observed in the deformed model of the bridge at flutter limit which were quantitatively not so significant.

6.5.5 Fully Coupled CFD Simulations (Model#5)

The method explained in Section (5.7 has been used here to perform fully-coupled CFD simulations on the reference sections. The same numerical flow solver which was used for the forced vibration simulations has been used here. Structural parameters given in Table 6.7 for Structure A and Structure H were used to model the sections (cf. Figure 6.1). The cross sections were modelled suspended on springs representing their structural properties. The simulations were performed at various wind speeds to identify the flutter limit. At 95 m/s Structure A becomes unstable after some cycles of oscillations. For Structure H, the divergent oscillations were observed at 15 m/s. Figure 6.30 shows flow visualisation in a CFD simulation for Structure A and Structure H in a uniform flow.

The flutter analysis presented in Section 6.5.1 provides a rough estimate of flutter limit which could be used to run the fully-coupled CFD simulations at wind speeds close to this value.
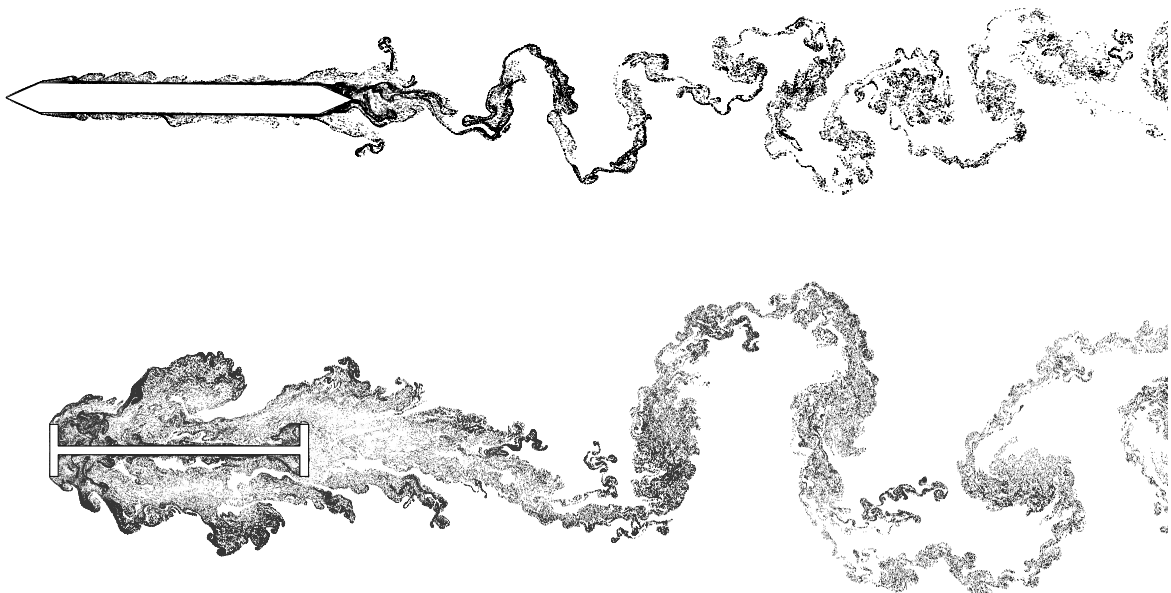
Figure 6.30: Fully-coupled CFD simulations: instantaneous vortex pattern for
(top) Structure A,
(bottom) Structure H.

Figure 6.31 shows a gradual increase in the oscillation response of Structure A at

different wind speeds around instability limit in a CFD simulation. The maximum response amplitudes and response frequencies at different wind speeds are presented in Figure 6.33.

Similarly, the oscillation response for Structure H for different wind speeds is shown in Figure 6.32. The simulations for Structure H were also performed considering a SDOF system in heave and in pitch separately. Figure C.5 and C.6 show the response amplitudes from the simulations on SDOF system at different wind speeds. Considering only vertical DOF, the section does not show instability for the selected wind speeds; however, the maximum repose appears to increase with wind speed, whereas in case of rotational SDOF simulations, the flutter instability limit is identified at a wind speed of 16 m/s which is slightly higher than 2DOF coupled flutter limit (i.e. 15 m/s). The maximum response amplitudes and response frequencies for SDOF and 2DOF systems at different wind speeds are presented in Figure 6.34, Figure 6.35 and Figure 6.36.

Multi-slice simulations were preformed only for Structure A, as it requires a great computational time and resources. Computational time for one multi-slice simulation was up to 30 days. For multi-slice simulations, 12 slices were considered as shown in Figure 6.37 with only first three bending and first two torsional modes. The flutter limit was calculated as 95 m/s in this case.
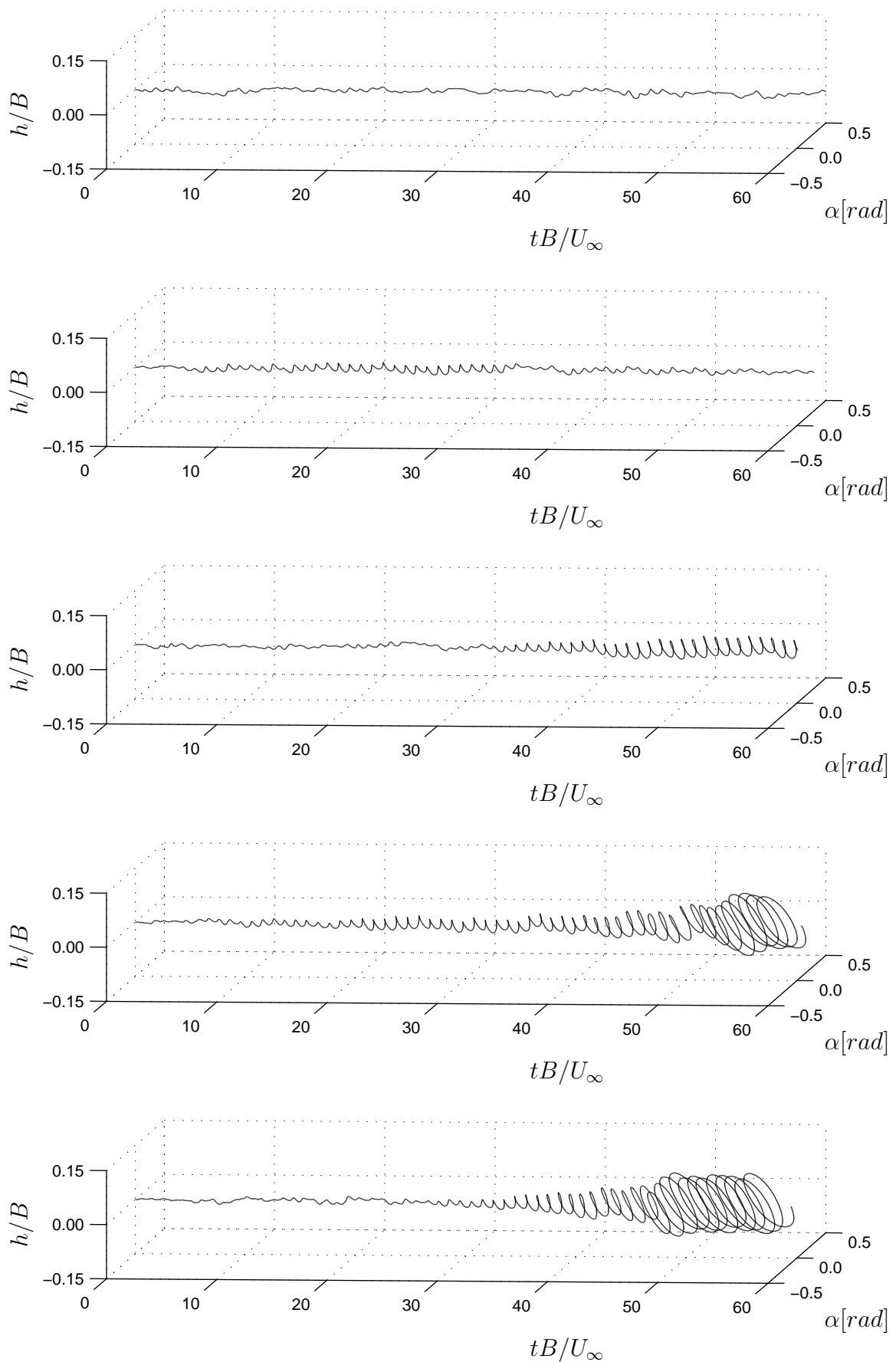
Figure 6.31: Fully-coupled CFD simulations: response of Structure A from single slice 2D simulations at wind speeds
(top to bottom) U_∞=92-96 m/s.
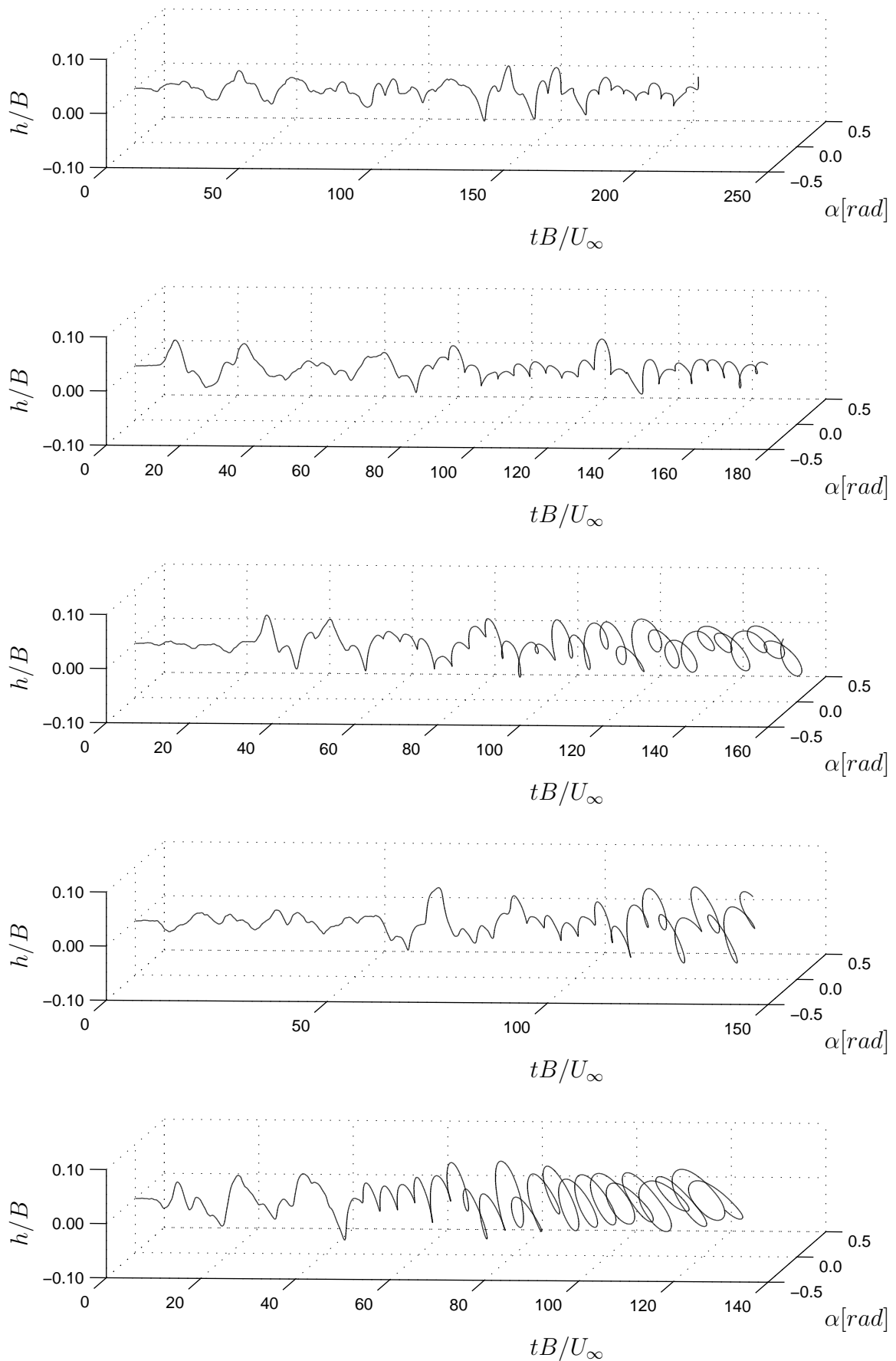
Figure 6.32: Fully-coupled CFD simulations: response of Structure H from single slice 2D simulations at wind speeds
(top to bottom) U_∞=13-17 m/s.

121
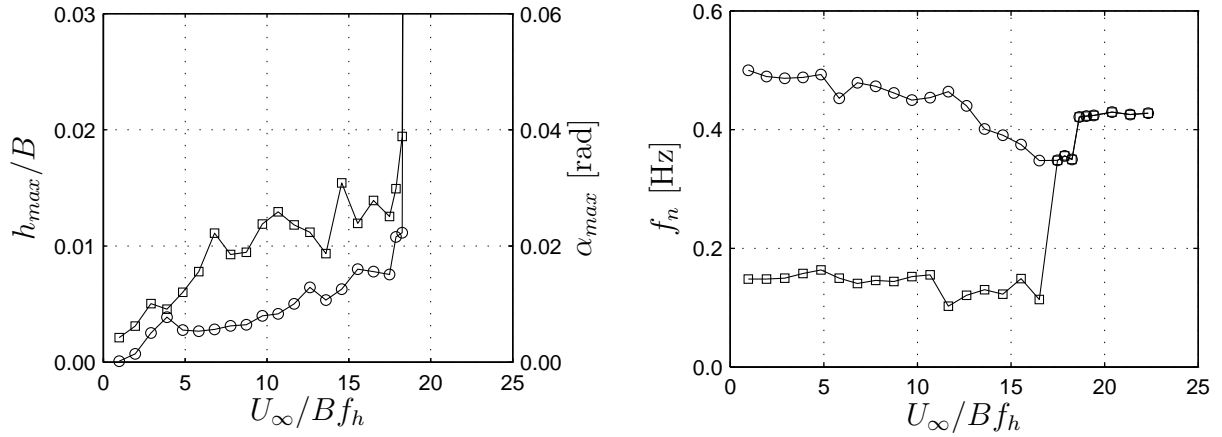
Figure 6.33: Fully-coupled CFD simulations: Structure A from 2DOF single slice 2D simulations at wind speeds U_∞=5-100 m/s,
(left) maximum response amplitudes,
(right) response frequencies,
(□) heave mode,
(○) pitch mode.
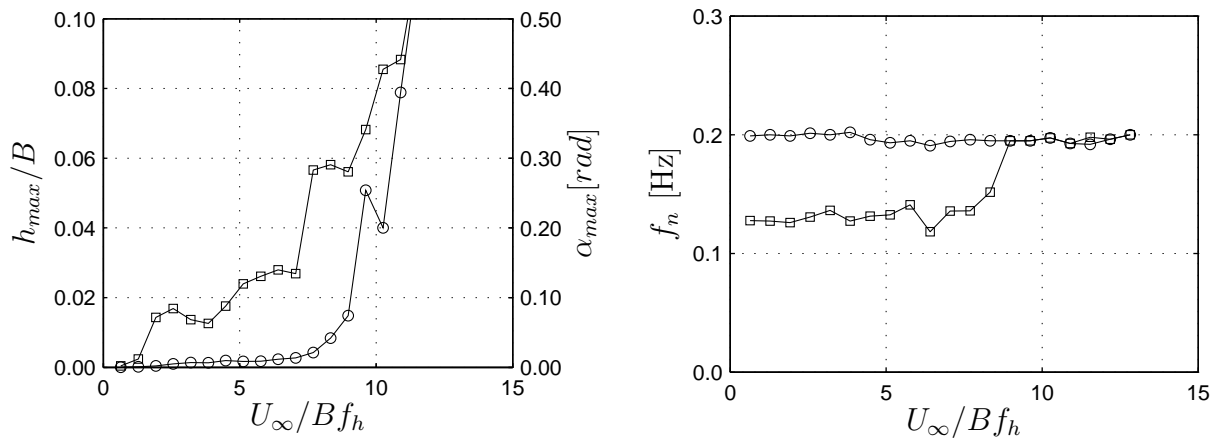
Figure 6.34: Fully-coupled CFD simulations: Structure H from 2DOF single slice 2D simulations at wind speeds U_∞=1-20 m/s,
(left) maximum response amplitudes,
(right) response frequencies,
(□) heave mode,
(○) pitch mode.
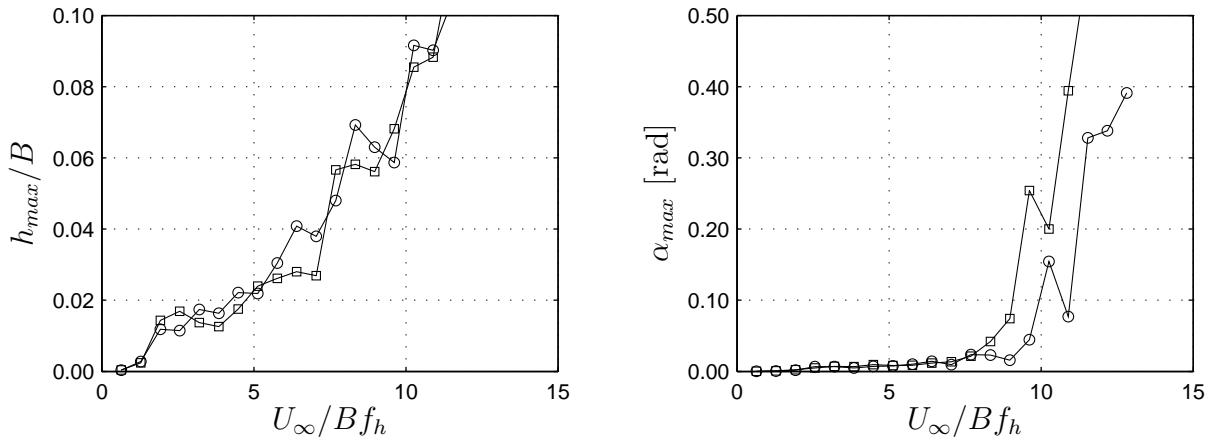
Figure 6.35: Fully-coupled CFD simulations: Structure H from SDOF and 2DOF single slice 2D simulations at wind speeds U_∞=1-20 m/s,
(left) maximum vertical displacements h_{max}/B,
(right) maximum rotation α_{max},
(□) 2DOF,
(○) SDOF.
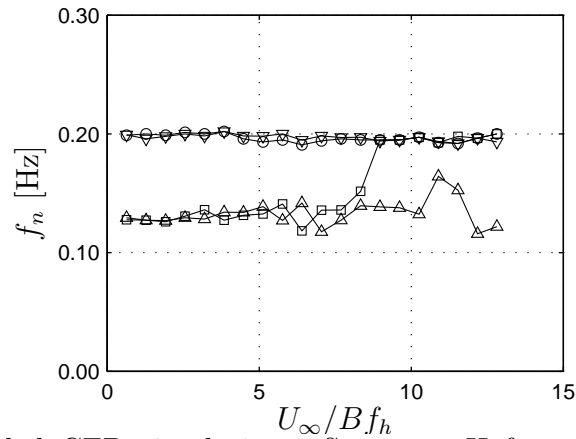
Figure 6.36: Fully-coupled CFD simulations: Structure H from SDOF and 2DOF single slice 2D simulations at wind speeds U_∞=1-20 m/s, response frequencies,
(□) 2DOF heave mode,
(○) 2DOF pitch mode,
(△) SDOF heave mode,
(▽) SDOF pitch mode.
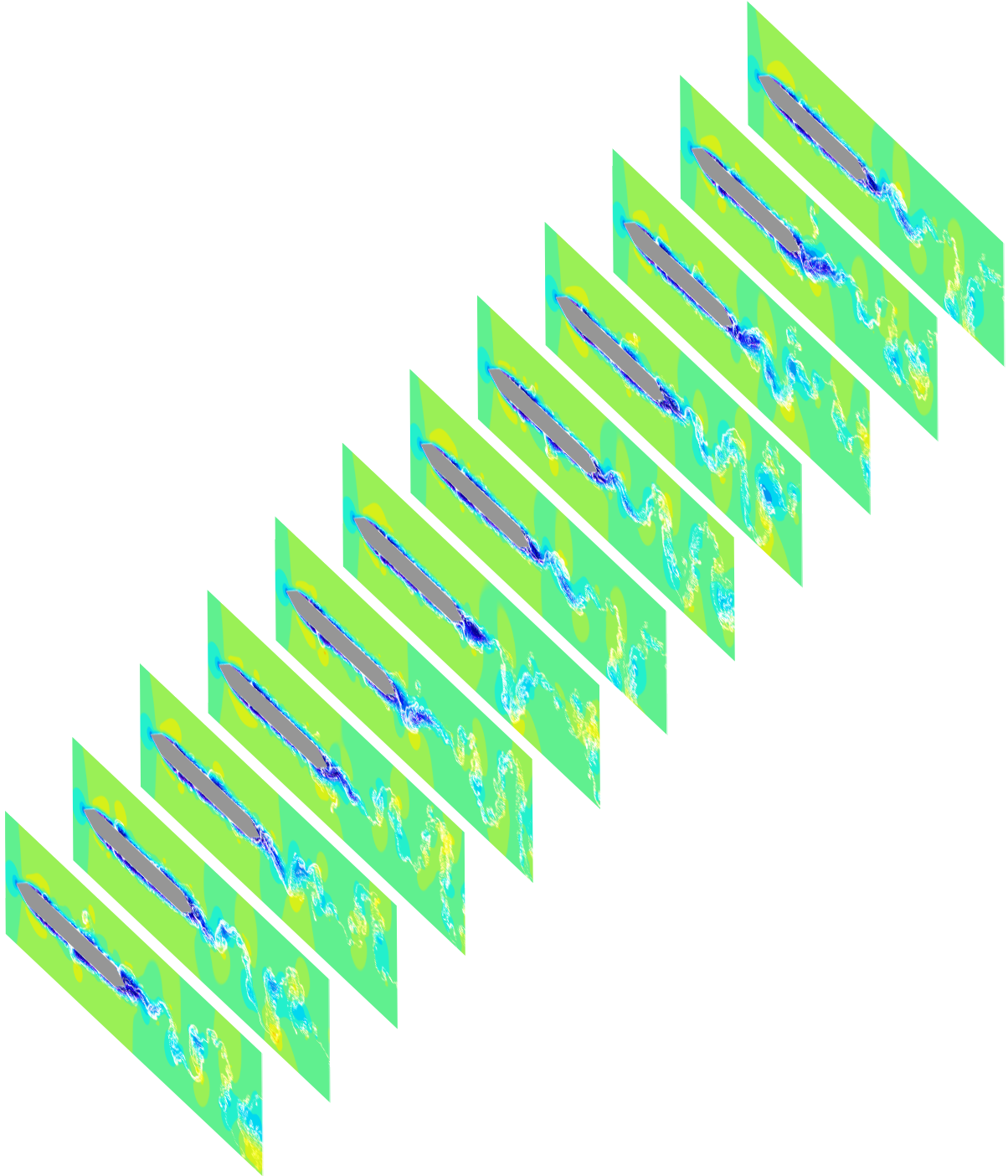
Figure 6.37: Fully-coupled CFD simulations: multi-slice (quasi-3D) simulations, instantaneous velocity fields and vortex pattern of a 12-slice model of the Lillebælt Suspension Bridge (cf. Section 6.2).

6.6   Summary

The flutter phenomenon was studied employing various combinations of analytical and numerical prediction models presented in Chapter 5.   The Lillebælt Suspension Bridge and the original Tacoma Narrows Suspension Bridge were used as study objects (cf. Section 6.2).   These structures were selected on the basis of a wider range of their structural and aerodynamic characteristics.   The structural representations were dimensionally reduced to 2DOF section models calibrated from global models as well as MDOF models.   The 2DOF systems were analysed analytically as well as numerically. Flutter analysis was also conducted by calculating the forced vibration response using a time domain scheme. With this scheme, the generalised self-excited forces were calculated based on the aerodynamic derivatives at each time step.   The CFD simulations using the VPM were also used to model the bridge section with its DOF. The results of the analyses are shown in Table 6.15.

Generally, all models were able to predict the flutter phenomenon and relatively close agreement was found for the particular bridge.   There are some common limitations in some models such as two-dimensionality of flow and considering only flat plate.   Fully-coupled CFD analyses have the advantage that no prior knowledge as to the phenomenon needs to be inserted into the model.   Three-dimensional structural representations are superior over dimensionally reduced models in that no prior knowledge as to the modes participating in the flutter coupling is required. Fully-analytical models are more direct models and allow a better insight into the force coupling. Simplified aerodynamic models need to be critically assessed with respect to their ability to predict the aerodynamic behaviour of the real cross section.

Table 6.15: Summary of flutter limit predictions (U_{cr}, unit: [m/s]) from different model combinations for Structure A / Structure H, (values in parentheses are for CFD flat plate) (cf. Table 5.1).

Structural	Aerodynamic		Analytical	Numerical
Analytical	Model#1	2D	94 / 26	-
	Model#2	2D	92 / 34	
	Model#3	2D	94 / 26	94 (89) / 11
		3D	98 / -	98 (92) / -
Numerical	Model#4	2D	96 / -	99 (92) / -
		3D	98 / -	101 (94) / -
	Model#5	2D	-	95 (98) / 15
		3D		95 (-) / -

Chapter 7

Sensitivity of Flutter Limit to Different Parameters

7.1 Introduction

This chapter discusses the influence of different input parameters on the flutter stability prediction. For this purpose, the variation in structural parameters and aerodynamic behaviour of the cross section is focused here. The aerodynamic behaviour is studied by changing the geometry of the cross section. These sections are modelled in the CFD flow solver to determine their aerodynamic derivatives. Response surface methods have been utilised to describe the aerodynamic derivatives to limit the number of simulations. Additionally, effects of turbulence in the flow on the flutter stability have been discussed. An approach has been presented to estimate flutter limit of a bridge deck section by making use of already available aerodynamic derivatives of similar cross sections employing response surface techniques.

7.2 Structural Parameters

The effects of change in the dynamic parameters of a bridge deck model on the aerodynamic derivatives are negligible in the wind tunnel experiments [248]. However, the uncertainty in the structural parameters can affect the flutter limit significantly especially torsional frequency and mass moment of inertia of the deck [127]. It is also important to consider the torsion-to-vertical bending frequency ratio. Bartoli et al. [249] studied the change in classical flutter onset by inverting this ratio. Moreover Zhang and Sun [250] presented the effect of cable sag, side span length, depth, dead load and supporting system on the flutter stability of a suspension bridge.

The structural damping ratio of up to 2% is generally used in the design; however, smaller damping ratios were observed from the outcome of vibration tests on suspension bridges [251]. The presence of structural damping results in a small increase in the flutter limit but the variability in it does not significantly affect the flutter limit [127, 252]. Jain et al. [253] observed that installing appropriate external dampers increases the flutter stability of a long-span bridge and can be a viable option to overcome the problems of low flutter speeds.

Long-span bridges under erection can be vulnerable to the aerodynamic instabilities than in the service state as the stiffening girder lacks torsional continuity [254]. Jones et al. [255] studied the effect of mode coupling on flutter during a retrofit and found that flutter can happen on a relatively short-span structure due to the peculiar modal profiles that are created as part of the retrofit procedure.

Here, the effects of structural parameters are studied first on the flutter limit prediction. Non-dimensionalisation is convenient to represent input-output behaviour. However, it

is important to note that the non-dimensionalisation sometimes could be misleading. To elaborate this, an example is presented in Figure 7.1. The non-dimensional parameters from Eq. (6.1) have been used with the structural properties of Structure A (cf. Table 6.7). The flutter limits are computed using Model#1 which has been already discussed in Section 6.5.1.

It is clear from the figure that the same non-dimensional parameter can have multiple outcomes. This could be misleading when studying the sensitivity of parameters while relying only on the value of the non-dimensional parameter by changing a single dimensional parameter. The non-dimensional parameter μ is the ratio of the mass of the deck to the mass of the air moved by the deck, r_α is the non-dimensional radius of gyration of the deck and γ_ω is the still air frequency ratio between pitch and heave [38]. For example, in Figure 7.1a the value of μ can be calculated by selecting different combinations of B and m which leads to two different flutter limits as shown.

The effects structural parameters explained above are discussed here for Structure A and Structure H using different models. Here only one parameter has been varied for each non-dimensional case. Only B is varied in μ, I in r_α and f_α in γ_ω, whereas ξ here is the damping ratio for heave and pitch modes. Analytical flat plate aerodynamic derivatives have been used for Model#1 whereas CFD aerodynamic derivatives (cf. Figure 6.16) are utilised for Model#3. Flutter limits were then computed for the variation in these parameters. Figure 7.2 shows the change in a non-dimensional parameter by changing only a single variable. It can be seen in this figure that the variation in the flutter limit prediction is not the same for all sets of structural and aerodynamic properties even in the case of a single non-dimensional parameter. This only provides a qualitative way of observing the effects of these parameters. Nevertheless, these plots help to understand the general trend of the predicted flutter limit due to change in the input parameters. However, it is expected from this that the quantification of uncertainties would also be different in each model case. This is further discussed in the next chapter in detail.

7.3   Aerodynamic Behaviour

The shape of the deck section greatly influences the flutter stability of long-span bridges. Increasing the aspect ratio (B/D) of the section, generally, improves the flutter behaviour [256]. Matsumoto et al. [161] studied the role of various aspect ratios of a rectangular section on aerodynamic derivatives and flutter stability behaviour. Different configurations of fairings [257, 258, 259], fairing angle [260], vertical plates [259], slot in the middle [172, 173, 257, 258, 261], double slot and the location of porous cavity or grating and its opening ratios [259, 262] have been studied and proposed to improve the flutter behaviour of the deck section. Some typical deck shapes for long-span cable-supported bridges have been already shown in Figure 3.7.

Aerodynamic derivatives provide a useful way of understanding the complex aerodynamic behaviour of bridge sections. This feature has already been highlighted in Section 4.3.2.1. An example of aerodynamic derivatives determined for three types of bridge decks is shown in Figure 7.3. As explained in Chapter 4, the aerodynamic derivative H_1^* is related to the vertical SDOF instability and the aerodynamic derivative A_2^* governs the rotational SDOF instability. For these two aerodynamic derivatives, the system will be stable as long as they remain negative (considering no structural damping). This figure elaborates that the shape of the cross section plays a vital role in the aeroelastic stability. Deep sections are more susceptible to SDOF vertical instability and the aerodynamic
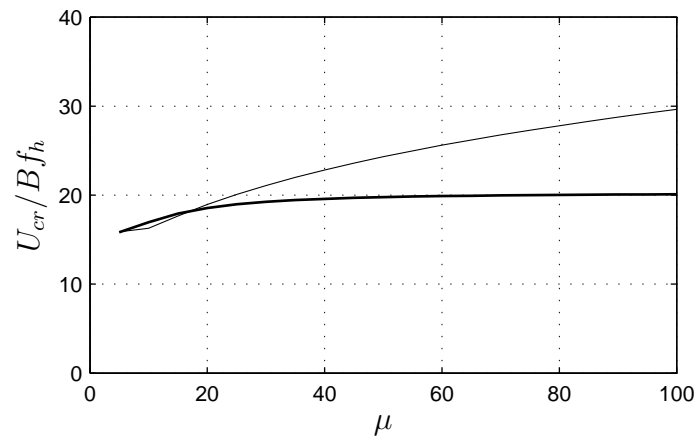
(a) changing (——) only B, (——) only m
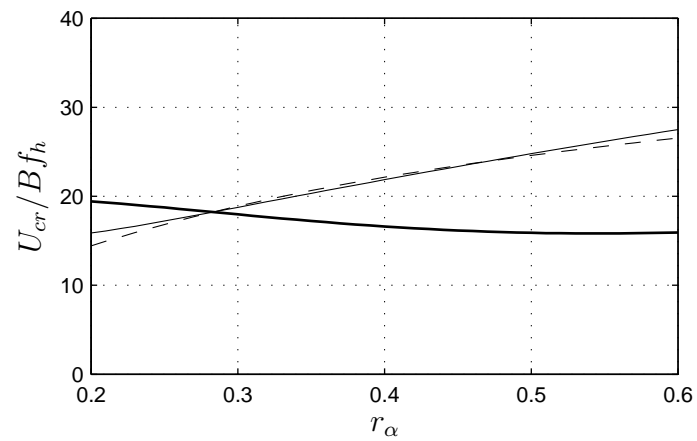
(b) changing (——) only B, (——) only m, (– –) only I
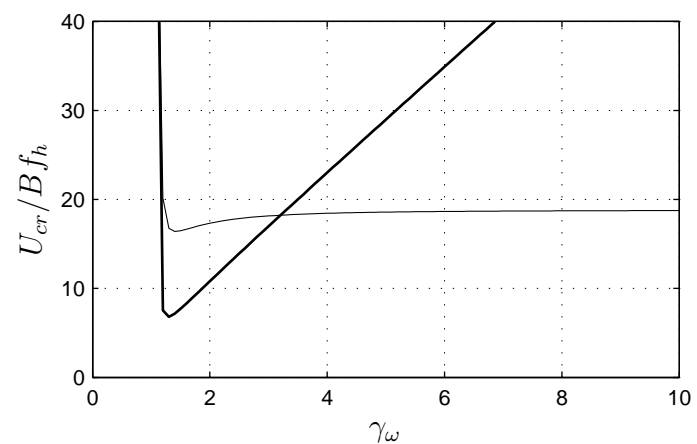
(c) changing (——) only f_h, (——) only f_α

Figure 7.1: Effect of structural input parameters on flutter limit of Structure A from Model#1, (cf. Eq. (6.1)).
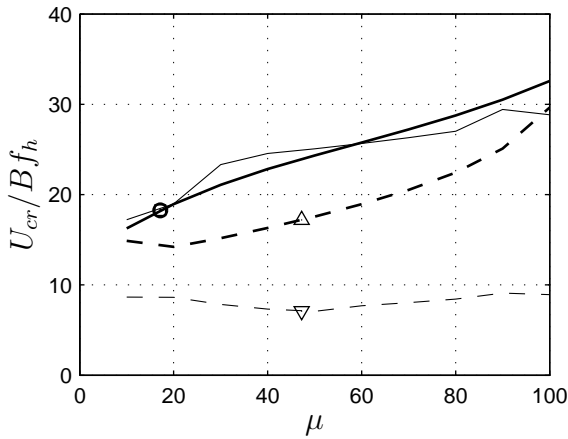
(a) changing only B in μ
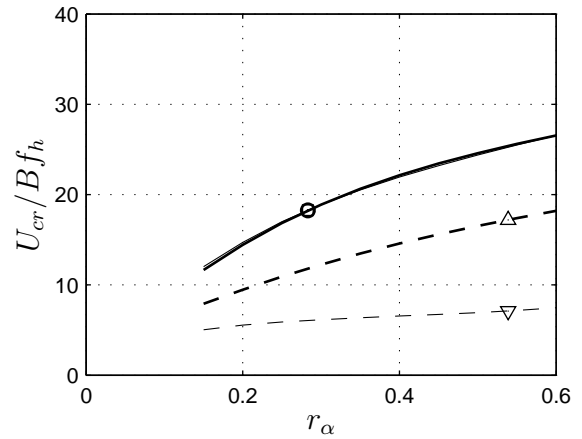
(b) changing only I in r_α
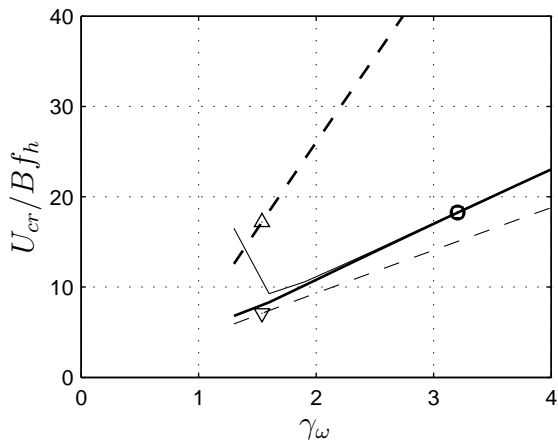
(c) changing only f_α in γ_ω
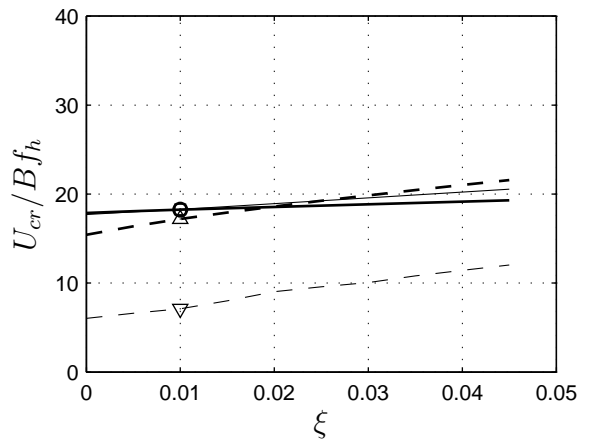
(d) $\xi = \xi_h = \xi_\alpha$

Figure 7.2: Effect of structural parameter change on the flutter stability limits:
(thick) Model#1,
(thin) Model#3,
(solid) Structure A,
(dash) Structure H,
($\circ$) Model#1 with Structure A properties,
($\square$) Model#3 with Structure A properties,
($\triangle$) Model#1 with Structure H properties,
($\triangledown$) Model#3 with Structure H properties.

derivative H_1^* for the rectangular section becomes positive which implies that after this reduced speed v_r the section will be unstable. However, for other two sections, H_1^* remain negative.
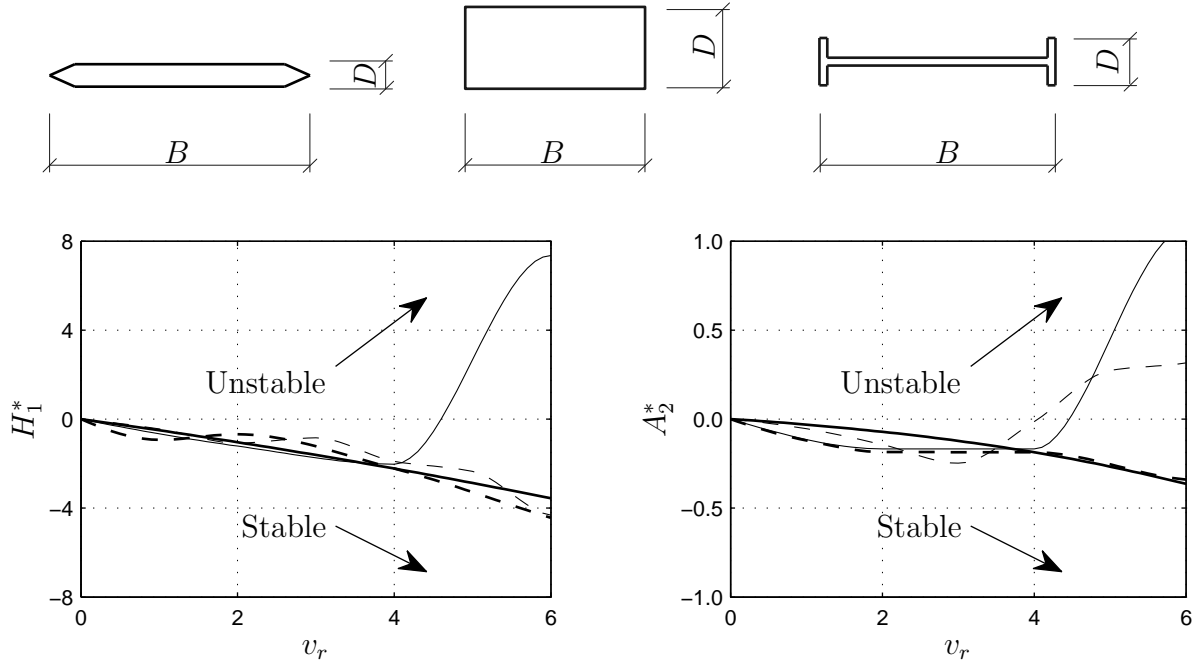
Figure 7.3: Typical characteristics of aerodynamic derivatives for different cross section geometries:
(top) section geometries,
(bottom) aerodynamic derivatives,
(——) flat plate,
(– –) streamlined section,
(——) deep rectangular section,
(– –) H-shaped.

H-shaped sections are more prone to the SDOF torsional instability where A_2^* becomes positive whereas, the streamlined and rectangular sections show stable behaviour. However, rectangular sections can also experience SDOF torsional instability at some aspect ratio. The streamlined section in the presented example appears to have the most stable behaviour as it does not have any problem of SDOF instability (H_1^* and A_2^* remains negative). Often classical flutter is dominant for such sections and 2DOF coupled flutter analysis is performed.

7.3.1 Numerical Parameters

Numerical uncertainty is also a major factor in the CFD simulations. The study of the sensitivity of numerical parameters on the results is also important. The aim of this research is not to cover the numerical uncertainly; however, this section highlights its significance. The aerodynamic derivatives are computed trough forced vibration simulations for which certain parameters are important such as amplitude of oscillation (h_o, α_o), period of oscillation (T_o), time step (Δt), section discretisation (N_{panel}: number of panels) and length of simulation time (t, $t*$). The balance between these parameters is not only necessary to achieve a certain quality but also important for required computational time. In case the discretisation is finer, it would improve the quality

but requires longer computation time which could be in some case upto more than
30 days and additionally, it requires more memory.

An example is presented using Structure A (cf. Section 6.2) to elaborate the importance
of numerical parameters on the least-square fit to calculate aerodynamic derivatives. The
section was modelled to perform CFD simulations as explained earlier in Section 6.4.
For this purpose, only one value of reduced speed (v_r=10) was selected to show this
effect. However, it is important to note that for any other reduce speeds, this effect
could be quantitatively different. First, the effect of selecting different time step Δt on
the prediction of aerodynamic derivatives was studied. The numerical parameters used
in these simulations are summarised in Table 7.1. The time step Δt was changed for
each simulation from 0.01 to 0.10 s whereas all other parameters were kept constant.
These simulations generate lift force and moment time histories on which least-squares
fit is performed to calculate aerodynamic derivatives as explained in Section 4.4.2. The
results of these simulations are shown in Figure 7.4. It can be seen that as the time
step reduces the values of aerodynamic derivatives changes but do not stabilise at a
certain level. The time step of 0.01 s was the lowest value which was used in this
example but at the same time, it was the most expensive in terms of computation time
which took over 30 days to complete on a computer system with specifications provided
in Appendix C.1. The simulation with a time step of 0.02 s took around 2 weeks to
finish, therefore this time step was chosen to perform further simulations on the other
sections.

Table 7.1: Forced vibration simulations on Structure A: effect of numerical parameters
on aerodynamic derivatives (cf. Figure 7.4).

Common parameters			
N_{panel}	340	v_r	10
L_{panel} [m]	0.2	T_o [s]	33
$\Delta t*$	1.0	U_∞ [m/s]	10
ν [m^2/s]	0.000015	h_o [m]	1.65
Re	22×10^6	α_o [°]	5
Effect of time step			
N_{step}	4,300-34,000	$t*$	103-130
$N_{particle}$	100,000-700,000	Δt [s]	0.01-0.1
Effect of length of time history			
N_{step}	2,000-20,000	$t*$	12-120
$N_{particle}$	450,000	Δt [s]	0.02

The effect of number of time steps N_{steps} or the length of time history t, $t*$ was also
studied. For this purpose, the same section was used in the simulation as before with
the numerical parameters shown in Table 7.1. The results of these simulations are
presented in Figure 7.4 where it can be seen that the aerodynamic derivatives start to
show stable behaviour after 18,000 steps; however, this also required over 20 days of
simulation runtime. The aerodynamic derivative H_4^* shows unstable behaviour in both
cases. The prediction of H_4^* is always uncertain and usually it is considered insignificant
in flutter analysis.
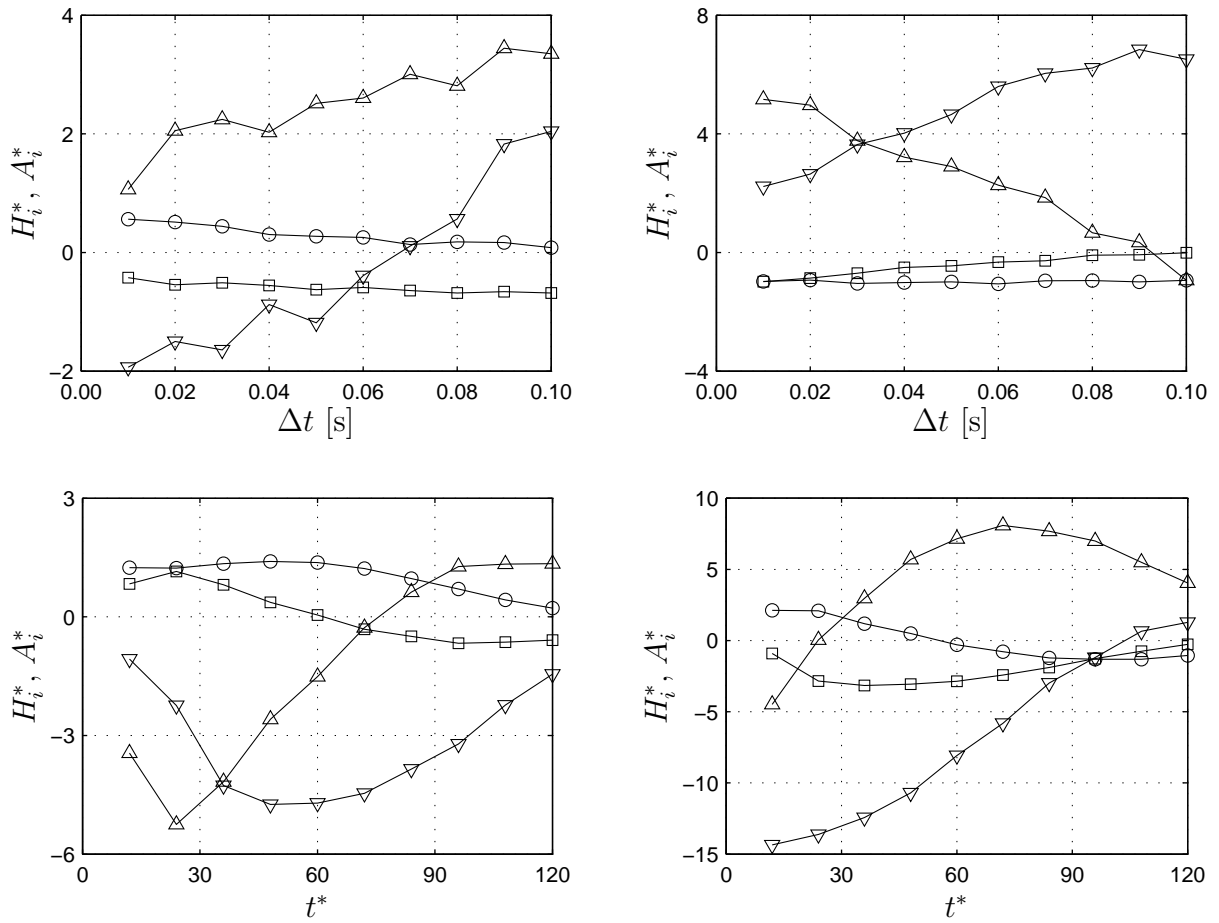
Figure 7.4: Aerodynamic derivatives from forced vibration simulations on Structure A:
(top) effect of time step Δt on aerodynamic derivatives,
(bottom) effect of length of time history t^* on aerodynamic derivatives.
(left) $\triangle$ H_1^*, $\triangledown$ H_4^*, $\square$ A_1^*, $\circ$ A_4^*,
(right) $\triangle$ H_2^*, $\triangledown$ H_3^*, $\square$ A_2^*, $\circ$ A_3^*, (cf. Table 7.1).

7.3.2 Section Classification

A useful way to describe the aerodynamic behaviour of motion-induced aerodynamic forces on the section is through the aerodynamic derivatives, cf. Section 4.3.2.1. The aerodynamic behaviour significantly depends on the shape of the section which is essential for the design and analysis of long-span bridges. At the initial design stage, it is often not possible to perform wind tunnel tests or even CFD simulations. An approach is proposed here to use the existing aerodynamic derivatives from WTT and numerical simulations for conventional classes of deck sections. The most common classification of deck sections is presented and the geometrical features of sections are highlighted. An attempt was made by [196] towards the generalisation of the aerodynamic derivatives for different types of cross sections.

The classification shown in Figure 7.5 has been considered here. Type I is the class of streamlined sections which are more common for medium to large-span suspension and cable-stayed bridges. This is a modern class of sections which have better aerodynamic performance. Lillebælt [33], Great Belt [84, 118], Millau Viaduct [238] Höga Kusten [230] and Sutong [136, 263] are some examples of this class of sections. Type II class is the sections common for medium-span bridges. Tacoma Narrows [139, 239], Nanpu Bridge [230] and Turin [264] fall under this category. This type has been used in the earliest long-span bridges. These sections have some construction advantages; however, the aerodynamic behaviour is inferior to that of Type I where sometimes the SDOF torsional instabilities have been a great challenged as experienced in case of Tacoma Narrows collapse in 1940. The third type i.e. Type III is the trapezoidal sections with cantilevers on edges. These sections are also common for medium-span cable-stayed bridges. The composite construction of such sections is a major advantage. However, the aerodynamic performance can be relatively inferior to Type I. Queensferry Crossing and Mersey Gateway are the cable-stayed bridges under construction which have this type of sections. Type IV is the class of sections which are relatively new and common for very large spans. The aerodynamic behaviour against aeroelastic instabilities is improved by introducing slots for pressure release. The proposed Messina Suspension Bridge and Stonecutters Cable-stayed Bridge are the examples of this type of sections. An extensive range of data about the aforementioned bridges is provided in Tables A.1, A.2, A.3, A.4 and A.5.

It is important to mention here that this classification has certain limitations and does not cover all aspects related to the aerodynamic behaviour. Several other parameters are important which can significantly change the typical performance of the section. These factors may include the following:

- as aspect ratio B/D decreases, the streamlined section can start to show SDOF torsional instability. Additionally, deep sections may also show SDOF galloping behaviour.

- Length of cantilever for a trapezoidal section

- Slopes of leading and trailing edges

- Degree of concavity for bi-girder section is very much related to SDOF torsional instability

- Non-structural attachments e.g. railings, barriers and wind shields may also change the aerodynamic behaviour.

The aim here is not to define a strict classification of sections but to provide a general framework to use data for a similar type of sections without performing WTT or CFD simulations for aeroelastic assessment of bridges. Some studies have been also made here to highlight the limitations of generalisation of aerodynamic derivatives in the next section. To the best of author's knowledge, this is the first work that shows the study of such a wide range of section geometry variation.

(a) Type I: steamlined sections

(b) Type II: bi-girder/multi-girder sections

(c) Type III: trapezoidal with cantilevers

(d) Type IV: sections with slots

Figure 7.5: Cross section classification for generalisation of aerodynamic derivatives.
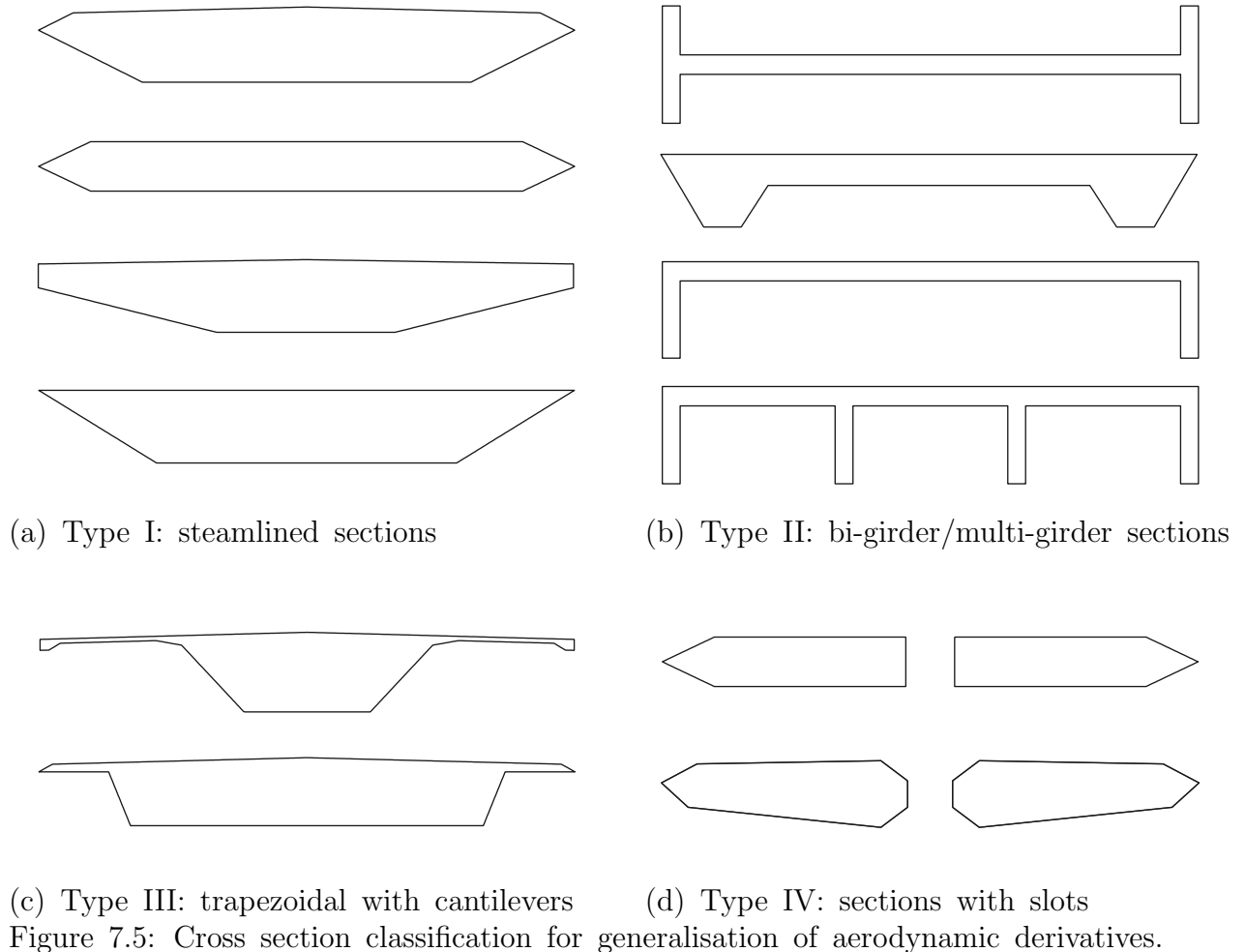
7.3.3 Sensitivity to Deck Shape

Some examples have been presented here by the change in section geometry and its effect on the flutter limit. The forced vibration simulations were performed to determine the aerodynamic derivatives and then these aerodynamic derivatives were used to compute SDOF and 2DOF flutter limits. For this purpose, the section geometry is changed and simulations are performed for each section with reduced speed v_r from 2 to 16. This requires a large number of simulations, whereas each simulation would take around 10 to 15 days to complete. Therefore response surface technique was used here to describe each aerodynamic derivative in the space of geometry parameter and reduced speed. The generated response surface representations of aerodynamic derivatives were then used to compute flutter limits. In the following section, the application of this approach is presented. The main steps are explained as follows:

- Set-up section with a parameter which defines the variation in the section geometry.

134

- Select suitable numerical parameters and create input files for numerical simulations (cf. Section 7.3.1).

- Carry out simulations and post process the results by performing least-squares fit to determine aerodynamic derivatives (cf. Section 4.4.2).

- Normalise domain of each aerodynamic derivative to perform response surface ensuring a certain quality (cf. Section 2.4).

- Compute SDOF and 2DOF instability limits using response surfaces of these aerodynamic derivatives (cf. Sections 5.6.4 and 5.6.5).

7.3.3.1 Sensitivity to Aspect Ratio

The first study is made on a thin rectangular plate by changing its aspect ratio D/B. The aspect ratio is changed from 0.01 to 0.45 and forced vibrations simulations are performed to determine aerodynamic derivatives. A total of 17 sections were thus created with different aspect ratios. Reduced speed was selected from 2 to 16 with an interval of 2. Each of section geometry at a given reduced speed requires two simulations separately: one in heave and the other in pitch DOF. This whole set-up requires $2\times8\times17=272$ simulations. Other numerical parameters are summarised in Table 7.2. These simulations were run on a 64 core computer system and took around 25 days to finish.

Figure 7.6 shows the cross section geometry variation used for these simulations. Aerodynamic derivatives were first determined after post processing the force and moment time histories. Figure 7.7 shows the aerodynamic derivative H_1^* and A_2^* where it can be seen that at some aspect ratio, the values of derivative becomes positive. A 2DOF coupled flutter analysis was performed and flutter limits were computed by using these aerodynamic derivatives and structural properties of Structure A. The resulting flutter limits are shown in Figure 7.8. Additionally, SDOF torsional flutter limits were also computed.
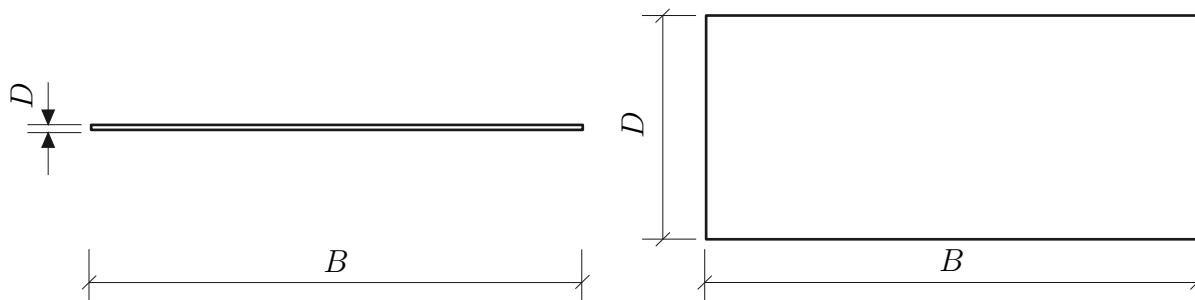
Figure 7.6: Forced vibration simulations on rectangular section with changing aspect ratio D/B from 0.01 to 0.45.

For an effective utilisation of these aerodynamic derivatives, repose surfaces were generated. These response surfaces were created for each aerodynamic derivative individually. Two types of response surfaces were tested and applied on these aerodynamic derivatives i.e. the polynomial functions and the moving least-squares (cf. Section 2.4). For this purpose, the domain of the aerodynamic derivatives was normalised and discretised in 50 segments each in the reduced speed and aspect ratio space.

First, the polynomial regression was applied with different degrees of polynomial function. The sufficient quality of fitting is important to be achieved through this

Table 7.2: Forced vibration simulations on rectangular section with changing aspect ratio: numerical parameters (cf. Figure 7.6).

N_{step}	10,000	v_r	2-16
N_{panel}	336-482	$t*$	60
L_{panel} [m]	0.2	T_o [s]	6.6-52.8
$\Delta t*$	1.0	U_∞ [m/s]	10
Δt [s]	0.02	h_o [m]	0.5
ν [m^2/s]	0.000015	α_o [°]	5
$N_{particle}$	80,000-120,000	Re	22×10^6

process. Table 7.3 describes the results of the Coefficient of Determination (CoD) to asses how good is the fitted function. This shows that the CoD for aerodynamic derivatives H_1^*, H_4^*, A_1^* and A_4^* is less than 0.50 even for polynomial of degree 5. This implies that the data contains such a scatter which can not be captured with even a higher degree of the fitted function. Figure D.1 shows the results of fitted aerodynamic derivatives by polynomial functions.

The second approach of response surface was used by the moving least-squares. The same procedure was repeated for this approach as before. In this case, the influence radius $\tilde{D}$ was decreased to achieve a better fit. The value of $\tilde{D}$=0.05 shows the CoD greater than 0.50 for all aerodynamic derivatives as depicted in Table 7.3. By reducing the vale of $\tilde{D}$ further would lead to a perfect fit where the CoD of almost 1.0 could be achieved. This would be similar to interpolation. This model of response surface is superior over the polynomial fitting as it provides better quality fitting; however, requires more computational time for fitting. The fitted response surfaces for the aerodynamic derivatives are shown in Figure 7.7.

Table 7.3: Response surface fitting for aerodynamic derivatives of rectangular section with changing aspect ratio (cf. Figures 7.6, D.1 and 7.7).

	CoD, R^2 [-]								Time
	H_1^*	H_2^*	H_3^*	H_4^*	A_1^*	A_2^*	A_3^*	A_4^*	[s]
Polynomial functions									
1°	0.04	0.47	0.85	0.02	0.16	0.07	0.50	0.03	0.5
2°	0.05	0.68	0.96	0.23	0.33	0.18	0.90	0.07	0.3
3°	0.12	0.81	0.97	0.38	0.35	0.33	0.92	0.19	0.3
4°	0.26	0.84	0.97	0.43	0.40	0.43	0.95	0.28	0.3
5°	0.37	0.86	0.98	0.48	0.48	0.54	0.96	0.33	0.4
Moving least-squares									
$\tilde{D}$=0.20	0.20	0.72	0.96	0.41	0.38	0.38	0.94	0.28	17.9
$\tilde{D}$=0.10	0.42	0.84	0.98	0.51	0.52	0.52	0.97	0.44	16.8
$\tilde{D}$=0.05	0.66	0.89	0.99	0.64	0.73	0.66	0.98	0.57	17.0
$\tilde{D}$=0.01	1.00	1.00	1.00	1.00	1.00	1.00	1.00	1.00	17.5

The flutter limits are calculated from the generated response surfaces by moving least-squares and are plotted on the Figure 7.8. Such a change in the geometry will
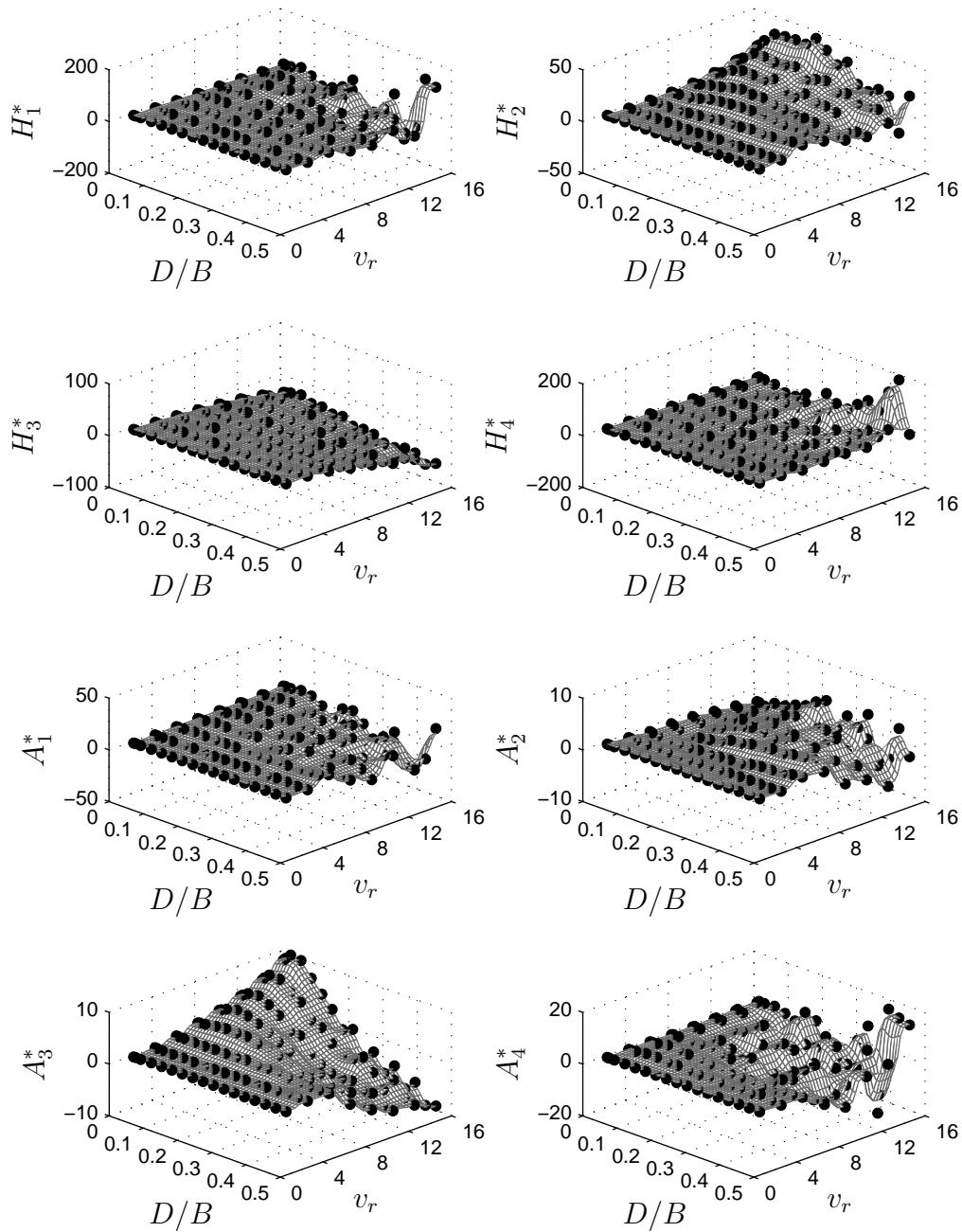
Figure 7.7: Response surface fitting for aerodynamic derivatives of rectangular section with changing aspect ratio: fitted surface by moving least-squares with $\tilde{D}$=0.05 and (•) actual aerodynamic derivatives.

have no effect on the analytical flat plate prediction because this analytical model does not capture the shape of the section and rather assumes cross section as an airfoil or a flat plate. It can be seen in the figure that at the ratios smaller than D/B=0.134, the SDOF flutter limit increases more than twice as compared to the prediction for the coupled 2DOF flutter by the analytical model (Model#1 in Section 5.4). At very low aspect ratios (D/B close to zero), the flutter limit from 2DOF model (cf. Section 5.6.5) becomes very close to Theodorsen flat plate prediction and as the aspect ratio increases this flutter limit decreases. This shows that flutter limit computed for bluff bodies by Theodorsen theory could be unreliable. Additionally, at such a low range of aspect ratios, the section is no more prone to the SDOF torsional instability and only 2DOF flutter remains. Another important point to note is that the SDOF flutter limit is higher than the 2DOF flutter limit which implies that considering the mode coupling is critical for aeroelastic instability analysis.
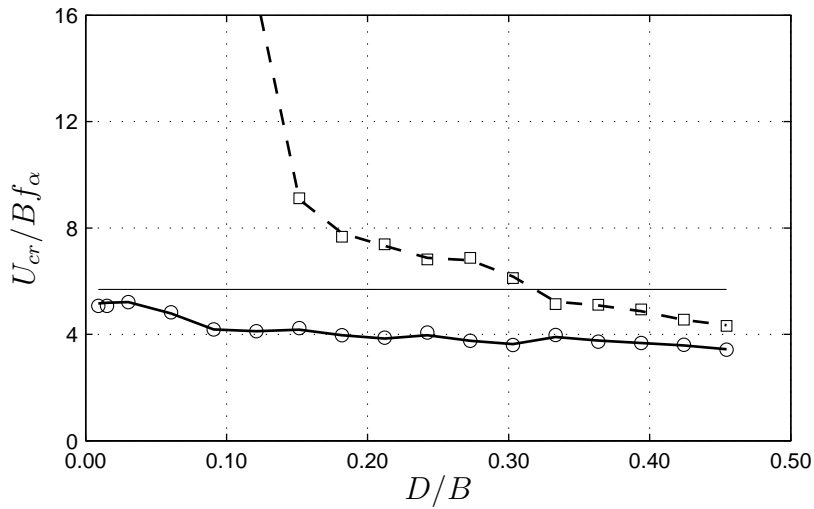
Figure 7.8: Sensitivity of flutter limit to section geometry using properties of Structure A for a rectangular section with increasing aspect ratio (D/B=0.01 - 0.45):
(——) analytical flat plate prediction for 2DOF system,
(○) 2DOF flutter analysis using aerodynamic derivatives,
(□) SDOF flutter limits from aerodynamic derivative A_2^*,
(——) 2DOF flutter analysis using response surface on aerodynamic derivatives,
(– –) SDOF flutter limits from response surface on aerodynamic derivative A_2^*
(CoD for 2DOF flutter analysis=0.992) (CoD for SDOF flutter limits=0.999).

Figure 7.9 illustrates the relative error between the flutter limits computed from actual aerodynamic derivatives and from the response surface on the aerodynamic derivatives given as

$$\text{Relative error} = \frac{(U_{cr,act.} - U_{cr,RS})}{U_{cr,act.}} \tag{7.1}$$

where $U_{cr,act.}$ is the flutter limit from actual aerodynamic derivatives and $U_{cr,RS}$ is the flutter limit from response surface on aerodynamic derivatives. Th figure shows that the relative error remains less than 3 % in all cases.

7.3.3.2   Sensitivity to Geometry

A series of simulations were performed to study the behaviour of the cross section under a specific and gradual change of geometry. For the purpose of brevity here only the
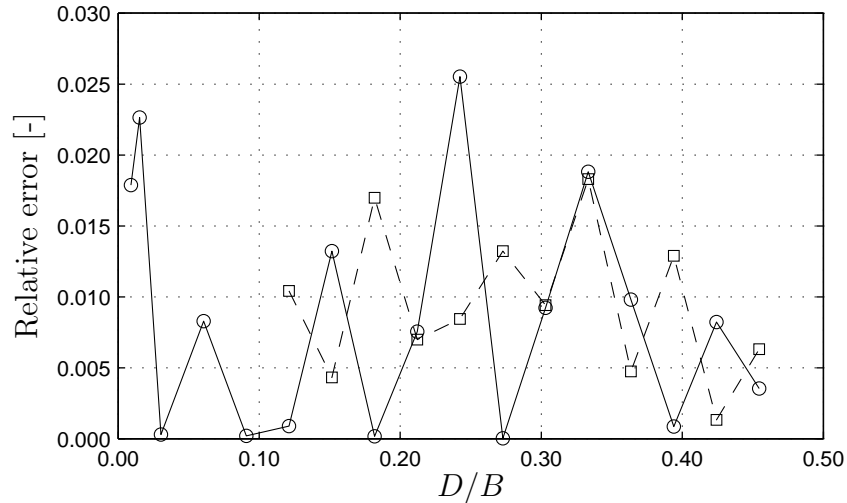
Figure 7.9: Sensitivity of flutter limit to section geometry using properties of Structure A for a rectangular section with increasing aspect ratio (D/B=0.01 - 0.45): relative error for flutter limits from direct method and from response surface on the aerodynamic derivatives (cf. Eq. (7.1))
($\circ$) 2DOF flutter analysis using response surface on aerodynamic derivatives,
($\square$) SDOF flutter limits from response surface on aerodynamic derivative A_2^*.

geometrical change and its effect on SDOF torsional flutter and coupled 2DOF flutter has been studied by using models explained in Section 5.6.

The common procedure to study the effect of change in geometry is summarised as follows:

- Starting section geometry is selected

- Change in the section geometry is parametrised by selecting some variables

- Forced vibration simulations are preformed in the flow solver

- Aerodynamic derivatives are computed

- SDOF and 2DOF flutter limits are determined using the aerodynamic derivatives.

It is important to mention here that for the following studies of the sensitivity of flutter limit to section geometry, response surfaces were not generated for the aerodynamic derivatives and flutter limits were computed directly from the aerodynamic derivatives. However, the same procedure is applicable to these cases as explained in Section 7.3.3.1.

7.3.3.2.1 Fairing Slope and Streamlined Section Depth

A rectangular section with aspect ratio of $D/B{=}2.85/33$ has been considered. The effect of the slope of the leading edge and the trailing edge is studied for b^*/B from 0 to 0.18 as shown in Figure 7.10a. Figure 7.11a illustrates that the coupled flutter limit increases with the increase in b^*/B. There exist no SDOF flutter problem for this section.

The effect of aspect ratio of the streamlines section is also studied. The increase in the aspect ration D^*/B from 0.01 to 0.30 is shown in Figure 7.10b. Figure 7.11b shows some decrease in the coupled flutter limit, whereas the problem of SDOF flutter instability appears at an aspect ratio of 0.18.

(a) Rectangular section with increasing fairing slope ($b^*/B = 0 - 0.18$, $D = 2.85$m, $d = D/2$)

(b) Streamlined section with increasing depth ($D^*/B = 0.01 - 0.3$, $b = 3.2$m, $B = 33$m)
Figure 7.10: Sensitivity of flutter limit to section geometry: section variation (cf. Figures D.3 and D.4).

Figure 7.11: Sensitivity of flutter limit to section geometry using properties of Structure A:
(left) rectangular section with increasing fairing slope ($b^*/B = 0 - 0.18$),
(right) streamlined section with increasing depth ($D^*/B = 0.01 - 0.3$),
($- -$) analytical flat plate prediction for 2DOF system,
($\circ$) 2DOF flutter analysis using aerodynamic derivatives,
($\square$) no SDOF flutter limit found.

7.3.3.2.2 Central Slot

The effect of the central slot was studied on the flat plate and Structure A. The slot was
introduced in the middle of section and was gradually increased as shown in Figure 7.12
with b^*/B from 0 to 0.15. These sections are not prone to SDOF torsional flutter;
however, behaviour against coupled flutter could be improved by these slots. Figure 7.13
show that there is an increase in the flutter limit up to 35 % due to a central slot.
The increase in the slot width however does not improve flutter limit.

Since both the sections are streamlined, the increase in flutter limit of both outcomes
is similar. A more bluff section could have a different effect on the flutter limit
quantitatively.

(a) Plate with increasing central slot $(b^*/B = 0 - 0.15, \ B/D = 100)$
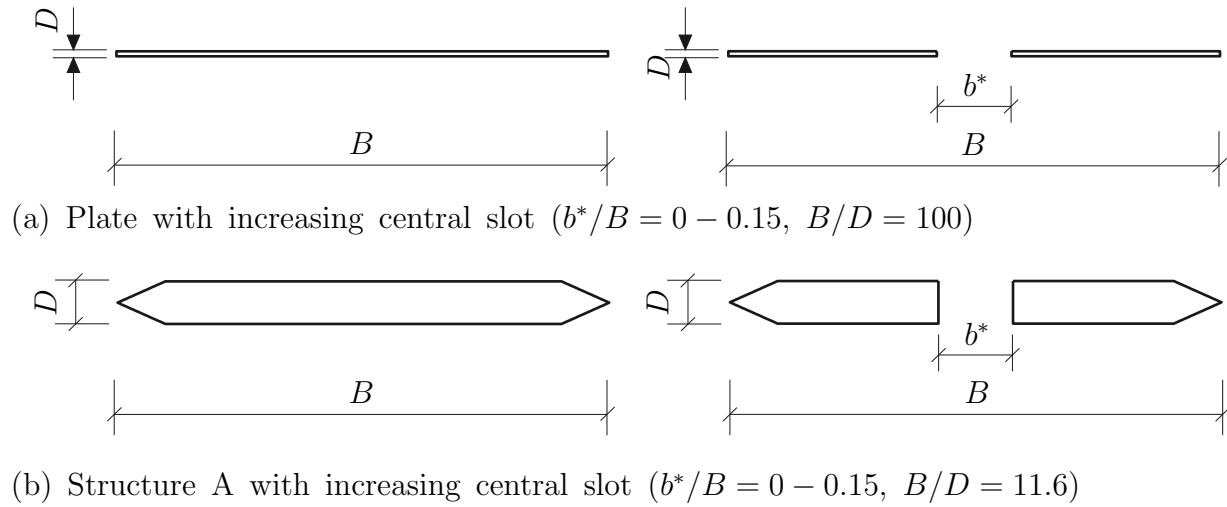
(b) Structure A with increasing central slot $(b^*/B = 0 - 0.15, \ B/D = 11.6)$
Figure 7.12: Sensitivity of flutter limit to section geometry: section variation
(cf. Figures D.5 and D.6).
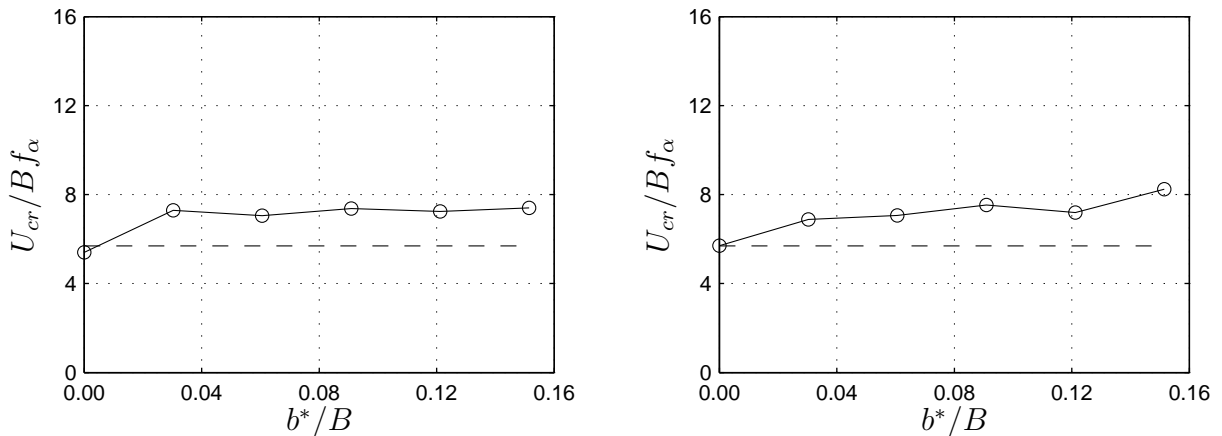
Figure 7.13: Sensitivity of flutter limit to section geometry using properties of
Structure A:
(left) flat plate with central slot $(b^*/B = 0 - 0.15)$,
(right) Structure A with central slot $(b^*/B = 0 - 0.15)$,
$(- -)$ analytical flat plate prediction for 2DOF system,
$(\circ)$ 2DOF flutter analysis using aerodynamic derivatives,
$(\square)$ SDOF flutter limit.

7.3.3.2.3   Straight Fairings and Circular Fairings

A rectangular section of aspect ratio $D/B = 0.24$ has been studied which is prone to SDOF flutter. In order to improve its behaviour against torsional instability, rectangular and circular fairings have been introduced as shown in Figure 7.14. The results from flutter analyses shown in Figure 7.15 implies that the circular fairings appear to be more effective against torsional flutter instability. Whereas there is a slight improvement in the case of coupled flutter. It is important to note that for a circular case the point of flow separation is not fixed, whereas in the case of straight fairing it is at the corner.
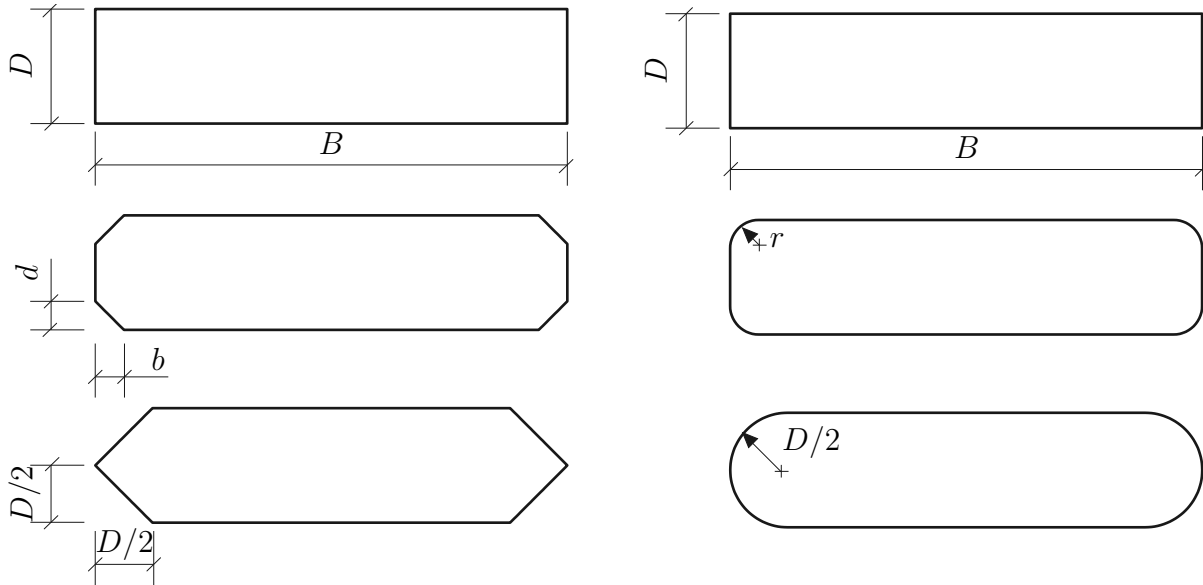
(a) Straight fairings ($b = d = 0 - D/2$)   (b) Curved fairings ($r = 0 - D/2$)

Figure 7.14: Sensitivity of flutter limit to section geometry: section variation ($D/B = 0.24$) (cf. Figures D.7 and D.8).
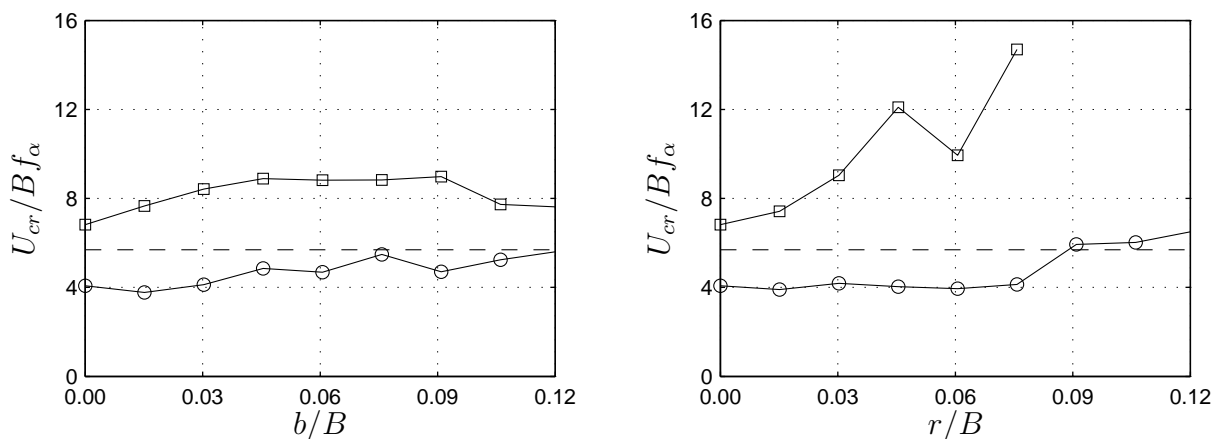
Figure 7.15:   Sensitivity of flutter limit to section geometry using properties of Structure A:
(left) rectangular section with straight fairing ($b = d = 0 - D/2$),
(right) rectangular section with curved fairing ($r = 0 - D/2$),
($- -$) analytical flat plate prediction for 2DOF system,
($\circ$) 2DOF flutter analysis using aerodynamic derivatives,
($\square$) SDOF flutter limit.

7.3.3.2.4 H-shape to Rectangular and Plate to H-shape

H-shape section is studied by increasing its depth to transform it into a rectangular section as shown in Figure 7.16a. The flutter limits show that with an increase in d^*/D, slightly increase the coupled flutter behaviour. However, the SDOF torsional flutter limit is increased much more. The flutter predictions are very far from the analytical flat plate prediction which shows that Theodorsen prediction can not be used for such a bluff section.

A thin plate is changed to H-shape by increasing depth at the two end girders as displayed in Figure 7.16b. The coupled, as well as SDOF torsional flutter, start to appear on after the other at certain d^*/D ratio. The difference with the analytical prediction gets more at a higher d^*/D ratio.
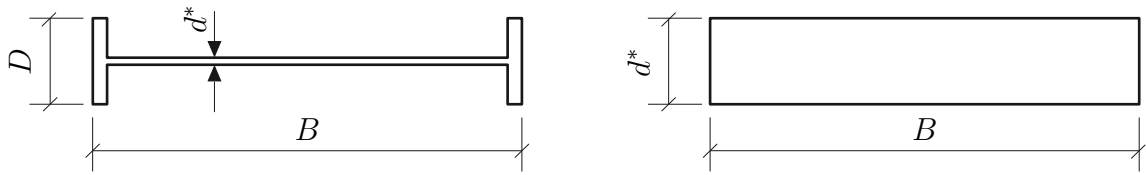
(a) H-section with increasing depth $(d^*/D = 0.04 - 1.00, \ D = 2.4\text{m}, \ B = 12\text{m})$
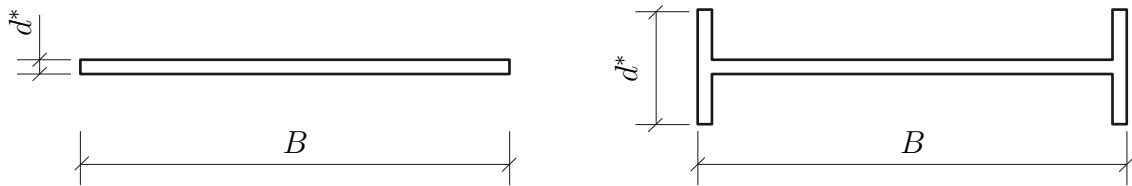
(b) Plate with increasing edges $(d^*/D = 0.13 - 1.25, \ D = 2.4\text{m}, \ B = 12\text{m})$

Figure 7.16: Sensitivity of flutter limit to section geometry: section variation (cf. Figures D.9 and D.10).
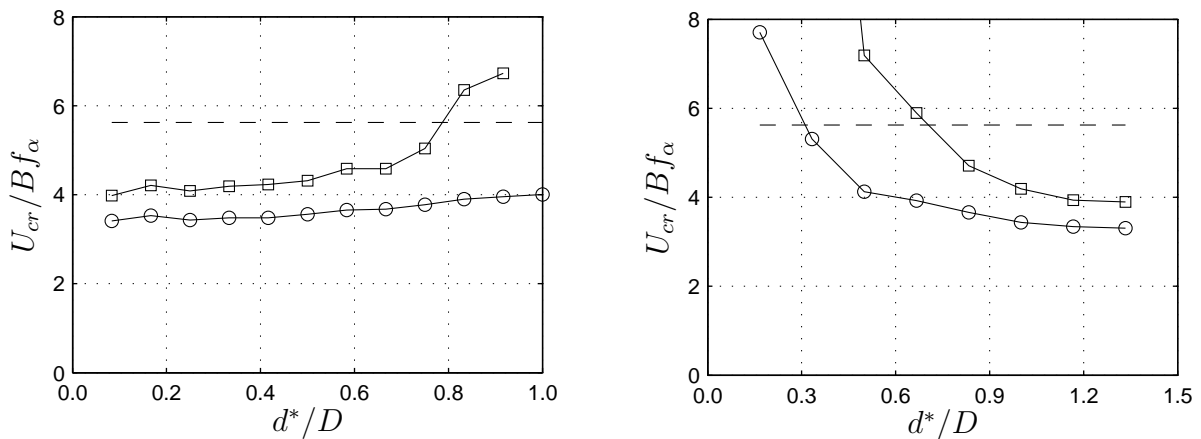
Figure 7.17: Sensitivity of flutter limit to section geometry using properties of Structure H:
(left) H-section with increasing depth $(d^*/D = 0.04 - 1.00)$,
(right) plate with increasing edges $(d^*/D = 0.13 - 1.25)$,
$(- \, -)$ analytical flat plate prediction for 2DOF system,
$(\circ)$ 2DOF flutter analysis using aerodynamic derivatives,
$(\square)$ SDOF flutter limit.

7.3.3.2.5 Bottom plate and Fairing on H-shape

The H-shape section was also an attempted to stabilise by using plates at the bottom of the section to close the lower concave region as shown in Figure 7.18a. The resulting flutter limits in Figure 7.19a does not show much improvement against SDOF torsional flutter and the 2DOF coupled flutter.

In the other study, fairings were introduced on the leading and trailing edges of H-section as shown in Figure 7.18b. It appears in Figure 7.19b that due to these fairings the flutter limits even decrease for some fairing angles and then slightly raised. This shows that the fairings are also not an effective solution against flutter for such type of sections.
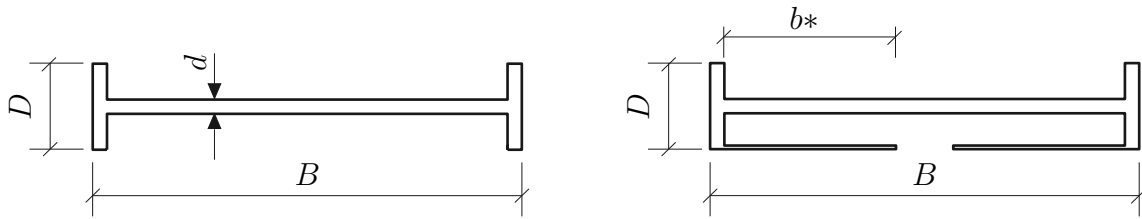
(a) H-shape with bottom plate ($b^*/B = 0 - 0.15$, $B/D = 5$)
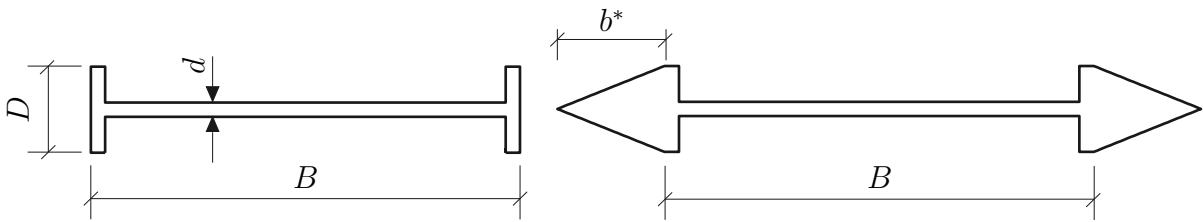
(b) H-shape with fairing ($b^*/B = 0 - 0.25$, $B/D = 5$)

Figure 7.18: Sensitivity of flutter limit to section geometry: section variation (cf. Figures D.11 and D.12).
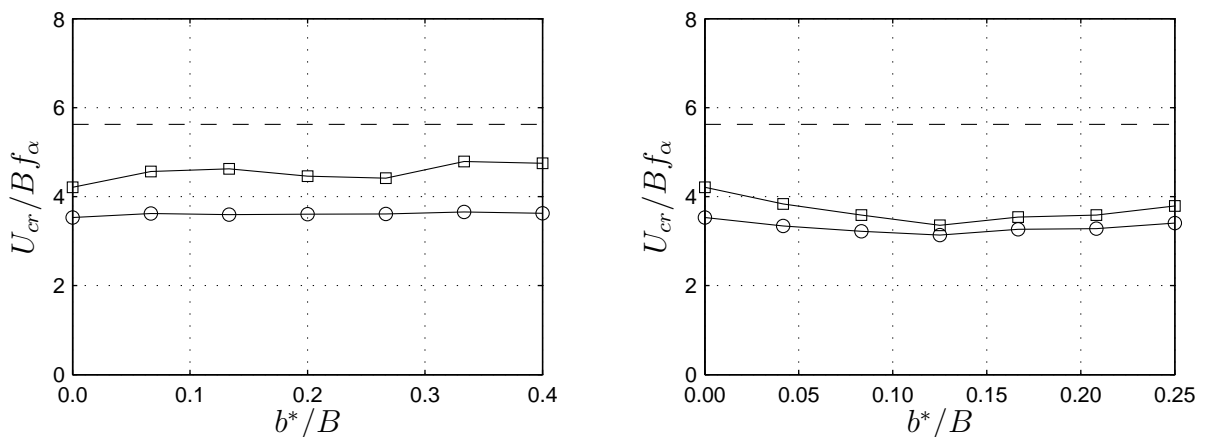
Figure 7.19: Sensitivity of flutter limit to section geometry using properties of Structure H:
(left) H-section with bottom plate ($b^*/B = 0 - 0.4$),
(right) plate with fairing ($b^*/B = 0 - 0.25$),
(– –) analytical flat plate prediction for 2DOF system,
(○) 2DOF flutter analysis using aerodynamic derivatives,
(□) SDOF flutter limit.

144

7.3.3.2.6 Forcing Amplitude for Streamlined and Flat plate

The motion-induced aerodynamic forces are considered linear in terms of their response. Often aerodynamic derivatives are computed at fixed values of amplitudes of motion with the assumption that the amplitudes are kept small. The effect of amplitudes of the forcing motion has been studied here with different heave and pitch amplitudes selected to perform forced vibration simulations and computing aerodynamic derivatives. For heave case amplitudes of forcing for vertical motion h_o/B=0.010, 0.013, 0.015, 0.020, 0.030 have been considered and for pitch case amplitude of forcing for rotational motion α_o=1.5°, 2.86°, 4°, 6°, 8° were used.
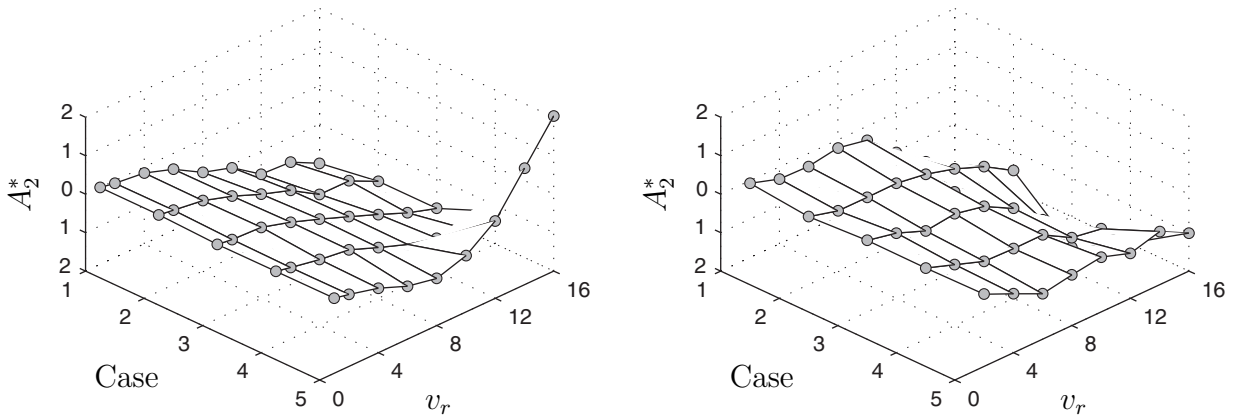
Figure 7.20: Aerodynamic derivative A_2^* from the forced vibration simulations with different forcing amplitude (α_o=1.5°, 2.86°, 4°, 6°, 8°) for
(left) Structure A,
(right) flat plate (aspect ratio 1:100) (cf. Figures D.13 and D.14).
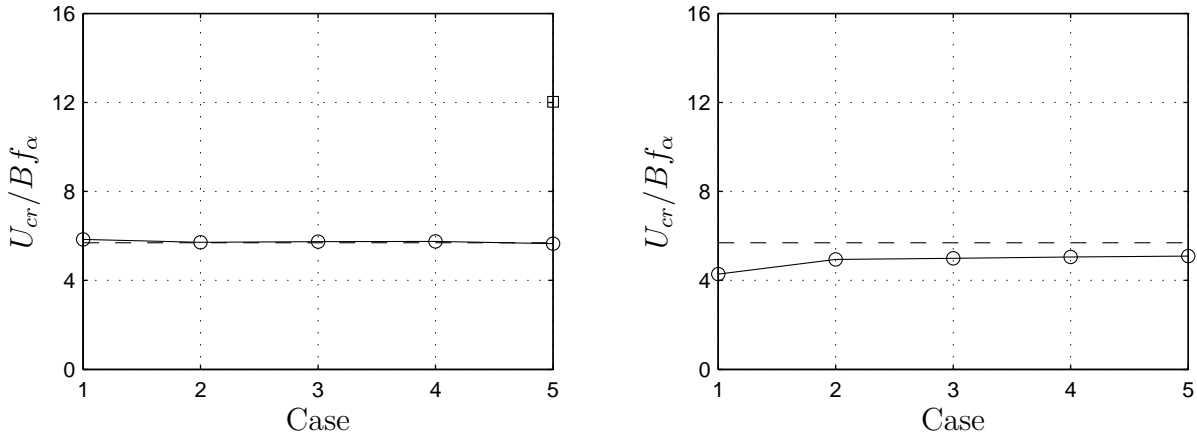
Figure 7.21: Sensitivity of flutter limit to forcing amplitude using properties of Structure A (h_o/B=0.010, 0.013, 0.015, 0.020, 0.030) (α_o=1.5°, 2.86°, 4°, 6°, 8°):
(left) Structure A cross section,
(right) flat plate (aspect ratio 1:100),
(– –) analytical flat plate prediction for 2DOF system,
(○) 2DOF flutter analysis using aerodynamic derivatives,
(□) SDOF flutter limit.

These forcing amplitudes were used for Structure A and the flat plate of aspect

ratio $B/D = 100$ to perform forced vibration simulations. The resulting flutter limits computed from the aerodynamic derivatives are shown in Figure 7.21. The figure shows that there is not a significant change in the coupled flutter limit for both sections with different amplitudes of forcing motion.

The aerodynamic derivative A_2^* is also shown for these sections in Figure 7.20 where it can be seen that at $\alpha_o=8°$, the derivative A_2^* becomes positive at some v_r. The reason of this could be numerical uncertainty originating for the length of time step which was kept same for all cases, whereas for large amplitudes, the smaller time step is required to resolve the flow properly. It should also be noted that the assumption of linear relationship between the amplitudes and motion-induced forces holds for small amplitudes. At larger amplitudes, nonlinear aerodynamic behaviour starts to appear.

7.3.4 Flutter Limit for Circular Section

Fully-analytical model presented in Section 5.4 assumes any cross section as flat plate and therefore does not take shape of the section into account. However, the cross-sectional shape is essential in the determination of flutter limit for a section as explained in the previous section. To elaborate this, an example of a circular cross section is presented here. A circular cross-section is considered and forced vibration simulations are performed. The resulting aerodynamic derivatives are shown in Figure D.2.

This is an academic example for which same structural properties are assumed as that of Structure A. By using Model#1 (cf. Section Section 5.4) the flutter limit has been computed for this section. This provides a flutter limit prediction of 93.4 m/s. When the same circular cross-section is used in Model#3 (cf. Section 5.6.5) by using the aerodynamic derivatives presented in Figure D.2, this model does not provide any flutter limit.

This is well-known that circular cross sections are not prone to flutter problem. However, using a model which is limited in its ability to consider such a cross-sectional shape may lead to incorrect outcomes. This shows Model#1 is not robust for such applications where cross section geometry is not similar to flat plate.

7.3.5 Aerodynamic Derivative Fusion

An approach is presented here to merge the aerodynamic derivatives for a cross section which could be obtained from the same as well as different sources. This enables the design engineer to obtain a set of aerodynamic derivatives for a section without performing WTT or CFD simulations which can be used for initial assessment in the early design stage. Three approaches are presented to merge these aerodynamic derivatives: direct weighted average, polynomial regression and moving least-squares. Weighting factors can also be introduced for these aerodynamic derivatives based on the importance or confidence of the results from a particular source. The choice of weights is important and may introduce some bias; however, without any knowledge, all weights may be assumed equal. The advantage of this approach is that the aerodynamic derivatives are achieved for a cross section from different sources and there is no need to run the same number of analyses as that of the number of sources and then to average the results. From the obtained aerodynamic derivatives, the flutter analysis is required to be performed once and these aerodynamic derivatives can be used for other purposes

such as sensitivity and uncertainty analyses which are discussed in the next chapter. To
elaborate this, examples are presented for the case of a flat plate and a box girder.

7.3.5.1 Application to Flat Plate

The aerodynamic derivatives have been taken for a flat plate by Theodorsen
theory (cf. Section 4.3.1), experimental [265] and numerical computed form CFD
(cf. Section 4.4.2). These aerodynamic derivatives are shown in Figure 7.22. Weighting
factors are also introduced for these aerodynamic derivatives which can be set higher or
lower based on the importance or confidence of the results from a particular source. For
this purpose, weighting factors of 0.30 was used for analytical, 0.30 for the CFD and
0.40 for experimental aerodynamic derivatives. A simplified approach has been used here
to introduce a weighting factor by simply repeating the aerodynamic derivatives relative
to others. That means for a weighting factor of 0.30, the aerodynamic derivatives are
repeated 30 times in the data set and for a weighting factor of 0.40, they are repeated
40 times. This allows to use the response surface codes without any modification. Some
details of the response surface methods are already provided in Section 2.4.

The resulting fitted aerodynamic derivatives are presented in Figure 7.22 where it can
be seen that the results from these three approaches are not much different from each
other for this example. One reason is that the aerodynamic derivatives from the selected
sources appear to be relatively similar; however, it is just a qualitative and does not
explain how this affects the flutter limit prediction.

The actual aerodynamic derivatives were used to calculate flutter limit by using
structural parameters of Structure A (cf. Section 6.2). These results were then directly
averaged by using weighting factors. The fitted aerodynamic derivatives were also used
to compute flutter limits. Table 7.4 provides the summary of these results. It is quite
clear from the results that there is a relatively large difference between the flutter
limits computed from the individual set of aerodynamic derivatives from a single source,
whereas the aerodynamic derivatives merged by the explained approach provide very
close values for the flutter limits.

Table 7.4: Aerodynamic derivative fusion: flutter limits computed for Structure A
using Model#3 directly from aerodynamic derivatives and from merged aerodynamic
derivatives.

Model	U_{cr}	U_{cr}/Bf_h	ω_{cr}	$v_{r_{cr}}$
	[m/s]	[-]	[rad/s]	[-]
Analytical	93.2	18.10	2.071	8.59
CFD (cf. Section 6.5.3)	83.3	16.18	2.086	7.62
WTT [265]	114.4	22.21	2.151	10.12
direct average on individual values	98.7	19.17	2.107	8.9
Weighted average	97.8	19.00	2.124	8.8
Polynomial 4°	99.4	19.30	2.122	8.9
MLS ($\tilde{D}$=0.05)	97.7	18.98	2.121	8.8

The main idea was to present the approach and to show how it can be utilised to
merge aerodynamic derivatives from different sources to conduct the flutter analysis.
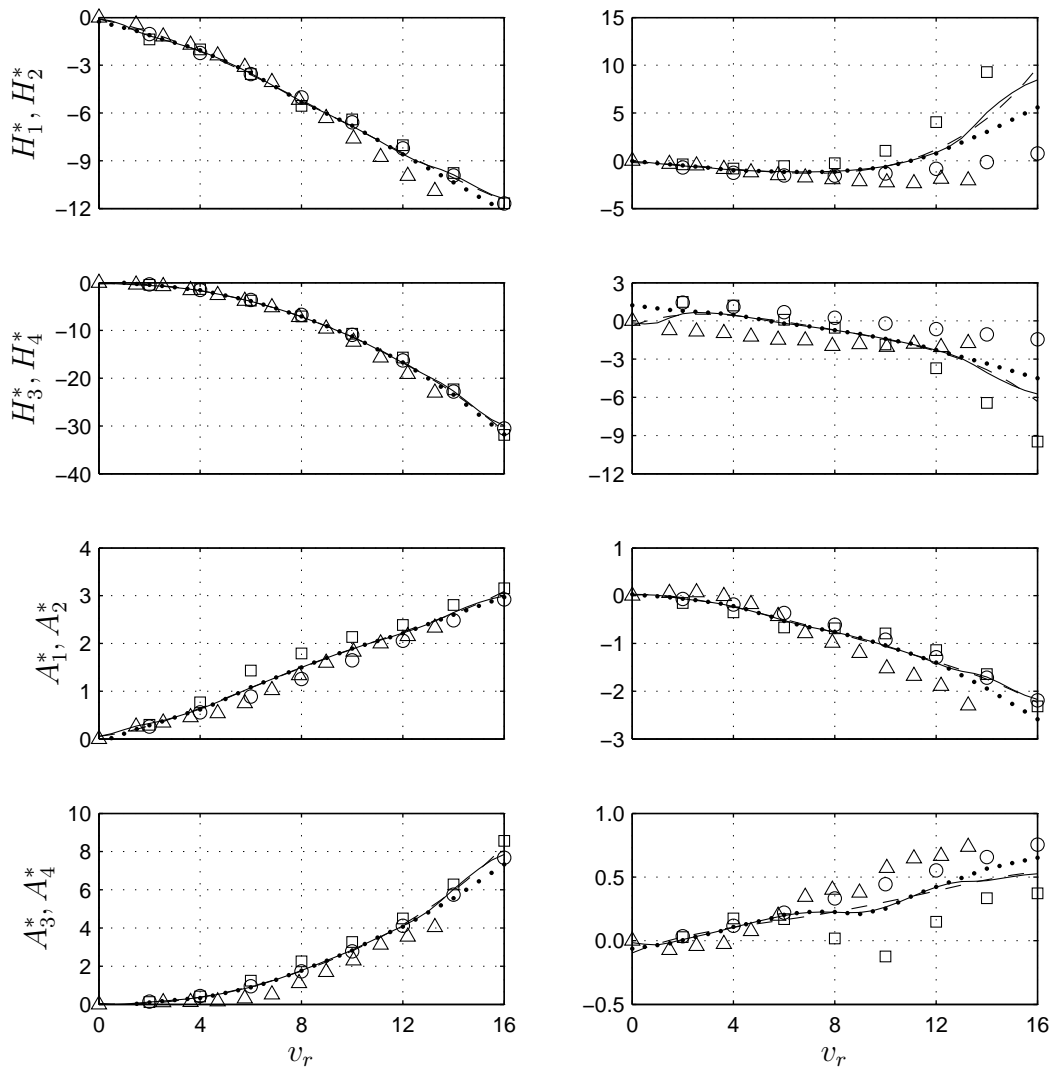
Figure 7.22: Aerodynamic derivatives (H_i^* and A_i^* where $i = 1, \ldots, 4$):
($\circ$) flat plate by Theodorsen theory,
($\square$) experimental [265],
($\triangle$) forced vibration simulations on a flat plate (aspect ratio 100),
($\cdots$) weighted average,
($--$) Polynomial,
(---) MLS.

This approach could be useful for cases where the aerodynamic derivatives of the cross section considered are not available. In such a situation, the aerodynamic derivatives of similar sections can be used for preliminary assessment.

7.3.5.2 Application to Bluff Section

The same approach is also presented for a semi-streamlined section. For this purpose Great Belt Suspension Bridge deck has been selected. This section is one of the most studied cross sections and there exist extensive data in the literature about the aerodynamic behaviour. A bare cross section without any attachments is presented in Figure 7.23. For further details about the bridge, the reader is referred to the publications presented in Tables A.1, A.2, A.3, A.4 and A.5.
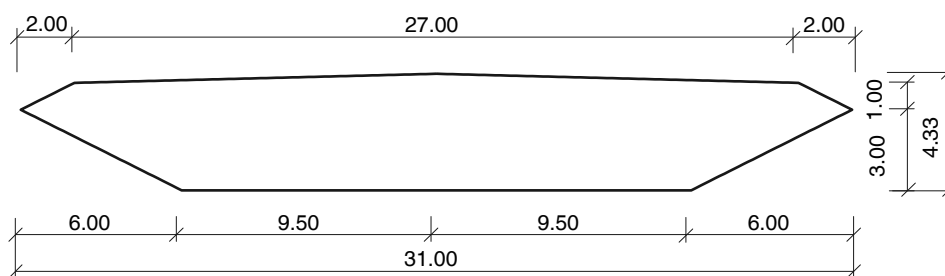
Figure 7.23: Simplified Great Belt Suspension Bridge deck sections (units: [m]).

The aerodynamic derivatives for this section were searched in the literature and some of the selected aerodynamic derivatives are plotted in Figure 7.24. The figure shows that there exist some differences in the aerodynamic derivatives since the methods of determination of the aerodynamic derivatives are quite different.

It is worth mentioning that these aerodynamic derivatives were mostly digitised from scanned literature and therefore may include some uncertainties. Additionally, some of the sets of aerodynamic derivatives did not include H_4^* and A_4^*. For these cases (WTT [141], RANS [266]), H_4^* and A_4^* were not considered.

The structural properties of the Great Belt section (cf. Table 7.5) were used and flutter analysis was performed for each set of aerodynamic derivatives using the method explained in Section 5.6.5. The computed flutter limit directly using the aerodynamic derivatives is summarised in Table 7.6 which show a large scatter in the values.

The aerodynamic derivatives are then merged by the scheme presented before. The weighted average, polynomial functions and moving least-squares fit was applied to the derivatives and from the resultant curves of aerodynamic derivative flutter limits are computed. These results are also summarised at the end of Table 7.6. A relatively close agreement is seen in the resulting values by these three approaches. For comparison, the direct average of flutter limit computed from the individual sets of aerodynamic derivatives is also calculated which is 71.8 m/s. This is also close to the MLS prediction. However, the main advantage of merging these aerodynamic derivatives is the availability of curves which can be used for further analyses.
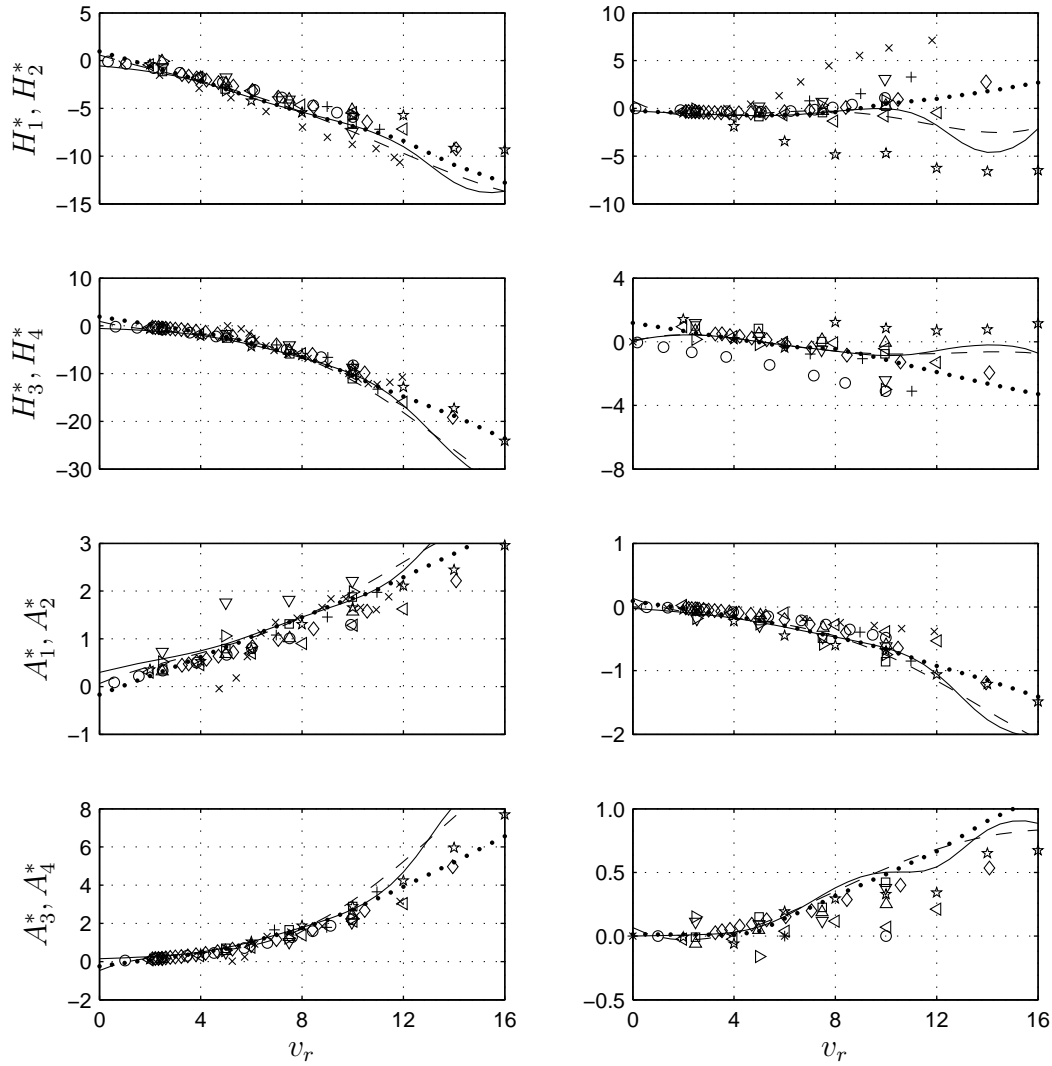
Figure 7.24: Aerodynamic derivatives (H_i^* and A_i^* where $i = 1, .., 4$): Great Belt section
($\circ$) WTT [84],
($\square$) FLUENT [84],
($\triangle$) FEM [84],
($\triangledown$) RVM [84],
($\triangleleft$) DVM [118],
($\triangleright$) DVMFLOW [141],
($\times$) WTT [141],
($\diamond$) Water tunnel [239],
($+$) RANS [266],
($\star$) VPM (this study),
($\cdots$) weighted average,
($--$) Polynomial,
($——$) MLS.

Table 7.5: Basic data and structural properties of the Great Belt bridge section [141].

B	m	I	f_h	f_α	ξ_h	ξ_α
[m]	[kg/m]	[kgm^2/m]	[Hz]	[Hz]	[-]	[-]
31	22700	2470000	0.099	0.272	0.01	0.01

Table 7.6: Aerodynamic derivative fusion: flutter limits computed from structural properties (cf. Table 7.5) and the merged aerodynamic derivatives (cf. Figure 7.24) of Great Belt section using Model#3.

Model	U_{cr}	U_{cr}/Bf_h	ω_{cr}	$v_{r_{cr}}$
	[m/s]	[-]	[rad/s]	[-]
WTT [84]	87.1	28.37	1.238	14.33
FLUENT [84]	72.8	23.73	1.246	11.88
FEM [84]	76.9	25.07	1.278	12.22
RVM [84]	68.8	22.40	1.377	10.16
DVM [118]	64.4	20.98	1.294	10.11
DVMFLOW [141]	72.2	23.52	1.378	10.67
WTT [141]	55.7	18.15	1.438	7.89
Water tunnel [239]	75.0	24.44	1.222	12.52
RANS [266]	67.5	22.00	1.261	10.92
VPM (this study)	77.6	25.29	1.164	13.58
direct average on individual values	71.8	23.40	1.289	11.43
Weighted average	68.5	22.32	1.291	10.75
Polynomial 4°	65.1	21.21	1.263	10.51
MLS ($\tilde{D}$=0.10)	68.8	22.43	1.277	10.95

7.4 Atmospheric Turbulence

The effects of turbulence on the aerodynamic forces have been studied for very limited cases so far [91]. Atmospheric turbulence is generally considered beneficial and found to raise the flutter limit. Therefore, it is usually ignored in the measurement of aerodynamic derivatives and flutter stability analysis [4, 5]. In other words, inflow turbulence tends to enhance the aerodynamic stability of long-span bridges. The main effect of the increase in the atmospheric turbulence on a bridge is not to change considerably its drag, lift, moment and aerodynamic derivatives but to excite several modes of vibration and such response will determine to what extent the bridge is prone to flutter instability.

Introducing turbulence in the wind often delays the flutter [100, 267] and stabilises the bridge deck response [268, 269] whereas sometimes flutter limit is found to increase monotonically with increasing turbulence intensity [256]. However, Frandsen [241] concluded that flutter limit for sharp edged bridge decks does not appear sensitive to turbulence in the flow. Parkinson [270] observed that in the case of large turbulence in wind flow causes a soft galloping section to becomes weaker and moving towards stability and a hard galloping section to becomes soft. Flutter occurs suddenly in a uniform flow but with atmospheric turbulence, it takes a smooth course; however, turbulent flow has a negative effect on the flutter stability of long-span bridges with streamlined section, therefore, it is important to consider this effect in the calculation of motion-induced force [271]. Cai and Albrecht [272] observed that wind turbulence may significantly reduces the flutter velocity. This has also been observed by the author [273] where the flutter limit seems to have decreased for a streamline section of a suspension bridge in a turbulent flow.

7.4.1 Fundamentals of Turbulence

Turbulence is one of the important parts of the boundary layer studies and must be quantified in order to study its effect on the structural behaviour exposed to wind action. The turbulence in the wind could be atmospheric or due to a structure on the upstream side. It creates an apparent random variations about the mean. The recorded wind time histories appear to be irregular; however, mean wind speed is often quite visible. The longitudinal U, transverse V and vertical W components of the time dependent wind velocity vector at a given location can be expressed as a sum of a constant term and a time dependent function with zero mean as:

$$U(x, y, z, t) = \bar{U}(x, y, z) + u(x, y, z, t), \tag{7.2}$$

$$V(x, y, z, t) = v(x, y, z, t), \tag{7.3}$$

$$W(x, y, z, t) = w(x, y, z, t), \tag{7.4}$$

where u, v and w are the turbulent velocity fluctuations in longitudinal, transverse and vertical directions, respectively. A dimensionless parameter that is often used as a measure of the turbulence is turbulence intensity I, also often referred to as turbulence level. Turbulent intensity is the ratio of the standard deviation or the root-mean-square of the turbulent velocity fluctuations, at a given location over a specified period of time, to the mean wind speed written as follows:

$$I_u = \frac{\sigma_u}{\bar{U}}, \tag{7.5}$$

$$I_v = \frac{\sigma_v}{\bar{U}}, \tag{7.6}$$

$$I_w = \frac{\sigma_w}{\bar{U}}, \tag{7.7}$$

where I_u, I_v and I_w are the turbulence intensities in longitudinal, lateral and vertical directions, respectively. σ_u, σ_v and σ_w are the root-mean-square or the standard deviation of the turbulent velocity fluctuations of the longitudinal, lateral and vertical components of the wind, respectively. Figure 7.25 shows turbulent intensities along height according to Eurocode [274] under ordinary conditions for different terrains.

7.4.2 Simulation Setup for Turbulent Flow Generation

Turbulence can be introduced in the wind tunnel by some disturbance upstream of the test region or by introducing surface roughness on the floor of the wind tunnel. This turbulence is carried by the flow and fills the entire tunnel cross-section. An analogous approach to the upstream disturbance to create turbulent flow in the wind tunnel was considered in this study for the numerical simulations. A number of rectangular cross-sections in the flow were placed on the upstream side of the main section to generate turbulence in the incident uniform flow. Vorticity shed from these cross sections evolved into a turbulent flow and was carried with the flow to the main section. The simulations were performed in the same numerical flow solver as explained in the earlier chapters. The arrangement and dimensions of the blocks in the simulation domain is shown in Figure 7.26.

Several simulations were performed with different block arrangements and the resulting flow properties were analysed so that the required turbulent flow is achieved. The uniform wind moving from the left of the blocks passes through the blocks and becomes unsteady or turbulent due to the vortex shedding from the blocks. This turbulence is
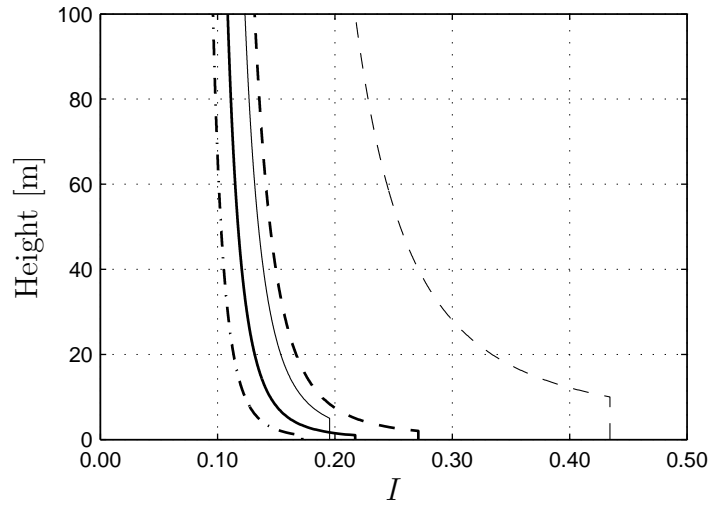
Figure 7.25: Turbulent intensity as a function of height and terrain category according to Eurocode [274]:
(– · –) Category I,
(——) Category II,
(——) Category III,
(– –) Category IV,
(– –) Category V.
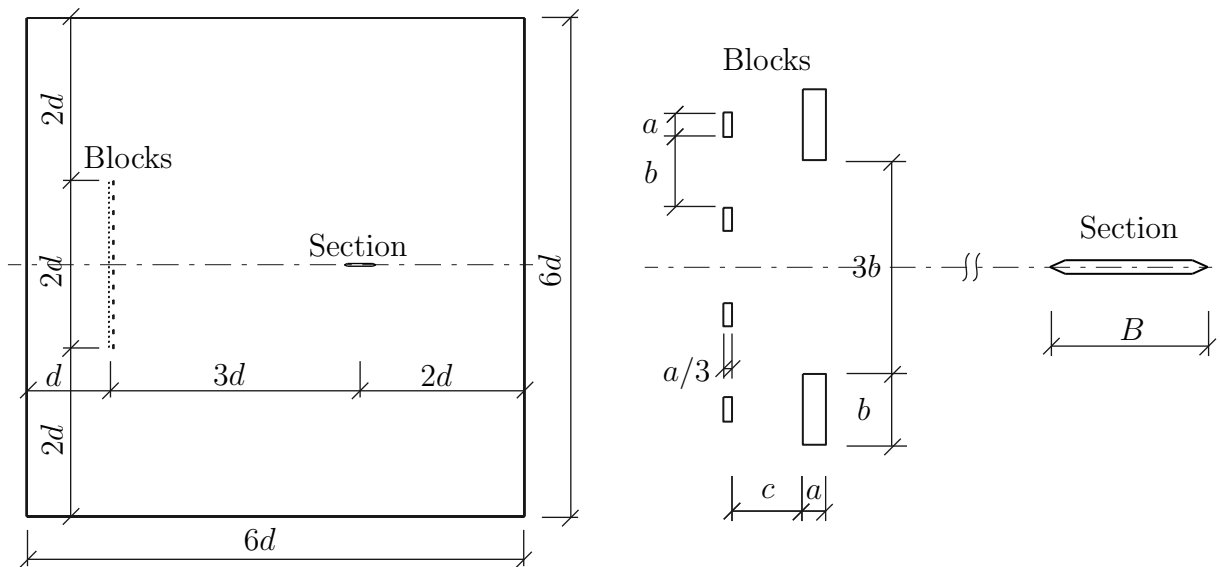
Figure 7.26: Turbulent flow in numerical simulations:
(left) domain of numerical simulation with section and upstream block setup,
(right) arrangement, size, spacing and location of blocks (cf. Table 7.7).

carried with the flow to the downstream side. The location of the bridge section was decided at a sufficient distance from the blocks such that the turbulent flow properties become almost stable. This distance depends on the size of blocks and range of wind speeds to be used. For simplicity, this distance was kept $3d$ (150 m) for all setups where the size of the domain is $6d \times 6d$ (300 m). Two block sizes were used so that the vortices shed from blocks with different frequencies cover wider part of the frequency spectrum of the flow. Four different setups were made with different block size and spacing for the bridge section as presented in Table 7.7.

Table 7.7: Turbulent flow in numerical simulations: block size and spacing for different setups and the corresponding flow parameters at the location of bridge section in the numerical simulations (cf. Figure 7.26).

Setup	a	b	c	$\bar{U}/U_\infty$	I_u	I_w
	[m]	[m]	[m]	[-]	[-]	[-]
1	0.60	1.80	1.80	0.72	0.320	0.342
2	0.30	1.80	1.80	0.88	0.126	0.130
3	0.45	1.35	1.80	0.73	0.260	0.270
4	0.45	2.70	1.80	0.89	0.176	0.172

7.4.3 Measurements of Turbulent Flow Properties

Simulations were run first with only blocks without placing the bridge section to analyse and quantify turbulent flow characteristics. One of the main effects of blocks on the flow regime is the reduction of wind speed due to blockage. The amount of blockage is related to the spacing between the blocks. Increasing the spacing leads to smaller blockage and vice versa. As a result, roughly 10-30 % blockage was observed depending on the block spacing from 1-10 times the block depth. Therefore, it is important to consider this reduction and quantify it for correct determination of turbulent flow parameters. The results for Setup 2 shown in Figure 7.27 and 7.28 are for free stream wind speed U_∞ of 100 m/s in the longitudinal direction. The point where turbulent flow properties stabilise was decided as the location of the section (i.e. 0 m in Figures 7.27 and 7.28) with respect to the location of blocks (i.e. -150 m). The resulting mean wind speed $\bar{U}$ at the intended location of the bridge section measures to be 88 m/s. The mean wind speed and turbulent intensity at the location of section measured for different setups are presented in Table 7.7.

It was observed that the turbulence level is directly related to the size of the blocks. Decreasing the size will decrease the turbulence intensity but increases computational effort due to increase in number of blocks. From Figure 7.28, it can be seen that the turbulence intensity I_w at the location of the section is 0.13 whereas in Figure 7.25 the turbulence intensity ranges roughly varies from 0.10 to 0.43. The results for the mean wind speeds and the turbulence intensities for four different setups used in this study are shown in Table 7.7.

In Figures 7.27 and 7.28, selected part from the simulation domain is shown. These figures show that fluctuations in the flow properties are more near and around the location of the blocks and as the flow moves away from the blocks, fluctuations decrease and stabilise. Figure 7.29 shows the frequency spectra of the fluctuating component of the flow in vertical direction compared with von Karman spectrum. There is a distinct
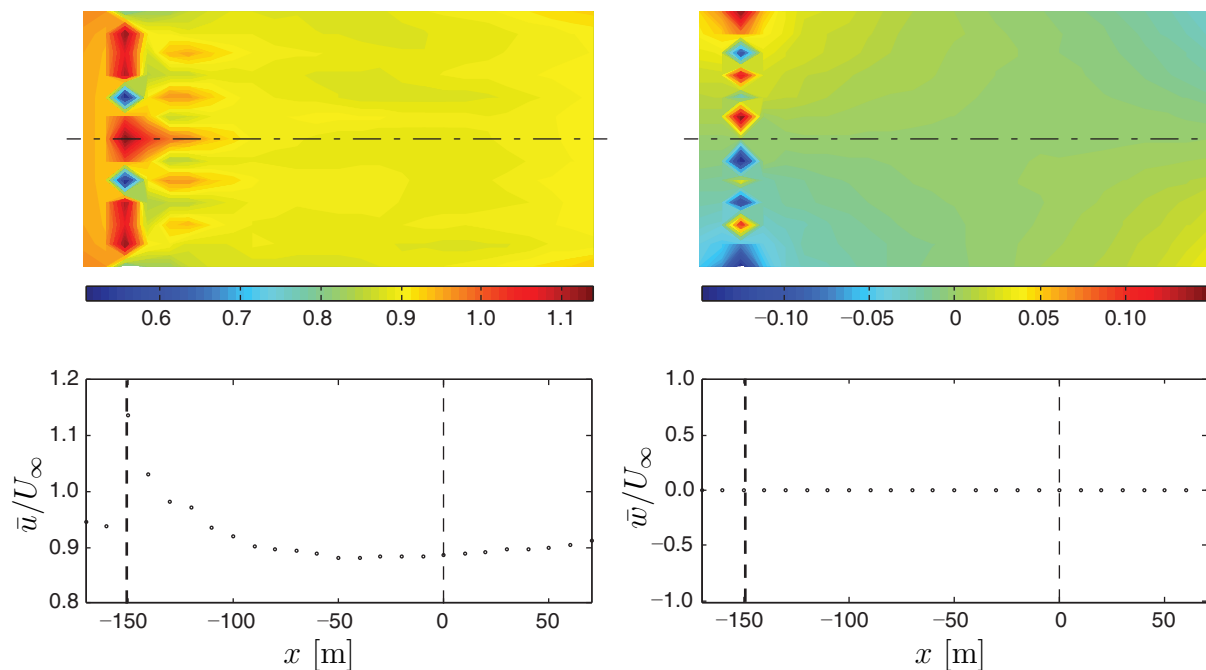
Figure 7.27: Turbulent flow in numerical simulations:
(left) ratio of longitudinal time averaged wind to free stream wind speed $\bar{u}/U_\infty$,
(right) ratio of vertical time averaged wind to free stream wind speed $\bar{w}/U_\infty$,
(top) values over the area,
(bottom) values along the centreline,
(– –) block location,
(– –) intended section location.

difference between the dominant frequencies for different setups which shows that the
size and spacing of blocks have a considerable effect on the frequency characteristics
of the flow. The values match relatively better for Setup 3 and 4 for high-frequency
range; however, discrepancies are seen in low-frequency ranges. This could be due to
insufficient length of simulation time.

7.4.4 Flutter Simulations on Bridge Section

The section of the bridge was supported on springs and was allowed to move under the
influence of flow in 2DOF corresponding to its first bending and first torsional mode
of vibrations. The simulations were performed at different wind speeds, the resulting
amplitudes were recorded along with the other parameters and the flutter limit was
determined. The same section of the bridge was modelled along with four block setups.
The generated turbulence from the blocks on the upstream of section travelled to the
section and it received the modified flow regime. The response of the section was
recorded for different wind speeds and the flutter limit was determined. Figure 7.30
demonstrates the bridge section in a uniform flow and the vortex stream from the
section on the downstream side of the section. It also shows qualitatively the interaction
of eddies in the incident turbulent flow with the vortex shedding process over the body
surface.
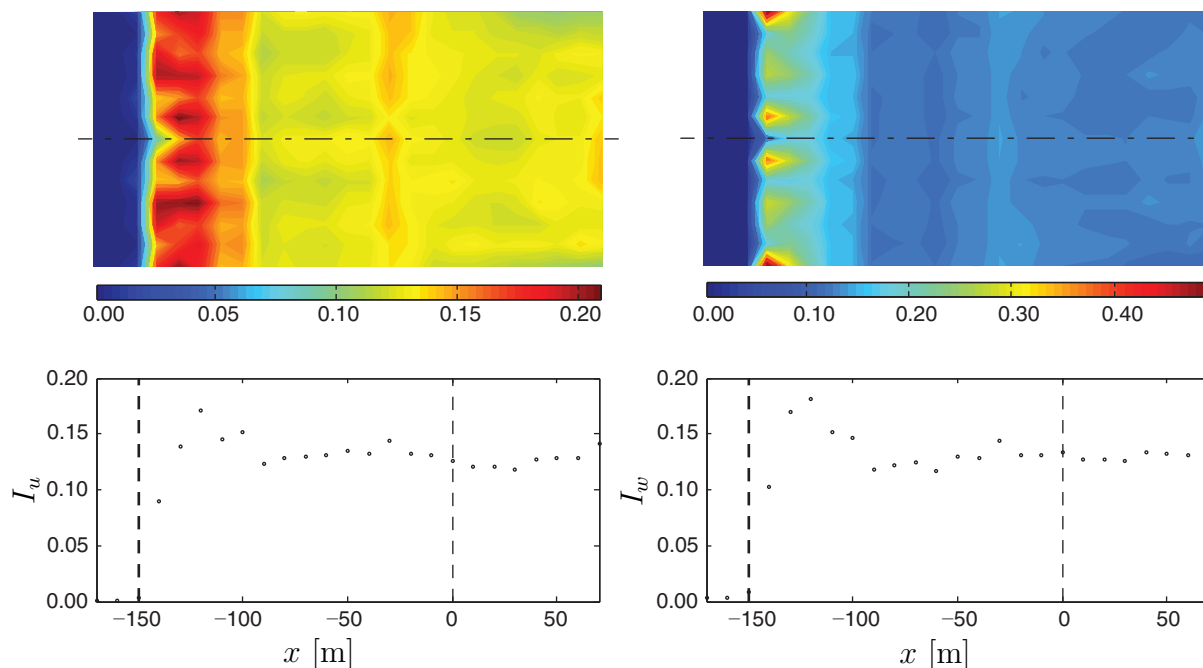
Figure 7.28: Turbulent flow in numerical simulations:
(left) turbulence intensity in longitudinal direction I_u,
(right) turbulence intensity in vertical direction I_w,
(top) values over the area,
(bottom) values along the centreline,
(– –) block location,
(– –) intended section location.
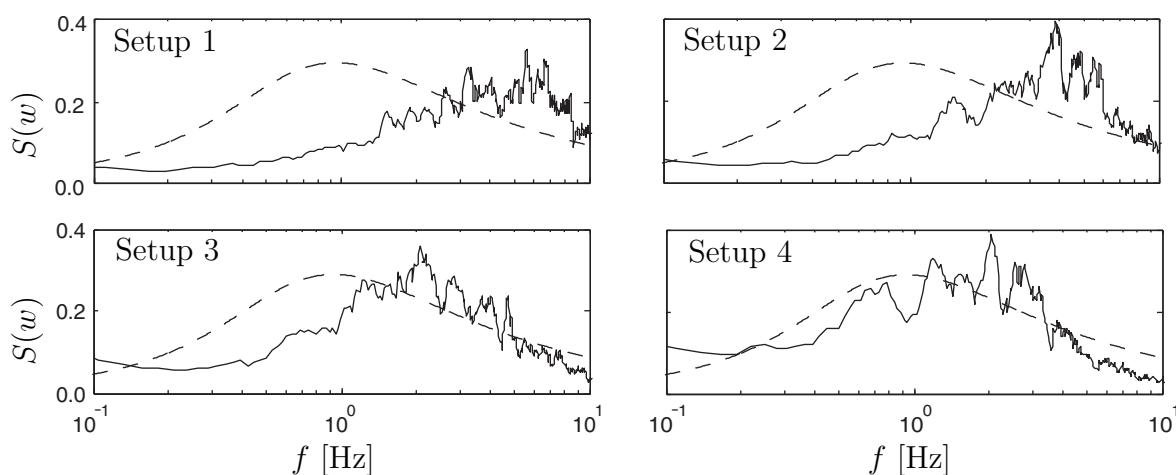
Figure 7.29: Turbulent flow in numerical simulations: spectra of fluctuating component of flow in vertical direction at the location of bridge section for different block setups,
(——) simulated (cf. Table 7.8),
(– –) von Karman.

7.4.5 Results of Turbulent Flow Simulations

The 2D numerical simulations were performed on Structure A (cf. Section 6.2). The simulations were run for a uniform flow first and the flutter limit was found to be 101 m/s. The same section was then used for different turbulent flow conditions. The simulations were run at various wind speeds and the flutter limits were determined. The
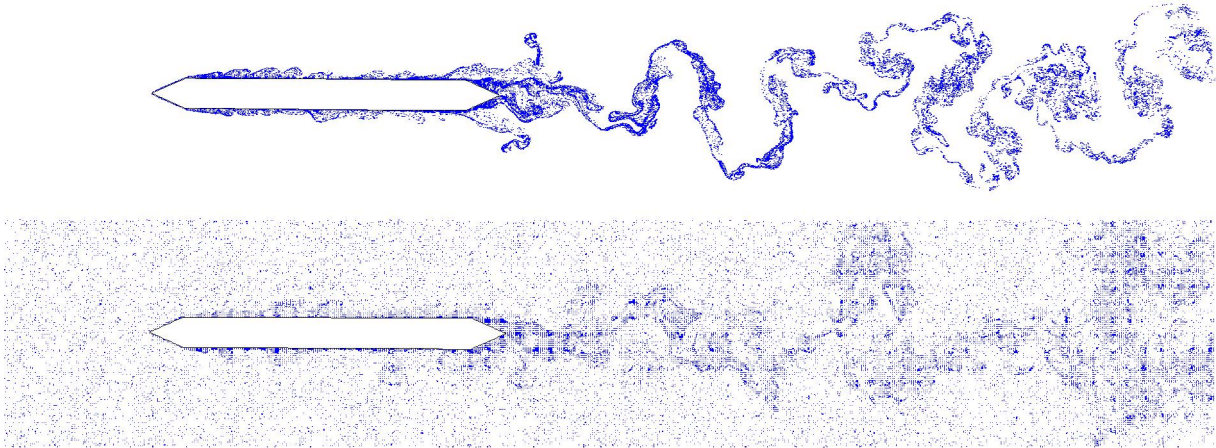
Figure 7.30: Instantaneous view of particle stream:
(top) bridge section in a uniform flow,
(bottom) bridge section in a turbulent flow.

summary of resulting flutter limits is presented in Table 7.8 and the maximum response
amplitudes are shown in Figure 7.31. Figure 7.31 shows that low turbulent intensities
have no considerable effect on the flutter limit; however, for larger turbulent intensities
the effect is a significant reduction in the flutter limit. This implies that for the terrain
categories, with smaller surface roughness, will have less effect on the flutter limit and
uniform flow conditions can be considered. However, for rough terrains, considering only
uniform flow could give unsafe results. It can be visualised in Figure 7.31 that in a
uniform flow, in general, the maximum dynamic amplitudes h_{max} for the section increases
with the increase in wind speed. In a turbulent flow, the amplitudes are generally higher
and before reaching the critical limit, the phenomenon of buffeting can be observed but
the flutter limits are different. It is observed that the increase in amplitudes due to
turbulence depends on the amount of turbulence and frequency characteristics of the
flow.

Table 7.8: Effect of turbulence on the flutter limit of Structure A from 2D numerical
simulations: critical flutter limits in uniform flow and in different turbulent flow
conditions (cf. Figure 7.31).

	Uniform flow	Setup 1	Setup 2	Setup 3	Setup 4
U_{cr} [m/s]	101.0	95.6	100.6	92.0	100.6
U_{cr}/Bf_h [-]	19.6	18.6	19.5	17.9	19.5
I_u [-]	-	0.320	0.126	0.260	0.176
I_w [-]	-	0.342	0.130	0.270	0.172
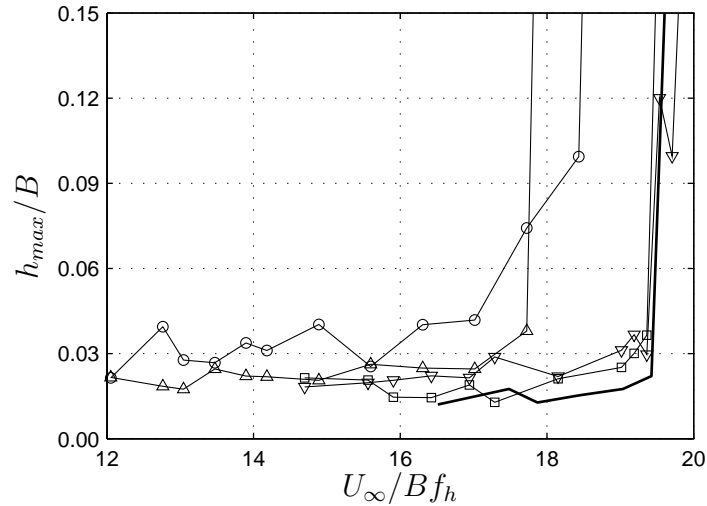
Figure 7.31: Effect of turbulence on the flutter limit of Structure A from 2D numerical simulations: maximum dynamic response amplitudes of bridge section with increasing wind speed in different flow conditions,
(—) uniform flow,
(○) I_w=0.342,
(□) I_w=0.130,
(△) I_w=0.270,
(▽) I_w=0.172 (cf. Table 7.8).

7.5 Results of Flutter Analyses

This section summarises the results of the flutter analyses from Chapter 6 and Chapter 7. The model combinations presented in Chapter 5 have been used to predict the flutter limits of the selected reference objects (cf. Section 6.2). The computed flutter limits are summarised in Table 7.10. Table 7.9 provides the model combinations and the parameters related to these model combinations.

A 2DOF system was analysed through analytical, empirical and numerical approaches. The first bending and the first torsional modes were selected for the coupled flutter analyses. Further, it was assumed that both the modes are exactly similar or in other words, the value of the MSSF is 1.0. Such simplifications are valid for the structures which have decoupled and distinct modes. Structural coupling of modes can have a significant effect on the onset of flutter for very long span bridges such as Akashi Kaikyo Bridge. However, for the selected reference object, this effect was insignificant due to relatively small span. Moreover, the frequency ratio between the torsional mode and the bending mode is another factor of major importance. A larger value of the frequency ratio increases the onset speed of flutter. The contribution of higher modes was also studied through the multimode flutter analysis. For the presented example (Structure A), the predicted flutter limit was unaffected by including more modes into the analysis. Two structures have been selected as the reference objects with distinct structural and aerodynamic properties. The predictions of simplified models are much higher than the complex model predictions in case of Structure H which could lead to an unsafe situation.

Table 7.9: Model comparison with the assumptions and considered parameters, (×) aspects covered in this study (cf. Table 7.10), (●) not covered here.

Criterion/parameter	Model										
	#1	#2	#3			#4			#5		
	a..g	a..f	a	b	c	a	b	c	a	b	c
Modal properties	×	×	×	×	×	×	×	×	×	×	×
Structural damping	×		×	×	×	×	×	×	×	×	×
Mode shape				×	×		×	×			×
Multi-mode					×			×			×
Cross section shape			×	×	×	×	×	×	×	×	×
Body generated turbulence									×	×	×
Variable cross section					●			●			●
Atmospheric wind conditions											
- mean wind profile						●	●	●	●	●	●
- turbulence characteristics						●	●	●		×	●
- correlation							●	●			●
Other excitation phenomenon											
- Buffeting							●	●	●	●	●
- VIV									●	●	●
Suitable for design stage					●			●		●	●

Model#1 Fully Analytical: Theodorsen equations for motion-induced aerodynamic forces with 2D structural model

(a..g: different Theodorsen circulation functions) (cf. Section 5.4)

Model#2 Empirical Approach: for 2D only

(a..f: Selberg, Rocard, etc.) (cf. Section 5.5)

Model#3 Derivative-based Eigenvalue Analysis: Theodorsen flat aerodynamic derivatives and Scanlan derivatives from CFD forced vibration simulations with 2D and 3D structural model

(a: 2D, b: with mode shape, c: multimode) (cf. Section 5.6.5)

Model#4 Derivative-based FSI Simulations: Theodorsen flat aerodynamic derivatives and Scanlan derivatives from the CFD forced vibration simulations with 2D and 3D structural model

(a: 2D, b: 2 modes, c: multimode) (cf. Section 5.6.6)

Model#5 Fully-coupled CFD Simulations: based on the VPM with 2D and quasi-3D structural model

(a: 2D laminar flow, b: 2D turbulent flow, c: quasi-3D laminar flow) (cf. Section 5.7)

Fully-analytical models are useful to gain insight of the force coupling. However, these models cannot be used for bluff sections due to their inability to take into account the shape of the section. This has been discussed in detail in Section 6.5.1. The cross-sectional shape plays an essential role in the aeroelastic behaviour of a long-span bridge and sometimes it is a decisive factor in the design of the bridge under wind action. The empirical formulas are the simplest to immediately calculate the flutter limit for a bridge section; however, their application is limited to only provide a rough estimate. The CFD simulations based on the VPM are convenient to model the aerodynamic behaviour of the cross section in the absence of the wind tunnel data. However, there is a large uncertainty associated with these simulations resulting from the choice of numerical parameters. This can be also due to under-resolved flow field at low Reynolds number and the quality of diffusion model used. The process of Vortex shedding and flow separation greatly depend on the Reynolds number. Nevertheless, numerical simulations provide a viable solution to study the complex aeroelastic phenomenon of flutter.

Table 7.10: Results of flutter limits (U_{cr} [m/s]) computed from different model combinations with assumptions made for Structure A and Structure H. (cf. Tables 6.15 and 7.9).

		Structure A		Structure H
		Lillebælt section	Flat plate (B/D=100)	
	a	93.8		26.2
	b	95.1		26.4
	c	94.0		26.0
Model#1	d	93.0		25.8
	e	91.8		25.3
	f	93.8		26.2
	g	93.6		26.0
	a	92.0		33.9
	b	90.0, 90.3, 90.6, 92.0, 90.6		24.0, 24.1, 24.1, 24.5, 24.1,
Model#2	c	90.6		24.1
	d	93.0		24.8
	e	108.4		29.5
	f	102.5		34.2
	a	94.1	89.0	11.1
Model#3	b	96.0	-	-
	c	98.0	92.0	-
	a	99.0	92.0	-
Model#4	b	101.0	94.0	-
	c	101.0	94.0	-
	a	95.0	98.0	15.0
Model#5	b	92.0	-	-
	c	95.0	-	-

In general, all modes were able to predict the flutter limit for the presented examples; however, there exist a large scatter among the model predictions as illustrated in Figure 7.32. It has been shown in Section 7.3.4 that the simplified models (Model#1 and Model#2) fail to predict the realistic situation in special circumstances. Such as, in the case of a circular section there exists no flutter instability. The simplified models predict flutter onset, whereas a superior model (Model#3) predicts the phenomenon correctly and does not give any instability limit even if the simulation is performed at a very high wind speed. The predictability of the phenomenon is a major advantage of the complex model over the simplified models which sometimes lack this important feature.
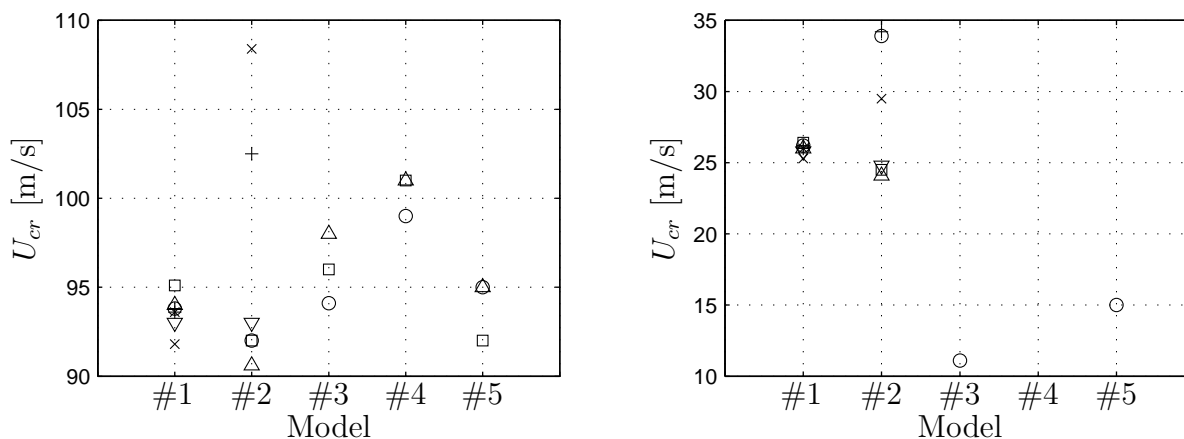
Figure 7.32: Results of flutter limit predictions from different model combinations with assumptions made for:
(left) Structure A,
(right) Structure H,
○ a, □ b, △ c, ▽ d, × e, + f * g (cf. Tables 7.9 and 7.10).

7.6 Summary

The influence of different input parameters on the flutter stability prediction has been discussed in this chapter. The structural parameters and the aerodynamic behaviour of the cross section are studied in detail. The non-dimensionalisation is common to use; however, the effects of changing only one or few parameters in the non-dimensional parameter on the output have been highlighted which could be sometimes misleading.

The aerodynamic behaviour is also studied with the sensitivity to the geometry of the cross section. A wide range of studies on the section geometry has been presented. A common categorisation of sections has been described and the features affecting the aerodynamic behaviour are highlighted. It was also pointed out that this type of categorisation of cross sections has some limitations in covering certain features which could change the aerodynamic behaviour significantly.

An approach is presented to use the existing aerodynamic derivatives for a cross section from different sources to merge and use the aerodynamic derivatives for the estimation of flutter stability limit. For this purpose, response surface methods were used. It is also possible to use different weighting factors for data obtained from different sources.

Furthermore, the effects of turbulence in the flow on the flutter stability has been

studied. An approach has been presented to generate turbulence in the flow solver which is based on a laminar inflow. The approach similar to that of the wind tunnel testing was employed by placing small rectangular sections on the upstream of the main section to generate turbulent flow. The results were favourable with reasonable quality; however, this approach has a limitation of being computationally expensive. Another approach could be to introduce a particle ladder which can release particles with a certain vorticity at each time step. This approach could reduce the computation time and serve as a more robust solution to achieve a certain quality of turbulent flow properties.

Chapter 8

Probabilistic Assessment of Coupled Models

8.1 Introduction

Flutter analysis is commonly performed through deterministic approach by using fixed values of the input parameters. However, the final flutter limit is significantly influenced by a small change in one or few input parameters. Thus calculations performed considering the stochastic input parameters results in a probabilistic flutter analysis, where the flutter limit is described as a stochastic variable which is a function of parameter variation. Probabilistic flutter analysis also helps to quantify the probability distribution and confidence intervals of the model prediction. Therefore, it is important to consider such variation in the input parameters and to perform the flutter analysis using a probabilistic approach.

The main objective here is to develop a framework to perform flutter stability analysis using probabilistic input parameters. In this chapter, deterministic and probabilistic sensitivity analyses have been used to identify the essential input parameters and their effect on the model response is quantified. A novel approach to consider aerodynamic uncertainties for bridge deck sections is presented. Input parameter uncertainties and model uncertainties are quantified for the selected models (i.e. Model#1 and Model#3) presented in Chapter 5. Finally, the ranking of models is done based on their total uncertainty.

8.2 Probabilistic Approach to Flutter Analysis

The probabilistic assessment of aeroelastic stability of flutter is important for design considerations of cable-supported long-span bridges [32]. The critical design wind speed is determined such that the probability of failure due to flutter is less than or equal to a specified target safety level for a given return period. Ianenti and Zasso [275] applied a probabilistic approach to identify the flutter instability for the case of a suspension bridge. Some studies have been conducted on the probabilistic assessment of flutter limit prediction from wind tunnel testing [276] and CFD applications [277]. The probabilistic assessment also consists of sensitivity analysis, uncertainty analysis, reliability analysis and design optimization. However, this study focuses only sensitivity and uncertainty analyses.

The sensitivity analysis can provide very important information about the dependence of the key chosen design variables on the flutter limit of a bridge. The objective of sensitivity analysis is to identify which parameters affect the response. Jurado and Hernández [157], Nieto et al. [278] carried out an analytical sensitivity analysis of the flutter phenomenon in long-span bridges. Sarkar et al. [279, 280], Caracoglia et al.

[281] studied the sensitivities related to extracting experimental aerodynamic derivatives between different laboratory environments. Abbas and Morgenthal [127, 282] studied sensitivity and uncertainty of structural parameters and aerodynamic derivatives on flutter limit.

Commonly the flutter analysis is performed considering complete deterministic structural parameters which is known as deterministic analysis. However, there are uncertainties in these design variables which include, geometric properties, material properties, load magnitude and distribution [283] as well as aerodynamic derivatives [284, 285, 286, 287]. This makes it necessary to consider these uncertainties in the analysis for complete information. Jakobsen and Tanaka [288] discussed uncertainties in the prediction of aeroelastic flutter response of cable-supported bridges. Ito and Fujino [289] discussed the effect of spatial and temporal fluctuations of wind flows on the torsional flutter of suspension bridges by using numerical analysis through Monte Carlo Simulation (MCS). Argentini et al. [290] also used MCS to considered the effects of structural and aerodynamic uncertainties. Structural mass and stiffness parameters are shown to have a significant effect upon the flutter limit especially torsional frequency and mass moment of inertia [127].

There have been several studies conducted on the flutter stability analysis considering parametric uncertainties [15, 283] as well as model-form and predictive uncertainty [20, 22, 23, 24] in the aeronautical industry by using Monte Carlo simulation and utilizing the advantages of the Response Surface Method (RSM). It is worth mentioning that to the best of author's knowledge, there have been no study to this time which provides a complete framework to consider input structural parameter uncertainty, aerodynamic uncertainty as well as model framework uncertainty in the flutter analysis of bridges. This study is an attempt to covering these aspects.

8.2.1 Parameters and Assumptions for Sensitivity and Uncertainty Analyses

The uncertainties can be generally classified into epistemic and aleatory uncertainties. There are different sources of uncertainties in the flutter stability analysis and these can be broadly categorised into four main types as shown in Figure 8.1. The uncertainties of structural input parameters and aerodynamic derivatives are included by modelling them as probabilistic input variables. The uncertainty for each parameter is assumed to be represented by a normal distribution and it is further assumed that the uncertainty of structural input parameters and aerodynamic derivatives are independent. All other input parameters are assumed to be deterministic.

In general, the structural dynamics of the bridge is governed by the structural input parameters such as mass, frequency and damping ratio. The predicted flutter limit of the bridge strongly depends on the fundamental natural frequencies of the bridge, especially the torsional frequency. The flutter limit also depends on the final magnitude of the aerodynamic derivatives. For this purpose, analytical aerodynamic derivatives for flat plate and aerodynamic derivatives from CFD forced vibration simulations for the reference sections have been used. Sensitivity and uncertainty analyses have been performed. The flutter limits for the reference objects (cf. Section 6.2) were computed on the basis of models described in Section 5.4 and 5.6.5. The importance of each structural parameter and the aerodynamic derivative has been quantified by the sensitivity analysis.

Flow Modelling
• Reynolds Number (turbulent or laminar flow) • Atmospheric turbulence: intensity, spectra, spacial correlations

Structural Modelling
• Solid, shell, beam elements • Linear system • Dimensional reduction from 3D to 2D • Number of modes considered • Prior knowledge of mode coupling • Modal or Rayleigh damping • Model calibration accuracy (natural frequencies) • Scaling of the bridge model

Aerodynamic Modelling
• Approximation of self-excited forces as linearly dependent of structural motion • Important details reproduced • 2D vs. quasi-3D (Multi-slice approach)

Fluid-structure Coupling Model
• Aerodynamic derivatives from free, forced or Buffeting response • Method of extracting aerodynamic derivatives • Length of measured time history • Accuracy of least-squares fit • Accuracy of measurement methods

Figure 8.1: Sources of uncertainty in flutter analysis.

8.2.2 Variation in Parameters and Application of Response Surface

The MCS is the traditional and the most commonly used method for a probabilistic analysis. Usually, the MCS require a great number of simulations to be performed for a different set of input parameters which increases the computation time. For this purpose, the RSM can be used to decrease the number of simulations and to make this process more efficient. The RSM represents the structural response by using a simple approximation function. To perform a numerical simulation may take from some minutes to a few days whereas running this function require only fraction of a second. The computation time can be greatly reduced without modifying the existing numerical code for the simulation. These RSMs have been used for the probabilistic torsional flutter [291, 292, 293] and coupled flutter [294] analyses considering structural parameter uncertainties.

Here, response surface analysis has been utilized to make the method of computing the flutter limit more efficient. Figure 8.2 shows the process of using the response surface method to compute the flutter limit and using it for further analyses. A polynomial regression model, as well as the MLS, were tested as response surfaces.

The variation in the structural input parameters and the aerodynamic derivatives has been treated separately. The input parameter space is discretized to generate combinations of sample sets according to DoE scheme presented in Section 2.3. The variation in the structural input parameters is considered first to show the application of response surface approach and its effectiveness. Table 8.1 presents the time required to compute flutter limits with the actual model and with the response surface method (cf. Section 2.4). It is evident that there is a significant improvement in the computational time. It is also important to consider the quality of meta-model used to accurately describe the model behaviour. The CoD shows the quality of the regression
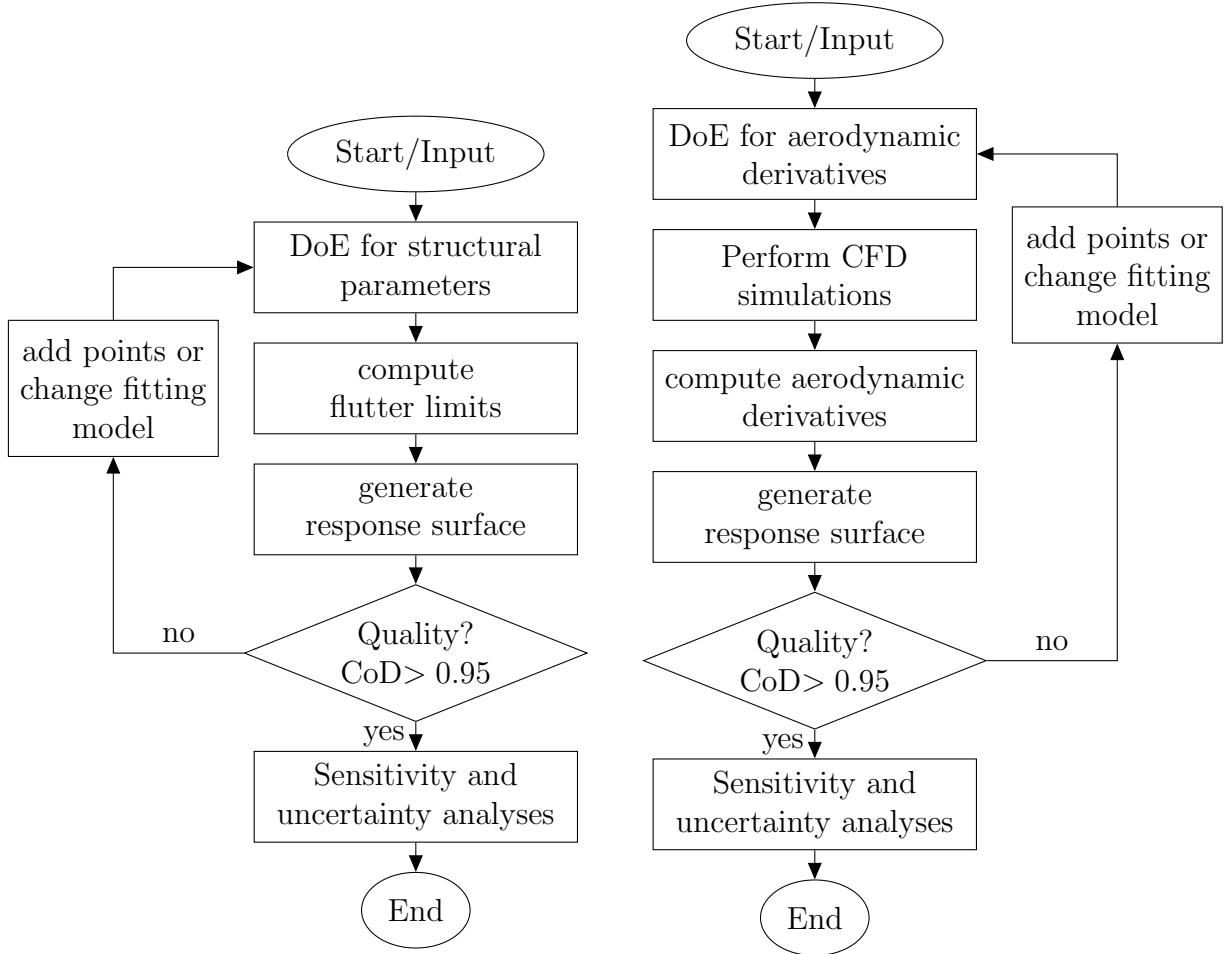
Figure 8.2: Procedure to use response surface methods to perform sensitivity and uncertainty analyses in computing flutter limit considering variation in
(left) structural input parameters,
(right) aerodynamic derivatives.

model which is close to 1 in the table. This means that the simplified mathematical model describes very well the behaviour of the complex model. Table 8.2 shows a good agreement of flutter limits computed with those from the actual model.

Table 8.1: Comparison of time required for the flutter analysis by the actual model and the response surface method (using variation of structural input parameters in Structure A).

	Model	No. of samples	Time [s]	CoD, R^2 [-]
Actual model	Model#1	100	7	-
Actual model	Model#3	100	102	-
RSM, Polynomial 4°	Model#1	10,000	<1	0.98
RSM, Polynomial 4°	Model#3	10,000	<1	0.98

The variation in the structural input parameters is straightforward as only mean, standard deviation and distribution are required to generate samples for the variance based approaches, whereas aerodynamic derivatives represent the motion-induced behaviour of the cross section which is a function of reduced speed v_r and has a physical

Table 8.2: Comparison of flutter analyses performed by the response surface method and the actual model (using variation of structural input parameters in Structure A).

Model	Structure	Actual model		RSM, Polynomial 4°	
		U_{cr} [m/s]	U_{cr}/Bf_h [-]	U_{cr} [m/s]	U_{cr}/Bf_h [-]
Model#1	A	93.8	18.2	94.2	18.3
Model#1	H	13.5	8.6	13.8	8.8
Model#3	A	116.8	22.7	118.4	23.00
Model#3	H	8.5	5.4	8.4	5.4

meaning. If a random sample is generated for the aerodynamic derivatives, it may not necessarily reflect physically possible behaviour.

The uncertainty evaluation of each aerodynamic derivative includes the sensitivity and scatter of the respective aerodynamic derivative. The scatter of the aerodynamic derivatives is small at lower v_r and gets large as the v_r increases. Therefore, linearly increasing standard deviation may be considered for the aerodynamic derivative which is a function of v_r. A probabilistic approach to modelling the aerodynamic derivatives for a flat plate is suggested by selecting the aerodynamic derivative curves added or subtracted with the uncertainty following the normal distribution. The condition of linearly increasing standard deviation of aerodynamic derivatives along v_r needs also to be satisfied.

The uncertainty in the aerodynamic derivatives can be quantified from the scatter or deviation of analytical flat plate derivatives and by comparing it to the experimental tests [264] or numerical forced vibration simulations on the thin rectangular plate. Another approach could be to quantify uncertainty from the residual obtained by the fitting function on the aerodynamic derivatives [35].

An approach has been suggested here to consider uncertainty in the aerodynamic derivatives by varying section geometry. The aerodynamic derivatives were computed from the CFD simulations at several reduced speeds with varying section geometry to account for better scatter for statistical measures. Figure 8.3 and 8.4 shows the variation of the deck shape and the effect on the aerodynamic derivative A_2^*. The aerodynamic Derivative A_2^* is the negative damping induced by torsional motion and is important for SDOF torsional flutter. The wind speed at which A_2^* becomes positive corresponds to SDOF critical limit (assuming no structural damping). Figure 8.4 indicates that Structure A does not have any problem against torsional flutter whereas Structure H is vulnerable in almost the whole range of d/D.
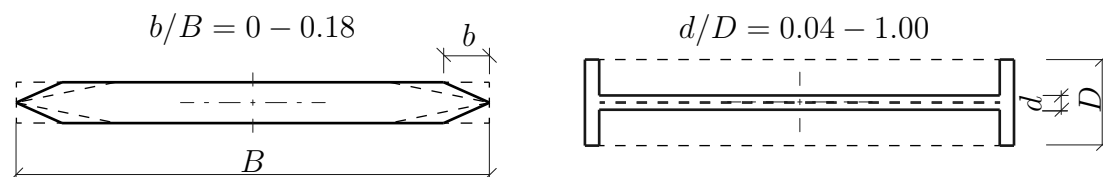
Figure 8.3: Section geometry variation considered for the CFD simulations to apply response surface.

Response surfaces were generated for these aerodynamic derivatives computed from the CDF simulations. For this purpose, both the polynomial functions and the MLS approaches were used. Table 8.3 shows the CoD from these approaches. It is clear
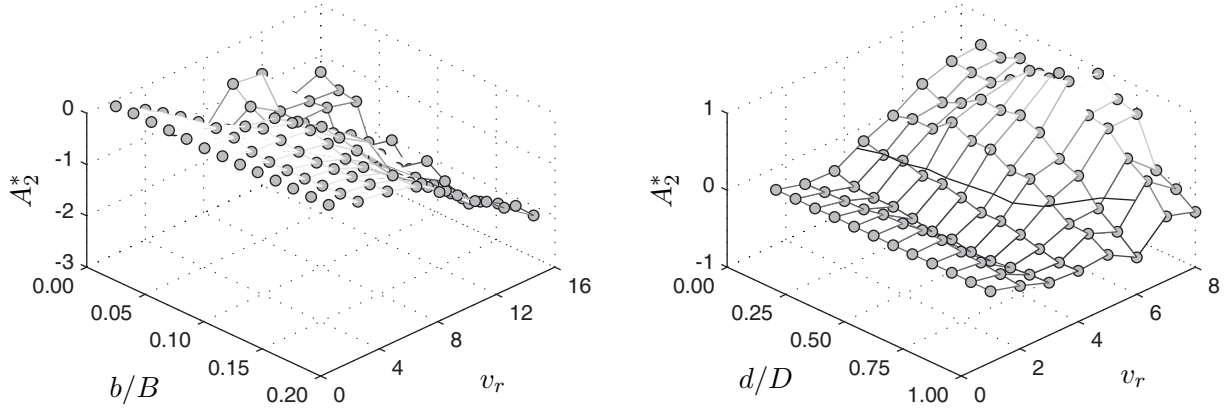
Figure 8.4: Aerodynamic derivative A_2^* from CFD simulations for
(left) Structure A and
(right) Structure H.
(——) SDOF torsional flutter limit (with $\xi_\alpha = 0$) (cf. Figure 8.3).

from the results that the MLS shows much better behaviour whereas even a polynomial of 5° is not sufficient to capture the behaviour of some aerodynamic derivatives where the CoD of less than 0.50 is achieved. However, the MLS approach takes much longer computational time. For comparison time requited for direct interpolation is also shown.

It is also important to see the quality of the response surface if it is applied on different reduced speed ranges. Table 8.4 summarizes the CoD by a polynomial model fitted on aerodynamic derivatives. It shows that for low reduced speeds, the quality of fit is better as this range has less scatter and the fitting quality decreases for higher reduced speed ranges which can be improved by adding more data points.

Table 8.3: Fitting quality measure (CoD [-]) and required time of response surface generation on the aerodynamic derivatives of Structure A.

Derivative	Interpolation		Polynomial					MLS		
	linear	cubic	1°	2°	3°	4°	5°	$\tilde{D}$=0.05	0.10	0.15
H_1^*	1.00	1.00	0.00	0.05	0.13	0.26	0.37	0.98	0.97	0.97
H_2^*	1.00	1.00	0.01	0.62	0.81	0.84	0.86	0.99	0.99	0.99
H_3^*	1.00	1.00	0.09	0.90	0.97	0.98	0.98	1.00	1.00	1.00
H_4^*	1.00	1.00	0.02	0.15	0.38	0.43	0.48	0.98	0.98	0.97
A_1^*	1.00	1.00	0.10	0.23	0.36	0.41	0.48	0.98	0.98	0.98
A_2^*	1.00	1.00	0.02	0.18	0.34	0.44	0.54	0.97	0.97	0.96
A_3^*	1.00	1.00	0.50	0.51	0.93	0.95	0.97	1.00	1.00	1.00
A_4^*	1.00	1.00	0.02	0.08	0.20	0.28	0.33	0.97	0.96	0.95
Time [s]	0.02	0.03	0.01	0.01	0.04	0.05	0.05	292	128	49

Aerodynamic derivatives were computed by the CFD simulations and response surfaces were generated. Figure 8.5 shows different approaches to account for the uncertainty in the aerodynamic derivatives. For a flat plate aerodynamic derivatives, the approach in the middle was employed and for aerodynamic derivatives from the CFD forced vibration simulations, the approach on the right was used.

Table 8.4: Fitting quality measure (CoD [-]) of response surface on different reduced speed v_r ranges (using polynomial 5°) (cf. Figure 8.4).

Derivative	Structure A				Structure H			
	v_r=2-8	6-12	10-16	2-16	1-4	3-6	5-8	1-8
H_1^*	0.94	0.55	0.36	0.78	0.97	0.95	0.93	0.96
H_2^*	0.99	0.92	0.84	0.94	0.99	1.00	0.99	0.98
H_3^*	1.00	0.99	0.99	0.99	0.96	0.99	0.99	0.98
H_4^*	0.69	0.75	0.49	0.49	0.99	0.92	0.91	0.96
A_1^*	0.94	0.56	0.72	0.84	0.95	0.77	0.75	0.77
A_2^*	0.99	0.98	0.98	0.98	0.97	0.99	0.88	0.96
A_3^*	1.00	1.00	1.00	1.00	0.98	0.96	0.96	0.83
A_4^*	0.62	0.29	0.53	0.64	0.99	0.90	0.72	0.91

Then sampling was performed for eight aerodynamic derivatives for global sensitivity and uncertainty analyses. Figure 8.6 provides different sampling techniques for the aerodynamic derivatives. The approach in the middle was utilized for flat plate aerodynamic derivatives whereas the approach on the right was used for aerodynamic derivatives from the CFD forced vibration simulations.
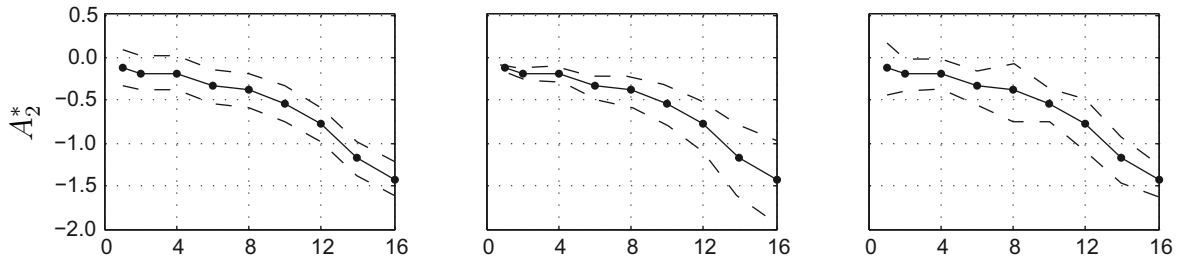
Figure 8.5: Approaches to consider uncertainty in the aerodynamic derivatives:
(left) average uncertainty over whole v_r range,
(middle) linearly increasing uncertainty depending on v_r,
(right) independent uncertainty at each v_r.
(—•—) mean values from the CFD simulations,
(– –) upper and lower limits corresponding to 95.44% ($\pm 2\sigma$) confidence interval.
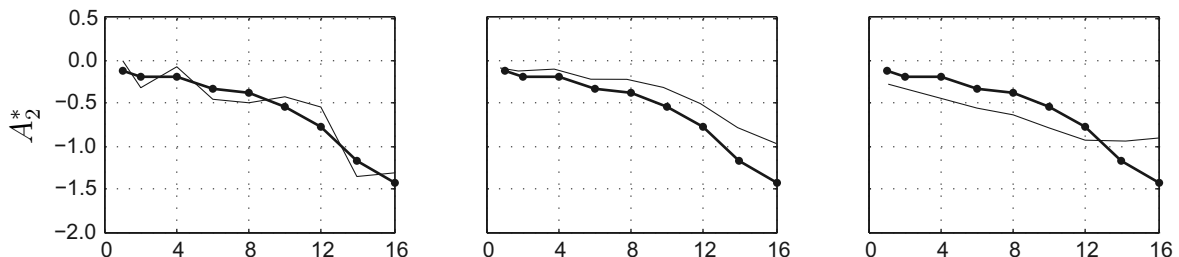
Figure 8.6: Approaches to generate sampled aerodynamic derivatives:
(left) random generation independent of v_r
(middle) following a scaled mean
(right) interpolation between geometric change.
(—•—) actual values from CFD simulations
(——) sampled aerodynamic derivatives.

8.3 Sensitivity Analysis

The structural parameters of Structure A and Structure H used in the sensitivity analysis are shown in Table 8.5. Local sensitivity analysis was performed first as explained in Section 2.5.1.1. The variations in the input parameters were assumed to be independent of each other. It is important to note that the non-dimensional parameters calculated are only based on changing single parameter as discussed in Section 7.2. The results of the analysis in Figure 8.7a show that the frequency ratio γ_ω is the most important input parameter affecting the flutter limit. Then the parameters μ and r_α also have significant effect whereas ξ has the least effect as compared to the other input parameters. The structural damping ratio ξ may have a significant effect on the flutter limit [295]. However, with the presence of uncertainty in the other parameters it has been noted that this effect is comparatively low.

On the same lines, a local sensitivity analysis was also performed for aerodynamic derivatives to quantify their importance on the flutter limit. Figure 8.7b shows the results of the analysis where it can be seen that H_3^*, A_1^*, A_2^*, A_3^* and to some extent H_1^* are the most significant aerodynamic derivatives. H_4^* seems to have almost no effect which confirms the outcome of other studies [35, 38, 264]. However, A_4^* has still some visible effect.

Figure 8.7: Sensitivity indices for flutter speed from local sensitivity analysis considering variation in
(left) structural input parameters,
(right) aerodynamic derivatives. (cf. Section 2.5.1.1)
($\triangle$) Model#1 Structure A,
($\triangledown$) Model#1 Structure H,
($\circ$) Model#3 Structure A,
($\square$) Model#3 Structure H.

Global sensitivity analysis was performed to overcome the problem of local effects as discussed in Section 2.5.1.2. The LHS approach was used to generate samples for the structural parameters with their distributions. The flutter limit was then computed for each sample set. Figure 8.8 show the convergence with the increasing number of samples. From the figure, it can be seen that 5,000 samples seem to have a sufficient accuracy. The outliers were ignored from the sample as they do not describe a flutter limit. Figure 8.9a shows the results of the global sensitivity analysis considering variation in the structural parameters only. Qualitatively, it shows similar results as before in the

case of local sensitivity analysis but with a slight difference that in this case r_α has much less effect than before. This method is superior to the local method as it covers a wider range of the variation of the input parameters and considers the interaction between them.

Similarly, the variation in the aerodynamic derivatives was considered and sampling was done for eight aerodynamic derivatives. Figure 8.9b shows that the aerodynamic derivatives H_3^*, A_2^* and A_3^* are the most influential whereas all others are relatively less significant. In most cases, H_2^* appears to be insignificant.
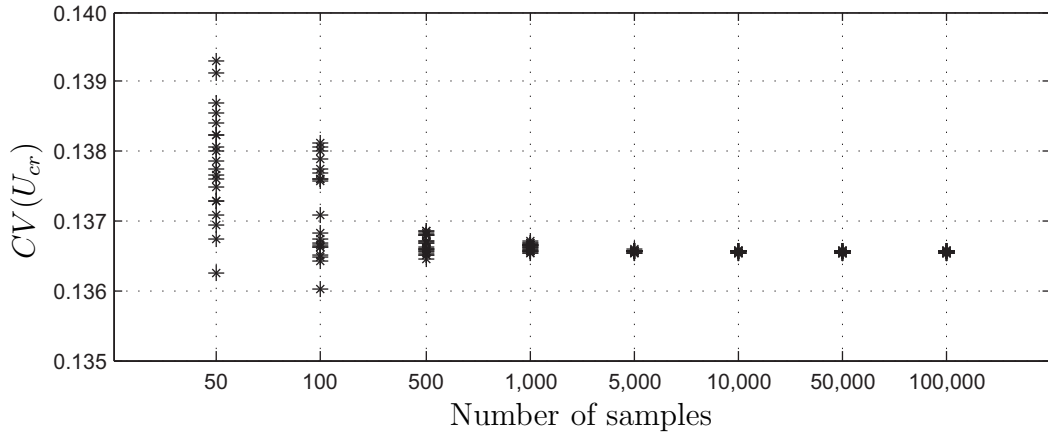
Figure 8.8: Convergence of CoV of flutter limit $(CV(U_{cr}))$ using response surface with increasing number of samples (Model#1-Structure A, 20 simulations).
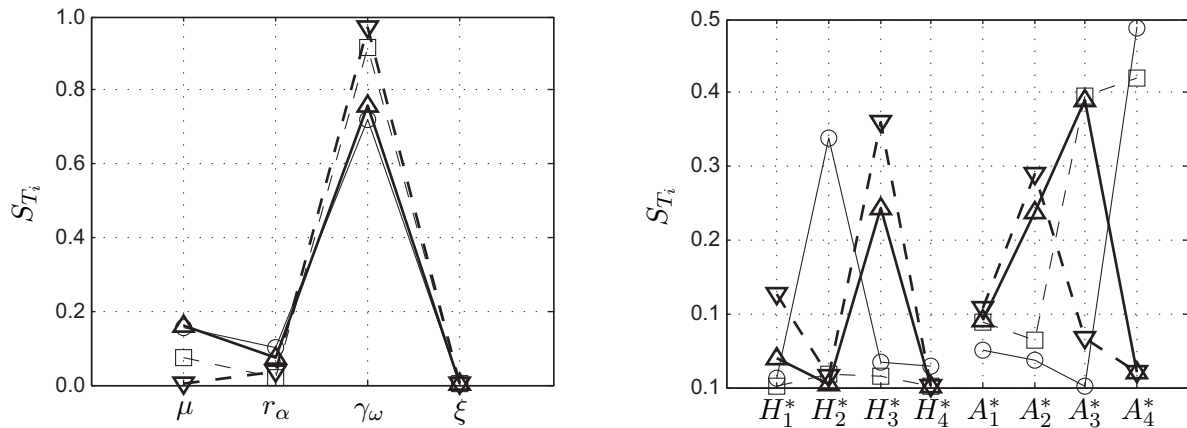
Figure 8.9: Sensitivity indices for flutter speed from global sensitivity analysis considering variation in
(left) structural input parameters,
(right) aerodynamic derivatives. (cf. Section 2.5.1.2)
($\triangle$) Model#1 Structure A,
($\triangledown$) Model#1 Structure H,
($\circ$) Model#3 Structure A,
($\square$) Model#3 Structure H.

Various studies [35, 38, 264, 286] describe A_1^*, A_2^*, A_3^*, H_3^* and to some extent H_1^* as the important aerodynamic derivatives. Derivatives H_4^* and A_4^* represent the aerodynamic

stiffness induced by the vertical displacement of the deck and are considered to have a small influence on the flutter limit. This may be considered valid in the case of a flat plate. However, the results of this study show that H_4^* or A_4^* can have a high influence for specific bluff sections, and thus significantly contribute to the overall uncertainty in the prediction of flutter limit. Here, A_2^* appears to be less significant in case of Model#3 Structure A as this section does not experience SDOF flutter problem. For Structure H, A_2^* is not the most influential aerodynamic derivative because the flutter limit is computed for a coupled 2DOF system. It is important to mention that the sensitivity analysis for aerodynamic derivatives depends on a number of factors such as the cross section shape and the structural input parameters. Changing these parameters can result in a different outcome.

The variance-based approach of sensitivity analysis has also been applied considering correlated input parameters. The correlation was considered between structural parameters $B - I$, $I - f_\alpha$ and $f_\alpha - \xi$. These parameters were assumed correlated with $\rho(X_i, X_j) = 0.0$ to 0.5. The results of sensitivity analysis performed considering correlated parameters are shown in Figure 8.10. It is visible that with the increase in the correlation between the structural parameters, the correlated sensitivity contribution also increases. However, total sensitivity indices do not change significantly. It also shows that the relative importance of μ and r_α changes.

Since the aerodynamic derivatives are computed from the same CFD simulations with two time series, it is evident that the aerodynamic derivatives can be correlated and modelling of uncertainty should include the effect of dependence between the aerodynamic derivatives. The covariance matrix describes the correlation between the aerodynamic derivatives from heave time histories and from the pitch time histories.

The correlation depends on the geometry of the section as the aerodynamic derivatives are functions of geometry. The range of reduced speed v_r is also important for which the correlations are being calculated. Therefore, the correlation of the aerodynamic derivatives for a particular case is not necessarily applicable to the aerodynamic derivatives of other cross sections. For this purpose, the following situations were studied:

(a) Synthetic or artificial correlation introduced between all aerodynamic derivatives as

    (i) no correlation $\rho(X_i, X_j)$=0.00

    (ii) full correlation $\rho(X_i, X_j)$=0.99

    (iii) partial correlation $\rho(X_i, X_j)$=0.50

(b) Correlation for lift force aerodynamic derivatives $H_1^* - H_4^*$ and $H_2^* - H_3^*$
    Correlation for moment aerodynamic derivatives $A_1^* - A_4^*$ and $A_2^* - A_3^*$

(c) Dependence of aerodynamic derivatives on each other

    (i) since aerodynamic derivatives for flat plate are approximated as $H_1^* = -K.H_3^*$ and $A_1^* = -K.A_3^*$ [38, 155, 190]

    (ii) it is also interesting to see the correlation between $H_1^* - H_2^*$, $H_3^* - H_4^*$, $A_1^* - A_2^*$ and $A_3^* - A_4^*$.

The correlation matrices are presented in Appendix E.1. Since the model response due to a variation in the aerodynamic derivatives is highly non-linear, the method proposed by Xu and Gertner [16] for sensitivity analysis with correlated parameters is not applicable.
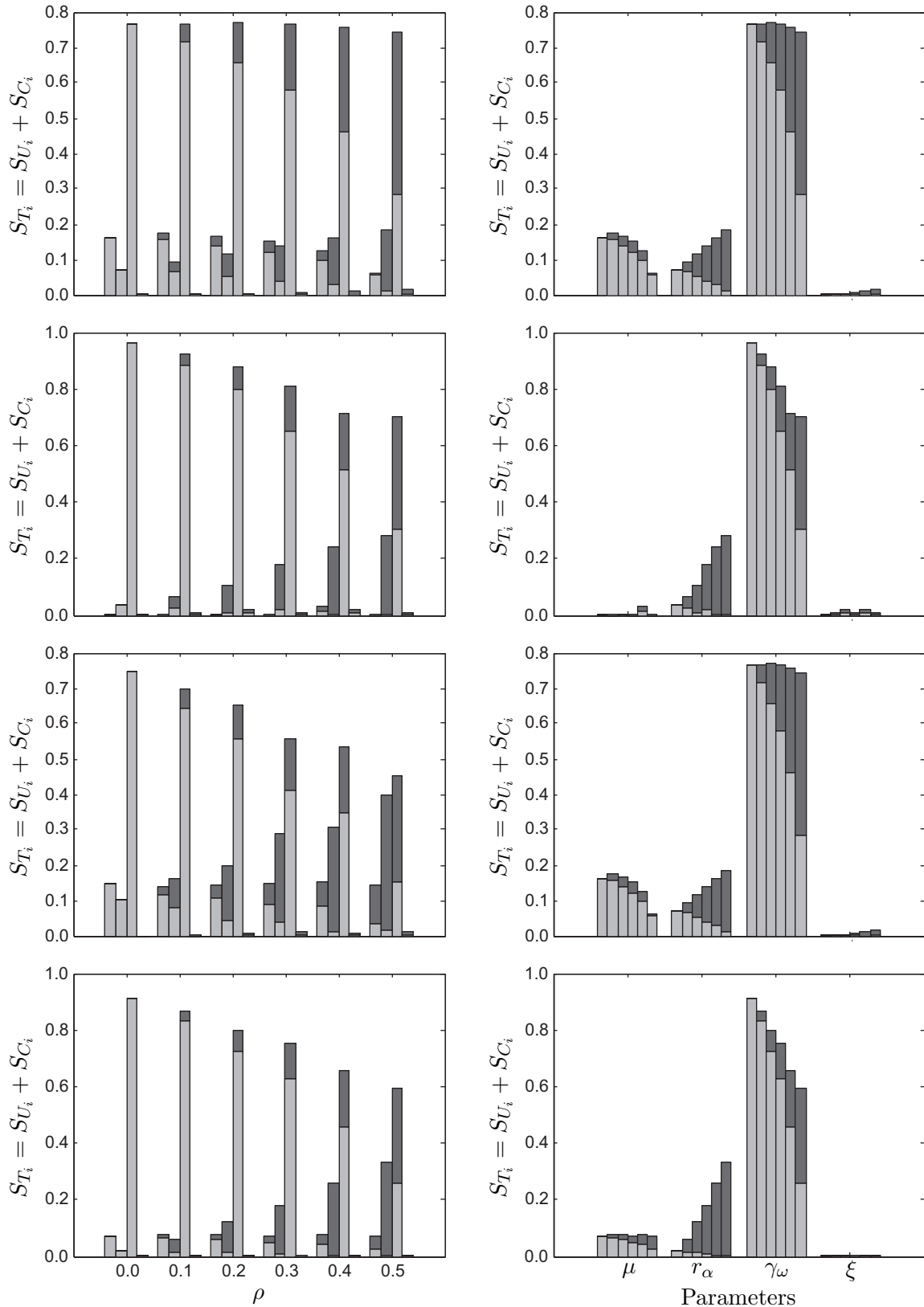
Figure 8.10:   Sensitivity indices for flutter speed from global sensitivity analysis considering correlated structural input parameters:
(left) parameters μ, r_α, γ_ω and ξ respectively for a given correlation coefficient ρ, (right) individual parameter with increasing correlation coefficient ρ from 0.1 to 0.5, (▨) uncorrelated contribution, (■) correlated contribution.
(top to bottom) Model#1 Structure A, Model#1 Structure H, Model#3 Structure A, Model#3 Structure H.

8.4 Parameter Uncertainty Analysis

The overall parametric uncertainty of the model depends on the uncertainty in the input parameter and their relative sensitivity on the model output. The local uncertainty analysis was first performed by considering uncertainty in the structural input parameters. Table 8.5 shows the structural input parameters used for the uncertainty analysis after [15].

Table 8.5: Mean values and distributions of probabilistic input parameters considered in sensitivity and uncertainty analyses (cf. Table 6.7).

Parameters	B	μ	I	r_α	f_α	γ_ω	ξ
	[m]	[-]	[kgm^2/m]	[-]	[Hz]	[-]	[-]
Mean (Structure A)	33	17.1	1017778	0.283	0.50	3.21	0.01
Mean (Structure H)	12	47.2	177730	0.539	0.20	1.54	0.01
CV [-]	0.05		0.10		0.11		0.10
Distribution	Normal		Normal		Normal		Normal

Figure 8.11a shows the results of structural parameter uncertainty contribution from local uncertainty analysis. The same procedure was adopted by considering uncertainties in the aerodynamic derivatives. Figure 8.11b shows the uncertainty contribution by the aerodynamic derivatives. Since same uncertainty in the aerodynamic derivatives has been assumed, qualitatively it is not much different from the sensitivity analysis.
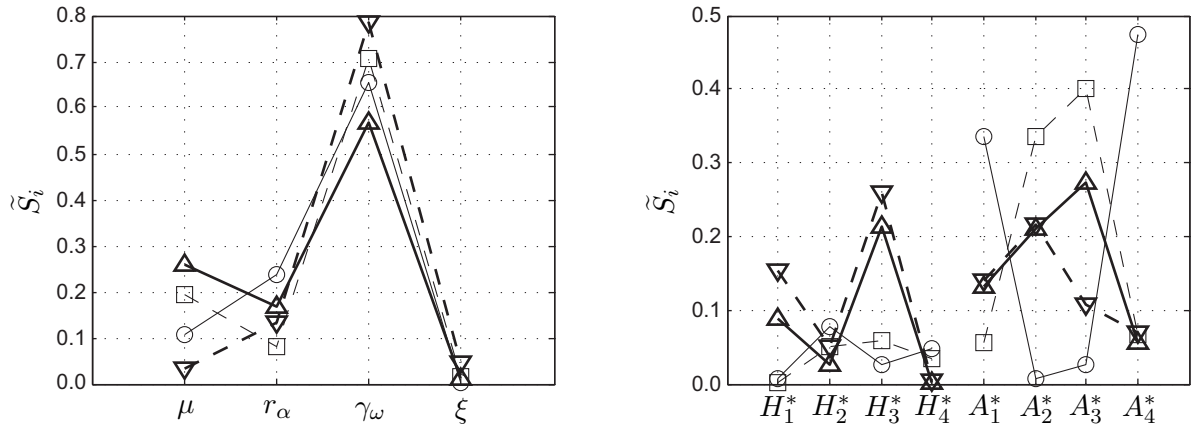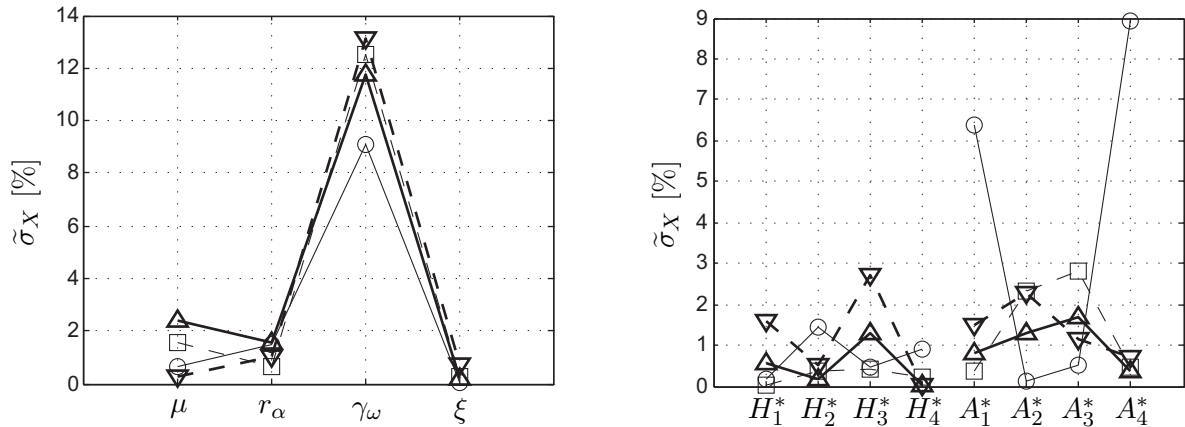

Figure 8.11: Uncertainty contribution of parameters for flutter speed from local uncertainty analysis considering variation in
(left) structural input parameters,
(right) aerodynamic derivatives. (cf. Section 2.5.2)
($\triangle$) Model#1 Structure A,
($\triangledown$) Model#1 Structure H,
($\circ$) Model#3 Structure A,
($\square$) Model#3 Structure H.

Figure 8.12 presents the individual and overall effect of considering uncertainty in the structural parameters and the aerodynamic derivatives. Structural parameters have much more contribution in the overall uncertainty.
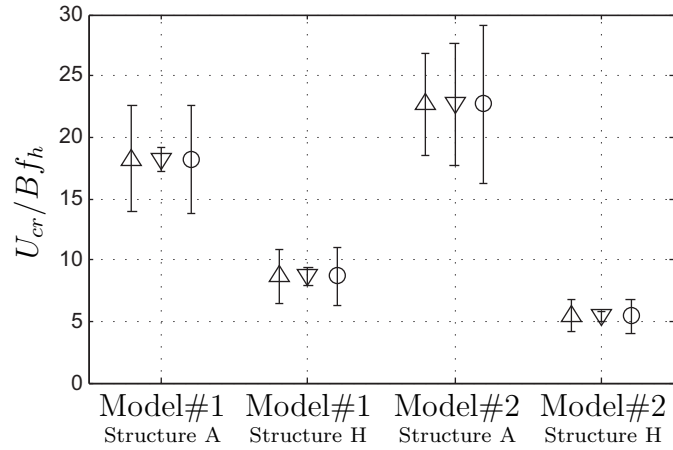
Figure 8.12: Parameter uncertainty contribution for flutter speed from local uncertainty analysis considering variation in
($\triangle$) structural input parameters only,
($\triangledown$) aerodynamic derivatives only,
($\circ$) structural input parameters and aerodynamic derivatives.

The uncertainties introduced in the parameters considering only a few data points may lead to inaccurate results. Therefore, a global uncertainty analysis was performed which considers the uncertainty in the input parameters with their respective distributions. The sampling was done with the LHS approach using 5,000 samples. Figure 8.13 shows the correlation coefficients between the input structural parameters and the output considering uncorrelated parameters. The uncertainty analysis was also performed considering the uncertainty in the aerodynamic derivatives. The quantification of uncertainty in the aerodynamic derivatives greatly depends on the cross section shape.
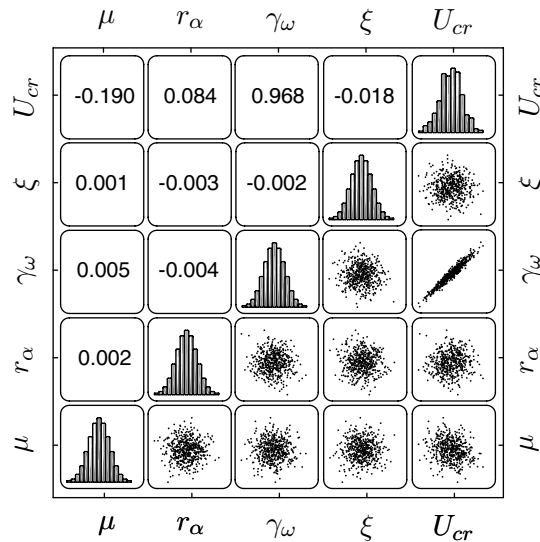
Figure 8.13: Extended correlation matrix for Structure A using Model#1 from global uncertainty analysis for flutter speed considering uncorrelated structural input parameters.

The larger confidence interval shows that there is more uncertainty in predicting the flutter limit. It shows the accuracy of flutter prediction. Table 8.6 and Figure 8.15 presents the results of uncertainty analysis considering structural parameters, aerodynamic derivatives and both at a time. It is important to visualise how uncertainty

175

Table 8.6: Global uncertainty analysis considering uncorrelated structural input parameters and aerodynamic derivatives: mean μ_Y and coefficient of variation CV_Y of flutter limits (Y: U_{cr} [m/s]).

| | Structure A | | | | Structure H | | | |
| | Model#1 | | Model#3 | | Model#1 | | Model#3 | |
	μ_Y [m/s]	CV_Y [-]	μ_Y [m/s]	CV_Y [-]	μ_Y [m/s]	CV_Y [-]	μ_Y [m/s]	CV_Y [-]
Parameters	94.2	0.121	118.7	0.086	13.7	0.125	8.4	0.126
Derivatives	93.9	0.027	117.6	0.052	13.5	0.046	8.5	0.002
Both	94.2	0.124	115.3	0.108	13.8	0.135	8.4	0.125

is depicted in the final flutter limit from the structural parameters and the aerodynamic derivatives. The distribution of the output also represents the characteristics of the model. Normal distribution fits very well on the model output. Figure 8.14 summarises the results of uncertainty analysis considering uncorrelated parameters. It can be seen that the uncertainty in the model output is relatively larger when the uncertainty in the structural parameters is considered and is less if only the uncertainty in aerodynamic derivatives is considered. The overall uncertainty does not change significantly by including uncertainty in the aerodynamic derivatives. However, the high scatter of H_4^* and A_4^* shows that the large uncertainty in the computation of these aerodynamic derivatives may lead to undesirable effect in the probabilistic flutter predictions. This also shows that the uncertainty due to aerodynamic derivatives greatly depends on the cross section type and not only on the individual contributions of aerodynamic derivatives.
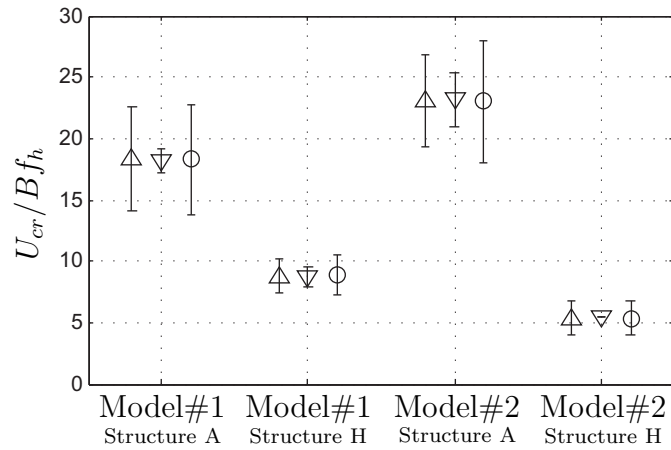
Figure 8.14: Parameter uncertainty contribution for flutter speed from global uncertainty analysis with uncorrelated parameters considering variation in
($\triangle$) structural input parameters only
($\triangledown$) aerodynamic derivatives only
($\circ$) structural input parameters and aerodynamic derivatives.

Figure 8.16 shows the effect of correlation considered for the structural input parameters and the aerodynamic derivatives. The correlation considered between the parameters does not affect the uncertainty much. The correlation considered between the aerodynamic derivatives, generally, reduces the scatter of the model output and in turn
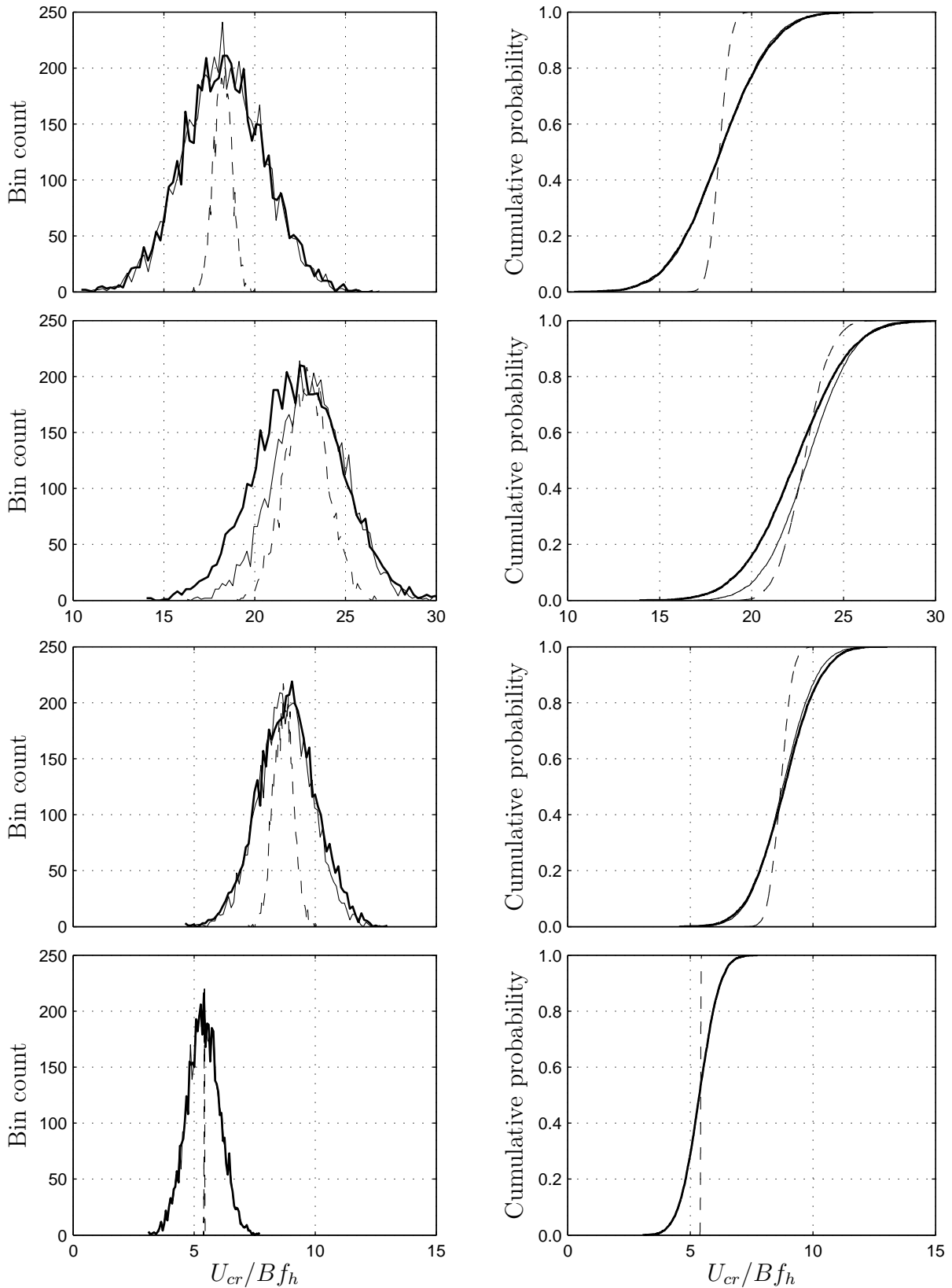
Figure 8.15: Parameter uncertainty contribution for flutter speed from global uncertainty analysis considering uncorrelated

(——) structural input parameters only,

(——) aerodynamic derivatives only,

(– –) structural input parameters and aerodynamic derivatives.

(top to bottom) Model#1 Structure A, Model#3 Structure A, Model#1 Structure H, Model#3 Structure H.

reduces the model uncertainty. Therefore, ignoring correlation will generally lead to conservative solutions in case of a probabilistic flutter prediction. This is also desirable because the actual correlation between the parameters is typically not well established.
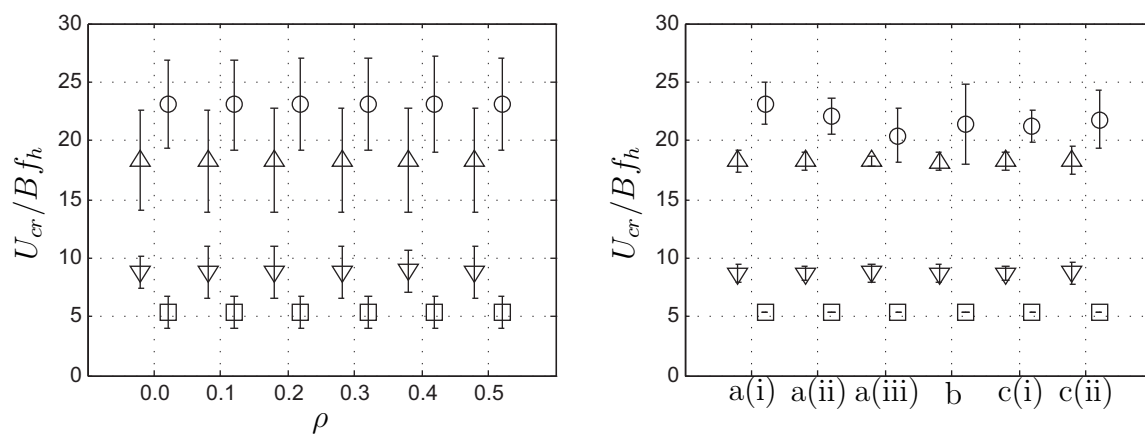
Figure 8.16: Parameter uncertainty contribution for flutter speed from global uncertainty analysis considering correlation between
(left) structural input parameters
(right) aerodynamic derivatives.
($\triangle$) Model#1 Structure A,
($\triangledown$) Model#3 Structure A,
($\circ$) Model#1 Structure H,
($\square$) Model#3 Structure H.

8.5 Model Uncertainty

Uncertainties related to the parameters are considered in the models; however, in many cases, uncertainties introduced by the modelling process can have a significant influence on the total uncertainty in the analysis. A methodology is presented here to quantify both parametric and model-form uncertainties in the prediction of flutter instability. This utilizes the Adjustment Factor Approach (AFA) and the Probabilistic Adjustment Factor Approach (PAFA) to quantify model-form uncertainties and ultimately to compute total uncertainties.

In the study of complex physical phenomena, a correct model may not exist which provides true value. Instead, a model can be chosen as best model from the considered set of models for the analysis of certain phenomena. The best model is selected assuming this model represents the physical phenomena most accurately. The choice of the model also introduces uncertainty on the assumptions made that the model represents best a given scenario. The uncertainty related to the identification of the'best model' for the prediction of model response is the model-form uncertainty. Therefore, complete quantification of uncertainty suggests that it is crucial to consider the uncertainty related to model selection. The model with the highest model probability is selected as 'best model' and in this case, where all models have equal probability, any model can be selected as 'best model'. The effect of selecting other models can also be studied; however, this was not done here. The AFA uses adjustment factors to update the results of the best model to take into account the uncertainty related to the selection of the best-model. Model probabilities are based on the expert opinion related to accuracy, merits and usage of individual models.

In this section, total uncertainty of the model originating form model input parameter uncertainty and model framework uncertainty are computed. Total uncertainty can serve as to rank and assess the considered models. The procedure to calculate total uncertainty is described in Section 2.5.3 where it consists of three major parts to compute. The model with the lowest uncertainty may be selected to compute model response.

The statistical parameters of model response $E(Y_i)$ and $V(Y_i)$ are computed considering random input parameters. Variance based global uncertainty analysis (cf. Section 8.4) was performed first on the input parameters of Structure A and Structure H using Model#1, Model#2 and Model#3 (cf. Chapter 5). The results of this analysis are presented in Table 8.7 along with the considered model probabilities. For this analysis, same model probabilities are assumed. The choice of model probabilities depends on the efficiency of use and numerical stability. This choice introduces some bias in the analysis but this bias can be reduced or kept to a minimum according to the experience and knowledge about the model. Neglecting the bias of models could lead to a situation where an inferior model may provide the best solution, therefore, it is recommended to use only the variation of the model prediction as model selection indicator [21].

Table 8.7: Model parameters from deterministic and probabilistic analysis considering stochastic input parameters (cf. Section 8.4).

Model	$P(M_i)$	Y_i		$E(Y_i)$		$V(Y_i)$	$\sigma(Y_i)$
		U_{cr}	U_{cr}/Bf_h	U_{cr}	U_{cr}/Bf_h		
	[-]	[m/s]	[-]	[m/s]	[-]	[m²/s²]	[m/s]
Structure A							
Model#1	0.33	93.8	18.22	94.2	18.31	136.6	11.69
Model#2	0.33	92.0	17.87	92.3	17.92	133.0	11.53
Model#3	0.34	116.8	22.69	115.3	22.40	154.8	12.44
Structure H							
Model#1	0.33	13.5	8.65	13.8	8.83	3.44	1.86
Model#2	0.33	11.5	7.30	11.5	7.35	5.05	2.25
Model#3	0.34	8.5	5.46	8.4	5.37	1.10	1.05

The values of $V(\epsilon^{ref})$ are not known, therefore different values are considered to see the effect of total uncertainty of model prediction. The model with least uncertainty $(V_i(Y_p))$ is assumed to provide the best prediction. The value of $V(\epsilon^{ref})$ affects each model variance; however, the ranking of the model is not changed by this.

The parameter uncertainties in the model predictions are shown in Figure 8.17 whereas the results of the AFA and PAFA can be visualised in Figure 8.19. It can be seen that there is not much difference between the two approaches for these models because the model predictions from the deterministic and the probabilistic approach are very close. Figure 8.18 illustrates the total variance of the individual model. It is clear that Model#3 appears to perform best out of the given models because of least total model variance, whereas Model#2 in the case of Structure A and Model#1 in the case of Structure H show the largest variances.

Table 8.8 shows the results of averaged model and its variance for Structure A and Structure H from the AFA and the PAFA.
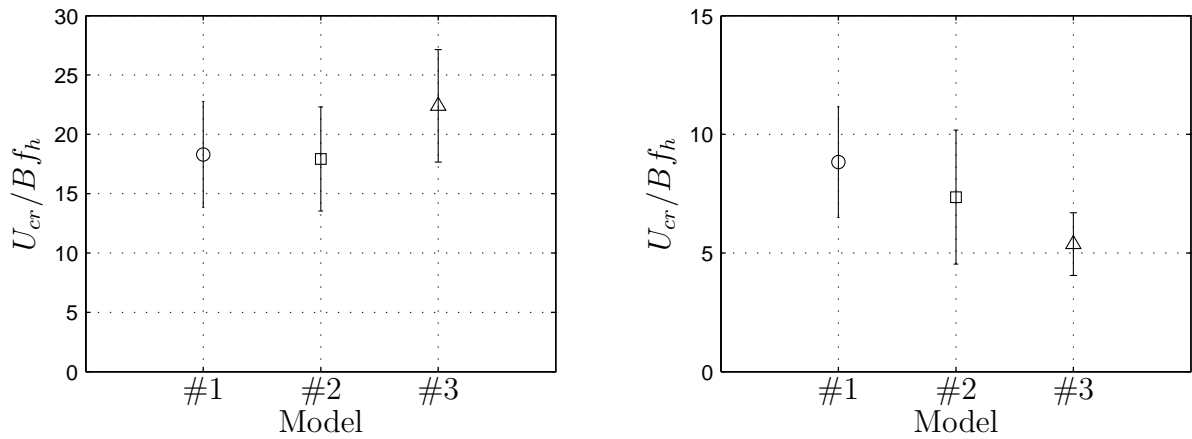
Figure 8.17: Parameter uncertainty in the selected models:
(left) Structure A,
(right) Structure H (cf. Table 8.7).
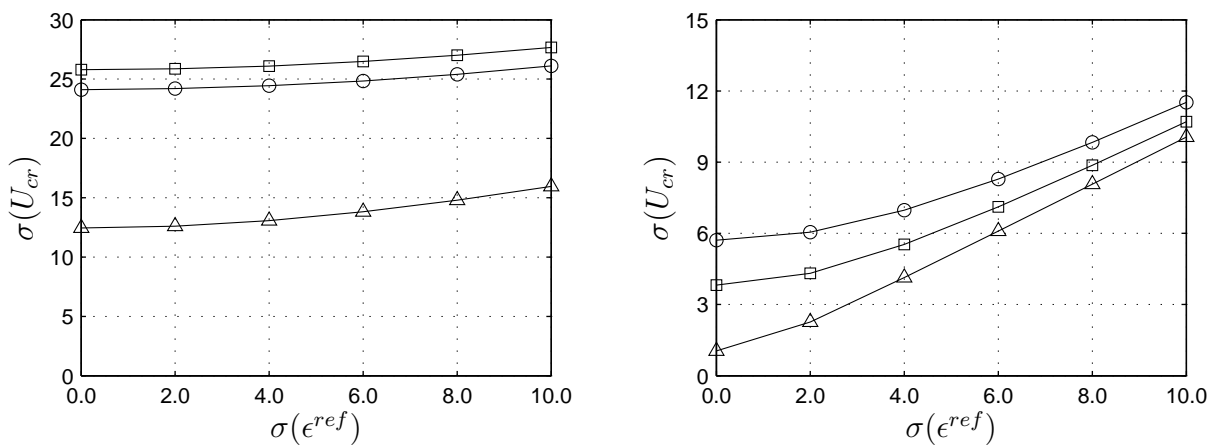
Figure 8.18: Model uncertainty: total uncertainty along reference model uncertainty,
(left) Structure A,
(right) Structure H,
($\circ$) Model#1,
($\square$) Model#2,
($\triangle$) Model#3.
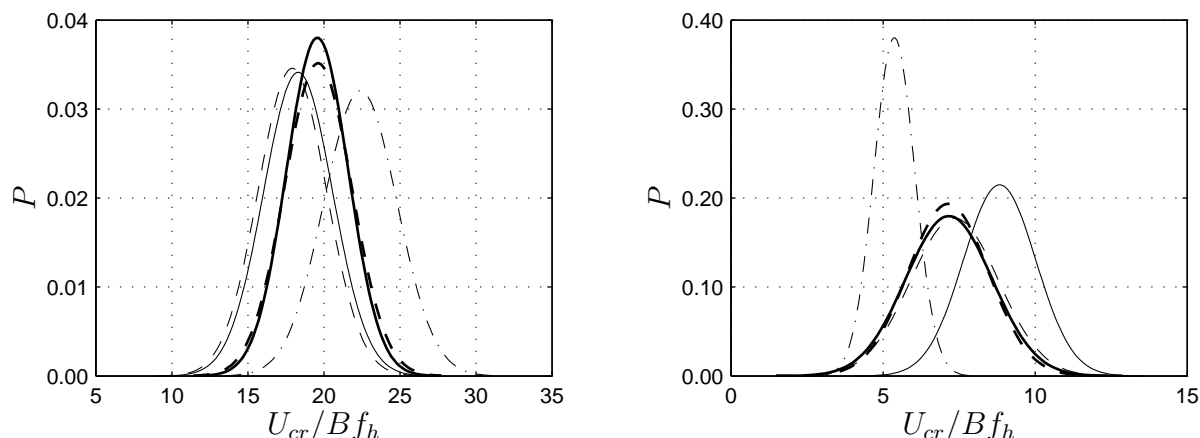
Figure 8.19: Model uncertainty: parameter uncertainty in the selected models and overall model uncertainty,
(left) Structure A,
(right) Structure H,
(– –) AFA and
(——) PAFA.
(——) Model#1,
(– –) Model#2,
(– · –) Model#3.

Table 8.8: Model uncertainty from the Adjustment Factor Approach (AFA) and the Probabilistic Adjustment Factor Approach (PAFA) (cf. Figure 8.19).

	AFA				PAFA		
$E(Y)$	$\sigma(Y)$	$V(Y)$	$CV(Y)$	$E(Y)$	$\sigma(Y)$	$V(Y)$	$CV(Y)$
[m/s]	[m/s]	[m^2/s^2]	[-]	[m/s]	[m/s]	[m^2/s^2]	[-]
Structure A							
101.02	11.34	128.7	0.112	100.75	10.49	110.04	0.104
Structure H							
11.14	2.06	4.25	0.185	11.18	2.21	4.92	0.198

8.5.1 Application to Theodorsen Circulation Function Approximations

Variance based global uncertainty analysis (cf. Section 8.4) was performed first on the input parameters of Structure A using Model#1 with different representations for Theodorsen circulation function (cf. Section 4.3.1). The results of this analysis are shown in Table 8.9 along with the considered model probabilities. For this analysis, same model probabilities are assumed. The choice of model probabilities depends on the efficiency of use and numerical stability.

Table 8.9: Model parameters for Theodorsen circulation function approximations from deterministic and probabilistic analysis considering stochastic input parameters (Model#1 Structure A).

Model	$P(M_i)$	Y_i		$E(Y_i)$		$V(Y_i)$	$\sigma(Y_i)$
		U_{cr}	$U_{cr}/B/f_h$	U_{cr}	$U_{cr}/B/f_h$		
	[-]	[m/s]	[-]	[m/s]	[-]	[m²/s²]	[m/s]
C_1 Eq. (4.24a)	0.143	93.8	18.23	93.8	18.20	137.3	11.72
C_2 Eq. (4.24b)	0.143	95.1	18.48	95.0	18.47	138.6	11.77
C_3 Eq. (4.24c)	0.143	93.9	18.25	93.9	18.24	135.8	11.65
C_4 Eq. (4.24d)	0.143	93.0	18.07	93.0	18.06	134.2	11.58
C_5 Eq. (4.24e)	0.143	91.7	17.83	91.7	17.82	129.1	11.36
C_6 Eq. (4.24f)	0.143	93.8	18.23	93.8	18.22	137.3	11.72
C_7 Eq. (4.24g)	0.143	93.6	18.19	93.6	18.18	135.5	11.64

The effect of parameter uncertainties on the model prediction can be seen in Figure 8.20a whereas the results of the AFA can be visualised in Figure 8.20b. The total uncertainty analysis is also plotted and it can be seen that there is not much difference between the two approaches for this model scenario because the model predictions do not differ much from each other and the deterministic values and the probabilistic mean values are very close. Additionally, the model variances are very similar. Figure 8.21 shows the total variance of the individual model. It is visible that the model from Eq. (4.24e) (C_5) appears to be the best model out of the given models because of least total model variance, whereas model from Eq. (4.24b) (C_2) has the largest variance. This figure also shows that the major contribution comes from parameter uncertainty. Model uncertainty is relatively small whereas uncertainty due to reference model is variable but quantitatively could be much less than the parameter uncertainty.
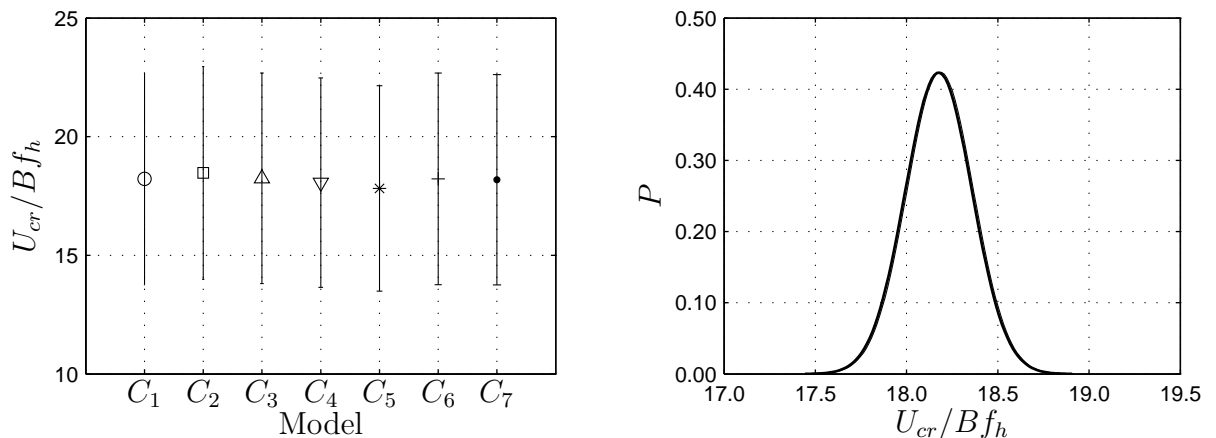
Figure 8.20: Model uncertainty for Theodorsen circulation function approximations:
(left) parameter uncertainty in the selected models,
(right) overall model variance from
(——) AFA and
(——) PAFA (cf. Section 8.9).

Table 8.10: Model uncertainty for Theodorsen circulation function approximations from the Adjustment Factor Approach (AFA) and the Probabilistic Adjustment Factor Approach (PAFA) (cf. Figure 8.20).

	AFA				PAFA		
$E(Y)$	$\sigma(Y)$	$V(Y)$	$CV(Y)$	$E(Y)$	$\sigma(Y)$	$V(Y)$	$CV(Y)$
[m/s]	[m/s]	[m²/s²]	[-]	[m/s]	[m/s]	[m²/s²]	[-]
93.62	0.9407	0.8848	0.01	93.57	0.9423	0.8879	0.01
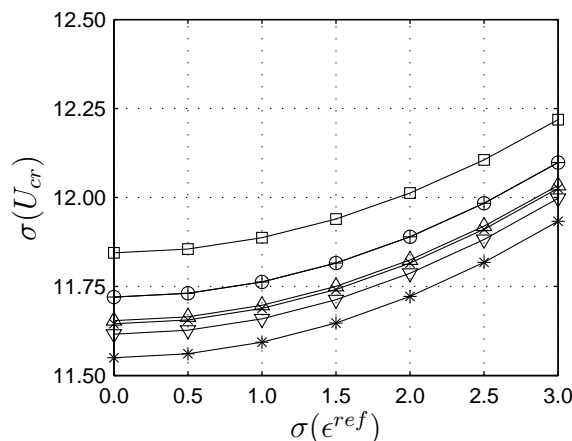
Figure 8.21: Model uncertainty for Theodorsen circulation function approximations: total uncertainty along reference model uncertainty.
(○) C_1,
(□) C_2,
(△) C_3,
(▽) C_4,
(∗) C_5,
(+) C_6,
(•) C_7

8.5.2 Application to Flat Plate Aerodynamic Derivatives

The same approach has been also used on the flat plate derivatives obtained from different sources to show its application. For this purpose, the aerodynamic derivatives presented in Section 7.3.5 have been used. The structural properties of Structure A were used to compute deterministic and probabilistic flutter limits using these aerodynamic derivatives. The results and relevant parameters used in this example are presented in Table 8.11.

Table 8.11: Model uncertainty for a flat plate: model parameters from deterministic and probabilistic analysis considering stochastic input parameters.

Model	$P(M_i)$	y_i		$E(y_i)$		$V(y_i)$	$\sigma(y_i)$
		U_{cr}	$U_{cr}/B/fh$	U_{cr}	$U_{cr}/B/fh$		
	[-]	[m/s]	[-]	[m/s]	[-]	[m²/s²]	[m/s]
Analytical	1/3	93.40	18.14	93.51	18.16	138.36	11.76
WTT [265]	1/3	114.19	22.18	114.28	22.19	138.24	11.75
CFD	1/3	88.70	17.23	88.65	17.22	115.00	10.72

Figure 8.22a shows the model prediction and parameter uncertainties of individual models. The results from the PAFA are plotted in Figure 8.22b along with the individual models and their uncertainties. These results are also summarized in Table 8.12. It is important to mention that only uncertainties in the structural input parameters have been considered and uncertainties in the determination of individual aerodynamic derivatives are not taken into consideration. The results show much higher model uncertainties than the previous example as the model predictions are relatively far from each other.
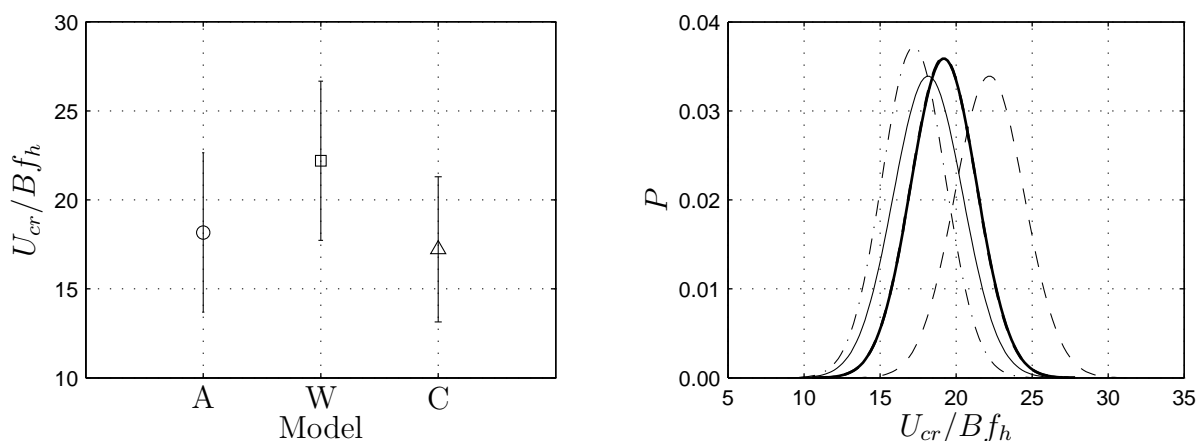
Figure 8.22: Model uncertainty for a flat plate:
(left) parameter uncertainty in the models,
(right) comparison with model uncertainty from
(– –) AFA and
(——) PAFA.
(——) A: analytical,
(– –) W: wind tunnel tests,
(– · –) C: CFD simulations.

Table 8.12: Model uncertainty for a flat plate from the AFA and the PAFA (cf. Figure 8.22).

Adjustment factor approach				Probabilistic adjustment factor approach			
$E(y)$	$\sigma(y)$	$V(y)$	$CV(y)$	$E(Y)$	$\sigma(Y)$	$V(Y)$	$CV(Y)$
[m/s]	[m/s]	[m²/s²]	[-]	[m/s]	[m/s]	[m²/s²]	[-]
98.76	11.07	122.62	0.112	98.81	11.11	123.50	0.112

8.6 Summary

Probabilistic flutter analysis has been presented here considering the variation in the input structural parameters and the aerodynamic derivatives. A novel approach to consider aerodynamic uncertainties for bridge deck sections is presented. Deterministic as well as probabilistic sensitivity and uncertainty analyses have been described here. A framework has been presented to consider the variation in the input parameters and to study the propagation of uncertainty in the model response. Finally, the ranking of the models is done based on the total uncertainty which includes parameter uncertainty, model uncertainty and uncertainty in the choice of reference model selection.

Chapter 9
Conclusions and Outlook

9.1 Summary

The objective of this study was to develop a framework for the assessment of numerical prediction models for aeroelastic instabilities of bridges. Hitherto, model quality assessment in bridge aerodynamics has not been able to attract much attention. The attempt has been made in this thesis to apply model assessment in practical engineering problems related to the field of bridge aerodynamics. It is hoped that this study will help engineers with decisions during different design stages and to make a choice of an appropriate model based on the problem in hand.

The assessment requires some mathematical measures and indicators to express the fitness of the model for the intended purpose. The proposed model assessment is based on sensitivity, parameter uncertainty, model uncertainty and model robustness. Deterministic as well as probabilistic studies were carried out using the concepts of sensitivity and uncertainty analyses in order to assess the model prediction.

Chapter 2 describes probabilistic fundamentals and assessment procedure based on the sensitivity and uncertainty analyses. A methodology has been explained to solve complex problems more efficiently by using a meta-modelling approach. The aeroelastic phenomena related to the design and analysis of long-span bridges are introduced in Chapter 3. The methods used for aerodynamic analysis are discussed in Chapter 4. A wide range of aerodynamic and structural models has been described based mainly on analytical and numerical methods. These aerodynamic and structural models were then coupled in different ways to perform flutter stability analysis. Chapter 5 was devoted to explain different model combinations and their possible applications were discussed in the practical scenario. The following models were studied:

- Model#1: Fully-Analytical based on Theodorsen equations for motion-induced aerodynamic forces with 2D structural model (Section 5.4).

- Model#2: Empirical approaches for 2D only, such as Selberg, Rocard etc. (Section 5.5).

- Model#3: Derivative-based eigenvalue analysis for Theodorsen flat plate aerodynamic derivatives and Scanlan derivatives from the CFD forced vibration simulations with 2D and 3D structural model (Section 5.6.5).

- Model#4: Derivative-based FSI simulations for Theodorsen flat plate aerodynamic derivatives and Scanlan derivatives from the CFD forced vibration simulations with 2D and 3D structural model (Section 5.6.6).

- Model#5: Fully-coupled CFD simulations based on the VPM with 2D and quasi-3D structural model (Section 5.7).

Computer codes were developed for the first four models, whereas numerical simulations were carried out for Model#5 in a flow solver based on the VPM. In Chapter 6, these models were applied to the selected reference objects to show their application to the engineering problems.

The sensitivity of flutter limit to different input parameters was also studied to highlight the importance of structural parameters and aerodynamic behaviour of the cross-sectional shape. To the best of author's knowledge, this is the first work that shows the study of such a wide range of section geometry variation. Chapter 7 describes the studies related to this aspect. A method has been presented to utilise existing data from WTT or CFD simulations to estimate the aeroelastic instability limit of a similar cross section by using response surface techniques.

A framework for the probabilistic flutter analysis is presented in Chapter 8. Concepts of sensitivity analysis have been used to identify and rank the important input parameters. First order and total sensitivity indices are used as mathematical indicators to express the relative importance of input parameters. A larger value of the sensitivity index shows that the input parameter has a greater influence on the model output, and vice versa. This could be useful for the engineer to choose the most influential input parameters for further investigations.

The sensitivity analyses were used for the structural input parameters as well as for the aerodynamic derivatives to identify their relative importance. For this purpose, a method of screening was used to show local effects and a variance-based sensitivity analysis was used for global effects. The response surface method was suggested to be used here for the complex model in order to make the variance-based approach more efficient. A novel approach to quantify the sensitivities of aerodynamic derivatives was developed. The sensitivity indices were computed in order to identify the aerodynamic derivatives that have a major influence on the flutter limit.

The effect of parameter uncertainty on the flutter limit was quantified as well. The same probabilistic approach as that of sensitivity analysis was used here. The CFD simulations were performed to obtain the probabilistic description of aerodynamic derivatives of real sections. Furthermore, models were ranked by using the concept of total uncertainty which includes the input parameter uncertainty and the model uncertainty. This was done by making use of the AFA to quantify model uncertainty which is estimated by the difference between the model average and the adjusted model.

9.2 Conclusions

Some main observations are made from the deterministic flutter analysis. The flutter limits computed from the simplified 2DOF model are considered conservative when compared to those obtained from more realistic 3DOF models. The effect of structural coupling between horizontal displacement and torsional motion is low on flutter onset for such a relatively shorter span of the selected reference object than Akashi-Kaikyo Bridge where a significant effect of structural mode coupling has been seen to decrease the flutter limit [62].

Theodorsen's flat plate prediction based on potential flow theory is simple and easy to use but is only applicable for a 2D flow and for a flat plate or an airfoil. It cannot be used for bridge cross sections which are bluff due to flow separation and reattachment. However, it serves as a starting point or providing with the reference value to compare

flutter predictions of other complex models. Scanlan's model is more commonly used and is preferred as it gives a more direct assessment about the nature of the aerodynamic behaviour of the cross section. Simplified approaches are useful to better understand the mechanism related to flutter phenomenon but cannot be trusted for the final design due to their inability to take into account an arbitrary shape of a section.

The choice of the bridge deck section is important where the aerodynamic behaviour is a governing design consideration. It can save a significant amount of effort and resources if suitably selected in the early design stage. The appropriate selection of the shape of the deck is much more effective than changing the structural properties of the bridge to improve its behaviour against aeroelastic instabilities. The structural input parameters which have the major influence on the flutter limit are the torsional frequency and, after that, the mass moment of inertia. The damping ratio has an insignificant effect on the flutter limit, since, in the case of aeroelastic instabilities, structural damping is not much effective as compared to in Buffeting response and Vortex-induced Vibrations.

Frequency domain methods are commonly used because of their simplicity and efficiency; however, they are only for a linear structural model and do not consider nonlinearities. Therefore, the major part of the current research on the analytical models is being carried out in the time domain in order to consider the aerodynamic nonlinearities and the nonlinear fluid memory.

Numerical methods have gained much attention and development in the last decades and are used beside the analytical and experimental methods. These methods still have limitations with the complexity and nature of 3D structures. It is a developing field, and at this point, it provides a useful alternative to the WTT only for preliminary studies; however, for final designs, the WTT are preferred.

These observations can help to explain findings of the sensitivity and uncertainty analyses. Some important conclusions are drawn in the light of this research. It is important to mention that these conclusions are based on the analyses of the reference examples with a moderate span length. The analysis on other spans and structural configurations might alter some outcomes. However, the framework explained can be applied on the same lines, irrespective of the structure type. It is also important to mention that although some procedures have been suggested and applied to improve efficiency, the computational cost of performing such analyses is usually high. Nevertheless, the results obtained are useful and can be used elsewhere for further investigations.

The probabilistic approach provides essential insight into the phenomena of aeroelastic instabilities. The results of variance-based sensitivity analysis show that the flutter limit is sensitive to the structural parameters as well as the aerodynamic derivatives. However, the mean value of the flutter limit is not very sensitive to the input parameter uncertainties. The effect of each aerodynamic derivative is different for different cross sections and it is also important that at what reduced speed range the final flutter limit is located. It can be concluded that the flutter limit is not sensitive to small variations in the aerodynamic derivatives but greatly depends on the type of cross section.

The effect of correlation was also shown to have some influence on the model predictions. The approach of considering several cases of correlation was used as the actual correlation was unknown. The importance of the correlation between the structural parameters was also highlighted. The correlation was considered for the aerodynamic

derivatives by using fully correlated, uncorrelated and partially correlated aerodynamic derivatives. It was observed that higher correlation between the aerodynamic derivatives leads to a smaller uncertainty in the model output.

The probabilistic flutter analysis provides more information on the nature of the flutter limit than the corresponding deterministic flutter analysis. The approach is superior to deterministic method as it shows the distribution of the flutter limit as well as the interval of the likelihood of flutter onset. Moreover, this method can be used for a probabilistic design or a performance-based design.

The detailed wind tunnel investigations are expensive and time-consuming; however, the presented approach for sensitivity and uncertainty analyses can limit these tests in the final design stage by focusing on the effects of those parameters which are more sensitive.

The flutter limit of a reference bridge was computed in a uniform as well as in a turbulent flow and the influence of turbulence on the flutter onset was quantified for several cases of interest. Most of the CFD codes are based on laminar flow and do not account for inflow turbulence. An analogous approach to the upstream disturbance to create turbulent flow in the wind tunnel was considered for the numerical simulations in this study. A number of rectangular cross-sections in the flow were placed on the upstream side of the main section to generate turbulence in the incident uniform flow. Vorticity shed from these cross sections evolved into a turbulent flow and carried with the flow to the main section. Fully-coupled CFD simulations were then performed on the reference section with different situations of turbulent flow. It was observed that the free stream turbulence can have a substantial and systematic effect on the response amplitude and the flutter limit. The flutter limit was observed to decrease for the studied reference object with a streamlined section. The approach is computationally feasible and is very similar to the well-accepted approach used in the WTT; however, it is important to meet the requirements of the atmospheric wind flow characteristics. The approach presented to generate turbulent flow in the numerical simulations is subjected to 2D limitations. However, it has been shown to provide the basis for capturing a 2D approximation of a 3D wind flow.

Only a few parameters have been considered probabilistic; however, it may be possible that the parameters which are considered deterministic can have some influence on the predicted flutter limit when considered probabilistic. Therefore, the model assessment must be considered a continuous process, as each model assessment is a specific case and is only applicable to similar cases. The model assessment results should not be used directly for any other type of problem if it is only assessed for a certain case.

9.3 Recommendations for Further Research

The limitations presented in the current model assessment scheme guide the way to develop even more advanced approach. The influence of the individual model components on the overall model prediction can be evaluated. This can be done by using the concepts of sensitivity and uncertainty analyses. It is viable to develop adaptive or hybrid models where the choice of these components is governed by keeping a balance between quality and efficiency.

A possible direction of further research could be towards efficiency, optimisation and reliability. The current implementation can be extended for the aerodynamic shape

optimisation to automatically optimise the most suitable shape against a critical aerodynamic phenomena.

The deck of a bridge is the most important component studied for the aeroelastic effects. Often 2D section models are generated which are calibrated from global models; however, these models cannot reproduce the 3D behaviour of the structure. This simplification is valid only for cases where uncoupled and distinct structural modes exist. The influence of some other parameters on the flutter limit can be studied such as variation in mode shapes, the coupling of structural modes and bridge configurations. Further case studies can be evaluated using different distributions of the input parameters. Response surface methods have been used here by utilising polynomial regression and moving least-squares. These methods reduce the number of required simulations to a great extent. However, there exist several other approaches which can work with even a smaller size of data which needs further examination.

The uncertainties in the numerical parameters have not been considered in this study. The models have been used without the optimum choice of numerical parameters. The aim of this research was not to improve the already existing models. The important points which still need to be investigated are the sensitivities to the numerical parameters and the optimum choice of numerical parameters. The concepts of sensitivity analysis and optimisation may be used to update these parameters. This investigation requires an efficient sensitivity analysis scheme for the choice of input parameters.

The approach presented for turbulence generation can also be used to study other phenomena, such as Vortex-induced Vibrations, to better understand the effect of turbulent flow on the FSI problems. Turbulent flow was studied and modelled by placing different geometrical shapes in the CFD simulations and the flow characteristics were quantified. Alternatively, vorticity defining the turbulent flow characteristics may be introduced on the upstream side of the main cross section.

Structural complexity and the uncertainty in the flow demands more complex models which can account for the aforementioned parameters. Therefore, the quasi-3D approach could be a viable solution which can take into account the 3D behaviour of the structure as well as oncoming turbulent flow. Consequently, more research is necessary on considering different wind characteristics in the flow.

The experimental methods have not been focused here. There exists uncertainty in the evaluation of experimental data obtained from different wind tunnels as well as different wind tunnel models, such as free or forced vibration tests and SDOF tests or 2DOF tests to determine aerodynamic derivatives. The model assessment for wind tunnel experiments can be carried out.

The CFD simulations provide useful insight to better understand the process of FSI by using flow fields as the information of the entire domain is available which is not possible to achieve in wind tunnels. It is also essential to establish a benchmark solution for the aeroelastic instability phenomenon of flutter in the CFD simulations as well as in the wind tunnel experiments. The future of aerodynamic analysis of structures is anticipated through the use of CFD approach coupled with the semi-analytical methods.

This study has a wide range of application in other fields as well. Flutter is generally considered as a destructive phenomenon but it can be turned into an environmentally friendly energy source by utilising small plate-like devices as energy harvesters. Energy harvesters transform kinetic energy of wind into electrical energy to provide power to

small-scale electronic devices such as wireless sensors and mobile electronic devices. The outcome of this research has enormous relevance to the development of energy harvesting which is an active research field and is growing as the demand for renewable energy sources continues to increase.

Bibliography

[1] Jurado, J. and Albarracín, J. *Bridge Aeroelasticity: Sensitivity Analysis and Optimal Design.* High performance structures and materials. WIT Press, 2011.

[2] Holmes, J. *Wind Loading of Structures, Third Edition.* CRC Press, 2015.

[3] Haifan, X. *Conceptual Design of Bridges.* China Communications Press, 2011.

[4] Chen, W. and Duan, L. *Bridge Engineering Handbook.* Taylor & Francis, 1999.

[5] Gimsing, N. J. and Georgakis, C. T. *Cable Supported Bridges: Concept and Design, Third Edition.* John Wiley & Sons, Ltd, Chichester, UK, 2011.

[6] Billah, K. Y. and Scanlan, R. H. Resonance, Tacoma Narrows bridge failure, and undergraduate physics textbooks. *American Journal of Physics*, 59(2):118–124, 1991.

[7] Montgomery, D. C. and Runger, G. C. *Applied Statistics and Probability for Engineers.* John Wiley & Sons, Inc., 2003.

[8] Keitel, H. *Evaluation Methods for Prediction Quality of Concrete Creep Models.* Ph.D. Thesis, Bauhaus-Universität Weimar, Weimar, Germany, 2011.

[9] Conner, B. O. Measurement uncertainty analysis, principles and methods. Handbook, NASA, 2010.

[10] Myers, R., Montgomery, D., and Anderson-Cook, C. *Response Surface Methodology: Process and Product Optimization Using Designed Experiments.* Wiley Series in Probability and Statistics. Wiley, 2009.

[11] Iman, R. L. and Conover, W. J. A distribution-free approach to inducing rank correlation among input variables. *Communications in Statistics - Simulation and Computation*, 11(3):311–334, 1982.

[12] Lancaster, P. and Salkauskas, K. Surfaces generated by moving least squares methods. *Mathematics of Computation*, 37(155):141–158, 1981.

[13] Most, T. and Will., J. Metamodel of optimal prognosis - an automatic approach for variable reduction and optimal metamodel selection. In *Weimarer Optimierungsund Stochastiktage 5.0, Weimar, Germany*, 2008.

[14] Saltelli, A., Ratto, M., Andres, T., Campolongo, F., Cariboni, J., Gatelli, D., Saisana, M., and Tarantola, S. *Global Sensitivity Analysis: The Primer.* Wiley, 2008.

[15] Kwon, S.-D. Uncertainty of bridge flutter velocity measured at wind tunnel tests. In *The 4th International Symposium on Computational Wind Engineering (CWE2010), Chapel Hill, North Carolina, USA*, 2010.

[16] Xu, C. and Gertner, G. Z. Uncertainty and sensitivity analysis for models with correlated parameters. *Reliability Engineering and System Safety*, 93(10):1563–1573, 2008.

[17] Mosleh, A. and Apostolakis, G. The assessment of probability distributions from expert opinions with an application to seismic fragility curves. *Risk Analysis*, 6(4): 447–461, 1986.

[18] Zio, E. and Apostolakis, G. Two methods for the structural assessment of model uncertainty by experts in performance assessments of radioactive waste repositories. *Reliability Engineering and System Safety*, 54:225–241, 1996.

[19] Park, I., Amarchinta, H. K., and Grandhi, R. V. A bayesian approach for quantification of model uncertainty. *Reliability Engineering and System Safety*, 95(7): 777–785, 2010.

[20] Riley, M. E. and Grandhi, R. V. A method for the quantification of model-form and parametric uncertainties in physics-based simulations. In *The 52nd AIAA/ASME/ASCE/AHS/ASC Structures, Structural Dynamics and Materials Conference, Denver, Colorado*. American Institute of Aeronautics and Astronautics, 2011.

[21] Most, T. Assessment of structural simulation models by estimating uncertainties due to model selection and model simplification. *Computers and Structures*, 89: 1664–1672, 2011.

[22] Riley, M. E. *Quantification of Model-Form, Predictive, and Parametric Uncertainties in Simulation-Based Design*. Ph.D. Thesis, Wright State University, Dayton, OH, 2011.

[23] Riley, M. E., Grandhi, R. V., and Kolonay, R. Quantification of modeling uncertainty in aeroelastic design. In *The 51st AIAA/ASME/ASCE/AHS/ASC Structures, Structural Dynamics, and Materials Conference, Orlando, Florida*. American Institute of Aeronautics and Astronautics, 2010.

[24] Riley, M. E. and Grandhi, R. V. Quantification of modeling uncertainty in aeroelastic design. In *The 13th AIAA/ISSMO Multidisciplinary Analysis Optimization Conference, Fort Worth, Texas*. American Institute of Aeronautics and Astronautics, 2010.

[25] Karaki, G. *Assessment of coupled models of bridges considering time-dependent vehicular loading*. Ph.D. Thesis, Bauhaus-Universität Weimar, Weimar, Germany, 2011.

[26] Scanlan, R. H. Observations on low-speed aeroelasticity. *ASCE Journal of Engineering Mechanics*, 128(12):1254–1258, 2002.

[27] Miyata, T. Historical view of long-span bridge aerodynamics. *Journal of Wind Engineering and Industrial Aerodynamics*, 91:1393–1410, 2003.

[28] Xu, Y.-L. *Wind Effects on Cable-Supported Bridges*. John Wiley & Sons Singapore Pte. Ltd., 2013.

[29] Myerscough, M. Suspension bridges: past and present. *The Structural Engineer*, 91(7):12–21, 2013.

[30] Weight, A. J. Critical analysis of the Great Belt East bridge, Denmark. In *Proceedings of Bridge Engineering 2nd Conference, University of Bath, Bath, UK*, 2009.

[31] Ge, Y. J. and Xiang, H. F. Great demand and great challenge: Chinese major bridges under construction for improving traffic infrastructure nationwide. In *Symposium of the International Association for Bridge and Structural Engineering (IABSE2007), Weimar, Germany*, pages 6–9, 2007.

[32] Ge, Y. and Xiang, H. Recent development of bridge aerodynamics in China. *Journal of Wind Engineering and Industrial Aerodynamics*, 96:736–768, 2008.

[33] Ostenfeld, C., Frandsen, A. G., Jessen, J. J., and Hass, G. Motorway bridge across Lillebælt, publication III: Design and construction of the bridge. Report, 1970.

[34] Larsen, A. Advances in aeroelastic analyses of suspension and cable-stayed bridges. *Journal of Wind Engineering and Industrial Aerodynamics*, 74-76:73–90, 1998.

[35] Kvamstad, T. H. Assessment of the flutter stability limit of the hålogaland bridge using aprobabilistic approach. Masters Thesis, Department of Structural Engineering, Norwegian University of Science and Technology, 2011.

[36] Selvam, R. P. and Govindaswamy, S. Aeroelastic analysis of bridge girder section using computer modelling. Report, Mack Blackwell Transportation Center, University of Arkansas, 2001.

[37] Larsen, A. Computation of flutter of long span cable supported bridges. In *The 4th International Symposium on Computational Wind Engineering (CWE2006), Yokohama, Japan*, 2006.

[38] Bartoli, G. and Mannini, C. A simplified approach to bridge deck flutter. *Journal of Wind Engineering and Industrial Aerodynamics*, 96:229–256, 2008.

[39] Ge, Y.-J. and Xiang, H.-F. Bluff body aerodynamics application in challenging bridge span length. In *The 6th International Colloquium on Bluff Body Aerodynamics and Applications (BBAA6), Milano, Italy*, 2008.

[40] Morgenthal, G., Kovacs, I., and Saul, R. Analysis of aeroelastic bridge deck response to natural wind. *Structural Engineering International (IABSE)*, 15(4): 232–235, 2005.

[41] Simiu, E. and Scanlan, R. H. *Wind Effects on Structures: Fundamentals and Applications to Design.* J. Wiley and Sons, New York, Chichester, Brisbane, 3rd edition, 1996.

[42] Davenport, A. G. The spectrum of horizontal gustiness near the ground in high winds. *Journal of the Royal Meteorological Society*, 87:194–211, 1961.

[43] Davenport, A. G. Gust loading factors. *Journal of the Structural Division*, 93:11–34, 1967.

[44] Isyumov, N. Announcement of the Alan G. Davenport wind loading chain. *The Wind Engineer*, 8:7, 2011.

[45] Strømmen, E. *Theory of Bridge Aerodynamics*. Springer, 2006.

[46] Fujino, Y. and Siringoringo, D. M. Vibration mechanisms and controls of long-span bridges: A review. *Structural Engineering International*, 23(3):248–268, 2013.

[47] Svensson, H. *Cable-Stayed Bridges: 40 Years of Experience Worldwide*. John Wiley & Sons, 2013.

[48] Dyrbye, C. and Hansen, S. *Wind Loads on Structures*. Wiley, 1997.

[49] Chen, X. and Kareem, A. Identification of critical structural modes and flutter derivatives for predicting coupled bridge flutter. *Journal of Wind Engineering and Industrial Aerodynamics*, 96:1856–1870, 2008.

[50] Washizu, K., Ohya, A., Otsuki, Y., and Fujii, K. Aeroelastic instability of rectangular cylinders in a heaving mode. *Journal of Sound and Vibration*, 59(2): 195–210, 1978.

[51] Ge, Y., Lin, Z., Cao, F., Pang, J., and Xiang, H. Investigation and prevention of deck galloping oscillation with computational and experimental techniques. *Journal of Wind Engineering and Industrial Aerodynamics*, 90:2087–2098, 2002.

[52] Blevins, R. and Iwan, W. The galloping response of a two-degree-of-freedom system. *Applied Mechanics*, 41:1113–1118, 1974.

[53] Nakamura, Y. and Mizota, T. Torsional flutter of rectangular prisms. *Engineering Mechanics*, 101:125–142, 1975.

[54] Nakamura, Y. On the aerodynamic mechanism of torsional flutter of bluff structures. *Journal of Sound and Vibration*, 67(2):163–177, 1979.

[55] Washizu, K., Ohya, A., Otsuki, Y., and Fujii, K. Aeroelastic instability of rectangular cylinders in a torsional mode due to a transverse wind. *Journal of Sound and Vibration*, 72(4):507–521, 1980.

[56] Zhou, Z., Chen, A., and Xiang, H. On the mechanism of torsional flutter instability for 1st tacoma narrow bridge by Discrete Vortex Method. In *The 4th International Symposium on Computational Wind Engineering (CWE2006), Yokohama, Japan*, 2006.

[57] Matsumoto, M., Daito, Y., Yoshizumi, F., Ichikawa, Y., and Yabutani, T. Torsional flutter of bluff bodies. *Journal of Wind Engineering and Industrial Aerodynamics*, 69-71:871–882, 1997.

[58] Matsumoto, M., Yagi, T., Tamaki, H., and Tsubota, T. Vortex-induced Vibration and its effect on torsional flutter instability in the case of B/D=4 rectangular cylinder. *Journal of Wind Engineering and Industrial Aerodynamics*, 96:971–983, 2008.

[59] Matsumoto, M. Vortex effect on torsional flutter. In *The 7th Asia-Pacific Conference on Wind Engineering (APCWE7), Taipei, Taiwan*, 2009.

[60] Daito, Y., Matsumoto, M., and Araki, K. Torsional flutter mechanism of two-edge girders for long-span cable-stayed bridge. *Journal of Wind Engineering and Industrial Aerodynamics*, 90:2127–2141, 2002.

[61] Starossek, U. *Brückendynamik: Winderregte Schwingungen von Seilbrücken*. Friedr. Vieweg & Sohn Verlagsgesellschaft GmbH, Braunschweig/ Wiesbaden, 1992.

[62] Matsumoto, M., Matsumiya, H., Fujiwara, S., and Ito, Y. New consideration on flutter properties based on step-by-step analysis. *Journal of Wind Engineering and Industrial Aerodynamics*, pages 429–437, 2010.

[63] Fujino, Y. and Siringoringo, D. M. Long-span bridges vibration, control, seismic retrofit and monitoring - recent studies and lessons learned. In *The 6th Civil Engineering Conference in Asia Region (CECAR6), Jakarta, Indonesia*, 2013.

[64] Fujino, Y., Siringoringo, D., Nagayama, T., and Su, D. Control, simulation and monitoring of bridge vibration - Japan's recent development and practice. In *IABSE-JSCE Joint Conference on Advances in Bridge Engineering-II, Dhaka, Bangladesh*, 2010.

[65] Fujino, Y., Kimura, K., and Tanaka, H. *Wind Resistant Design of Bridges in Japan: Developments and Practices*. Springer Japan, 2012.

[66] Ogawa, K., Shimodoi, H., and Oryu, T. Aerodynamic characteristics of a 2-box girder section adaptable for a super-long span suspension bridge. *Journal of Wind Engineering and Industrial Aerodynamics*, 90:2033–2043, 2002.

[67] Ge, Y. and Xiang, H. Aerodynamic stabilization for box-girder suspension bridges with super-long span. In *The 5th European and African conference on Wind Engineering (EACWE2009), Florence, Italy*, 2009.

[68] Sato, H., Hirahara, N., Fumoto, K., Hirano, S., and Kusuhara, S. Full aeroelastic model test of a super long-span bridge with slotted box girder. *Journal of Wind Engineering and Industrial Aerodynamics*, 90:2023–2032, 2002.

[69] Chen, X. and Kareem, A. Efficacy of tuned mass dampers for bridge flutter control. *Journal of Structural Engineering*, 129(10):1291–1300, 2003.

[70] Lin, Y.-Y., Cheng, C.-M., and Sun, D. Wind-induced vibration control of long-span bridges by multiple tuned mass dampers. *Tamkang Journal of Science and Engineering*, 3(1):1–13, 2000.

[71] Gattulli, V., Fabio, F. D., and Luongo, A. Nonlinear tuned mass damper for self-excited oscillations. *Wind and Structures*, 7(4):251–264, 2004.

[72] Körlin, R. and Starossek, U. Active mass dampers for flutter control of bridges. In *The 8th International Conference on Flow-induced Vibrations (FIV2004), Paris, France*, 2004.

[73] Körlin, R., Boonto, S., Werner, H., and Starossek, U. Lmi-based gain scheduling for bridge flutter control using eccentric rotational actuators. *Optimal Control Applications and Methods*, 33(4):488–500, 2012.

[74] Phongkumsing, S., Wilde, K., and Fujino, Y. Analytical study on flutter suppression by eccentric mass method on FEM model of long-span suspension bridge. *Journal of Wind Engineering and Industrial Aerodynamics*, 89:515–534, 2001.

[75] Aslan, H. and Starossek, U. Passive control of bridge deck flutter using tuned mass dampers and control surfaces. In *The 7th European Conference on Structural Dynamics (EURODYN2008), Southampton, U.K.*, 2008.

[76] Graham, J., Limebeer, D., and Zhao, X. Aeroelastic modelling of long-span suspension bridges. In *The 18th World Congress of the International Federation of Automatic Control (IFAC2011), Milano, Italy*, volume 18(1), pages 9212–9217, 2011.

[77] Huynh, T. and Thoft-Christensen, P. Suspension bridge flutter for girders with separate control flaps. *Journal of Bridge Engineering*, 6(3):168–175, 2001.

[78] Huynh, T. and Thoft-Christensen, P. Suspension bridge flutter for girder with separate control flaps. Report, Department of Building Technology and Structural Engineering, 2000.

[79] Phan, D.-H. and Nguyen, N.-T. Flutter and buffeting control of long-span suspension bridge by passive flaps: Experiment and numerical simulation. *Journal of Aeronautical and Space Sciences*, 14(1):46–57, 2013.

[80] Li, K., Ge, Y., Guo, Z., and Zhao, L. Theoretical framework of feedback aerodynamic control of flutter oscillation for long-span suspension bridges by the twin-winglet system. *Journal of Wind Engineering and Industrial Aerodynamics*, 145: 166–177, 2015.

[81] Collar, A. R. Aeroelastic problems at high speed. *Journal of the Royal Aeronuatical Society*, 51(1), 1947.

[82] Clough, R. W. and Penzien, J. *Dynamics of Structures*. Civil Engineering series. McGraw-Hill Ryerson, Limited, New York, 1993.

[83] Chopra, A. *Dynamics of Structures*. Pearson Education, Limited, 2014.

[84] Ge, Y. J. and Xiang, H. F. Computational models and methods for aerodynamic flutter of long-span bridges. *Journal of Wind Engineering and Industrial Aerodynamics*, 96:1912–1924, 2008.

[85] Dowell, E. H. *A Modern Course in Aeroelasticity*. Springer, 2004.

[86] Fung, Y. *An Introduction to the Theory of Aeroelasticity*. Dover Publications, 2002.

[87] Jurado, J. A. and Hernández, S. Theories of aerodynamic forces on decks of long span bridges. *Journal of Bridge Engineering*, 5(1):813, 2000.

[88] Wagner, H. Über die entstehung des dynamischen auftriebes von tragflügeln. *ZAMM - Journal of Applied Mathematics and Mechanics / Zeitschrift für Angewandte Mathematik und Mechanik*, 5(1):17–35, 1925.

[89] Jones, R. T. The unsteady lift of a wing of a finite aspect ratio. Report 681, NACA, 1940.

[90] Theodorsen, T. General theory of aerodynamic instability and the mechanism of flutter. Report 496, NACA, 1935.

[91] Tamura, Y. and Kareem, A. *Advanced Structural Wind Engineering*. Springer Japan, 2013.

[92] Gu, M., Zhang, R., and Xiang, H. Identification of flutter derivatives of bridge decks. *Journal of Wind Engineering and Industrial Aerodynamics*, 84(2):151–162, 2000.

[93] Eversman, W. and Tewarit, A. Modified exponential series approximation for the Theodorsen function. *American Institute of Aeronautics and Astronautics*, 28(9): 553–557, 1991.

[94] Wu, T. and Kareem, A. Bridge aerodynamics and aeroelasticity: A comparison of modeling schemes. *Journal of Fluids and Structures*, 43:347–370, 2013.

[95] Duncan, W. J. and Frazer, R. A. A brief survey of wing flutter with an abstract of design recommendations. Technical report, Aeronautical Research Commission R. & M. 1177, 1928.

[96] Bleich, F. Dynamic instability of truss-stiffened suspension bridges under wind action. *Proceedings of ASCE*, 78(8):1269–1314, 1948.

[97] Scanlan, R. H. and Tomko, J. J. Airfoil and bridge deck flutter derivatives. *ASCE Journal of Engineering Mechanics*, 97:1717–1737, 1971.

[98] Ge, Y. and Xiang, H. Theoretical model and method for self-excited aerodynamic forces of long-span bridges. In *The International Symposium on Computational Structural Engineering, Shanghai, China*, 2009.

[99] Scanlan, R. H. The action of flexible bridges under wind, i: Flutter theory. *Journal of Sound and Vibration*, 60(2):187–199, 1978.

[100] Scanlan, R. H. The action of flexible bridges under wind, ii: Buffeting theory. *Journal of Sound and Vibration*, 60(2):201–211, 1978.

[101] Jain, A., Jones, N. P., and Scanlan, R. H. Coupled flutter and buffeting analysis of long-span bridges. *Structural Engineering*, 122(7):716–725, 1996.

[102] Jain, A., Jones, N. P., and Scanlan, R. H. Coupled aeroelastic and aerodynamic response analysis of long-span bridges. *Journal of Wind Engineering and Industrial Aerodynamics*, 60:69–80, 1996.

[103] Zhan, H., Fang, T., and Zhang, Z. Flutter stability studies of Great Belt East suspension bridge by two CFD numerical simulation methods. In *The 6th European and African conference on Wind Engineering (EACWE2013), Cambridge, UK*, 2013.

[104] Trein, C. A. and Shirato, H. Coupled flutter stability from the unsteady pressure characteristics point of view. *Journal of Wind Engineering and Industrial Aerodynamics*, 99:114–122, 2011.

[105] Matsumoto, M. Flutter and its application: Flutter mode and ship navigation. *Journal of Wind Engineering and Industrial Aerodynamics*, 122:10–20, 2013.

[106] Miyata, T., Kubo, Y., and Ito, M. Analysis of aeroelastic oscillations of long-span structures by nonlinear multi-dimensional procedures, heathrow, cambridge. In *Proc. of the 4th Int. Conf. on Wind Effects on Buildings and Structures.* Cambridge University Press, 1975.

[107] Zasso, A. Flutter derivatives: Advantages of a new representation convention. *Journal of Wind Engineering and Industrial Aerodynamics*, 60:35–47, 1996.

[108] Starossek, U. Complex notation in flutter analysis. *Journal of Structural Engineering, ASCE*, 124(8):975–977, 1998.

[109] Starossek, U. Prediction of flutter through the use of finite elements. *Structural Engineering Review*, 5(4):301–307, 1993.

[110] Starossek, U. Simplified flutter prediction for bridges with bluff cross-section. *Structural Engineering Review*, 6(1):35–38, 1994.

[111] Starossek, U., Aslan, H., and Thiesemann, L. Experimental and numerical identification of flutter derivatives for nine bridge deck sections. *Wind and Structures*, 12(6):519–540, 2009.

[112] Szechenyi, E. Etude du comportement aéroélastique du pont de saint-nazaire à saint-brévin. Report NT 2/3044 RY, ONERA, 1973.

[113] Borri, C. and Höffer. Aeroelastic wind forces on flexible bridge girders. *Meccanica*, 35:1–15, 2000.

[114] Jensen, A. G. Aeroelastic wind forces on flexible bridge girders. *Journal of Wind Engineering and Industrial Aerodynamics*, 69-71:777–793, 1997.

[115] Larsen, A. Prediction of aeroelastic stability of suspension bridges during erection. *Journal of Wind Engineering and Industrial Aerodynamics*, 72:265–274, 1997.

[116] Blocken, B. 50 years of Computational Wind Engineering: Past, present and future. *Journal of Wind Engineering and Industrial Aerodynamics*, 129:69–102, 2014.

[117] Larsen, A. and Walther, J. H. Aeroelastic analysis of bridge girder section based on Discrete Vortex simulations. *Journal of Wind Engineering and Industrial Aerodynamics*, 67-68:253–265, 1997.

[118] Walther, J. H. *Discrete Vortex Method for Two-dimensional Flow past Bodies of Arbitrary Shape Undergoing Prescribed Rotary and Translational Motion.* Ph.D. Thesis, Technical University of Denmark (DTU), Kgs. Lyngby, Denmark, 1994.

[119] Larsen, A. and Walther, J. Discrete Vortex simulation of vortex excitation and mitigation in bridge engineering. In *The 2nd M.I.T. Conference on Computational Fluid and Solid Mechanics, Cambridge, U.S.A.*, 2003.

[120] Morgenthal, G. Advances in numerical bridge aerodynamics and recent applications. *Structural Engineering International (IABSE)*, 15:95–100, 2005.

[121] Morgenthal, G. Numerical analysis of bridge aerodynamics. *Structural Concrete (fib)*, 6:35–41, 2006.

[122] Morgenthal, G. and Walther, J. H. An immersed interface method for the vortex-in-cell algorithm. *Computers and Structures*, 85:712–726, 2007.

[123] Morgenthal, G., Corriols, A. S., and Bendig, B. A GPU-accelerated Pseudo-3D Vortex Method for aerodynamic analysis. *Journal of Wind Engineering and Industrial Aerodynamics*, 125:69–80, 2014.

[124] Abbas, T. and Morgenthal, G. Quantification of the effects of turbulence in wind on the Vortex-induced Vibrations. In *The 36th Symposium of the International Association for Bridge and Structural Engineering (IABSE2014), Kolkata, India*, 2013.

[125] Abbas, T. and Morgenthal, G. Quantification of the effects of turbulence in wind on the aeroelastic behaviour of suspension bridges. In *Der 13. Dreiländertagung der Windtechnologischen Gesellschaft (WtG2013), Wien*, 2013.

[126] Abbas, T. and Morgenthal, G. Numerical models for flutter analysis. In *The 6th International Symposium on Computational Wind Engineering (CWE2014), Hamburg, Germany*, 2014.

[127] Abbas, T. and Morgenthal, G. Assessment of the flutter stability of bridges using a probabilistic approach. In *The 12th International Probabilistic Workshop (IPW12), Weimar, Germany*, 2014.

[128] Morgenthal, G. *Aerodynamic Analysis of Structures Using High-resolution Vortex Particle Methods*. Ph.D. Thesis, University of Cambridge, Cambridge, 2002.

[129] Frandsen, J. Simultaneous pressures and accelerations measured full-scale on the Great Belt East suspension bridge. *Journal of Wind Engineering and Industrial Aerodynamics*, 89:95–129, 2001.

[130] Jones, N. P. and Ozkan, E. Wind effects on long span cable stayed bridges: Assessment and validation. In *Joint Meeting of U.S./Japan Natural Resources Development Program (UJNR), Gaithesburg, MD*, 2002.

[131] Nikitas, N., Jakobsen, J. B., and Macdonald, J. H. G. Full-scale identification of modal and aeroelastic parameters of the clifton suspension bridge. In *The 6th International Colloquium on Bluff Body Aerodynamics and Applications (BBAA6), Milano, Italy*, 2008.

[132] Miyata, T. and Yamaguchi, K. Aerodynamics of wind effects on the akashi kaikyo bridge. *Journal of Wind Engineering and Industrial Aerodynamics*, 48:287–315, 1993.

[133] Larsen, A. Aerodynamic aspects of the final design of the 1624 m suspension bridge across the Great Belt. *Journal of Wind Engineering and Industrial Aerodynamics*, 48:261–285, 1993.

[134] Yoshizumi, F. and Inoue, H. An experimental approach on aerodynamic stability of a cable-stayed cantilever bridge. *Journal of Wind Engineering and Industrial Aerodynamics*, 90:2099–2111, 2002.

[135] Davenport, A. and King, J. Dynamic wind forces on long span bridges. Report, IABSE congress report, 1984.

[136] Xu, F., Zhu, L., Ge, X., and Zhang, Z. Some new insights into the identification of bridge deck flutter derivatives. *Engineering Structures*, 75:418–428, 2014.

[137] Wu, J.-C., Liu, W.-C., and Juang, J.-Y. Identification of flutter derivatives by forced vibration technique. In *The 4th International Symposium on Computational Wind Engineering (CWE2006), Yokohama, Japan*, 2006.

[138] Haung, L. and Liao, H. Identification of flutter derivatives of bridge deck under multi-frequency vibration. *Engineering Applications of Computational Fluid Mechanics*, 5(1):16–25, 2011.

[139] Neuhaus, C., Roesler, S., Höffer, R., and Hortmanns, M. Identification of 18 flutter derivatives by forced vibration tests: A new experimental rig. In *The 5th European and African conference on Wind Engineering (EACWE2009), Florence, Italy*, 2009.

[140] Larsen, S., Sinding, P., and Smitt, L. Extraction of aerodynamic flutter derivatives in newly developed forced motion rig with 3 degrees of freedom. In *The 13th International Conference on Wind Engineering (ICWE13), Amsterdam, The Netherlands*, 2011.

[141] Larsen, A. and Walther, J. H. Discrete Vortex simulation of flow around five generic bridge deck sections. *Journal of Wind Engineering and Industrial Aerodynamics*, 77-78:591–602, 1998.

[142] Xin, D. and Ou, J. Numerical simulation of aerodynamic derivatives and critical wind speed for long-span bridges based on simplified steady wind field. *Earthquake Engineering and Engineering Vibration*, 6(2):197–203, 2007.

[143] Kreis, E. and André, J. A numerical inquiry into the flutter phenomenon in long-span bridges. *Latin American Journal of Solids and Structures*, 2:321–337, 2005.

[144] Chen, W.-F. and Duan, L. *Bridge Engineering Handbook, Superstructure Design, Second Edition*. CRC Press, 2014.

[145] Theodorsen, T. and Garrick, I. E. Mechanism of flutter a theoretical and experimental investigation of the flutter problem. Report 685, NACA, 1940.

[146] Abbas, T. Flutter analysis of suspension bridges using a two-stage numerical approach and aerodynamic derivatives. Masters Thesis, Bauhaus-Universität Weimar, Germany, 2011.

[147] Abbas, T. and Morgenthal, G. Hybrid models for assessing the flutter stability of suspension bridges. In *The 7th International Colloquium on Bluff Body Aerodynamics and Applications (BBAA7), Shanghai, China*, 2012.

[148] Abbas, T. and Morgenthal, G. Model combinations for assessing the flutter stability of suspension bridges. In *The 19th International Conference on the Applications of Computer Science and Mathematics in Architecture and Civil Engineering (IKM2012), Weimar, Germany*, 2012.

[149] Frandsen, A. Wind stability of suspension bridges. application of the theory of thin airfoils. In *Proceedings of the International Symposium on Suspension Bridges, Lisbon*, pages 609–627, 1966.

[150] Selberg, A. Oscillation and aerodynamic stability of suspension bridges. In *Civil Engineering and Construction*. 13. ACTA Polytechnica Scandinavica, 1961.

[151] Klöppel, K. and Thiele, F. Modellversuche im windkanal zur bemessung von brücken gegen die gefahr winderregter schwingungen. *Der Stahlbau*, 36(12):353–365, 1967.

[152] Matsumoto, M., Matsumiya, H., Fujiwara, S., and Ito, Y. New consideration on flutter properties basing on sbs: Fundamental flutter mode, similar selberg's formula, torsional divergence instability, and new coupled flutter phenomena affected by structural coupling. In *The 6th International Colloquium on Bluff Body Aerodynamics and Applications (BBAA6), Milano, Italy*, 2008.

[153] Put, T. v. d. Rigidity of structures against aerodynamic forces. *IABSE publications*, 36:189–196, 1976.

[154] Fu, C. and Wang, S. *Computational Analysis and Design of Bridge Structures*. CRC Press, 2014.

[155] Matsumoto, M. Aerodynamic damping of prisms. *Journal of Wind Engineering and Industrial Aerodynamics*, 59:159–175, 1996.

[156] Hoa, L. T. Flutter stability analysis theory and example. Technical report, 2004.

[157] Jurado, J. and Hernández, S. Sensitivity analysis of bridge flutter with respect to mechanical parameters of the deck. *Structural and Multidisciplinary Optimization*, 27(4):272–283, 2004.

[158] Hernández, S., Jurado, J. A., Nieto, F., and Mosquera, A. Multidisciplinary approach to aeroelastic studies of long-span bridges. *Structural and Multidisciplinary Optimization*, 35(4):365–374, 2008.

[159] Dung, N. N., Miyata, T., Yamada, H., and Minh, N. N. Flutter responses in long span bridges with wind induced displacement by the mode tracing method. *Journal of Wind Engineering and Industrial Aerodynamics*, 77-78:367–379, 1998.

[160] Matsumoto, M., Nihara, Y., Kobayashi, Y., Sato, H., and Hamasaki, H. Flutter mechanism and its stabilization of bluff bodies. In *The 9th International Conference on Wind Engineering (ICWE1995), New Delhi, India*, pages 827–838, 1995.

[161] Matsumoto, M., Kobayashi, Y., and Shirato, H. The influence of aerodynamic derivatives on flutter. *Journal of Wind Engineering and Industrial Aerodynamics*, 60:227–239, 1996.

[162] Matsumoto, M., Mizuno, K., Okubo, K., Ito, Y., and Matsumiya, H. Flutter instability and recent development in stabilization of structures. *Journal of Wind Engineering and Industrial Aerodynamics*, 95:888–907, 2007.

[163] Matsumoto, M., Goto, K., and Yabutani, T. Heaving branch coupled flutter for long span bridge. In *Long-Span and High-Rise Structures, IABSE Symposium, Kobe*, pages 259–264, 1998.

[164] Matsumoto, M., Yoshizumi, F., Yabutani, T., Abe, K., and Nakajima, N. Flutter stabilization and heaving-branch flutter. *Journal of Wind Engineering and Industrial Aerodynamics*, 83:289–299, 1999.

[165] Matsumoto, M., Okubo, K., Ito, Y., Matsumiya, H., Trein, C. A., and Kim, G. Branch switching characteristics of coupled flutter instability. In *The 19th KKCNN Symposium on Civil Engineering, Kyoto, Japan*, 2006.

[166] Matsumoto, M., Mizuno, K., Okubo, K., and Ito, Y. The complex branch characteristics of coupled flutter. In *The 4th International Symposium on Computational Wind Engineering (CWE2006), Yokohama, Japan*, 2006.

[167] Matsumoto, M., Okubo, K., Ito, Y., Matsumiya, H., and Kim, G. The complex branch characteristics of coupled flutter. *Journal of Wind Engineering and Industrial Aerodynamics*, 96:1843–1855, 2008.

[168] Matsumoto, M., Matsumiya, H., and Fujiwara, S. Branch switch of coupled flutter. In *The 7th Asia-Pacific Conference on Wind Engineering (APCWE7), Taipei, Taiwan*, 2009.

[169] Matsumoto, M., Taniwaki, Y., and Shijo, R. Frequency characteristics in various flutter instabilities of bridge girders. *Journal of Wind Engineering and Industrial Aerodynamics*, 90:1973–1980, 2002.

[170] Matsumoto, M., Shirato, H., Mizuno, K., Shijo, R., and Hikida, T. Flutter characteristics of h-shaped cylinders with various side-ratios and comparisons with characteristics of rectangular cylinders. *Journal of Wind Engineering and Industrial Aerodynamics*, 96:963–970, 2008.

[171] Yang, Y.-X., Ge, Y.-J., and Xiang, H.-F. Flutter mechanism and flutter modality investigation for thin plate sections. In *The 4th International Symposium on Computational Wind Engineering (CWE2006), Yokohama, Japan*, 2006.

[172] Yang, Y.-X., Ge, Y.-J., and Zhang, W. Investigation on the flutter mechanism of thin plate sections. In *The 5th European and African conference on Wind Engineering (EACWE2009), Florence, Italy*, 2009.

[173] Yang, Y., Ge, Y., and Xiang, H. Flutter control effect and mechanism of central-slotting for long-span bridges. *Frontiers of Architecture and Civil Engineering in China*, 1(3):298–304, 2007.

[174] Chen, X. Improved understanding of bimodal coupled bridge flutter based on closed-form solutions. *Journal of Structural Engineering*, 133(1):22–31, 2007.

[175] Beliveau, J. G., Shinozuka, M., and Vaicaitis, R. Motion of suspension bridge subjected to wind loads. *Journal of the Structural Division*, 103(6):1189–1205, 1977.

[176] Diana, G., Bruni, S., Cigada, A., and Collina, A. Turbulence effect on flutter velocity in long span suspension bridges. *Journal of Wing Engineering and Industrial Aerodynamics*, 48:329–342, 1993.

[177] Kovacs, I., Svensson, H. S., and Jordet, E. Analytical aerodynamic investigation of cable-stayed helgeland bridge. *Journal of Structural Engineering*, 118:147–168, 1992.

[178] Miyata, T., Yamada, H., Boonyapinyo, V., and Santos. Full model testing of large cable-supported bridges. In *The 9th International Conference on Wind Engineering (ICWE1995), New Delhi, India*, pages 249–280, 1995.

[179] Miyata, T., Yamada, H., Boonyapinyo, V., and Santos. Analyitical investigation on the response of a very long suspension bridge under gusty wind. In *The 9th International Conference on Wind Engineering (ICWE1995), New Delhi, India*, pages 1006–1017, 1995.

[180] Xiang, H., Liu, C., and Gu, M. Time-domain analysis for coupled buffeting response on long span bridge. In *The 9th International Conference on Wind Engineering (ICWE1995), New Delhi, India*, pages 881–892, 1995.

[181] Boonyapinyo, V., Miyata, T., and Yamada, H. Advanced aerodynamic analysis of suspension bridges by state-space approach. *Journal of Structural Engineering*, 125: 1357–1366, 1999.

[182] Chen, X., Matsumoto, M., and Kareem, A. Aerodynamic coupling effects on flutter and buffeting of bridges. *Journal of Engineering Mechanics*, 126(1):7–16, 2000.

[183] Chen, X., Matsumoto, M., and Kareem, A. Time domain flutter and buffeting response analysis of bridges. *Journal of Engineering Mechanics*, 126(1):17–26, 2000.

[184] Chen, X., Kareem, A., and Matsumoto, M. Multimode coupled flutter and buffeting analysis of long span bridges. *Journal of Wind Engineering and Industrial Aerodynamics*, 89:649–664, 2001.

[185] Chen, X. and Kareem, A. Aeroelastic analysis of bridges under multicorrelated winds: Integrated state-space approach. *Journal of Engineering Mechanics*, 127(11): 1124–1134, 2001.

[186] Thang, N. D., Katsuchi, H., Yamada, H., and Saski, E. Effects of approximation of self-excited forces by rational function on wind-induced response of long span bridge. *Journal of Structural Engineering*, 54:420–428, 2008.

[187] Øiseth, O., Rönnquist, A., and Sigbjörnsson, R. Time domain modeling of self-excited aerodynamic forces for cable-supported bridges: A comparative study. *Computers and Structures*, 89:1306–1322, 2011.

[188] Øiseth, O., Rönnquist, A., and Sigbjörnsson, R. Finite element formulation of the self-excited forces for time-domain assessment of wind-induced dynamic response and flutter stability limit of cable-supported bridges. *Finite Elements in Analysis and Design*, 50:173–183, 2012.

[189] Guo, Z. and Ge, Y. A new state-space model for self-excited forces and straight forward analysis of bridge deck flutter. In *The 7th International Colloquium on Bluff Body Aerodynamics and Applications (BBAA7), Shanghai, China*, pages 480–489, 2012.

[190] Scanlan, R., Jones, N., and Singh, L. Inter-relations among flutter derivatives. *Journal of Wind Engineering and Industrial Aerodynamics*, 69-71:829–837, 1997.

[191] Xu, X. Parametric studies on relationships between flutter derivatives of slender bridge (I). *Applied Mathematics and Mechanics*, 30(2):237–245, 2009.

[192] Xu, X. Parametric studies on relationships between flutter derivatives of slender bridge (II). *Applied Mathematics and Mechanics*, 30(3):335–341, 2009.

[193] Tubino, F. Relationships among aerodynamic admittance functions, flutter derivatives and static coefficients for long-span bridges. *Journal of Wind Engineering and Industrial Aerodynamics*, 93:929–950, 2005.

[194] Al-Assaf, A. *Flutter Analysis of Open-Truss Stiffened Suspension Bridges Using Synthesized Aerodynamic Derivatives*. Ph.D. Thesis, Washington State University, Washington, USA, 2006.

[195] Lute, V., Upadhyay, A., and Singh, K. Support vector machine based aerodynamic analysis of cable stayed bridges. *Advances in Engineering Software*, 40:830–835, 2009.

[196] Mannini, C. *Flutter Vulnerability Assessment of Flexible Bridges*. Ph.D. Thesis, University of Florence, Florence, Italy, 2006.

[197] Borri, C. and Mannini, C. *Aeroelastic Phenomena and Pedestrian-structure Dynamic Interaction on Non-conventional Bridges and Footbridges*. Strumenti per la didattica e la ricerca. Firenze University Press, 2010.

[198] Mannini, C., Bartoli, G., and Borri, C. New developments in bridge flutter analysis. *Proceedings of the Institution of Civil Engineers*, 165(SB3):139–159, 2012.

[199] Lee, H. E., Vu, T. V., Yoo, S. Y., and Lee, H. Y. A simplified evaluation in critical frequency and wind speed to bridge deck flutter. *Procedia Engineering*, 14: 1784–1790, 2011.

[200] Øiseth, O. and Sigbjörnsson, R. An alternative analytical approach to prediction of flutter stability limits of cable supported bridges. *Journal of Sound and Vibration*, 330:2784–2800, 2011.

[201] Øiseth, O., Rönnquist, A., and Sigbjörnsson, R. Simplified prediction of wind-induced response and stability limit of slender long-span suspension bridges, based on modified quasi-steady theory: A case study. *Journal of Wind Engineering and Industrial Aerodynamics*, 98:730–741, 2010.

[202] Banerjee, J. A simplified method for the free vibration and flutter analysis of bridge decks. *Journal of Sound and Vibration*, 260:829–845, 2003.

[203] Vairo, G. A simple analytical approach to the aeroelastic stability problem of long-span cable-stayed bridges. *International Journal for Computational Methods in Engineering Science and Mechanics*, 11(1):1–19, 2010.

[204] Chen, X. and Kareem, A. Revisiting multimode coupled bridge flutter: some new insights. *Journal of Engineering Mechanics ASCE*, 132(10):1115–1123, 2006.

[205] Yamada, H., Katsuchi, H., and Kien, P. H. A study on understanding of coupled flutter of long-span bridges. In *The 4th International Symposium on Computational Wind Engineering (CWE2006), Yokohama, Japan*, 2006.

[206] Scanlan, R. Interpreting aeroelastic models of cable-stayed bridges. *Journal of Engineering Mechanics*, 113(4):555–575, 1987.

[207] Scanlan, R. H. and Jones, N. P. Aeroelastic analysis of cable-stayed bridges. *Journal of Structural Engineering*, 116(2):279–297, 1990.

[208] Tanaka, H., Yamamura, N., and Tatsumi, M. Coupled mode flutter analysis using flutter derivatives. *Journal of Wind Engineering and Industrial Aerodynamics*, 41-44: 1279–1290, 1992.

[209] D'Asdia, P. and Sepe, V. Aeroelastic instability of long-span suspended bridges: a multi-mode approach. *Journal of Wind Engineering and Industrial Aerodynamics*, 74-76:849–857, 1998.

[210] Mishra, S. S., Kumar, K., and Krishna, P. Multimode flutter of long-span cable-stayed bridge based on 18 experimental aeroelastic derivatives. *Journal of Wind Engineering and Industrial Aerodynamics*, 96:83–102, 2008.

[211] Mishra, S. S., Kumar, K., , and Krishna, P. Relevance of eighteen flutter derivatives in wind response of a long-span cable-stayed bridge. *Journal of Structural Engineering*, 134(5):769–781, 2008.

[212] Katsuchi, H., Jones, N. P., Scanlan, R. H., and Akiyama, H. Multi-mode flutter and buffeting analysis of the akashi-kaikyo bridge. *Journal of Wind Engineering and Industrial Aerodynamics*, 77-78:431–441, 1998.

[213] Katsuchi, H., Jones, N. P., and Scanlan, R. H. Multimode coupled flutter and buffeting analysis of the akashi-kaikyo bridge. *Structural Engineering*, 125(1):60–70, 1999.

[214] Zhang, X. and Brownjohn, J. M. W. Effect of relative amplitude on bridge deck flutter. *Journal of Wind Engineering and Industrial Aerodynamics*, 92:493–508, 2004.

[215] Hoa, L. T. Flutter instability of cable-stayed bridges. In *National Scientific Seminar on Vibration of Cable-stayed Bridges, Hanoi, Vietnam*, 2008.

[216] Nakamura, H. and Ogaki, I. Flutter simulation for bridges. In *The MSC 1990 World Users Conference*, volume I, 1990.

[217] Namini, A., Albrecht, P., and Bosch, H. Finite element-based flutter analysis of cable-suspended bridges. *Journal of Structural Engineering*, 118(6):1509–1526, 1992.

[218] Astiz, M. Flutter stability of very long suspension bridges. *Journal of Bridge Engineering*, 3(3):132–139, 1998.

[219] Hua, X. and Chen, Z. Full-order and multimode flutter analysis using ansys. *Finite Elements in Analysis and Design*, 44:537–551, 2008.

[220] Øiseth, O., Rönnquist, A., and Sigbjörnsson, R. Prediction of wind-induced dynamic response and flutter stability limit of long-span bridges using the finite element method. In *Strait Crossings 2013, Bergen, Norway*, 2013.

[221] Vu, T.-V., Kim, Y.-M., and Lee, H.-E. Coupled flutter analysis of long-span bridges using full set of flutter derivatives. *KSCE Journal of Civil Engineering*, pages 1–13, 2015.

[222] Pleif, M. S. and Batista, R. C. Aerodynamic stability analysis of cable-stayed bridges. *Journal of Structural Engineering*, 121(12):1784–1788, 1995.

[223] Jurado, J. A., Kusano, I., Hernández, S., and Nieto, F. Improvement of multimodal flutter analysis code, flas. In *The 6th European and African conference on Wind Engineering (EACWE2013), Cambridge, UK*, 2013.

[224] Agar, T. J. A. Aerodynamic flutter analysis of suspension bridges by a modal technique. *Engineering Structures*, 11:75–82, 1989.

[225] Agar, T. J. A. Dynamic instability of suspension bridges. *Computers and Structures*, 41(6):1321–1328, 1991.

[226] Hoa, L. T. Aerodynamics, stability and response prediction of bridges due to turbulent atmospheric flow. In *National Conference on Aero-Fluid Mechanics, VungTau, Vietnam*, 2006.

[227] Gu, M., Xiang, H., and Lin, Z. Flutter- and buffeting-based selection for long-span bridges. *Journal of Wind Engineering and Industrial Aerodynamics*, 80:373–382, 1999.

[228] Ge, Y. J., Xiang, H. F., and Tanaka, H. Application of a reliability analysis model to bridge flutter under extreme winds. *Journal of Wind Engineering and Industrial Aerodynamics*, 86:155–167, 2000.

[229] Vu, T.-V., Lee, H.-Y., Chun, N.-H., Oh, S.-T., Kim, Y.-M., and Lee, H.-E. Flutter analysis of bridges through use of state space method. In *The 8th International Conference on Structural Dynamics (EURODYN2011), Leuven, Belgium*, 2011.

[230] Ge, Y. and Tanaka, H. Aerodynamic flutter analysis of cable-supported bridges by multi-mode and full-mode approaches. *Journal of Wind Engineering and Industrial Aerodynamics*, 86:123–153, 2000.

[231] Ding, Q., Chen, A., and Xiang, H. Coupled flutter analysis of long-span bridges by multimode and full-order approaches. *Journal of Wind Engineering and Industrial Aerodynamics*, 90:1981–1993, 2002.

[232] Chen, X. and Kareem, A. Curve veering of eigenvalue loci of bridges with aeroelastic effects. *Journal of Engineering Mechanics*, 129(2):146–159, 2003.

[233] Chen, X. and Kareem, A. Anatomy of bridge flutter: Some new insights. In *The 11th International Conference on Wind Engineering (ICWE11), Lubbock, Texas*, 2003.

[234] Chen, X. and Kareem, A. Efficacy of the implied approximation in the identification of flutter derivatives. *Journal of Structural Engineering*, 130(12): 2070–2074, 2004.

[235] Chen, X. and Kareem, A. Understanding the underlying physics of multimode coupled bridge flutter based on closed-form solutions. In *The 4th International Symposium on Computational Wind Engineering (CWE2006), Yokohama, Japan*, 2006.

[236] Starossek, U. Bridge flutter prediction with finite beam element in complex notation. In *The 7th International Conference on Computing in Civil and Building Engineering (ICCCBE-VII), Seoul, South Korea*, pages 2099–2104, 1997.

[237] Starossek, U. Bridge instability in wind and spatial flutter analysis. In *Korean Society of Civil Engineers Annual Conference, Seoul, Korea*, 1998.

[238] Thiesemann, L., Bergmann, D., and Starossek, U. Numerical and experimental evaluation of flutter derivatives by means of the forced vibration method. In *The Eleventh International Conference on Wind Engineering (ICWE2003), Lubbock, Texas*, 2003.

[239] Thiesemann, L. and Starossek, U. Numerische und experimentelle ermittlung von instationären luftkräften zum nachweis der aeroelastischen stabilität weitgespannter brücken (numerical and experimental determination of flutter derivatives for aeroelastic stability analysis of long-span bridges). In *Forschungskolloquium Baustatik-Baupraxis, Neubiberg/München*, pages 247–258, 2003.

[240] Qiu, J. and Sun, Q. Flutter solution by use of eigenvalues and eigenvectors of a complex general matrix. *Modern Applied Science*, 3(10):42–46, 2009.

[241] Frandsen, J. Numerical bridge deck studies using Finite Elements. Part I: flutter. *Journal of Wind Engineering and Industrial Aerodynamics*, 19:171–191, 2004.

[242] Robertson, I., Sherwin, S., and Bearman, P. Prediction of flutter instability due to cross winds of the second forth road bridge. In *European congress on computational methods in applied sciences and engineering (ECCOMAS), Swansea, Wales*, 2001.

[243] Morgenthal, G. and McRobie, F. A. A comparative study of numerical methods for fluid structure interaction analysis in long-span bridge design. *Wind and Structures*, 5:101–114, 2002.

[244] Nowicki, T. and Flaga, A. Modelling aeroelastic response of bridge decks using Discrete Vortex Method. In *The 19th International Conference on Computer Methods in Mechanics (CMM2011), Warsaw, Poland*, 2011.

[245] Zhan, H. and Fang, T. Flutter stability studies of Great Belt East bridge and Tacoma Narrows bridge by CFD numerical simulation. In *The 7th International Colloquium on Bluff Body Aerodynamics and Applications (BBAA7), Shanghai, China*, 2012.

[246] Ostenfeld, C., Frandsen, A. G., Jessen, J. J., and Hass, G. Motorway bridge across Lillebælt, publication XI: Model tests for the superstructure of the suspension bridge. Report, 1970.

[247] Scanlan, R. H. Reexamination of sectional aerodynamic force functions for bridges. *Journal of Wind Engineering and Industrial Aerodynamics*, 89:1257–1266, 2001.

[248] Gu, M., Zhang, R., and Xiang, H. Parametric study on flutter derivatives of bridge decks. *Engineering Structures*, 23:1607–1613, 2001.

[249] Bartoli, G., D'Asdia, P., Febo, S., Mannini, C., Pasto, S., and Procino, L. Innovative solutions for long-span suspension bridges. In *The 6th International Colloquium on Bluff Body Aerodynamics and Applications (BBAA6), Milano, Italy*, 2008.

[250] Zhang, X. and Sun, B. Short note: Parametric study on the aerodynamic stability of a long-span suspension bridge. *Journal of Wind Engineering and Industrial Aerodynamics*, 92:431–439, 2004.

[251] Unjoh, S. and Adachi, Y. Damping characteristics of long-span suspension bridges. Report, IABSE congress report, 1998.

[252] Khodaparast, H. H., Mottershead, J. E., and Badcock, K. J. Propagation of structural uncertainty to linear aeroelastic stability. *Computers and Structures*, 88: 223–236, 2010.

[253] Jain, A., Jones, N. P., and Scanlan, R. H. Effect of modal damping on bridge aeroelasticity. *Journal of Wind Engineering and Industrial Aerodynamics*, 77-78: 421–430, 1998.

[254] Zhang, X. Investigation on aerodynamic stability of long-span suspension bridges under erection. *Journal of Wind Engineering and Industrial Aerodynamics*, 92:1–8, 2004.

[255] Jones, N. P., Raggett, J. D., and Ozkan, E. Prediction of cable-supported bridge response to wind: coupled flutter assessment during retrofit. *Journal of Wind Engineering and Industrial Aerodynamics*, 91(12-15):1445–1464, 2003.

[256] Lin, Y.-Y., Cheng, C.-M., Wu, J.-C., Lan, T.-L., and Wu, K.-T. Effects of deck shape and oncoming turbulence on bridge aerodynamics. *Tamkang Journal of Science and Engineering*, 8(1):43–56, 2005.

[257] Miranda, M. and Bartoli, G. Aerodynamic optimization of decks of cable-stayed bridges. In *Symposium of the International Association for Bridge and Structural Engineering (IABSE2001), Seoul, South Korea*, 2001.

[258] Fumoto, K., Hata, K., Matsuda, K., Murakami, T., Saito, Y., and Shirai, S. Aerodynamic improvement of slotted one-box girder section for super long suspension bridge. In *The 6th Asia-Pacific Conference on Wind Engineering (APCWE6), Seoul, South Korea*, 2005.

[259] Permata, R., Yonamine, K., Hattori, H., and Shirato, H. Aerodynamics and flutter stability of slender bridge deck with double slot and porous cavity. In *The 6th Civil Engineering Conference in Asia Region (CECAR6), Jakarta, Indonesia*, 2013.

[260] Wang, Q., Liao, H.-L., Li, M.-S., and Xian, R. Wind tunnel study on aerodynamic optimization of suspension bridge deck based on flutter stability. In *The 7th Asia-Pacific Conference on Wind Engineering (APCWE7), Taipei, Taiwan*, 2009.

[261] Yang, Y., Zhou, R., Ge, Y., Mohotti, D., and Mendis, P. Aerodynamic instability performance of twin box girders for long-span bridges. *Journal of Wind Engineering and Industrial Aerodynamics*, 145:196–208, 2015.

[262] Matsumoto, M., Nakajima, N., Taniwaki, Y., and Shijo, R. Grating effect on flutter instability. *Journal of Wind Engineering and Industrial Aerodynamics*, 89: 1487–1497, 2001.

[263] Xu, F. Y., Chen, X. Z., Cai, C. S., and Chen, A. R. Determination of 18 flutter derivatives of bridge decks by an improved stochastic search algorithm. *Journal of Bridge Engineering*, 17(4):576–588, 2012.

[264] Mannini, C. and Bartoli, G. Investigation on the dependence of bridge deck flutter derivatives on steady angle of attack. In *The 6th International Colloquium on Bluff Body Aerodynamics and Applications (BBAA6), Milano, Italy*, 2008.

[265] Chowdhury, A. G. and Sarkar, P. P. A new technique for identification of eighteen flutter derivatives using a three-degree-of-freedom section model. *Engineering Structures*, 25:1763–1772, 2003.

[266] Brusiani, F., Cazzoli, G., Miranda, S., Ubertini, F., and Vaona., P. Estimation of the flutter derivatives of a long-span bridge using the k-omega turbulence model. In *XVIII GIMC Conference, Siracusa*, 2010.

[267] Scanlan, R. H. Some observations on the state of bluff-body aeroelasticity. *Journal of Wind Engineering and Industrial Aerodynamics*, 69-71:77–90, 1997.

[268] Haan, F. L. *The Effects of Turbulence on the Aerodynamics of Long-span Bridges*. Ph.D. Thesis, University of Notre Dame, Notre Dame, Indiana, USA, 2000.

[269] Bartoli, G. and Righi, M. Flutter mechanism for rectangular prisms in smooth and turbulent flow. *Journal of Wind Engineering and Industrial Aerodynamics*, 94: 275–291, 2006.

[270] Parkinson, G. V. Phenomena and modeling of flow-induced vibrations of bluff bodies. *Progress in Aerospace Sciences*, 26(2):169–224, 1989.

[271] Huang, H. and Li, M. Flutter and buffeting analysis in time domain for suspension bridge in operation and erection stage. In *The 4th International Symposium on Computational Wind Engineering (CWE2006), Yokohama, Japan*, 2006.

[272] Cai, C. S. and Albrecht, P. Flutter derivatives based random parametric excitation aerodynamic analysis. *Computers and Structures*, 75:463–477, 2000.

[273] Abbas, T. and Morgenthal, G. Quantification of the effects of turbulence in wind on the flutter stability of suspension bridges. In *The 6th European and African conference on Wind Engineering (EACWE2013), Cambridge, UK*, 2013.

[274] Eurocode 1: Actions on structures, part 1-4: Wind actions (4.4 wind turbulence). Technical report, 2004.

[275] Ianenti, A. and Zasso, A. Probabilistic approach to the identification of the flutter instability conditions: an application to the long span suspension bridge case. In *The Ninth International Conference on Wind Engineering, New Delhi, India*, 1995.

[276] Ostenfeld-Rosenthar, P., Madsen, H., and Larsen, A. Probabilistic flutter criteria for long span bridges. *Journal of Wind Engineering and Industrial Aerodynamics*, 41-44:1265–1276, 1992.

[277] Xiang, H. and Ge, Y. Refinements on aerodynamic stability analysis of super long-span bridges. *Journal of Wind Engineering and Industrial Aerodynamics*, 90: 1493–1515, 2002.

[278] Nieto, F., Hernández, S., Jurado, J. A., and Mosquera, A. Analytical approach to sensitivity analysis of flutter speed in bridges considering variable deck mass. *Advances in Engineering Software*, 42:117–129, 2011.

[279] Sarkar, P., Caracoglia, L., and Haan, F. Parametric study of flutter derivatives of bluff cross sections and their implications on the aeroelastic stability of flexible bridges. In *The 39th Joint Meeting of U.S./Japan Natural Resources Development Program (UJNR), Tsukuba, Japan*, pages 432–441, 2007.

[280] Sarkar, P. P., Caracoglia, L., Haan-Jr., F. L., Sato, H., and Murakoshi, J. Comparative and sensitivity study of flutter derivatives of selected bridge deck sections, part 1: Analysis of inter-laboratory experimental data. *Engineering Structures*, 31:158–169, 2009.

[281] Caracoglia, L., Sarkar, P. P., Haan-Jr., F. L., Sato, H., and Murakoshi, J. Comparative and sensitivity study of flutter derivatives of selected bridge deck sections, part 2: Implications on the aerodynamic stability of long-span bridges. *Engineering Structures*, 31:2194–2202, 2009.

[282] Abbas, T. and Morgenthal, G. Framework for sensitivity and uncertainty quantification in the flutter assessment of bridges. *Probabilistic Engineering Mechanics*, 43:91–105, 2016.

[283] Cheng, J., Jiang, J.-J., and Xiao, R.-C. Aerostatic stability analysis of suspension bridges under parametric uncertainty. *Engineering Structures*, 25:1675–1684, 2003.

[284] Caracoglia, L. Influence of uncertainty in selected aerodynamic and structural parameters on the buffeting response of long-span bridges. *Journal of Wind Engineering and Industrial Aerodynamics*, 96:327–344, 2008.

[285] Seo, D.-W. *Effects of errors in flutter derivatives on the wind-induced response of cable-supported bridges*. Ph.D. Thesis, Northeastern University, Massachusetts, USA., 2013.

[286] Mannini, C. and Bartoli, G. Uncertainty propagation in bridge flutter analysis. In *The 11th International Conference on Structural Safety and Reliability (ICOSSAR2013), New York City, USA*, 2013.

[287] Mannini, C. and Bartoli, G. Aerodynamic uncertainty propagation in bridge flutter analysis. *Structural Safety*, 52:29–39, 2015.

[288] Jakobsen, J. and Tanaka, H. Modelling uncertainties in prediction of aeroelastic bridge behaviour. *Journal of Wind Engineering and Industrial Aerodynamics*, 91: 1485–1498, 2003.

[289] Ito, M. and Fujino, Y. Probabilistic study of torsional flutter of suspension bridge under fluctuating wind. In *International Association for Structural Safety and Reliability*, volume 3, pages 161–170, 1985.

[290] Argentini, T., A.Pagani, D.Rocchi, and Zasso, A. Monte carlo analysis of total damping and flutter speed of a long span bridge: Effects of structural and aerodynamic uncertainties. *Journal of Wind Engineering and Industrial Aerodynamics*, 128:90–104, 2014.

[291] Seo, D.-W. and Caracoglia, L. Estimation of torsional-flutter probability in flexible bridges considering randomness in flutter derivatives. *Engineering Structures*, 33: 2284–2296, 2011.

[292] Seo, D.-W. and Caracoglia, L. Monte-carlo methods for estimating the buffeting response of a bridge contaminated by flutter-derivative errors. In *The 13th International Conference on Wind Engineering (ICWE13), Amsterdam, The Netherlands*, 2011.

[293] Seo, D. and Caracoglia, L. Lifetime cost analysis of slender bridges due to flutter occurrence using the data of the united states - japan benchmark study on flutter derivatives. In *The 44th Joint Meeting of US-Japan Panel on Wind and Seismic Effects (UJNR), Maryland, USA*, 2013.

[294] Cheng, J. and Xiao, R. Probabilistic free vibration and flutter analyses of suspension bridges. *Engineering Structures*, 27:1509–1518, 2005.

[295] Cheng, J., Cai, C. S., Xiao, R.-C., and Che, S. R. Flutter reliability analysis of suspension bridges. *Journal of Wind Engineering and Industrial Aerodynamics*, 93: 757–775, 2005.

[296] Abbas, T., Kavrakov, I., and Morgenthal, G. Methods for flutter stability analysis of long-span bridges: A review. *Proceedings of the Institution of Civil Engineers: Bridge Engineering*, 2017.

[297] Deeb, M., Abbas, T., Ghorashi, S., Stade, I., Wudtke, I., and Zabel, V. Modellbasierte schadens idetifikation an turmbauwerken (model-based damage idetifikation of tower structures). *Bautechnik, Bewertung gekoppelter numerischer Partialmodelle im konstruktiven Ingenieurbau*, pages 80–89, 2013.

[298] Morgenthal, G., Rau, S., Taraben, J., and Abbas, T. Determination of stay cable forces using highly mobile vibration measurement devices. *Proceedings of the Institution of Civil Engineers: Bridge Engineering*, 2016.

[299] Abbas, T. and Morgenthal, G. Numerical models for flutter stability analysis of long-span bridges. In *The 20th International Conference on the Applications of Computer Science and Mathematics in Architecture and Civil Engineering (IKM2015), Weimar, Germany*, 2015.

[300] Maîytre, O. L., Scanlan, R., and Knio, O. Estimation of the flutter derivatives of an NACA airfoil by means of navier-stokes simulation. *Journal of Fluids and Structures*, 17:1–28, 2003.

[301] Shirai, S. and Ueda, T. Aerodynamic simulation by CFD on flat box girder of super-long-span suspension bridge. *Journal of Wind Engineering and Industrial Aerodynamics*, 91(1):279–290, 2003.

[302] Vairo, G. A numerical model for wind loads simulation on long-span bridges. *Simulation Modelling Practice and Theory*, 11:315–351, 2003.

[303] Diogo, G., Lopes, A. V., and Simões, L. M. C. A CFD based numerical study on aerodynamic characteristics of Pi cross sections using baffle plates. In *The 3rd International Conference on Fluid Structure Interaction, Corunha, Spain*, volume 84, pages 35–44, 2005.

[304] Stærdahl, J. W., Sørensen, N., and Nielsen, S. R. K. Aeroelastic stability of suspension bridges using CFD. In *Symposium of the International Association for Shell and Spatial Structures (IASS), Venice, Italy*, 2007.

[305] Watanabe, S. and Fumoto, K. Aerodynamic study of slotted box girder using computational fluid dynamics. *Journal of Wind Engineering and Industrial Aerodynamics*, 96:1885–1894, 2008.

[306] Kalesar, H. E. and Ali, F. S. Aeroelastic analysis of suspension bridge decks using finite element method. In *The 6th International Colloquium on Bluff Body Aerodynamics and Applications (BBAA6), Milano, Italy*, 2008.

[307] Sarwar, M., Ishihara, T., Shimada, K., Yamasaki, Y., and Ikeda, T. Prediction of aerodynamic characteristics of a box girder bridge section using the les turbulence model. *Journal of Wind Engineering and Industrial Aerodynamics*, 96:1895–1911, 2008.

[308] Sun, D., Owen, J. S., Wright, N. G., and Liaw, K. F. Fluid-structure interaction of prismatic line-like structures, using les and block-iterative coupling. *Journal of Wind Engineering and Industrial Aerodynamics*, 96:840–858, 2008.

[309] Sun, D., Owen, J. S., and Wright, N. G. Application of the k-omega turbulence model for a wind-induced vibration study of 2d bluff bodies. *Journal of Wind Engineering and Industrial Aerodynamics*, 97:77–87, 2009.

[310] Szabó, G. and Györgyi, J. Fluid-structure interaction analysis with the ansys software in bridge aeroelasticity. In *The 5th European and African conference on Wind Engineering (EACWE2009), Florence, Italy*, 2009.

[311] Szabó, G. and Györgyi, J. Three-dimensional fluid-structure interaction analysis for bridge aeroelasticity. In *The World Congress on Engineering and Computer Science (WCECS2009), San Francisco, USA*, 2009.

[312] Huang, L., Liao, H., Wang, B., and Li, Y. Numerical simulation for aerodynamic derivatives of bridge deck. *Simulation Modelling Practice and Theory*, 17:719–729, 2009.

[313] Xin, D., Ou, J., and Li, H. Flutter stability analysis of long-span bridge based on numerical calculation applying dynamic mesh technique. In *The 4th International Symposium on Computational Wind Engineering (CWE2010), Chapel Hill, North Carolina, USA*, 2010.

[314] Bai, Y., Sun, D., and Lin, J. Three dimensional numerical simulations of long-span bridge aerodynamics, using block-iterative coupling and DES. *Computers & Fluids*, 39:1549–1561, 2010.

[315] Szabó, G. and Györgyi, J. Numerical simulation of the flutter performance of different generic bridge cross sections. *Journal of Civil Engineering*, 55(2):137–146, 2011.

[316] Šarkić, A., Fisch, R., Bletzinger, K.-U., and Höffer, R. Bridge flutter derivatives based on computed, validated pressure fields. In *The 13th International Conference on Wind Engineering (ICWE13), Amsterdam, The Netherlands*, 2011.

[317] Šarkić, A., Fisch, R., Höffer, R., and Bletzinger, K.-U. Bridge flutter derivatives based on computed, validated pressure fields. *Journal of Wind Engineering and Industrial Aerodynamics*, 104-106:141–151, 2012.

[318] Liua, X., Chen, Z., and Liu, Z. Direct simulation method for flutter stability of bridge deck. In *The 7th International Colloquium on Bluff Body Aerodynamics and Applications (BBAA7), Shanghai, China*, 2012.

[319] Brusiani, F., Miranda, S., Patruno, L., Ubertini, F., and Vaona, P. On the evaluation of bridge deck flutter derivatives using RANS turbulence models. *Journal of Wind Engineering and Industrial Aerodynamics*, 119:39–47, 2013.

[320] Miranda, S., Patruno, L., Ubertini, F., and Vairo, G. On the identification of flutter derivatives of bridge decks via rans turbulence models: Benchmarking on rectangular prisms. *Engineering Structures*, 76:359–370, 2014.

[321] Ketong, L. and Aiping, T. Numerical investigation for aerodynamic derivatives of bridge deck using des. *The Open Civil Engineering Journal*, 8:326–334, 2014.

[322] Šarkić, A. *Validated numerical simulation of fluid-structure interactions of bridge girders in turbulent wind fields*. Ph.D. Thesis, Ruhr-Universität Bochum, Bochum, Germany, 2014.

[323] Šarkić, A., Höffer, R., and Brčić, S. Numerical simulations and experimental validations of force coefficients and flutter derivatives of a bridge deck. *Journal of Wind Engineering and Industrial Aerodynamics*, 144:172–182, 2015.

[324] Nieto, F., Hargreaves, D., Owen, J., and Hernández, S. On the applicability of 2d urans and sst $k - \omega$ turbulence model to the fluid-structure interaction of rectangular cylinders. *Engineering Applications of Computational Fluid Mechanics*, 9(1):157–173, 2015.

[325] Nieto, F., Owen, J., Hargreaves, D., and Hernández, S. Bridge deck flutter derivatives: Efficient numerical evaluation exploiting their interdependence. *Journal of Wind Engineering and Industrial Aerodynamics*, 136:138–150, 2015.

[326] Patruno, L. Accuracy of numerically evaluated flutter derivatives of bridge deck sections using rans: Effects on the flutter onset velocity. *Engineering Structures*, 89:49–65, 2015.

[327] Larsen, A. and Walther, J. H. A new computational method for assessment of the aeroelastic stability of long span bridges. In *IABSE congress report*, volume 15, 1996.

[328] Walther, J. H. and Larsen, A. Two dimensional Discrete Vortex Method for application to bluff body aerodynamics. *Journal of Wind Engineering and Industrial Aerodynamics*, 67-68:183–193, 1997.

[329] Larsen, A. and Walther, J. H. A two dimensional Discrete Vortex Method for bridge aerodynamics applications. *Journal of Wind Engineering and Industrial Aerodynamics*, 67-68:183–193, 1997.

[330] Morgenthal, G. Comparison of numerical methods for bridge-deck aerodynamics. MPhil Thesis, University of Cambridge, 2000.

[331] Zhou, Z., Chen, A., and Xiang, H. Identification of aeroelastic parameter of flexible bridge decks by random Discrete Vortex Method. In *The 11th International Conference on Wind Engineering (ICWE11), Lubbock, Texas, USA*, 2003.

[332] Janjic, D., Stampler, J., and Domaingo, A. Software tool for wind design of cable stayed bridges. In *Structures Congress*, pages 1–10, 2008.

[333] McRobie, A., Morgenthal, G., Abrams, D., and Prendergast, J. Parallels between wind and crowd loading of bridges. *Philosophical Transactions of the Royal Society A*, 371:1–17, 2013.

[334] Matsumoto, M., Shiraishi, N., Shirato, H., Shigetaka, K., and Niihara, Y. Aerodynamic derivatives of coupled/hybrid flutter of fundamental structural sections. *Journal of Wind Engineering and Industrial Aerodynamics*, 49:575–584, 1993.

[335] Iwamoto, M. and Fujino, Y. Identification of flutter derivatives of bridge deck from free vibration data. *Journal of Wind Engineering and Industrial Aerodynamics*, 54-55:55–63, 1995.

[336] Brownjohn, J. and Jakobsen, J. B. Strategies for aeroelastic parameter identification from bridge deck free vibration data. *Journal of Wind Engineering and Industrial Aerodynamics*, 89:1113–1136, 2001.

[337] Chen, A., He, X., and Xiang, H. Identification of 18 flutter derivatives of bridge decks. *Journal of Wind Engineering and Industrial Aerodynamics*, 90:2007–2022, 2002.

[338] Chen, C.-H., Wu, J.-C., and Chen, J.-H. Prediction of flutter derivatives by artificial neural networks. *Journal of Wind Engineering and Industrial Aerodynamics*, 96:1925–1937, 2008.

[339] Piña, R. B. and Caracoglia, L. Extraction of flutter derivatives from small-scale wind tunnel experiments. In *The 11th American Conference on Wind Engineering (ACWE11), San Jaun, Puerto Rico*, 2009.

[340] Hunyadi, M. Flutter analysis of an extradosed bridge in hungary. In *The 5th European and African conference on Wind Engineering (EACWE2009), Florence, Italy*, 2009.

[341] Boonyapinyo, V. and Janesupasaeree, T. Identification of flutter derivatives of bridge decks in wind tunnel test by stochastic subspace identification. *American Jounal of Engineering and Applied Sciences*, 2(2):304–316, 2009.

[342] Boonyapinyo, V., Janesupasaeree, T., and Thamasungkeeti, W. Identification of flutter derivatives of bridge decks by stochastic subspace method. In *The 7th Asia-Pacific Conference on Wind Engineering (APCWE7), Taipei, Taiwan*, 2009.

[343] Bartoli, G., Contri, S., Mannini, C., and Righi, M. Toward an improvement in the identification of bridge deck flutter derivatives. *Journal of Engineering Mechanics*, 135(8):771–785, 2009.

Publications by the Author

Abbas, T. and Morgenthal, G. Framework for sensitivity and uncertainty quantification in the flutter assessment of bridges. *Probabilistic Engineering Mechanics*, 43:91–105, 2016

Abbas, T., Kavrakov, I., and Morgenthal, G. Methods for flutter stability analysis of long-span bridges: A review. *Proceedings of the Institution of Civil Engineers: Bridge Engineering*, 2017 (accepted)

Deeb, M., Abbas, T., Ghorashi, S., Stade, I., Wudtke, I., and Zabel, V. Modellbasierte schadens idetifikation an turmbauwerken (model-based damage idetifikation of tower structures). *Bautechnik, Bewertung gekoppelter numerischer Partialmodelle im konstruktiven Ingenieurbau*, pages 80–89, 2013

Morgenthal, G., Rau, S., Taraben, J., and Abbas, T. Determination of stay cable forces using highly mobile vibration measurement devices. *Proceedings of the Institution of Civil Engineers: Bridge Engineering*, 2016 (submitted)

Abbas, T. and Morgenthal, G. Model combinations for assessing the flutter stability of suspension bridges. In *The 19th International Conference on the Applications of Computer Science and Mathematics in Architecture and Civil Engineering (IKM2012), Weimar, Germany*, 2012

Abbas, T. and Morgenthal, G. Hybrid models for assessing the flutter stability of suspension bridges. In *The 7th International Colloquium on Bluff Body Aerodynamics and Applications (BBAA7), Shanghai, China*, 2012

Abbas, T. and Morgenthal, G. Quantification of the effects of turbulence in wind on the flutter stability of suspension bridges. In *The 6th European and African conference on Wind Engineering (EACWE2013), Cambridge, UK*, 2013

Abbas, T. and Morgenthal, G. Quantification of the effects of turbulence in wind on the Vortex-induced Vibrations. In *The 36th Symposium of the International Association for Bridge and Structural Engineering (IABSE2014), Kolkata, India*, 2013

Abbas, T. and Morgenthal, G. Quantification of the effects of turbulence in wind on the aeroelastic behaviour of suspension bridges. In *Der 13. Dreiländertagung der Windtechnologischen Gesellschaft (WtG2013), Wien*, 2013

Abbas, T. and Morgenthal, G. Numerical models for flutter analysis. In *The 6th International Symposium on Computational Wind Engineering (CWE2014), Hamburg, Germany*, 2014

Abbas, T. and Morgenthal, G. Assessment of the flutter stability of bridges using a probabilistic approach. In *The 12th International Probabilistic Workshop (IPW12), Weimar, Germany*, 2014

Abbas, T. and Morgenthal, G. Numerical models for flutter stability analysis of long-span bridges. In *The 20th International Conference on the Applications of Computer Science and Mathematics in Architecture and Civil Engineering (IKM2015), Weimar, Germany*, 2015

Appendix A
Methods of Aerodynamic Analysis

Chapter 4 explains the methods of aerodynamic analysis. Section 4.3.3 of this chapter focuses on the numerical methods in general where commonly used CFD approach have been listed. Table A.1 and A.2 provide some of the studies made on different study objects with the help of these approaches. Table A.3 shows the selected studies based on the vortex method.

Section 4.4 discusses the determination of aerodynamic derivatives from different methods. Table A.4 provides wind tunnel tests performed to obtain aerodynamic derivatives by using free, forced and buffeting response. The forceed vibration tests were performed in this dissertation therefore, Table A.5 provides amplitudes of oscillations considered for forced vibration tests conducted for different structures.

Table A.1: Different CFD approaches based on FVM and FEM used to study aerodynamic phenomena (F: Flutter limit, D: Aerodynamic derivative, C: Static wind coefficients, P: Pressure, R: Reynolds number dependence).

Structure	Phenomena	Reference
NACA-0012	D, R	[300]
Rectangular, B/D=8	D	[238]
Great Belt, 200mm	D	[239]
Millau Viaduct, 200mm	D	[239]
Tacoma Narrows, 200mm	D	[239]
Slotted rectangular, 450mm	P, D	[301]
Slotted flat box, 370mm	P, D	[301]
Great Belt	C, D	[302]
Normandy	C, D	[302]
π-sec with B/D=6	A_2^*	[303]
Great Belt	D	[304]
Hume, 445×33.4mm	D, F	[142]
Slotted box girder	C	[305]
Great Belt	F	[306]
Tacoma	F	[306]
Box girder, $B/D = 11.6$	C, D, F	[307]
Rectangular, $B/D = 4$	C, D	[308]
Rectangular, $B/D = 4$	C, D	[309]
Flat plate	D	[310]
Bridge section	D	[310]
Incheon, 200×30mm	D	[311]
Nine bridge decks, 200mm	D, R	[111]
Five bridge sections	D	[312]
Hume, 445×33.4mm	D, F	[313]

Table A.2:   Different CFD approaches based on FVM and FEM used to study aerodynamic phenomena (F: Flutter limit, D: Aerodynamic derivative, C: Static wind coefficients, P: Pressure, R: Reynolds number dependence).

Structure	Phenomena	Reference
Circular cylinder	C	[266]
Great Belt, 375×54.7mm	D	[266]
NACA0012	C, D	[314]
U-shape, G1, G2	C, D	[314]
Four generic sections	C, D, L	[315]
Thin flat plate, 700×3.5mm	D	[138]
2nd Nanjing Yangtze, 772×63mm	D	[138]
Bridge deck, 369×60mm	P, C, D	[316]
Bridge deck, 366×66mm	P, C, D	[317]
Rectangular, 300×60mm	F	[318]
Streamlined, 404×60mm	F	[318]
Great Belt, 31×4.34m	D, F	[103]
Circular cylinder	C	[319]
Great Belt, 375×54.7mm	D	[266]
R-5, 8, 10, 12.5, 15, 20	C, D, F	[320]
Flat plate, 1000×10mm	P, D	[321]
Great Belt, 31×4.4m	P, D	[321]
Bridge deck, 366×66mm	P, C, D	[322]
Bridge deck, 366×66mm	P, C, D	[323]
Rectangular cylinder, B/D=4	C, D	[324]
Rectangular cylinder, B/D=4.9	C, D	[325]
G1 section	C, D	[325]
Six deck sections, 366×66mm	R, C, D, F	[326]

Table A.3: Different CFD approaches based on vortex method used to study aerodynamic phenomena (F: Flutter limit, D: Aerodynamic derivative, C: Static wind coefficients, P: Pressure, R: Reynolds number dependence).

Structure	Phenomena	Reference
Great Belt, 31000×4337mm	P, C, D, F	[118]
Great Belt	D, F	[327]
Flat plate, $B/D==200$	D	[328]
Tacoma Narrows, 12×2.4m	C, D	[117, 329]
Great Belt, 31×4.4	C, D	[117, 329]
Approach span, 25.8×7m	C, D	[117, 329]
Gibraltar APP, 65×2.5m	C, D	[117]
Five generic sections, G1-G5	C, D	[141]
Five generic sections, G1-G5	C, D	[34]
Great Belt, 31×4m	D, F	[330]
Flat plate, $B/D=100$	D, F	[128]
Millau Viaduct, 388×60.2mm	D, F	[128]
Great Belt, 31×4m	C, D	[243]
H-shaped	C	[119]
Humen and Great Belt	C	[331]
Nanjing and Runyang	C	[331]
Jinsha	D, F	[331]
Tacoma Narrows	C, A_2^*	[56]
Stonecutters	C, D, F	[332]
Tacoma Narrows	A_2^*	[333]

Table A.4: Wind tunnel tests performed for different structures to obtain aerodynamic derivatives.

Structure	Size $B \times D$ [mm] $(B/D$ [-])	Response	Reference
Rectangular	200×20	Coupled-Forced	[334]
Rectangular	200×10	Coupled-Forced	[334]
Box girder	292.7×33.7	Free	[335]
Flat plate	450×20	Free	[92]
Jiangyin, 1:70	36.9×3.0m	Free	[92]
Streamlined	-	Free, Buffeting	[336]
Dual carriageway	-	Free, Buffeting	[336]
Plate, 2DOF, 3DOF	460×45	Free	[337]
Streamlined box	450×32	Free	[337]
P-shaped	452×46	Free	[337]
NACA-0020, 3DOF	314	Free	[265]
Chamfered plate	(25)	Forced	[137]
Rectangle	(5,8,10,12.5,15,20)	Free	[338]
NACA-0020	456	Forced	[139]
Tacoma Narrows	411×82	Forced	[139]
Strelasund	324×103	Forced	[139]
Model A, 1:250	123×13	Free, Forced	[339]
Model B, 1:500	61.33×6.35	Free, Forced	[339]
Extradosed, 1:100	295.4	Forced	[340]
Flat plate	450×20	Free	[341]
Industrial-Ring-Road	399×35	Free	[341]
Industrial-Ring-Road	399×35	Free	[342]
Fairing-modified, 1:90	399×35	Free	[342]
Soffit plate modified	399×35	Free	[342]
Combination of two	399×35	Free	[342]
Single-box	450×70	Free	[343]
Multiple-box girder	609×52	Free	[343]
Great Belt, 1:60	31×4m	Free	[140]
Sutong	812	Free	[263]
Suramadu	600	Free	[263]
Flat plate	-	Free	[136]
Sutong	41×4m	Free	[136]
Stonecutters	53.3×4m	Free	[136]
Akashi-Kaikyo	35.5×14m	Free	[136]

Table A.5: Amplitudes of heave and pitch used for forced vibration tests.

Structure	Size $B \times D$ [mm] (B/D [-])	Heave amplitude h_o/B [-] (h_o [mm])	Pitch amplitude α_o [°]	Reference
Rectangular	200×20	$h_o/\alpha_o = 0.0637$		[334]
Rectangular	200×10	$h_o/\alpha_o = 0.1408$		[334]
Great Belt	31000	0.05	5	[118]
Five generic	-	0.05	3	[34],
sections, G1-G5	-	0.05	3	[141]
Flat plate	(100)	0.50	3	[128]
Great Belt	200	0.04	5	[239]
Tacoma Narrows	200	0.04	5	[239]
Rectangular	200	0.04	5	[239]
Rectangular	200 (8)	0.04	8	[238]
Great Belt	200	0.04	8	[238]
Millau Viaduct	200	0.04	8	[238]
Tacoma Narrows	200	0.04	8	[238]
π-section	12000×2000	-	1.72	[303]
Thin plate	40000(100)	(100)	3	[84]
H-shape	11900	(100)	3	[84]
Great Belt	31000	(100)	3	[84]
PWRI	-	0.01	1	[280]
ISU	300	0.05	2.8	[280]
Rectangular	(2-5)	0.01-0.20	2.8	[280]
Nine bridge decks	200	0.01, 0.02, 0.04	2, 5, 8	[111]
Model A, 1:250	123×13	(0.5-1.49)	1.77-2.35	[339]
Model B, 1:500	61.33×6.35	(5-6)	3.43	[339]
Thin flat plate	700×3.5	(2.5-6.12)	0.35-0.86	[138]
2nd Nanjing Yangtze	772×63	(2.5-5.59)	0.40-0.89	[138]
Great Belt East, 1:60	31000×4000	(16)	2	[140]
Bridge Section	369.5×60.6	(4)	1	[316]
Bridge Section	366×66.6	(4)	1	[317]
Bridge Section	366×66.6	(4)	1	[322]
Bridge Section	366×66.6	(4)	1	[323]

Appendix B
Models for Flutter Analysis

Section 5.6.4.2 discusses SDOF torsional instability. Scanlan's form of aerodynamic derivatives is commonly used; however, representation of motion-induced forces Starossek [61] in complex form are also used sometimes. The SDOF torsional instability limit can be determined using complex representation in the following section.

B.1 Pure Torsional Motion in Complex Form

In complex form the areoelastic instability in torsional motion is shown as follows:

$$c''_{\alpha\alpha} = g_\alpha \left(\frac{I}{\pi\rho b^4} + c'_{\alpha\alpha} \right), \tag{B.1}$$

$$\mu_\gamma = \frac{m}{\pi\rho b^2}, \qquad r = \sqrt{I/M} \tag{B.2}$$

$$g_\alpha = 2\xi_\alpha, \tag{B.3}$$

$$U_{cr} = \frac{\omega_\alpha b}{k \left(c''_{\alpha\alpha} = g_\alpha \mu_\gamma r^2 \right)}. \tag{B.4}$$

Appendix C

Flutter Analysis of Reference Objects

Chapter 6 provides the application of models presented in Chapter 5 on the reference objects. Some details of the analyses made on the reference objects are presented here.

C.1 Specifications of Computer used for VXflow Simulations

The system used to run the VXflow simulations has the following specifications:

- Processor: Intel Core i7-2600K 3.4GHz
- RAM: DDR3-1600 16GB
- Cache: 8MB
- Operating System: Ubuntu
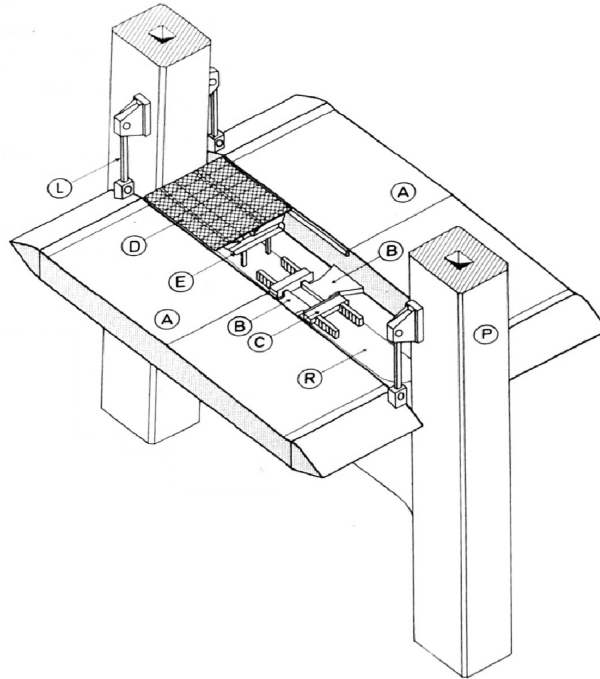
Figure C.1: Isometric view of bearing arrangement, and arrangements of joints in bridge deck at main tower of the Lillebælt suspension bridge.
A: Stiffening box girder,
B: Bracket for wind bearing,
C: Wind bearing support,
D: Expansion joint on bridge deck,
E: Support for expansion joint,
L: Pendulum bearing,
P: Main tower,
R: Main tower portal beam
(cf. Section 6.3) [33].

Table C.1: Modal properties from finite element model of the Lillebælt Suspension Bridge (Mode 1 to 30) (cf. Table 6.3)
(V: vertical, H: horizontal, T: torsional, S: symmetrical, A: unsymmetrical).

Mode	Circular frequency	Frequency	Period	Damping ratio	Modal mass	Mode type
#	[rad/s]	[Hz]	[s]	[%]	[t]	
1	0.982	0.156	6.40	1.0	4599	VS
2	1.010	0.161	6.22	1.0	4218	VA
3	1.303	0.207	4.82	1.0	4308	VA side span
4	1.805	0.287	3.48	1.0	3505	HS
5	1.845	0.294	3.41	1.0	3032	VS
6	2.893	0.460	2.17	1.0	3379	VA
7	3.068	0.488	2.05	1.0	4488	VS side span
8	3.142	0.500	2.00	1.0	7342	TS
9	3.518	0.560	1.79	1.0	18041	TA
10	4.173	0.664	1.51	1.0	3873	VA side span
11	4.233	0.674	1.48	1.0	4601	VS
12	4.257	0.678	1.48	1.0	3429	VS side span
13	4.286	0.682	1.47	1.0	2576	VA side span
14	4.946	0.787	1.27	1.0	2506	TS+Tower rotation
15	4.960	0.789	1.27	1.0	8723	Tower long A
16	4.988	0.794	1.26	1.0	9364	TS+Tower long S
17	5.479	0.872	1.15	1.0	11835	VS+Tower tran A
18	5.676	0.903	1.11	1.0	3866	VA
19	6.087	0.969	1.03	1.0	8018	VS+Tower tran A
20	6.480	1.031	0.97	1.0	2322	TA
21	7.010	1.116	0.90	1.0	4258	HA+TA
22	7.457	1.187	0.84	1.0	3300	VS
23	8.019	1.276	0.78	1.0	1767	TS side span
24	8.191	1.304	0.77	1.0	3035	VS side span
25	8.195	1.304	0.77	1.0	3037	VA side span
26	8.235	1.311	0.76	1.0	1870	TA side span
27	8.738	1.391	0.72	1.0	1720	TS+Cable mode
28	9.149	1.456	0.69	1.0	4691	VA
29	9.774	1.556	0.64	1.0	11123	Tower long S
30	10.217	1.626	0.62	1.0	8160	VA

Table C.2: Modal properties from finite element model of the Lillebælt Suspension Bridge (Mode 31 to 50) (cf. Table 6.3)
(V: vertical, H: horizontal, T: torsional, S: symmetrical, A: unsymmetrical).

Mode	Circular frequency	Frequency	Period	Damping ratio	Modal mass	Mode type
#	[rad/s]	[Hz]	[s]	[%]	[t]	
31	10.355	1.648	0.61	1.0	3585	HS side span
32	10.357	1.648	0.61	1.0	3599	HA side span
33	11.298	1.798	0.56	1.0	2775	VS
34	11.401	1.814	0.55	1.0	13907	Tower tran S+TS side span
35	11.423	1.818	0.55	1.0	13969	Tower tran A+TA side span
36	11.582	1.843	0.54	1.0	1643	TA
37	13.100	2.085	0.48	1.0	2614	VA+VA side span
38	13.155	2.094	0.48	1.0	2142	VS side span
39	13.479	2.145	0.47	1.0	2844	VA
40	14.163	2.254	0.44	1.0	1355	TS side span
41	14.164	2.254	0.44	1.0	1350	TA side span
42	14.298	2.276	0.44	1.0	14632	Tower tran S+VS side span
43	14.330	2.281	0.44	1.0	16379	Tower tran A+VA side span
44	14.418	2.295	0.44	1.0	5059	HS
45	14.570	2.319	0.43	1.0	1663	TS
46	15.539	2.473	0.40	1.0	1560	VS
47	16.613	2.644	0.38	1.0	13979	HA+Tower long
48	17.578	2.798	0.36	1.0	1639	TA
49	17.906	2.850	0.35	1.0	9567	HS
50	18.029	2.869	0.35	1.0	1297	VA
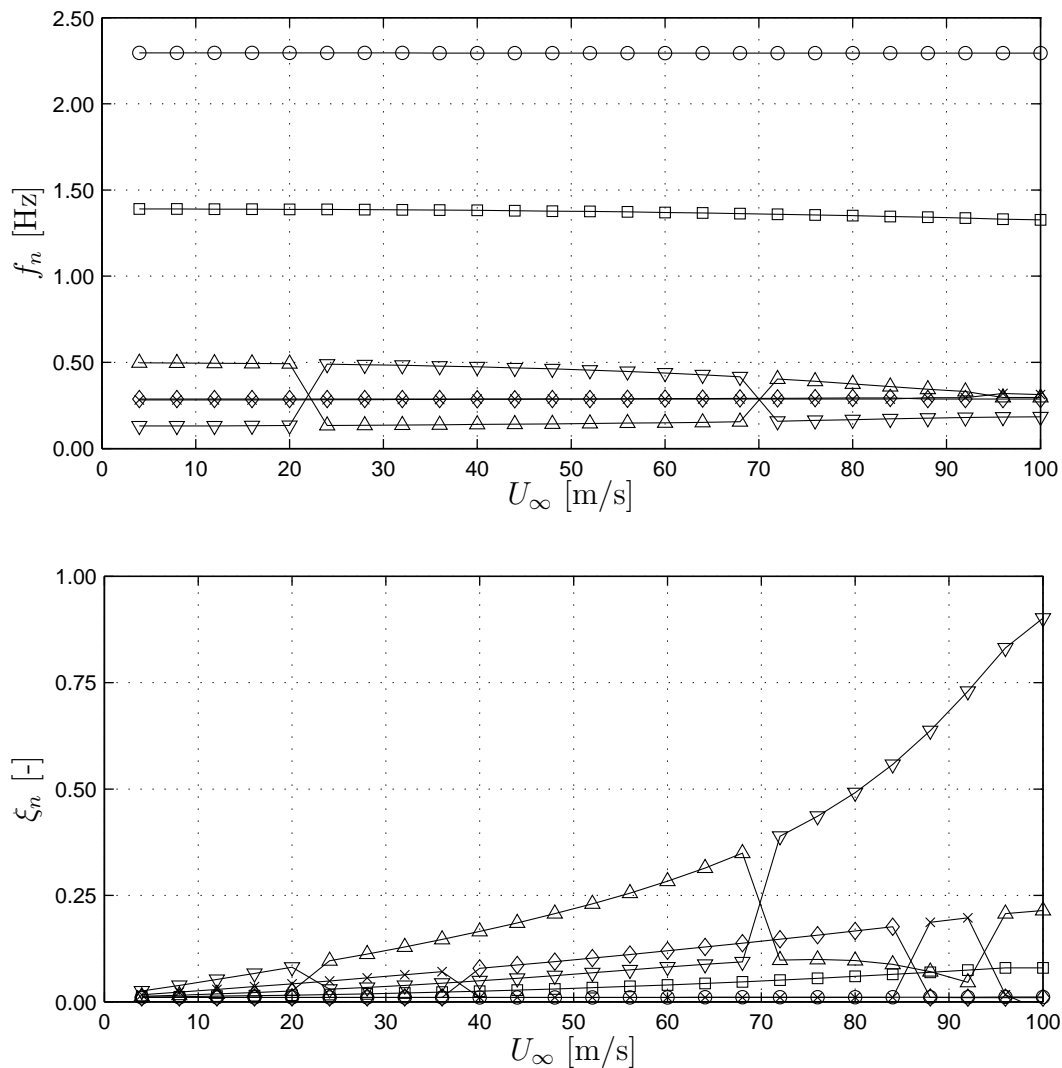
Figure C.2: Derivative-based eigenvalue analysis: multimode flutter analysis for the Lillebælt Suspension Bridge using analytical aerodynamic derivatives with unsorted eigenvalues:
(top) effective frequencies,
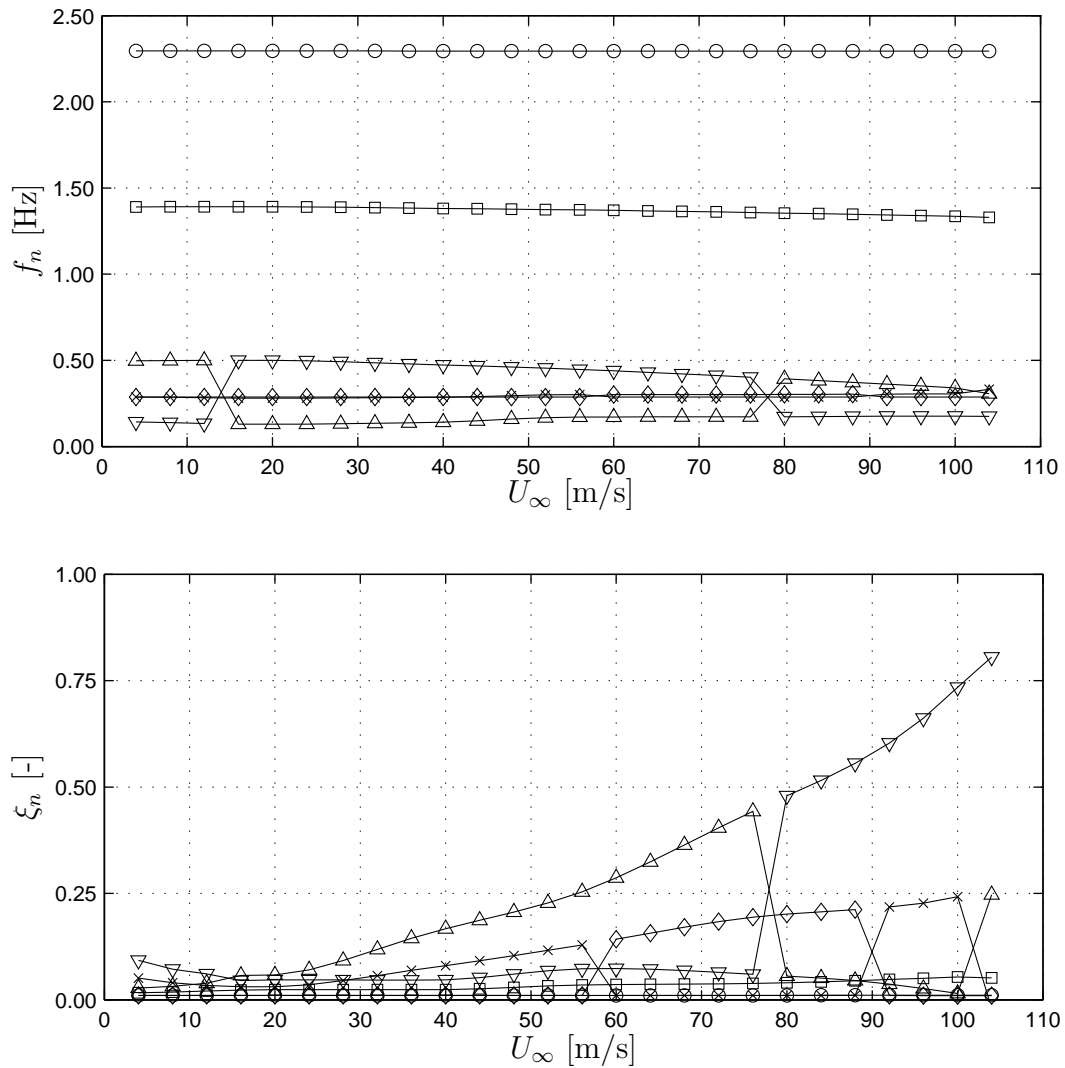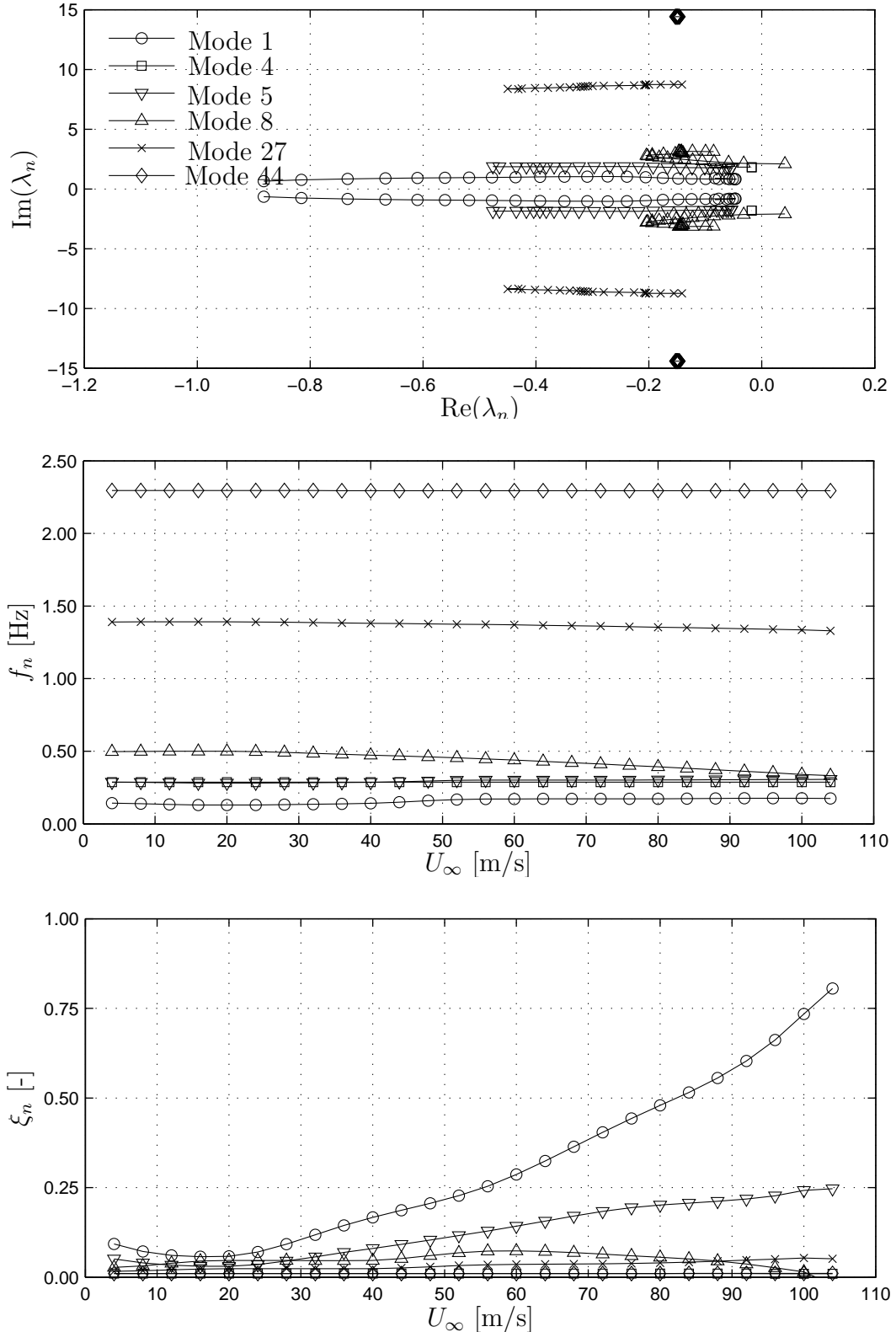(bottom) effective damping ratios (cf. Section 6.5.3).

Figure C.3: Derivative-based eigenvalue analysis: multimode flutter analysis for the Lillebælt Suspension Bridge using CFD aerodynamic derivatives for Structure A with unsorted eigenvalues:
(top) effective frequencies,
(bottom) effective damping ratios (cf. Section 6.5.3).

Figure C.4: Derivative-based eigenvalue analysis: multimode flutter analysis for the Lillebælt Suspension Bridge using CFD aerodynamic derivatives for Structure A:
(top) eigenvalue paths λ_n as wind speed U_∞ increases to the instability limit
(middle) effective frequencies f_n,
(bottom) effective damping ratios ξ_n,
(mode combination V, start U_∞=1 m/s, ΔU_∞=0.5 m/s, U_{cr}=101.0 m/s)
(cf. Section 6.5.3).
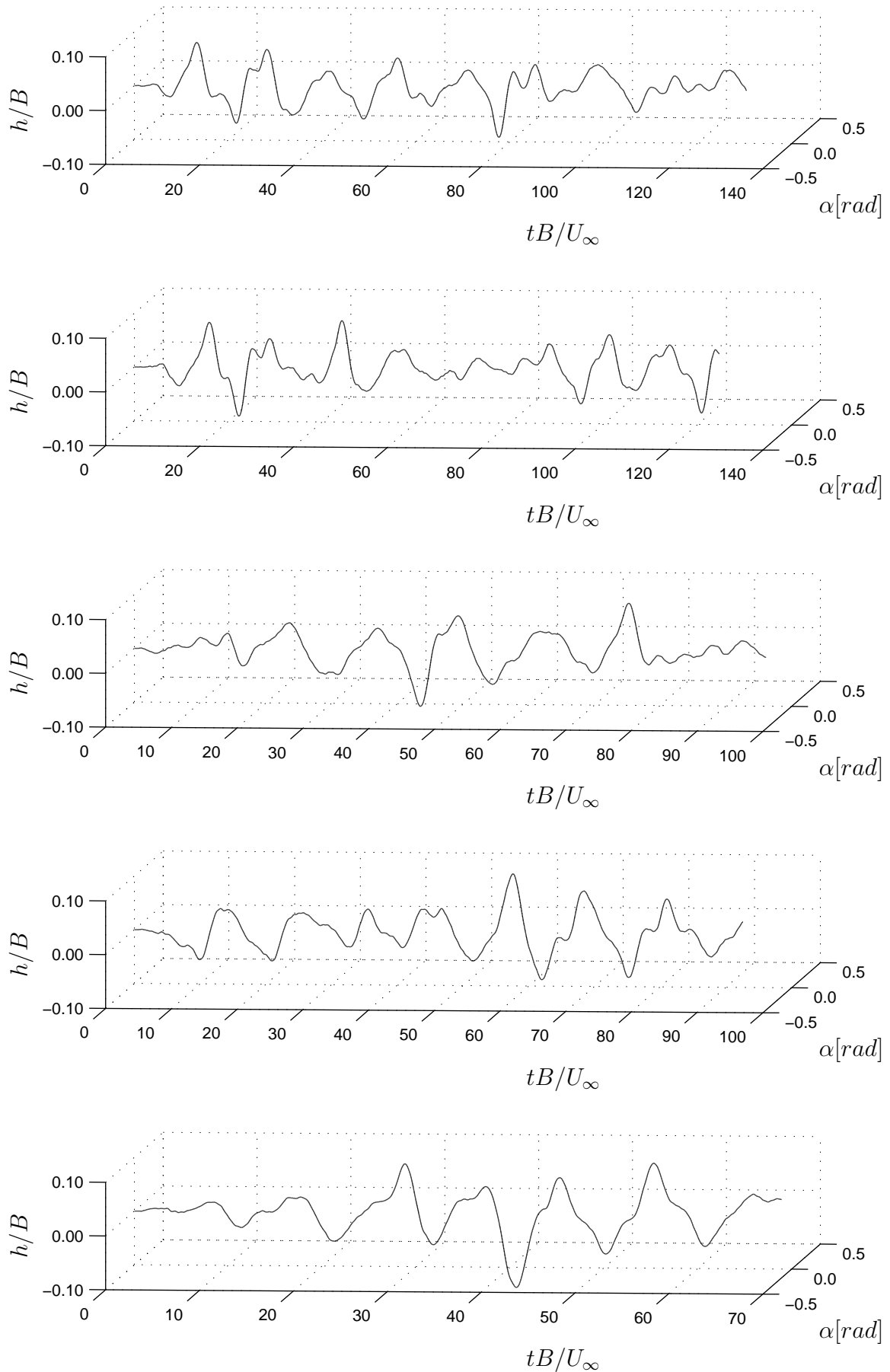
Figure C.5: Fully-coupled CFD simulations: response of Structure H from single slice 2D simulations at wind speeds considering only heave DOF
(top to bottom) U_∞=16-20 m/s (cf. Section 6.5.5).
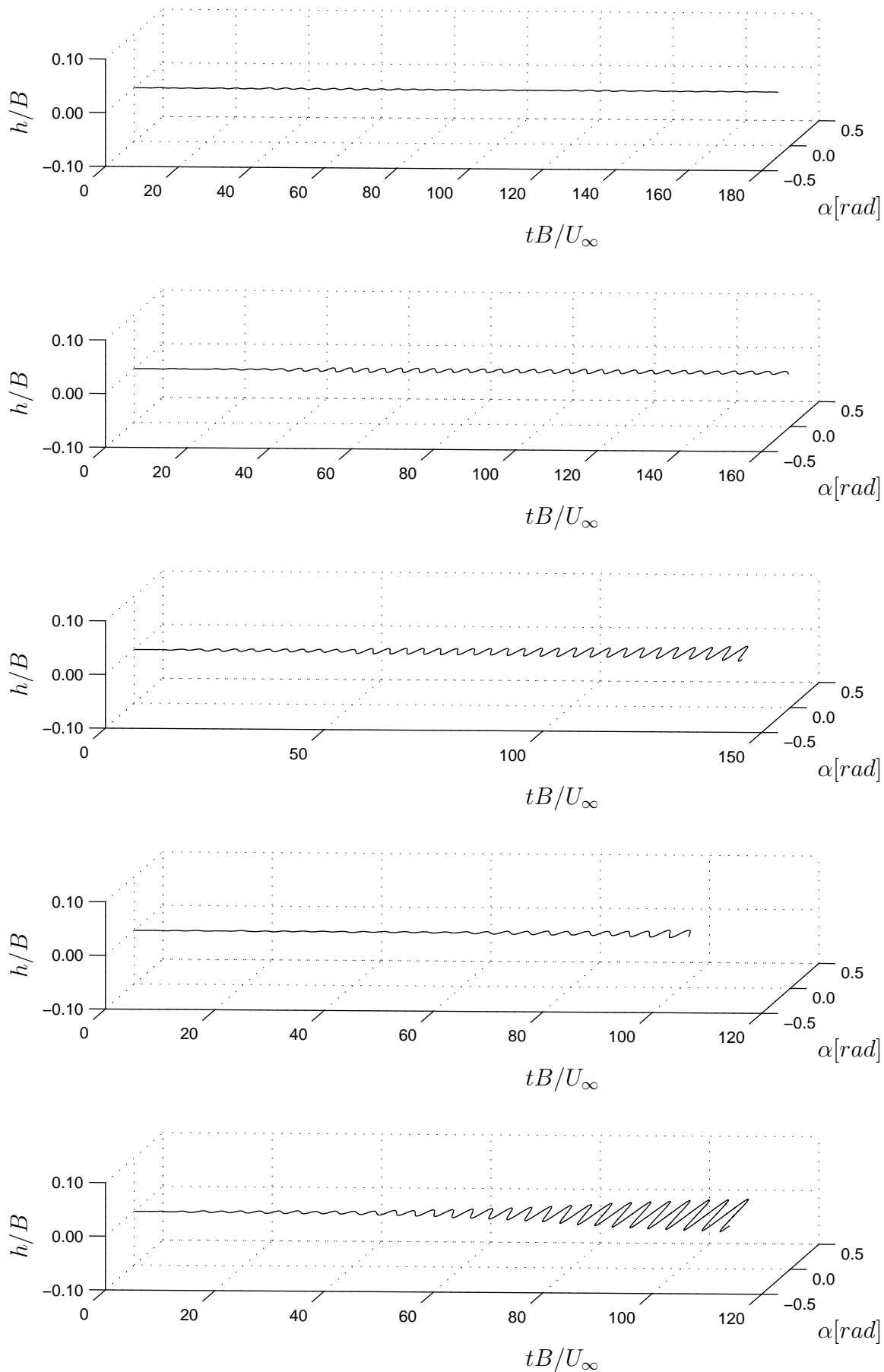
Figure C.6: Fully-coupled CFD simulations: response of Structure H from single slice 2D simulations at wind speeds considering only pitch DOF
(top to bottom) U_∞=14-18 m/s (cf. Section 6.5.5).

Appendix D

Sensitivity of Flutter Limit to Different Parameters

Chapter 7 focuses on the sensitivity of parameters to flutter limit. This appendix shows the aerodynamic derivatives determined from forced vibration simulations corresponding to these studies.
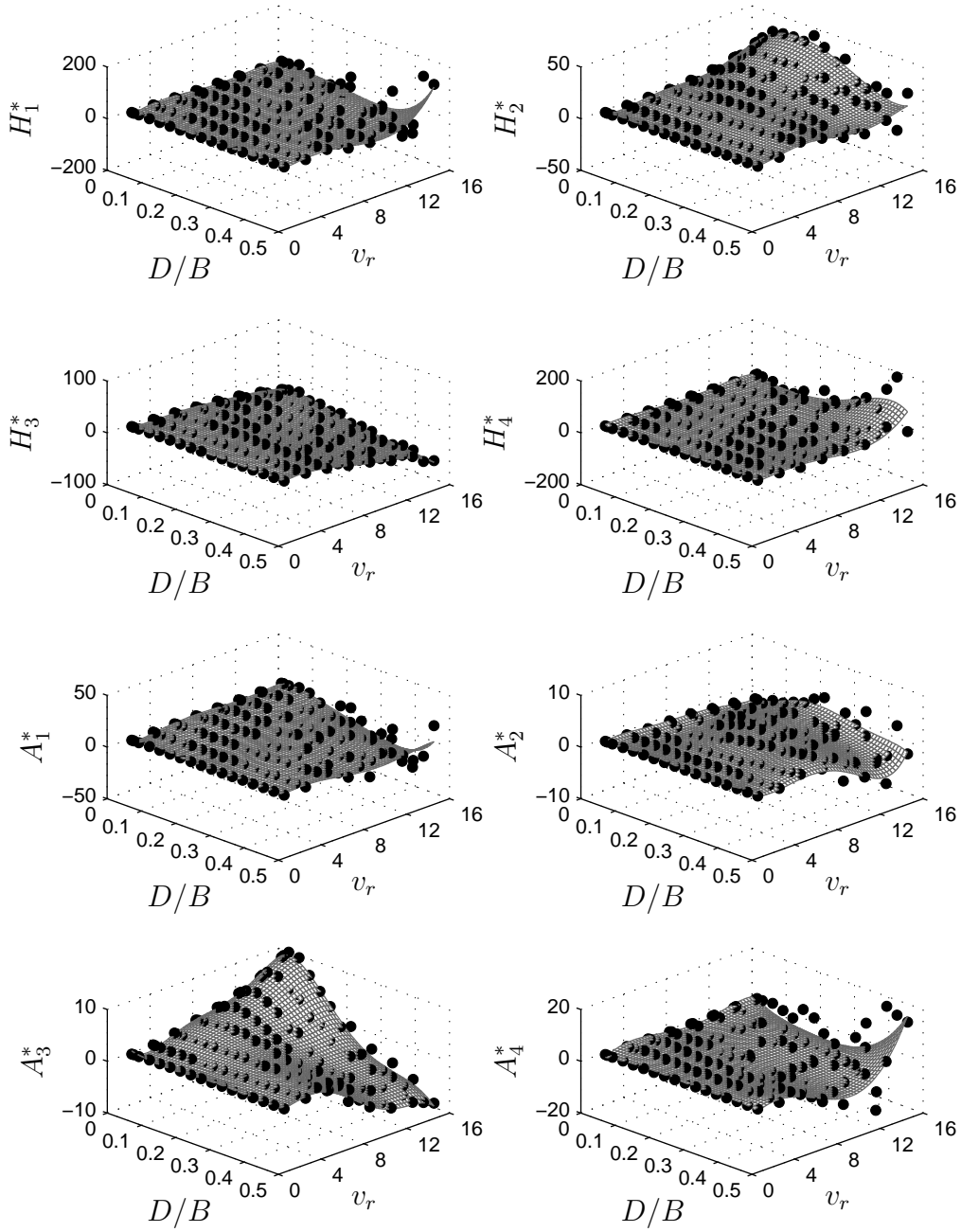
Figure D.1: Response surface fitting for aerodynamic derivatives of rectangular section with changing aspect ratio: fitted surface by polynomial functions of 5° and (•) actual aerodynamic derivatives (cf. Figure 7.7).
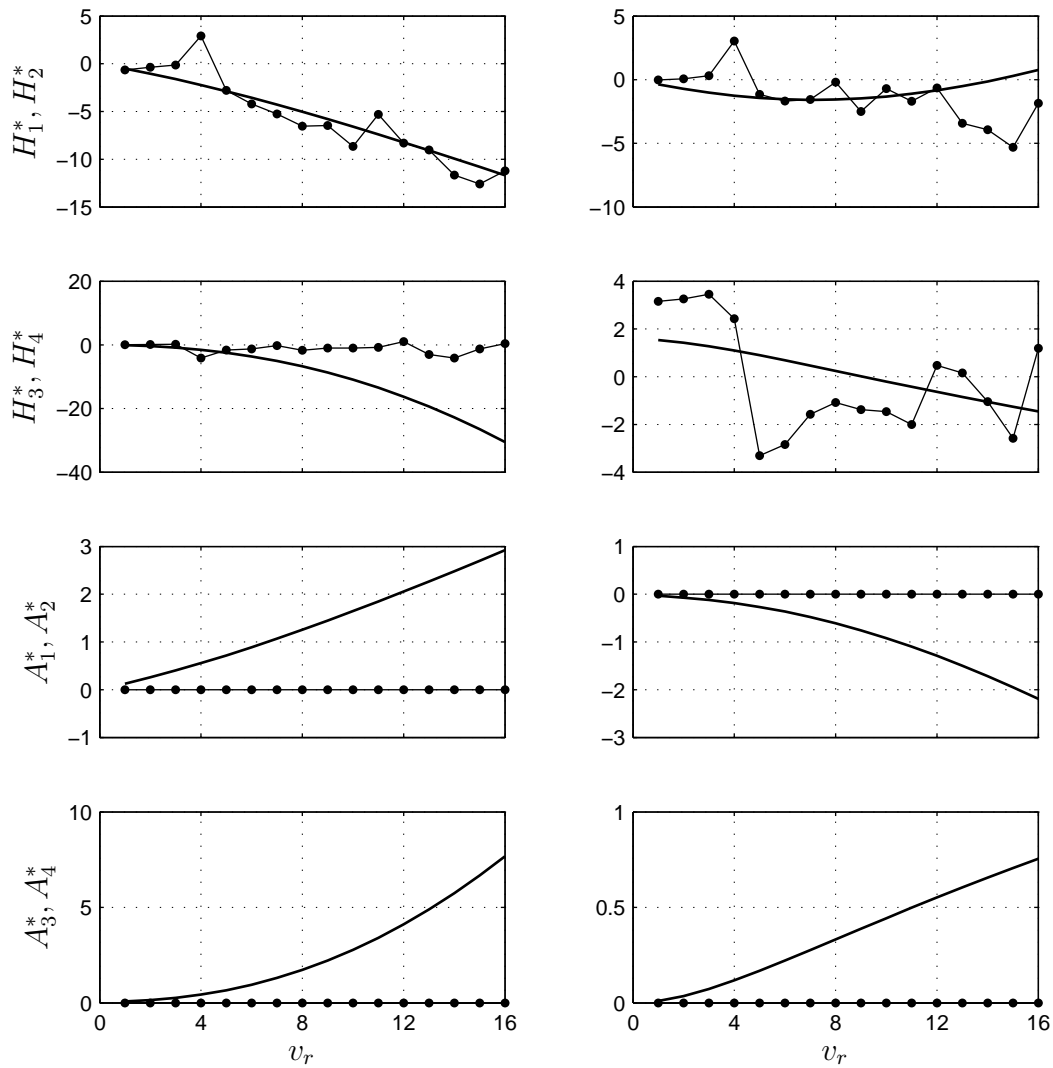
Figure D.2: Aerodynamic derivatives for a circular section:
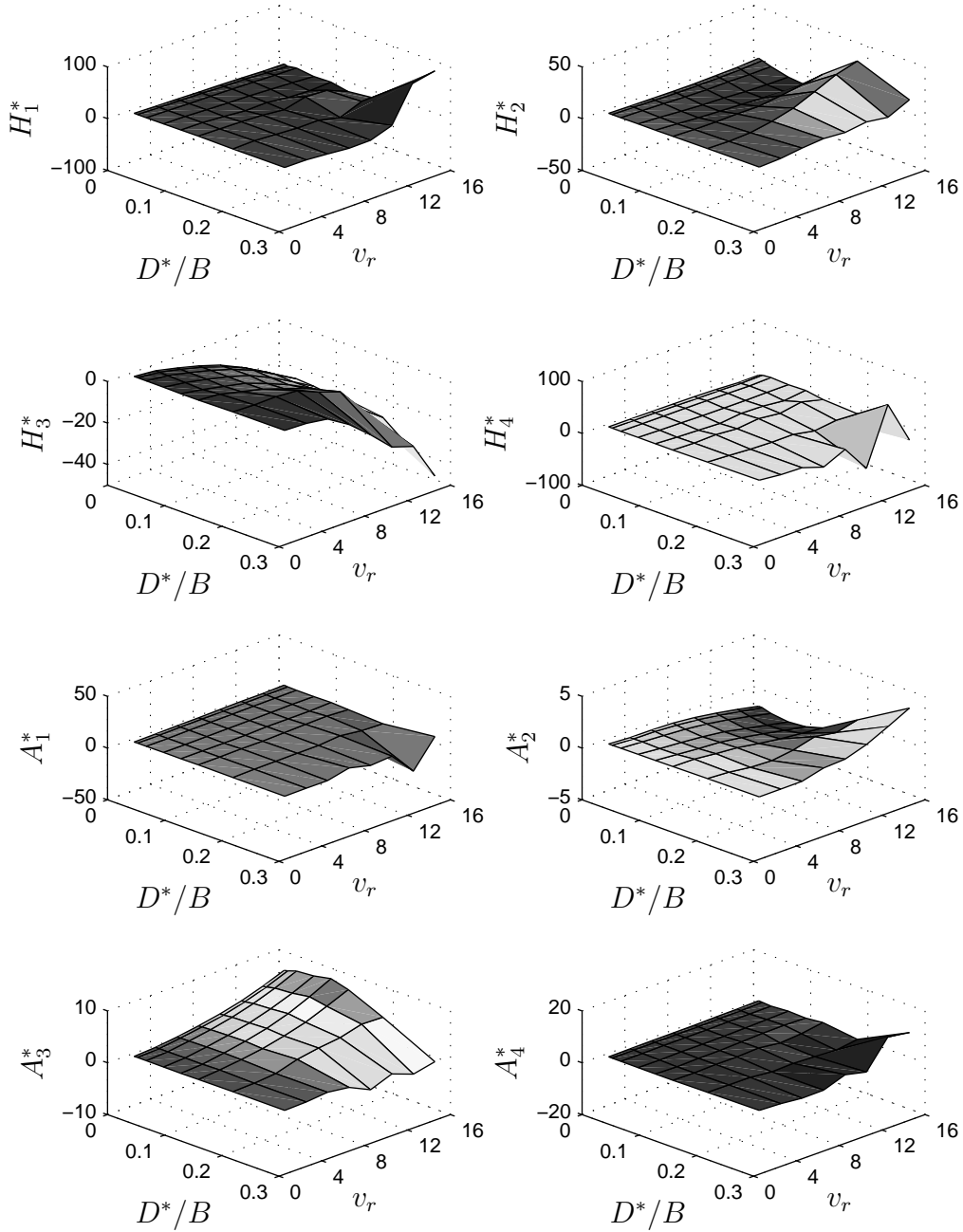(——) Theodorsen theory,
(—•—) forced vibration analysis (cf. Section 7.3.4).
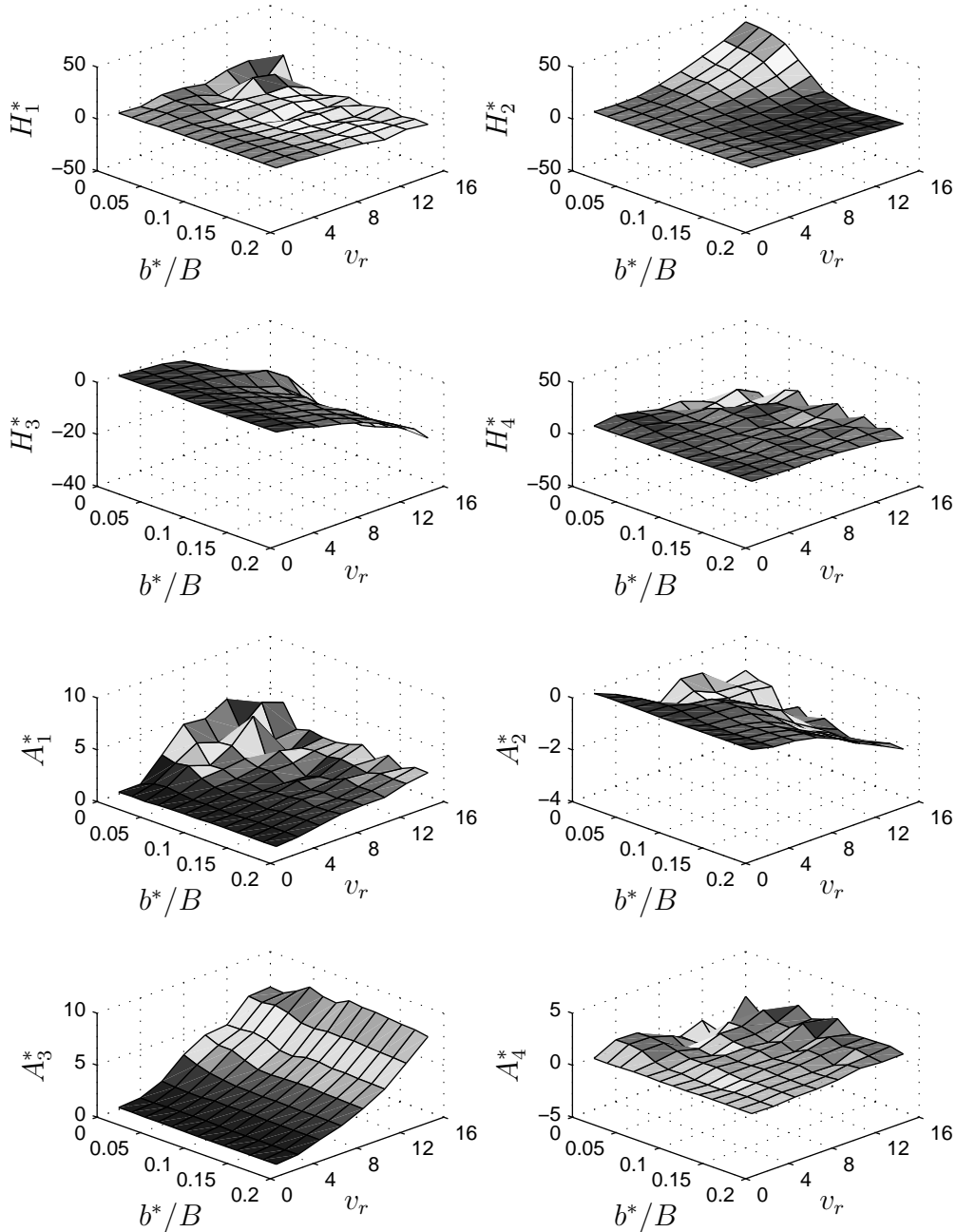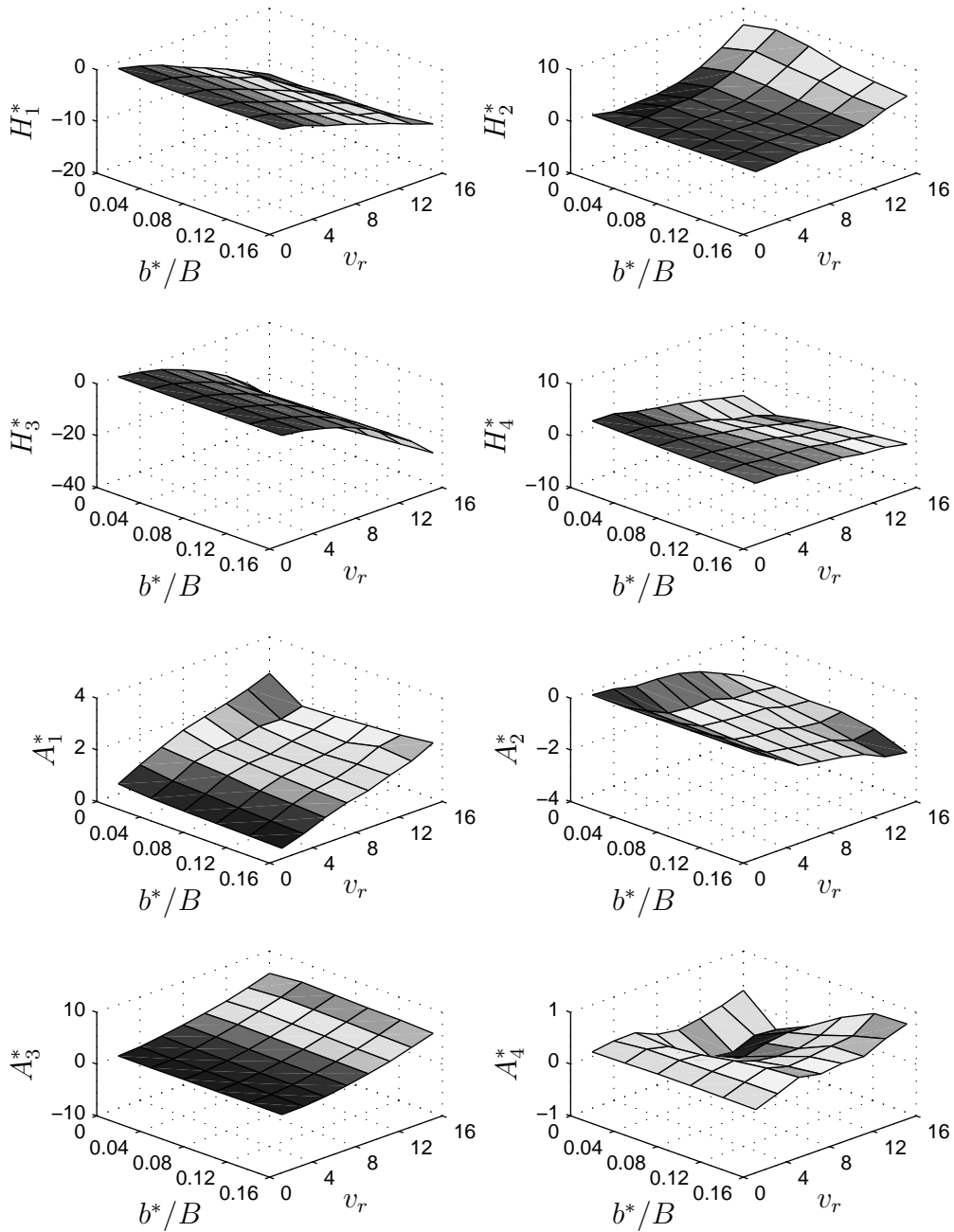
Figure D.3: Sensitivity of flutter limit to section geometry: aerodynamic derivatives from forced vibration simulations on a rectangular section with increasing fairing slope ($b^*/B = 0 - 0.18$) (cf. Figure 7.10).

Figure D.4: Sensitivity of flutter limit to section geometry: aerodynamic derivatives from forced vibration simulations on a streamlined section with increasing depth ($D^*/B = 0.01 - 0.3$) (cf. Figure 7.10).

Figure D.5: Sensitivity of flutter limit to section geometry: aerodynamic derivatives from forced vibration simulations on a plate with increasing central slot ($b^*/B = 0 - 0.15$, $B/D = 100$) (cf. Figure 7.12).
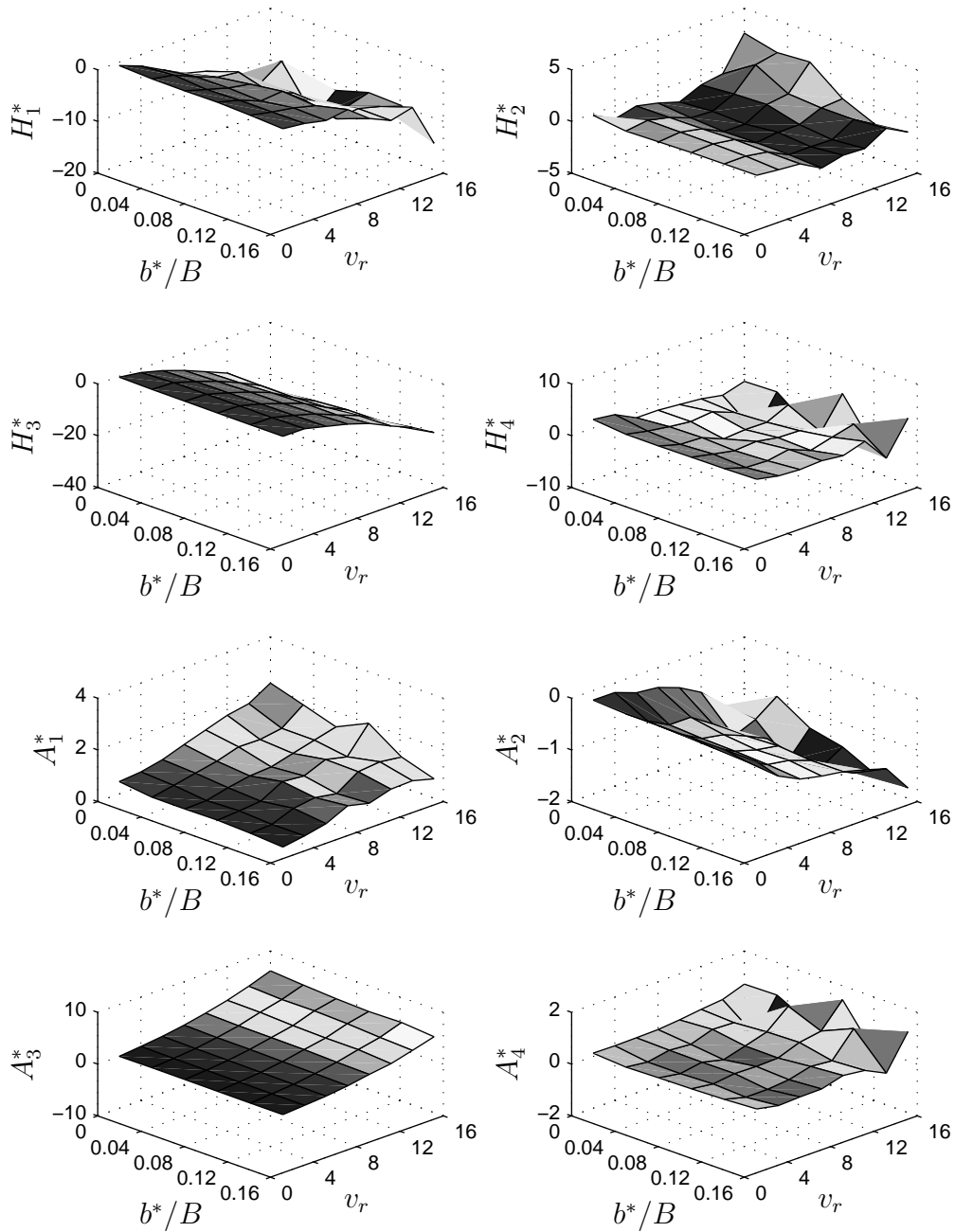
Figure D.6: Sensitivity of flutter limit to section geometry: aerodynamic derivatives from forced vibration simulations on Structure A with increasing central slot ($b^*/B = 0 - 0.15$, $B/D = 11.6$) (cf. Figure 7.12).
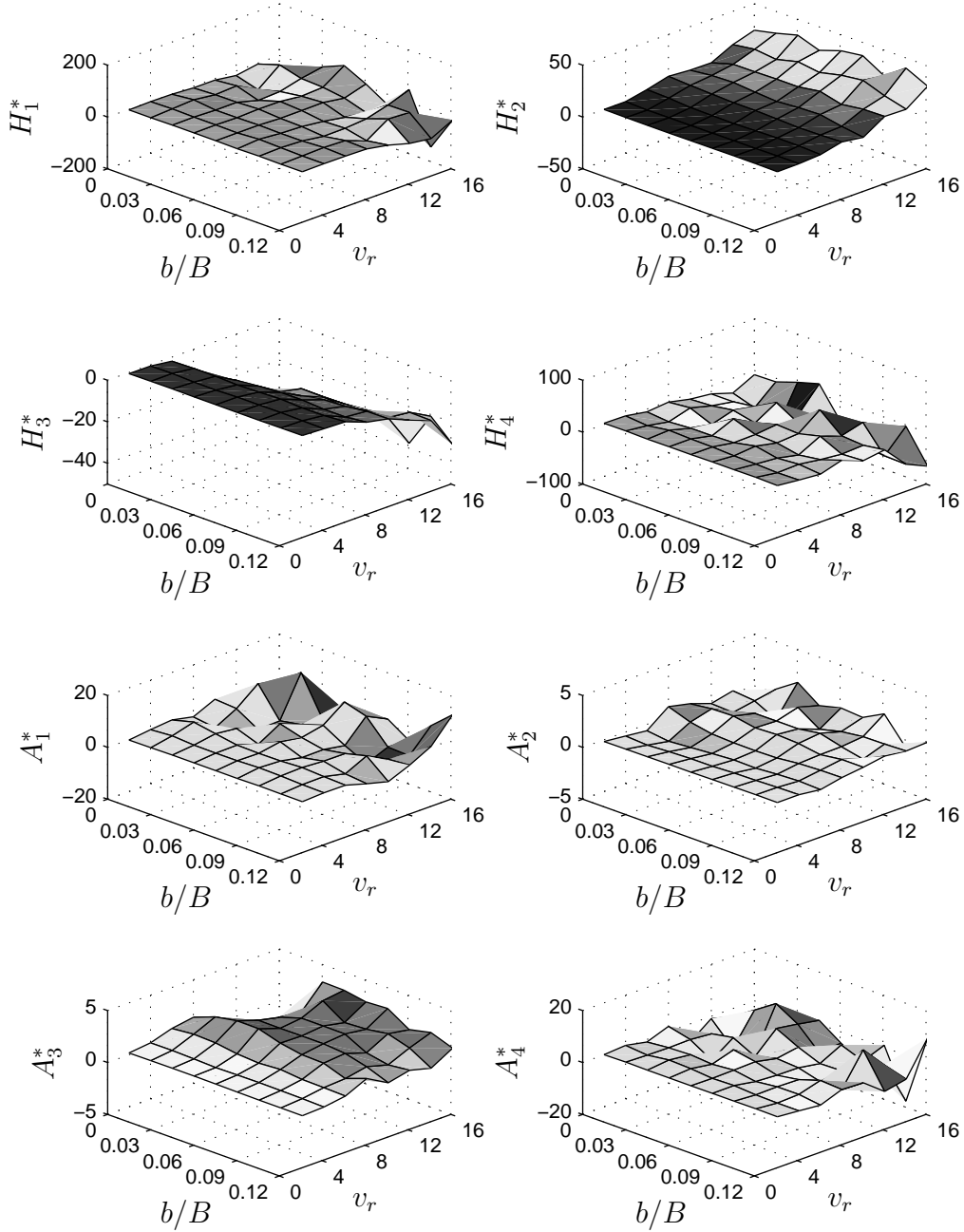
Figure D.7: Sensitivity of flutter limit to section geometry: aerodynamic derivatives from forced vibration simulations on section with straight fairings ($b = d = 0 - D/2$) (cf. Figure 7.14).
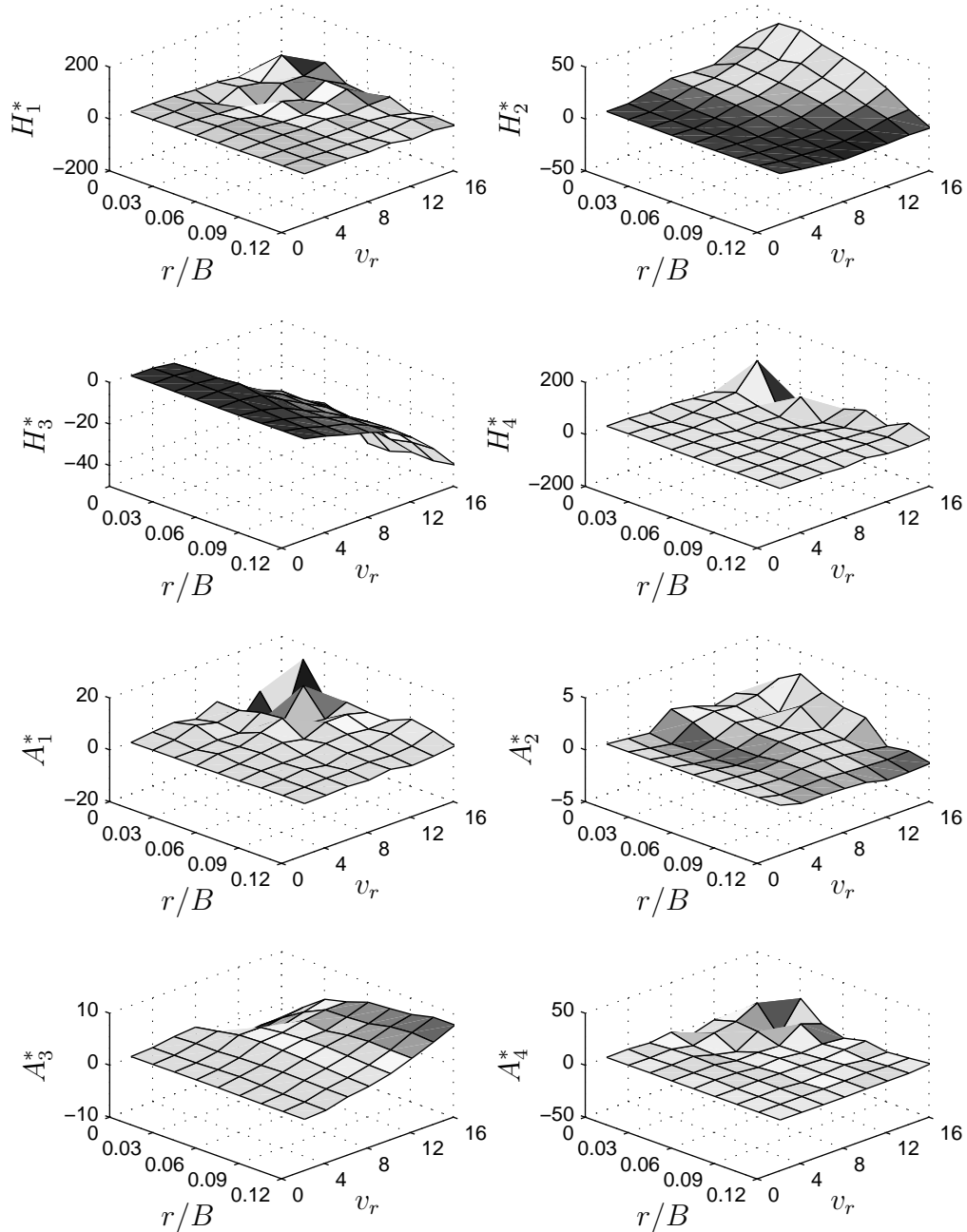
Figure D.8: Sensitivity of flutter limit to section geometry: aerodynamic derivatives
from forced vibration simulations on section with curved fairings $(r = 0 - D/2)$
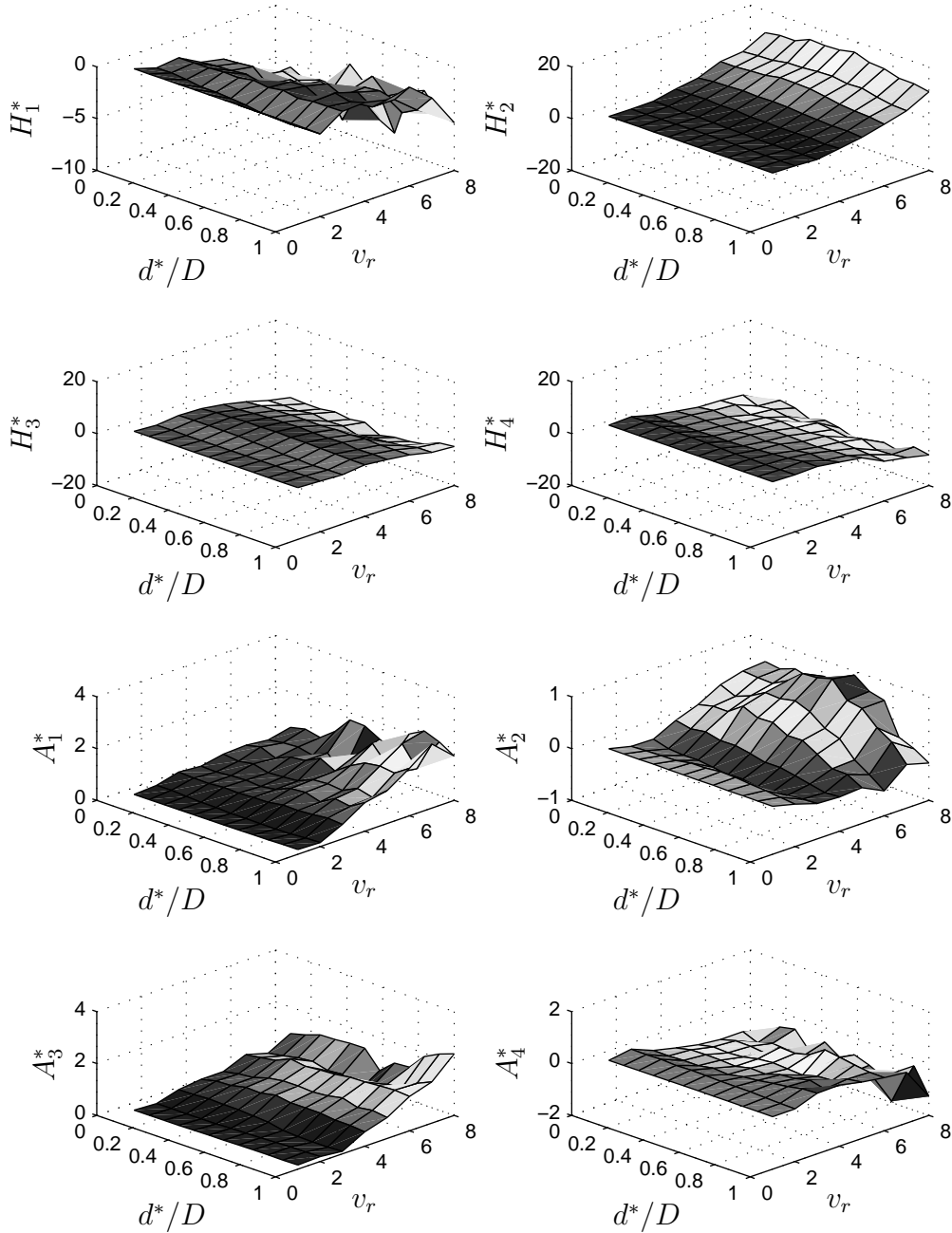(cf. Figure 7.14).

Figure D.9: Sensitivity of flutter limit to section geometry: aerodynamic derivatives from forced vibration simulations on H-section with increasing depth ($d^*/D = 0.04 - 1.00$) (cf. Figure 7.16).
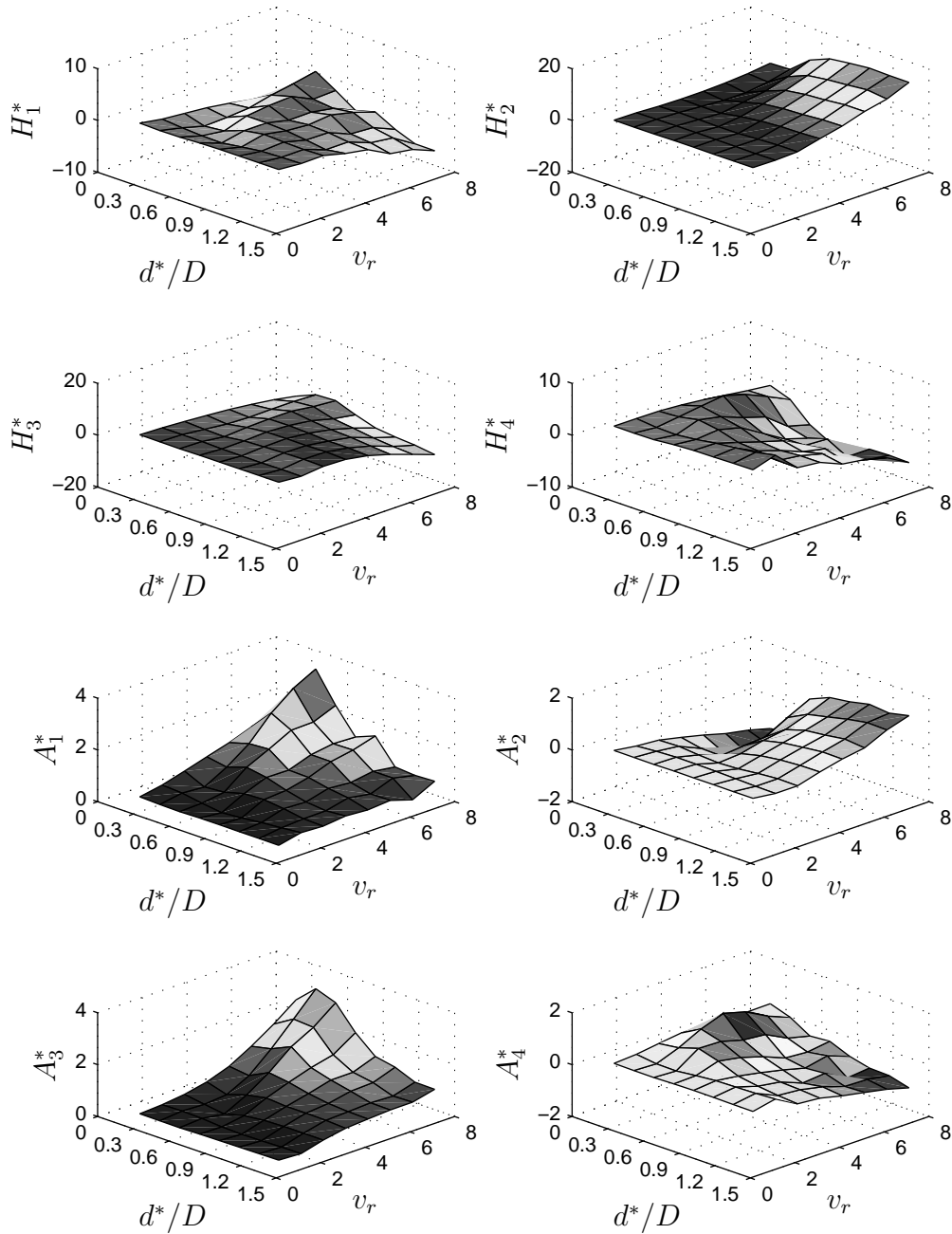
Figure D.10: Sensitivity of flutter limit to section geometry: aerodynamic derivatives from forced vibration simulations on plate with increasing edges ($d^*/D = 0.13 - 1.25$) (cf. Figure 7.16).
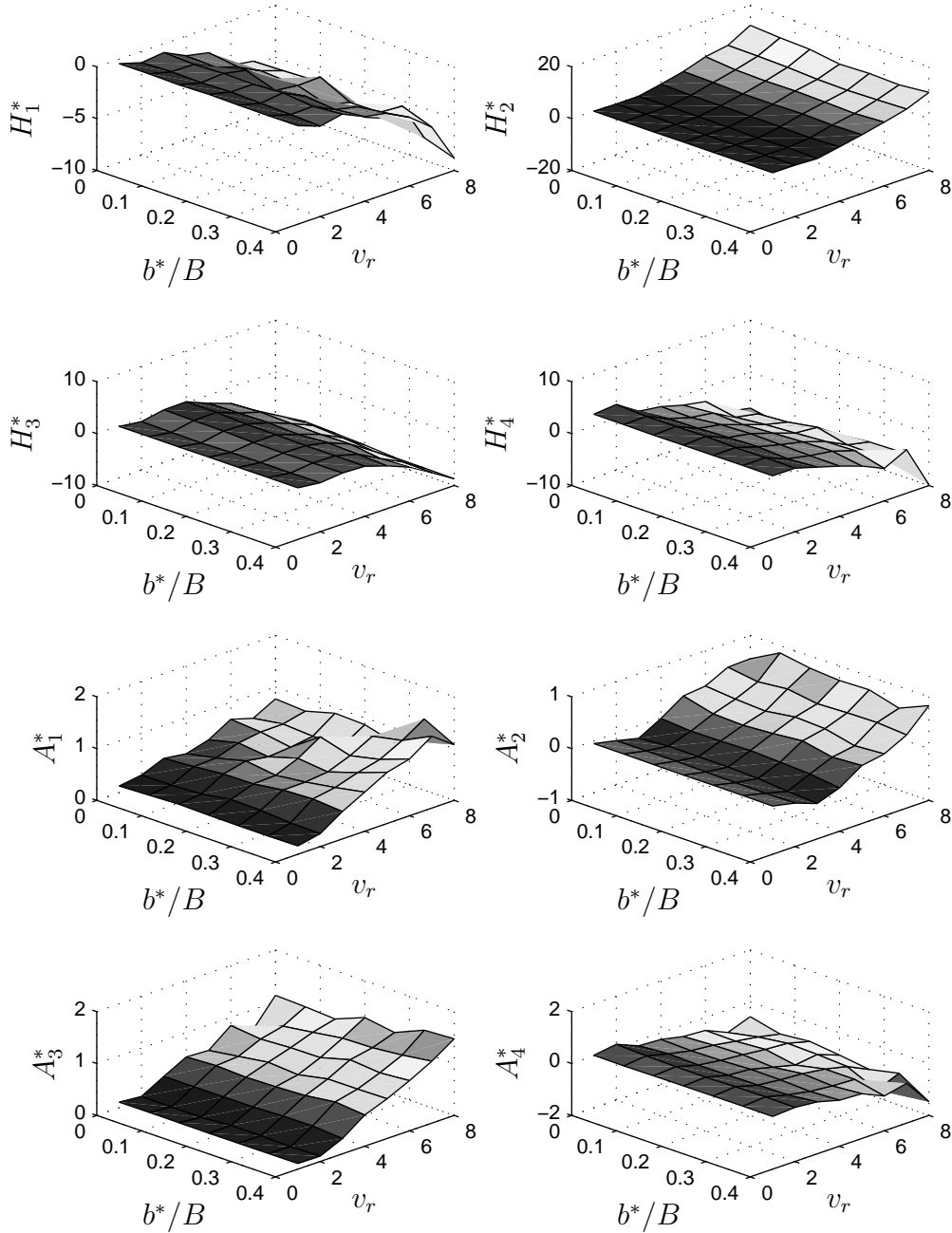
Figure D.11: Sensitivity of flutter limit to section geometry: aerodynamic derivatives from forced vibration simulations on H-shape with bottom plate ($b^*/B = 0-0.15$, $B/D = 5$) (cf. Figure 7.18).
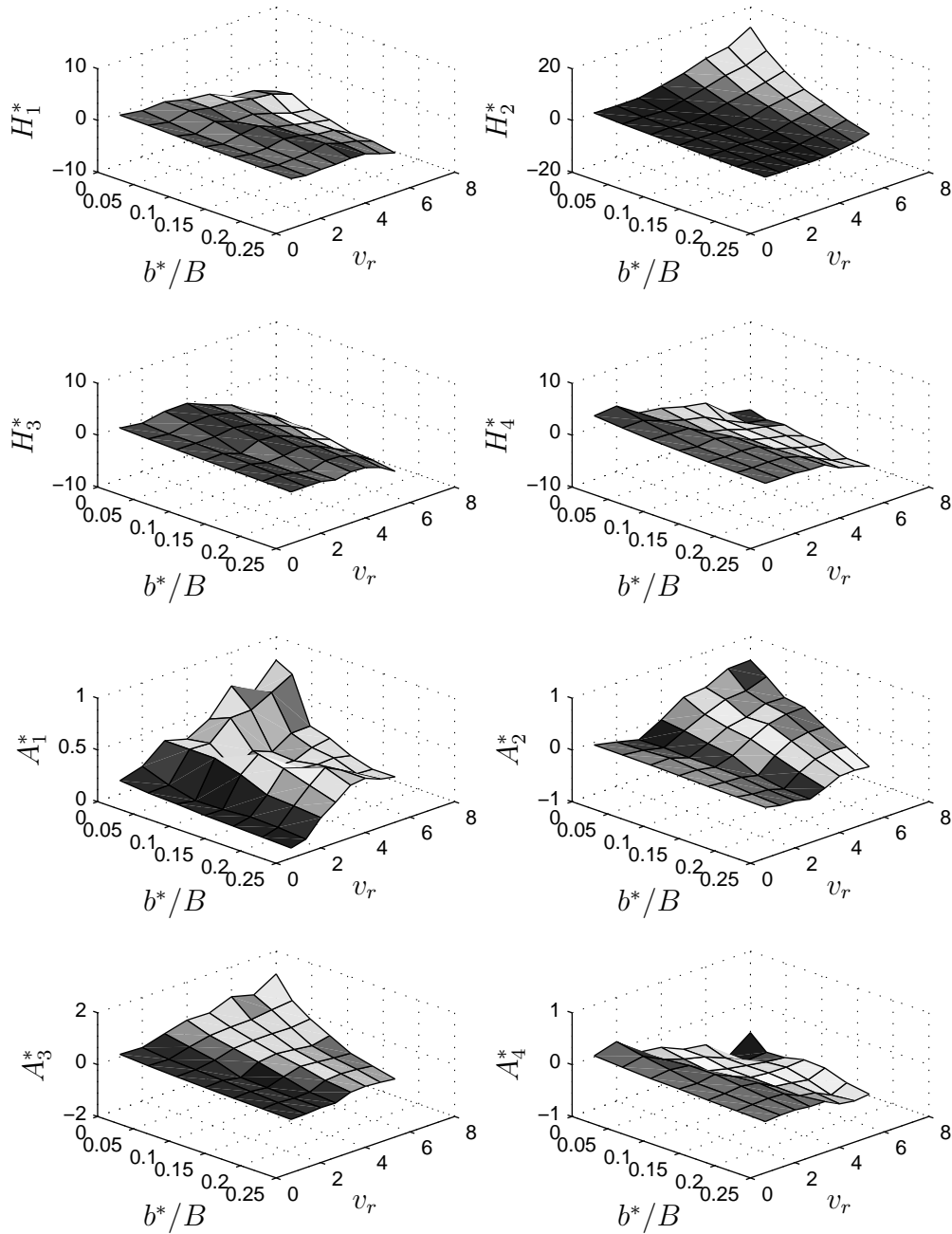
Figure D.12: Sensitivity of flutter limit to section geometry: aerodynamic derivatives from forced vibration simulations on H-shape with fairing ($b^*/B = 0 - 0.25$, $B/D = 5$) (cf. Figure 7.18).
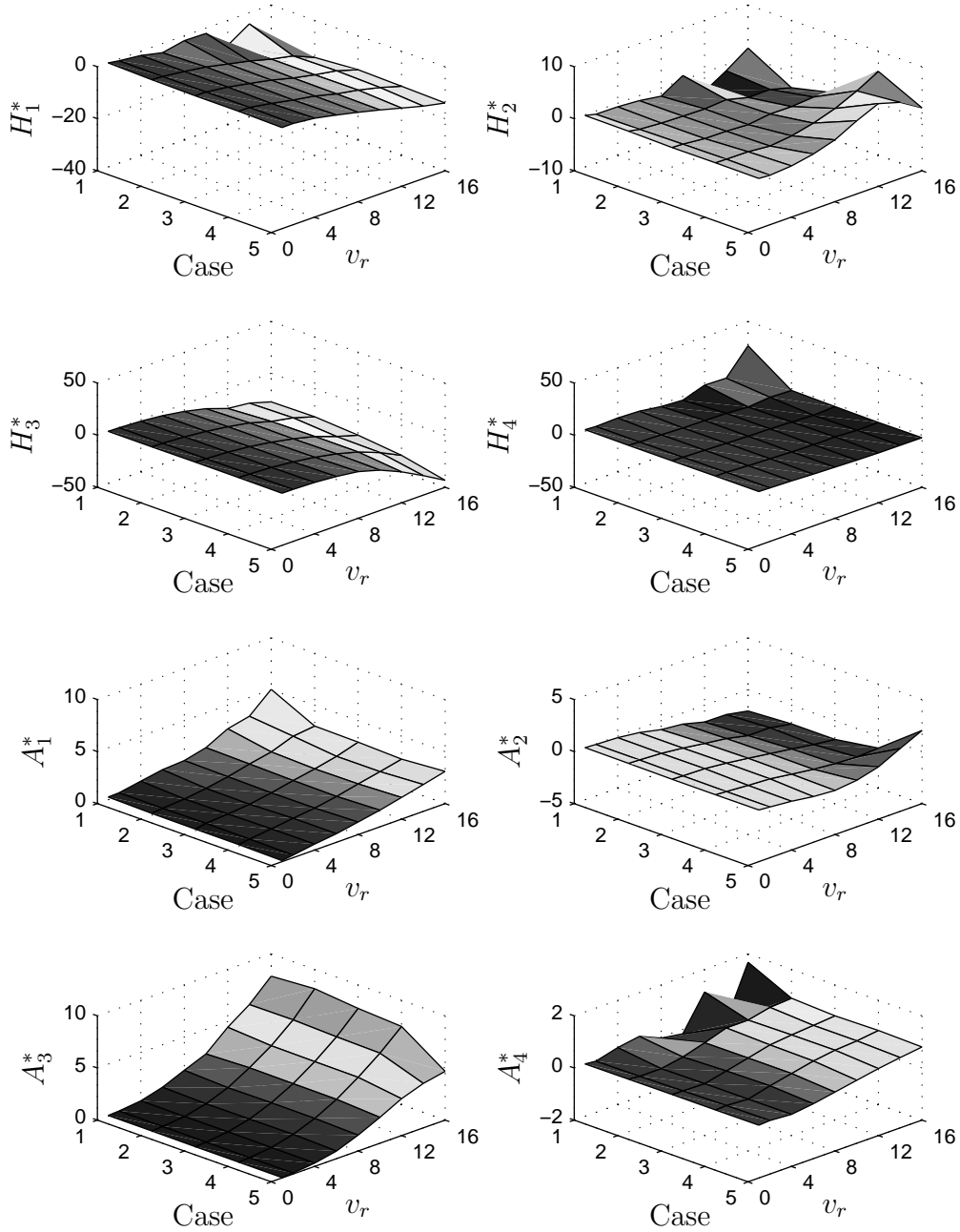
Figure D.13: Sensitivity of flutter limit to forcing amplitudes: aerodynamic derivatives from forced vibration simulations on Structure A (cf. Figure 7.20).
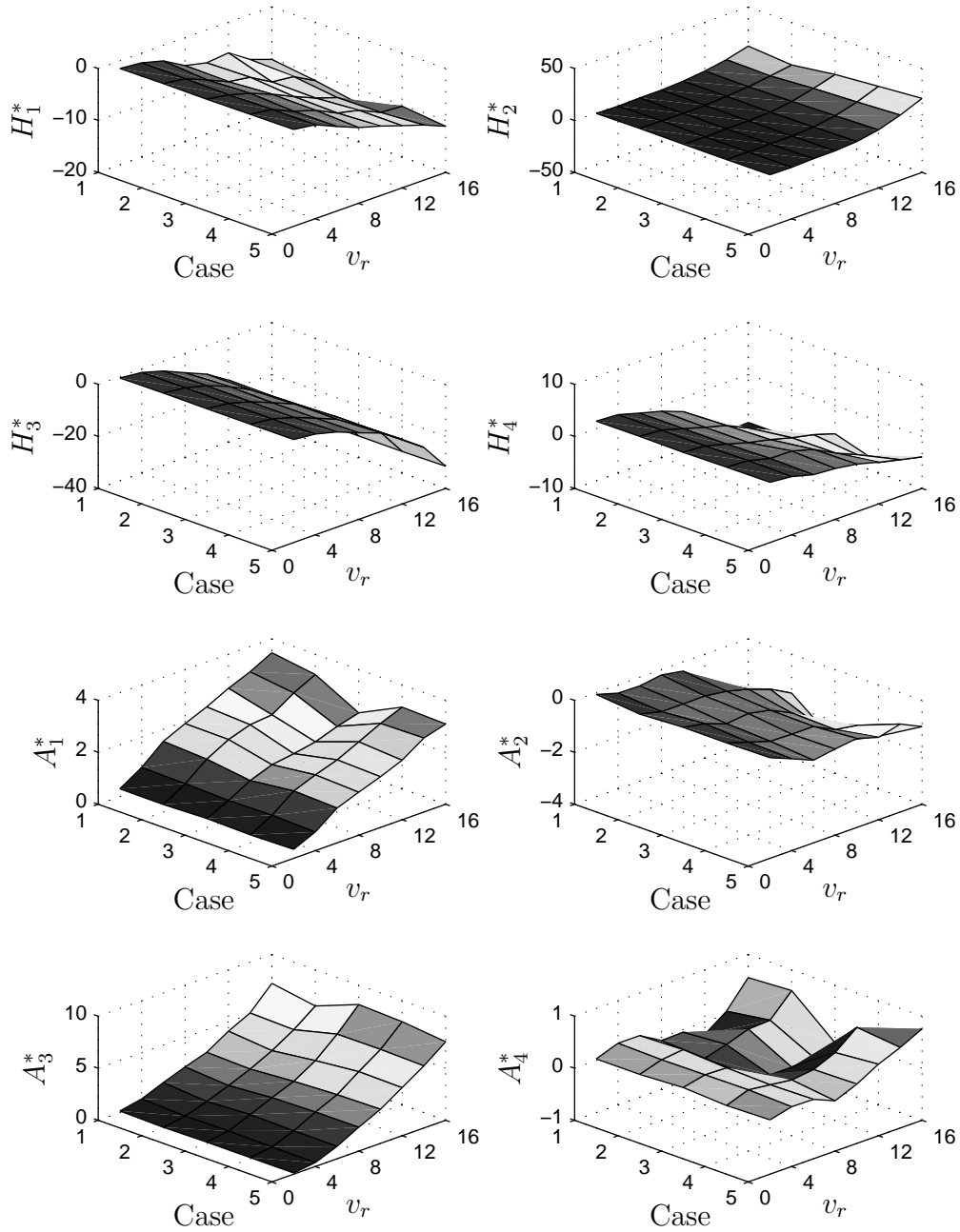
Figure D.14: Sensitivity of flutter limit to forcing amplitudes: aerodynamic derivatives from forced vibration simulations on flat plate (aspect ratio 1:100) (cf. Figure 7.20).

Appendix E
Probabilistic Assessment of Coupled Models

E.1 Correlation Matrices

Section 8.3 discusses the correlation considered between different structural input parameters and the aerodynamic derivatives. The following correlation matrices have been used to generate correlated samples for sensitivity and uncertainty analyses.

E.1.1 Structural Parameters

The correlation was considered between structural parameters $B - I$, $I - f_\alpha$ and $f_\alpha - \xi$. These parameters were assumed correlated with $\rho(X_i, X_j) = 0.0$ to 0.5.

$$\rho(X_i, X_j) = \begin{array}{c} \text{parameter} \\ B \\ I \\ f_\alpha \\ \xi \end{array} \begin{array}{cccc} B & I & f_\alpha & \xi \\ \left[\begin{array}{cccc} 1.0 & \mathbf{0.5} & 0.0 & 0.0 \\ \mathbf{0.5} & 1.0 & \mathbf{0.5} & 0.0 \\ 0.0 & \mathbf{0.5} & 1.0 & \mathbf{0.5} \\ 0.0 & 0.0 & \mathbf{0.5} & 1.0 \end{array}\right] \end{array} \tag{E.1}$$

E.1.2 Aerodynamic Derivatives

(a) Synthetic or artificial correlation introduced between all aerodynamic derivatives as

    (i) no correlation $\rho(X_i, X_j)=0.00$

    (ii) full correlation $\rho(X_i, X_j)=0.99$

    (iii) partial correlation $\rho(X_i, X_j)=0.50$

$$\rho(X_i, X_j) = \begin{array}{c} \text{derivative} \\ H_1^* \\ H_2^* \\ H_3^* \\ H_4^* \\ A_1^* \\ A_2^* \\ A_3^* \\ A_4^* \end{array} \begin{array}{cccccccc} H_1^* & H_2^* & H_3^* & H_4^* & A_1^* & A_2^* & A_3^* & A_4^* \\ \left[\begin{array}{cccccccc} 1.0 & 0.5 & 0.5 & 0.5 & 0.5 & 0.5 & 0.5 & 0.5 \\ 0.5 & 1.0 & 0.5 & 0.5 & 0.5 & 0.5 & 0.5 & 0.5 \\ 0.5 & 0.5 & 1.0 & 0.5 & 0.5 & 0.5 & 0.5 & 0.5 \\ 0.5 & 0.5 & 0.5 & 1.0 & 0.5 & 0.5 & 0.5 & 0.5 \\ 0.5 & 0.5 & 0.5 & 0.5 & 1.0 & 0.5 & 0.5 & 0.5 \\ 0.5 & 0.5 & 0.5 & 0.5 & 0.5 & 1.0 & 0.5 & 0.5 \\ 0.5 & 0.5 & 0.5 & 0.5 & 0.5 & 0.5 & 1.0 & 0.5 \\ 0.5 & 0.5 & 0.5 & 0.5 & 0.5 & 0.5 & 0.5 & 1.0 \end{array}\right] \end{array} \tag{E.2}$$

(b) Correlation for lift force aerodynamic derivatives $H_1^* - H_4^*$ and $H_2^* - H_3^*$
Correlation for moment aerodynamic derivatives $A_1^* - A_4^*$ and $A_2^* - A_3^*$

$$\rho(X_i, X_j) = \begin{array}{c} \\ H_1^* \\ H_2^* \\ H_3^* \\ H_4^* \\ A_1^* \\ A_2^* \\ A_3^* \\ A_4^* \end{array} \begin{array}{cccccccc} \text{derivative} & H_1^* & H_2^* & H_3^* & H_4^* & A_1^* & A_2^* & A_3^* & A_4^* \\ \left[\begin{array}{cccccccc} 1.0 & 0.0 & 0.0 & \mathbf{0.99} & 0.0 & 0.0 & 0.0 & 0.0 \\ 0.0 & 1.0 & \mathbf{0.99} & 0.0 & 0.0 & 0.0 & 0.0 & 0.0 \\ 0.0 & \mathbf{0.99} & 1.0 & 0.0 & 0.0 & 0.0 & 0.0 & 0.0 \\ \mathbf{0.99} & 0.0 & 0.0 & 1.0 & 0.0 & 0.0 & 0.0 & 0.0 \\ 0.0 & 0.0 & 0.0 & 0.0 & 1.0 & 0.0 & 0.0 & \mathbf{0.99} \\ 0.0 & 0.0 & 0.0 & 0.0 & 0.0 & 1.0 & \mathbf{0.99} & 0.0 \\ 0.0 & 0.0 & 0.0 & 0.0 & 0.0 & \mathbf{0.99} & 1.0 & 0.0 \\ 0.0 & 0.0 & 0.0 & 0.0 & \mathbf{0.99} & 0.0 & 0.0 & 1.0 \end{array}\right] \end{array} \quad \text{(E.3)}$$

(c) Dependence of aerodynamic derivatives on each other

(i) since aerodynamic derivatives for flat plate are approximated as $H_1^* = -K.H_3^*$ and $A_1^* = -K.A_3^*$

$$\rho(X_i, X_j) = \begin{array}{c} \\ H_1^* \\ H_2^* \\ H_3^* \\ H_4^* \\ A_1^* \\ A_2^* \\ A_3^* \\ A_4^* \end{array} \begin{array}{cccccccc} \text{derivative} & H_1^* & H_2^* & H_3^* & H_4^* & A_1^* & A_2^* & A_3^* & A_4^* \\ \left[\begin{array}{cccccccc} 1.0 & 0.0 & \mathbf{0.99} & 0.0 & 0.0 & 0.0 & 0.0 & 0.0 \\ 0.0 & 1.0 & 0.0 & 0.0 & 0.0 & 0.0 & 0.0 & 0.0 \\ \mathbf{0.99} & 0.0 & 1.0 & 0.0 & 0.0 & 0.0 & 0.0 & 0.0 \\ 0.0 & 0.0 & 0.0 & 1.0 & 0.0 & 0.0 & 0.0 & 0.0 \\ 0.0 & 0.0 & 0.0 & 0.0 & 1.0 & 0.0 & \mathbf{0.99} & 0.0 \\ 0.0 & 0.0 & 0.0 & 0.0 & 0.0 & 1.0 & 0.0 & 0.0 \\ 0.0 & 0.0 & 0.0 & 0.0 & \mathbf{0.99} & 0.0 & 1.0 & 0.0 \\ 0.0 & 0.0 & 0.0 & 0.0 & 0.0 & 0.0 & 0.0 & 1.0 \end{array}\right] \end{array} \quad \text{(E.4)}$$

(ii) it is also interesting to see the correlation between $H_1^* - H_2^*$, $H_3^* - H_4^*$, $A_1^* - A_2^*$ and $A_3^* - A_4^*$.

$$\rho(X_i, X_j) = \begin{array}{c} \\ H_1^* \\ H_2^* \\ H_3^* \\ H_4^* \\ A_1^* \\ A_2^* \\ A_3^* \\ A_4^* \end{array} \begin{array}{cccccccc} \text{derivative} & H_1^* & H_2^* & H_3^* & H_4^* & A_1^* & A_2^* & A_3^* & A_4^* \\ \left[\begin{array}{cccccccc} 1.0 & \mathbf{0.99} & 0.0 & 0.0 & 0.0 & 0.0 & 0.0 & 0.0 \\ \mathbf{0.99} & 1.0 & 0.0 & 0.0 & 0.0 & 0.0 & 0.0 & 0.0 \\ 0.0 & 0.0 & 1.0 & \mathbf{0.99} & 0.0 & 0.0 & 0.0 & 0.0 \\ 0.0 & 0.0 & \mathbf{0.99} & 1.0 & \mathbf{0.99} & 0.0 & 0.0 & 0.0 \\ 0.0 & 0.0 & 0.0 & \mathbf{0.99} & 1.0 & 0.0 & 0.0 & 0.0 \\ 0.0 & 0.0 & 0.0 & 0.0 & 0.0 & 1.0 & 0.0 & 0.0 \\ 0.0 & 0.0 & 0.0 & 0.0 & 0.0 & 0.0 & 1.0 & \mathbf{0.99} \\ 0.0 & 0.0 & 0.0 & 0.0 & 0.0 & 0.0 & \mathbf{0.99} & 1.0 \end{array}\right] \end{array}$$
$$\text{(E.5)}$$